A Functional Monte Carlo Method for k-Eigenvalue Problems

by

Jinan Yang

A dissertation submitted in partial fulfillment
of the requirements for the degree of
Doctor of Philosophy
(Nuclear Engineering and Radiological Sciences)
in The University of Michigan
2011

Doctoral Committee:

Professor Edward W. Larsen, Chair
Research Professor Michael R. Combi
Professor Thomas J. Downar
Professor James P. Holloway
Professor William R. Martin

Dedicated to the memory of my mother and my husband.

To my father and my daughter

Acknowledgments

I would like to thank my advisor, Professor Edward Larsen, for his unconditional support, guidance and patience throughout my graduate studies at the University of Michigan. He has provided me invaluable knowledge and skills in doing scientific research. His enthusiasm and hard working attitude have inspired me deeply. I would also like to thank my committee members, William Martin, James Holloway, Thomas Downar, and Michael Combi, for their advice and comments.

I would like to thank Professor Ahmet Ziyaeddin Akcasu, Professor Ronald Fleming, Professor Han Gyu Joo (Seoul National University), and Dr. YunLin Xu (Argonne National Laboratory) for valuable discussions.

I would like to thank Peggy Gramer, who added unforgettable memories to my study years. She made the NERS a family for me. I would like to thank my fellow students Emily Wolters, Tiberius Moran, Eva Sunny, Wei Ji, Yan Cao, and Haori Yang for their in class and out of class encouragement and support.

I would like to thank Sheila Motomatsu, Tomoko Ishizu, Chiaki Horie, Nobushika Kawasaki, Russell Walstedt, and Yishu Zhang for their life long friendship.

Finally, heartfelt thanks to my daughter Zijun Zhao. Without her full support and understanding, this work would not have been possible.

Table of Contents

List of Tables

Table

List of Figures

Figure

Abstract

A longstanding problem for Monte Carlo (MC) criticality simulation is the slow convergence of the fission source distribution for systems with a high dominance ratio (DR). In this thesis, we have developed and tested a new hybrid deterministic and MC method, called the Functional Monte Carlo (FMC) method, to solve such problems. We show herein that the FMC method produces a significant improvement in the speed of convergence and accuracy of criticality calculations, which are particularly important for nuclear reactor operation and design, as well as for nuclear safety applications. Different from any previous hybrid method, the FMC method does not directly estimate the eigenfunction and eigenvalue via MC particle simulation. Instead, it uses MC techniques to directly estimate certain *nonlinear functionals*. These functionals are then used in the low-order FMC equations to calculate the k-eigenfunction and eigenvalue. The resulting estimates have no spatial or angular truncation errors, and are generally more accurate than estimates obtained using conventional MC methods.

The FMC method is based on two assumptions:

1. The functionals depend weakly on the angular flux and can be evaluated with MC more accurately than direct MC estimates of the angular or scalar flux.
2. If the low-order FMC equations are solved with small errors in the functionals, the resulting errors in the eigenfunction and eigenvalue will be small.

In this work, we have developed the FMC method for monoenergetic, multigroup, and continuous energy k-eigenvalue problems in 1-D planar geometry. We have tested the FMC method on various problems, in which standard MC estimates of the eigenfunction tend

to “wobble.” Our numerical results indicate that the fission source distribution is found to converge orders of magnitude faster using the FMC approach. Inter-cycle correlation is very weak for the FMC method. The true and apparent relative errors are about the same for the FMC method. And with FMC feedback, the performance of MC estimates of the eigenfunction improved significantly. For future research, it remains to extend the FMC method to include realistic cross sections and multi-dimensional problems. We see no fundamental impediment to doing this.

Chapter 1
Introduction

Nuclear criticality is the ability to sustain a nuclear fission chain reaction in the absence of external sources - that is, to make the fission chain reaction maintain a steady state. This is particularly important for nuclear reactor operation, nuclear reactor design, and nuclear safety applications. Nuclear criticality analyses include k-eigenvalue (core multiplication) and fundamental mode eigenfunction calculations (flux or power distribution). The calculation of these quantities is the most common analysis performed in nuclear core studies. The power distribution is of significant importance to thermal analysis and fuel depletion studies of the reactor core. These quantities may be obtained by solving a steady-state Boltzmann transport equation, which can be derived from the general time-dependent Boltzmann transport equation [4; 10; 11; 21], given by

$$\begin{aligned}\frac{1}{v}\frac{\partial \psi}{\partial t}(\vec{r},\vec{\Omega},E,t)+\vec{\Omega}\cdot\nabla\psi(\vec{r},\ \vec{\Omega},E,t)+\Sigma_t(\vec{r},E)\psi(\vec{r},\vec{\Omega},E,t)\\ =\int_0^\infty\int_{4\pi}\Sigma_s(\vec{r},\vec{\Omega}'\cdot\vec{\Omega},E'\to E)\psi(\vec{r},\vec{\Omega}',E',t)d\Omega' dE'\\ +\frac{\chi(E)}{4\pi}\int_0^\infty\int_{4\pi}\nu\Sigma_f(\vec{r},E')\psi(\vec{r},\vec{\Omega}',E',t)d\Omega' dE'+\frac{1}{4\pi}Q(\vec{r},\vec{\Omega},E,t)\ ,\end{aligned}\tag{1.1}$$

with boundary condition:

$$\psi(\vec{r},\vec{\Omega},E,t)=\psi^b(\vec{r},\vec{\Omega},E,t)\ ,\ \vec{r}\in\partial R\ ,\ \vec{\Omega}\cdot\vec{n}<0\ ,\ 0<E<\infty\ ,\ t>0\ ,\tag{1.2}$$

where ψ^b is specified. If $\psi^b=0$, then ∂R becomes a vacuum boundary.

Also, $\psi(\vec{r},\vec{\Omega},E,t)$ should satisfy the initial condition:

$$\psi(\vec{r},\vec{\Omega},E,t) = \psi(\vec{r},\vec{\Omega},E,0)\ ,\ \vec{r}\in R\ ,\ \vec{\Omega}\in 4\pi\ ,\ 0<E<\infty\ . \tag{1.3}$$

The variables and the physical meaning of each term in Eq. (1.1) are given as follows:

$\vec{r} = (x,y,z) =$ spatial variable,

$\vec{\Omega} = (\Omega_x,\Omega_y,\Omega_z) =$ direction, or angular variable,

$E =$ energy,

$t =$ time,

$\psi(\vec{r},\vec{\Omega},E) =$ angular flux,

$\vec{\Omega}\cdot\nabla\psi(\vec{r},\vec{\Omega},E) =$ net leakage rate,

$\Sigma_t(\vec{r},E)\psi(\vec{r},\vec{\Omega},E) =$ collision rate,

$\int_0^\infty\int_{4\pi}\Sigma_s(\vec{r},\vec{\Omega}'\cdot\vec{\Omega},E'\to E)\psi(\vec{r},\vec{\Omega}',E')d\Omega'dE' =$ in-scattering rate,

$\frac{\chi(E)}{4\pi}\int_0^\infty\int_{4\pi}\nu\Sigma_f(\vec{r},E')\psi(\vec{r},\vec{\Omega}',E')d\Omega'dE' =$ fission neutron production rate, and

$Q(\vec{r},\vec{\Omega},E,t) =$ external source.

It is possible to obtain a static eigenvalue problem by setting $\partial\psi/\partial t = 0$ and $Q = 0$ in Eq. (1.1), and modifying the fission source term by a factor $1/k$. Then Eq. (1.1) becomes a steady-state Boltzmann transport equation,

$$\begin{aligned}
&\vec{\Omega}\cdot\nabla\psi(\vec{r},\vec{\Omega},E) + \Sigma_t(\vec{r},E)\psi(\vec{r},\vec{\Omega},E)\\
&\quad = \int_0^\infty\int_{4\pi}\Sigma_s(\vec{r},\vec{\Omega}'\cdot\vec{\Omega},E'\to E)\psi(\vec{r},\vec{\Omega}',E')d\vec{\Omega}'dE'\\
&\qquad + \frac{1}{k}\frac{\chi(E)}{4\pi}\int_0^\infty\int_{4\pi}\nu\Sigma_f(\vec{r},E')\psi(\vec{r},\vec{\Omega}',E')d\vec{\Omega}'dE'\ ,
\end{aligned} \tag{1.4}$$

where $k =$ eigenvalue = effective multiplication factor, and $\psi(\vec{r},\vec{\Omega},E) =$ fundamental mode eigenfunction.

Eq. (1.4) can be solved by varying k to adjust the magnitude of the fission source. The significance of the effective multiplication factor k can be understood as follows: If $k = 1$, the production of neutrons due to fission exactly balances the loss of neutrons due to leakage and capture, i.e. a steady state is achieved. In this case, the fission system is *critical*. If $k > 1$, the production of neutrons is greater than the loss of neutrons. In this case, the fission system is *supercritical*. If $k < 1$, the production of neutrons is less than the loss of neutrons. In this case, the fission system is *subcritical*.

Eq. (1.4) can be written in an matrix form:

$$L\psi + C\psi = S\psi + \frac{1}{k}F\psi \,, \tag{1.5}$$

where $L =$ Leakage operator, $C =$ Collision operator, $S =$Scattering operator, and $F =$ fission operator.

Letting $M = (L + C - S)^{-1}F$, Eq. (1.5) can be further simplified as

$$\psi = \frac{1}{k}M\psi \,. \tag{1.6}$$

In general, M has $k_1 > k_2 > \cdots > k_m$ eigenvalues, and $\vec{u}_1 \,, \vec{u}_2 \,, \cdots \,, \vec{u}_m$ are the corresponding normalized eigenfunctions. Eq. (1.6) may be solved using power iteration [4; 27], i.e.

$$\psi^{(n+1)} = \frac{1}{k^{(n)}}M\psi^{(n)} \,, \tag{1.7}$$

that is to solve

$$(L + C - S)\psi^{(n+1)} = \frac{1}{k^{(n)}}F\psi^{(n)} \,.$$

The next estimate of the effective multiplication factor k is obtained by

$$k^{(n+1)} = k^{(n)} \frac{\int F\psi^{(n+1)} dV}{\int F\psi^{(n)} dV} \,. \tag{1.8}$$

We express the initial flux guess $\psi^{(0)}$ in terms of the normalized eigenfunctions, giving

$$\psi^{(0)} = c_1\vec{u_1} + c_2\vec{u_2} + \cdots + c_m\vec{u_m} \,. \tag{1.9}$$

Substituting Eq. (1.9) into Eq. (1.7), we obtain

$$\begin{aligned}
\psi^{(n+1)} &= \frac{1}{k^{(n)}} M\psi^{(n)} \\
&= \frac{1}{k^{(n)}}\frac{1}{k^{(n-1)}} \cdot \frac{1}{k^{(0)}} M^{n+1}\psi^{(0)} \\
&= \Big[\prod_{i=0}^{n}\frac{1}{k^{(i)}}\Big](c_1 \cdot k_1^{n+1}\vec{u_1} + c_2 \cdot k_2^{n+1}\vec{u_2} + \cdots c_m \cdot k_m^{n+1}\vec{u_m}) \\
&= \Big[\prod_{i=0}^{n}\frac{k_1}{k^{(i)}}\Big] \cdot c_1\Big[\vec{u_1} + \frac{c_2}{c_1}\big(\frac{k_2}{k_1}\big)^{(n+1)}\vec{u_2} + \ldots\Big] \\
&= C_1\Big[\vec{u_1} + C_2(\frac{k_2}{k_1})^{(n+1)}\vec{u_2} + \ldots\Big] \,.
\end{aligned} \tag{1.10}$$

Also, substituting Eq. (1.10) into Eq. (1.8), we obtain

$$\begin{aligned}
k^{(n+1)} &= k^{(n)}\frac{\int FC_1\Big[\vec{u_1} + C_2(\frac{k_2}{k_1})^{(n+1)}\vec{u_2} + \ldots\Big]dV}{\int FC_1\Big[\vec{u_1} + C_2(\frac{k_2}{k_1})^{(n)}\vec{u_2} + \ldots\Big]dV} \\
&= k^{(n)}\frac{1 + C_3(\frac{k_2}{k_1})^{(n+1)} + \ldots}{1 + C_3(\frac{k_2}{k_1})^{(n)} + \ldots} \\
&\approx k_1\Big[1 + C_3(\frac{k_2}{k_1})^{(n+1)} + \ldots\Big]\Big[1 - C_3(\frac{k_2}{k_1})^{(n)} + \ldots\Big] \\
&= k_1\big[1 + C_3(\frac{k_2}{k_1})^n(\frac{k_2}{k_1} - 1) + \ldots\big] \,.
\end{aligned} \tag{1.11}$$

In these equations, $k_1 > k_2 > \cdots$ are the eigenvalues and $\vec{u_1}\,, \vec{u_2}\,, \cdots$ are the corresponding eigenfunctions of the transport equation. Then k_1 and $\vec{u_1}$ are the fundamental eigenvalue and eigenfunction, respectively. C_1, C_2, and C_3 are constants, and n is the number of iterations.

The dominance ratio (DR) [27; 30] is defined as k_2/k_1. DR can be obtained using Eq.

(1.10). We rewrite Eq. (1.10) as

$$\begin{aligned}\frac{\psi^{(n+1)}}{C_1} &= \vec{u_1} + C_2(\frac{k_2}{k_1})^{(n+1)}\vec{u_2} + \dots \\ &= \vec{u_1} + C_2 DR^{(n+1)}\vec{u_2} + \dots ,\end{aligned}$$

then the error after $n+1$ iterations becomes

$$\vec{e}^{(n+1)} = \frac{\psi^{(n+1)}}{C_1} - \vec{u_1} = C_2 DR^{(n+1)}\vec{u_2} + \dots .$$

Thus the dominance ratio satisfies the following condition:

$$DR = \frac{\|\vec{e}^{(n+1)}\|}{\|\vec{e}^{(n)}\|} . \tag{1.12}$$

Since the absolute true errors are generally unknown, one can use pseudo-errors instead in calculating the dominance ratio, i.e.

$$DR = \frac{\|\phi^{(n+1)} - \phi^{(n)}\|}{\|\phi^{(n)} - \phi^{(n-1)}\|} . \tag{1.13}$$

DR is the key parameter that determines the convergence rate of the power iteration procedure. As the number of iterations increases, the higher order terms die away as $DR^n \to 0$, the eigenfunction will converge to the fundamental eigenfunction $\vec{u_1}$, and k will converge to the largest eigenvalue k_1 . However, for optically thick fissile systems, $k_2 \to k_1$ and $DR \to 1$. In this case, the eigenfunction and the eigenvalue do not converge at the same rate. As shown in Eq. (1.11), the higher mode terms in the eigenvalue contain terms like $DR^n(DR-1)$. The additional factor $(DR-1)$ will guarantee that the eigenvalue converges quickly even for optically thick fissile systems. The convergence of the eigenfunction in optically thick fissile systems is not as fast, because the higher mode terms contain only the factor DR^n. It may take several hundreds or thousands of iterations for the higher mode

terms to die away. The slow convergence of the eigenfunction with Monte Carlo has been known for decades and has been examined in several recent publications [36; 29; 30]. In this dissertation we propose a new hybrid deterministic and Monte Carlo method called the "Functional Monte Carlo" (FMC) method for k-eigenvalue problems. This new method improves the convergence of the eigenfunction significantly.

The calculation of the fundamental k-eigenvalue and eigenfunction is one of the most important calculations in nuclear reactor design. Typically, there are two sets of methods that are most commonly used for this calculation: *deterministic* methods and *Monte Carlo* methods.

In the deterministic approach, the integro-differential transport equation is discretized in space, angle, and energy, and the resulting algebraic equations are solved using iteration methods. In energy discretization, the energy variable E is discretized into a number of energy bins or groups, i.e. the multigroup energy approximation. Within each energy group the fission source, fission spectrum, and flux are integrated. The multigroup cross sections are treated as flux-weighted cross sections over the given energy group. There are two types of angular discretization methods, the P_N method and the S_N method. The S_N method discretizes the angular flux using a quadrature set, and assumes further that the particles can only travel along a finite number of directions. The P_N method approximates the angular flux by a finite sum of spherical harmonic moments. In spatial discretizations, we impose a spatial grid on the system. We can then approximate the relation between the cell-averaged flux and cell-edge flux using finite difference, diamond difference, or step characteristic methods. Owing to these discretizations in energy, angle and space, a deterministic solution contains truncation errors.

In the Monte Carlo approach [15; 27], another form of the transport equation, i.e. the integral transport equation, is solved by simulating a large number of Monte Carlo particles and recording tallies of their average behavior. Due to the stochastic nature of the Monte Carlo simulation, this solution contains statistical errors. The advantage of Monte Carlo

simulations is that there is no approximation in modeling the geometries and physics behind the theory (there are no truncation errors). However, to simulate a large system, such as a loosely coupled reactor, within a reasonable statistic error, one needs to process an extraordinarily large number of Monte Carlo particles. Thus in general, the Monte Carlo approach is more expensive computationally, as compared with the deterministic approach. It is natural to think that if one could combine deterministic methods with the Monte Carlo methods for solving k-eigenvalue problems, some distinct advantages would be gained. Techniques used to couple the deterministic and Monte Carlo methods are called *hybrid* methods.

Historically, Monte Carlo simulations have often been used to generate limited information about a physical problem – for instance, "source-detector" problems in which the goal is to calculate a single detector response. Here, one runs an entire transport calculation with the goal of calculating a single number. When this is done properly (i.e. when the weight windows are chosen optimally), one gets accurate estimates of the solution in a small part of phase space (the part needed to calculate the desired response), but not elsewhere.

Over time, several hybrid methods have been developed for source-detector problems [9; 13; 14; 32]. In this type of problem, the source and detector are separated far enough that relatively few Monte Carlo particles can actually reach the detector. In order to decrease the statistical error, a variance reduction technique called *weight window* was introduced. The principle idea of the weight window technique is to keep the Monte Carlo particle's weight within a certain "window" by *splitting* and *Russian roulette* algorithms. By doing this, a Monte Carlo particle's weight can only fluctuate within the "window", and this will greatly decease the statistical error if the window is chosen properly. Historically, users must design the window manually by trial and error. Recently, adjoint deterministic fluxes (A^3MCNP approach) [13; 32] have been used to automatically generate the weight window. In source-detector problems, we mainly try to have better statistics at the "local" detector regions. Recently, Cooper's weight window method [6; 7; 8] utilized the forward deterministic solution of the "Quasidiffusion" (QD) equation [12; 22; 23] to generate weight

windows, which were then used to solve global deep-penetration transport problems with the Monte Carlo method. At Oak Ridge National Laboratory (ORNL), the Forward-Weighted Consistent Adjoint Driven Importance Sampling (FW-CADIS) method [24; 31] has been developed for effective global variance reduction. In the FW-CADIS method, a forward deterministic calculation is performed first. Then, the forward results are used to define an adjoint source, which is then used in a deterministic adjoint calculation to generate the adjoint importance function. Finally, the adjoint importance function is employed to calculate weight windows to be used in a Monte Carlo simulation. The work was done during the past five years at ORNL by John Wagner and his group. To date, Becker and Larsen [2; 3] have developed hybrid user-specified particle distribution methods which can be used to solve many types of shielding problems such as a single response classic source-detector problem, or a global problem in which accurate estimates of the angular flux are made in all of phase space. However, the work in this thesis departs from all the prior work. Our work is not based on the weight window, nor is Monte Carlo used to directly simulate the flux.

We propose a new hybrid method called the Functional Monte Carlo (FMC) method to solve the slow convergence k-eigenvalue problem. The FMC method does not employ standard Monte Carlo particle transport techniques to directly estimate the eigenfunction and eigenvalue. Instead, the FMC method uses these techniques to directly estimate certain *nonlinear functionals*, which depend only weakly on the eigenfunction. These estimated functionals are then used to calculate the k-eigenfunction and eigenvalue. Because the functionals depend only weakly on the eigenfunction, the resulting estimates of the k-eigenfunction and eigenvalue are generally more accurate and have less statistical noise than estimates obtained using conventional Monte Carlo methods.

The approach of using Monte Carlo to estimate a set of nonlinear functionals, and solving a discrete algebraic set of low-order equations containing these functionals for the k-eigenvalue and eigenfunction, has recently been considered by other authors [19; 20; 34; 33].

In some of this prior work, the discrete low-order equations resemble spatially-discretized S_2 equations [33]; in the rest, the low-order equations resemble discretized diffusion equations [19; 20; 33]. Two of these papers treat 2-D, multigroup problems [19; 20]. The work in [19; 20; 33] is based on the Coarse Mesh Finite Difference (CMFD) method, which has been used for more than two decades to accelerate the iterative convergence of deterministic high-order transport calculations for reactor physics problems [25; 5; 18; 26; 35]. The CMFD approach consists of deriving from the (high-order) transport equation an algebraic system of low-order equations obtained from the exact neutron balance equation, integrated over a coarse spatial cell, together with an equation containing a discrete version of Fick's Law and a nonlinear functional $\hat{D}$. (The functional $\hat{D}$ is calculated from the high-order transport equation; it accounts for the fact that Fick's Law is not exact.) The resulting low-order CMFD equations yield coarse-grid scalar fluxes, which are used to update the fine-grid scalar fluxes in the high-order equation. In the Monte Carlo work using this approach, the high-order transport calculations, previously performed deterministically, are now performed with Monte Carlo [19; 20; 33]. Variations of this work include modifying the nonlinear functional $\hat{D}$, to try to make it less sensitive to statistical noise [33].

The basic approach in the CMFD-based Monte Carlo work and FMC is the same. The differences occur in how the low-order equations are constructed; and in making these choices, there are many logical possibilities. CMFD-based methods have used the standard neutron balance equation, obtained by spatially integrating the angularly-integrated transport equation over a coarse spatial cell. FMC methods have used higher spatial moments of the angularly-integrated transport equation (involving spatial tent functions) and attempt to minimize the effect of the terms involving the neutron current in the low-order equations. (These terms have been seen to produce larger statistical fluctuations than desired in the solutions of the low-order equations.)

The FMC method is related to the deterministic QD method, sometimes called the "Variable Eddington Factor" method [12; 22; 23]. This iterative technique for eigenvalue (and

fixed-source) problems does *not* employ "high-order" transport sweeps to directly estimate the eigenfunction, but rather to directly estimate Eddington factors, which depend weakly on the eigenfunction. The Eddington factors are then used in a "low-order" quasi-diffusion eigenvalue problem to determine new estimates of the eigenvalue and eigenfunction. These estimates are used to construct an updated fission source, which enables a new QD iteration to begin. Because the Eddington factors generally depend weakly on the eigenfunction, the QD iteration process usually converges rapidly.

The QD method is a deterministic approach for solving particle transport problems; its converged estimates of the scalar flux have spatial and angular truncation errors. The QD method can be implemented with Monte Carlo-estimated Eddington factors [12]; the resulting scalar flux estimates have spatial truncation errors *and* statistical errors arising from the Monte Carlo-estimated Eddington factors.

Like the QD method, the FMC method employs a "high-order" particle transport process to estimate nonlinear functionals, which are then used in a "low-order" equation to estimate the eigenfunction and eigenvalue (One FMC functional is closely-related to the QD Eddington factor). Another similarity is that the QD and FMC eigenfunctions are estimated on a preassigned spatial grid.

The FMC method differs from the QD method in the following ways: (i) the FMC method uses Monte Carlo (rather than a deterministic method) to perform the high-order calculations used to estimate the functionals; and (ii) the FMC method yields estimates of the eigenfunction and eigenvalue that have no spatial truncation errors. The only errors in the FMC estimates of the k-eigenfunction and eigenvalue are those arising from the statistical errors in the Monte Carlo estimates of the functionals. In this sense, the FMC method is a pure Monte Carlo method – although the use of a spatial grid could tempt one to think otherwise.

In this dissertation, all analyses are restricted to 1-D planar geometry. Energy dependence is first taken to be monoenergetic; then multigroup; and finally, continuous energy.

There appears to be no fundamental obstacle to extending the FMC method to 3-D problems. (This will be discussed later.) The remaining chapters of this thesis are organized as follows.

Chapter 2: The FMC method for Mono-energetic k-eigenvalue Problems

In this chapter, we first discuss the relationship between the new functional Monte Carlo method, the previous QD method [12], and Cooper's work [6; 7; 8]. We then present the mathematical theory of the FMC method [17; 16] for a monoenergetic k-eigenvalue problem. We motivate the use of the tent function for the FMC method. A procedure to generate low-order equations with material discontinuity within a cell is presented. Finally, we give a brief overview of the Monte Carlo tallies, and the FMC feedback technique used in this thesis.

Chapter 3: Monoenergetic k-Eigenvalue Problems: Numerical Results

In this chapter, we compare the FMC and standard MC numerical simulations of k-eigenfunctions and eigenvalues for four mono-energetic problems (including a 1-D full PWR reactor core). We find that the FMC method significantly reduces the "tilting" that is often seen in simulations of systems containing one large fissile region, or in systems with tightly-coupled fissile regions (e.g. nuclear reactor cores). For these problems, FMC estimates of the k-eigenfunctions and eigenvalues are significantly more accurate than those obtained using standard Monte Carlo methods. Problems involving weakly-coupled fissile regions (e.g. storage tanks for spent fuel rods) are inherently more difficult, because the eigenfunctions for these problems can be highly sensitive to small perturbations. For such problems, the FMC estimates of the eigenfunction have larger variations from one cycle to the next than standard Monte Carlo estimates. Nonetheless, our numerical simulations indicate that the FMC estimate of the eigenvalue and eigenfunction are more accurate than standard Monte Carlo estimates. We further compare the Shannon entropy behavior of the fission source for the problems with FMC feedback and without FMC feedback.

Chapter 4: The FMC method for Multigroup Energy k-eigenvalue Problems

In this chapter, we extend the one-group FMC method derived in Chapter 2 to multigroup k-eigenvalue problems. We follow the same basic procedure in developing the multigroup FMC method as was used for monoenergetic problems, but now there is additional complexity because of the occurrence of between-group scattering processes. We successfully tested the multigroup FMC method on a homogeneous slab problem. We did not further develop and test the multigroup FMC method, because it is a straightforward extension of the monoenergetic FMC method.

Chapter 5: The FMC method for Continuous Energy k-Eigenvalue Problems

In this chapter, we extend the FMC method to planar geometry continuous-energy k-eigenvalue problems [37; 38]. This is an important step, because energy-varying cross-sections are necessary for practical applications. In the formulation given here, energy-integrated or multigroup nonlinear functionals are estimated using the standard Monte Carlo method. These functionals are then used in multigroup, low-order FMC equations to estimate the eigenvalue and eigenfunctions. Here the tent functions are defined on the original spatial grid; initially there is only one kind of material in each spatial cell and the scalar fluxes are averaged on a staggered grid. Later, we generalize the method to: (1) accommodate any number of materials within one coarse spatial cell; (2) define the tent functions on a staggered grid; and (3) obtain the averaged scalar fluxes on the original spatial grid. To accommodate the continuous-energy feature, we introduce a U-function into the calculation. The U-function satisfies an adjoint equation. We also give a detailed procedure to solve for U-function for both the energy-independent case and the multigroup case.

Chapter 6: Continuous Energy k-Eigenvalue Problems: Numerical Results

In this chapter, we compare the FMC and standard MC numerical simulations of k-eigenfunctions and eigenvalues for two representative problems. Again, FMC estimates of the k-eigenfunctions and eigenvalues are shown to be significantly more accurate than those obtained using standard Monte Carlo methods. We further compare the Shannon entropy for the standard Monte Carlo calculation and the FMC calculation. Finally, we compare the true variance and apparent variance for the Monte Carlo simulation with and without FMC feedback.

Chapter 7: Conclusions and Future Work

We conclude with a summary of the numerical results, and then outline our future work to extend the FMC method to 3-D problems with a more realistic continuous energy library.

Chapter 2

The FMC method for 1-D Monoenergetic k-Eigenvalue Problems

In this chapter, we first discuss the mathematical basis for the Functional Monte Carlo (FMC) method. We then present the mathematical theory of the FMC method for a monoenergetic k-eigenvalue problem. We motivate the use of the tent function for the FMC method. A procedure to generate low-order equations with material discontinuity within a cell is presented. Finally, we give a brief overview of the Monte Carlo tallies used in this thesis.

2.1 Mathematical Basis for the Functional Monte Carlo Method

Motivated by Cooper's work on global Monte Carlo simulations for deep penetration problems [6; 7; 8], we decided to investigate the quasidiffusion (QD) method as the first step in a hybrid technique for eigenvalue problems. To describe the QD method, we consider for simplicity a slab-geometry monoenergetic problem with isotropic scattering:

$$\mu\frac{\partial\psi}{\partial x}(x,\mu)+\Sigma_t(x)\psi(x,\mu)=\frac{1}{2}\left(\Sigma_s(x)+\frac{\nu\Sigma_f(x)}{k}\right)\int_{-1}^{1}\psi(x,\mu')d\mu' \ , \ 0<x<X \ , \quad (2.1a)$$

$$\psi(0,\mu)=0 \ , \ 0<\mu\leq 1 \ , \quad (2.1b)$$

$$\psi(X,\mu)=0 \ , \ -1\leq\mu<0 \ . \quad (2.1c)$$

We define the angular flux moments as

$$\phi_m(x) = \int_{-1}^{1} \mu^m \psi(x,\mu) d\mu \ , \ m = 0,1,2 \ . \tag{2.2}$$

Operating on Eq. (2.1a) by

$$\int_{-1}^{1} \mu^m (\cdot)\, d\mu \ , \ m = 0,1 \ ,$$

we obtain:

$$\frac{d\phi_1}{dx}(x) + \Sigma_a(x)\phi_0(x) = \frac{\nu\Sigma_f(x)}{k}\phi_0(x) \ , \tag{2.3a}$$

$$\frac{d\phi_2}{dx}(x) + \Sigma_t(x)\phi_1(x) = 0 \ . \tag{2.3b}$$

Eq. (2.3b) gives:

$$\phi_1(x) = -\frac{1}{\Sigma_t(x)}\frac{d\phi_2}{dx}(x) \ . \tag{2.4}$$

Introducing this into Eq. (2.3a), we obtain:

$$-\frac{d}{dx}\frac{1}{\Sigma_t(x)}\frac{d\phi_2}{dx}(x) + \Sigma_a(x)\phi_0(x) = \frac{\nu\Sigma_f(x)}{k}\phi_0(x) \ , \ 0 < x < X \ . \tag{2.5a}$$

Next, operating on Eq. (2.1b) by $\int_0^1 2\mu(\cdot)d\mu$ and using Eqs. (2.2) and (2.4), we obtain:

$$\begin{aligned} 0 &= \int_0^1 2\mu\,\psi(0,\mu)d\mu \\ &= \int_{-1}^1 \mu\,\psi(0,\mu)d\mu \ + \int_{-1}^1 |\mu|\psi(0,\mu)d\mu \\ &= \phi_1(0) + \int_{-1}^1 |\mu|\psi(0,\mu)d\mu \\ &= -\frac{1}{\Sigma_t(0)}\frac{d\phi_2}{dx}(0) + \int_{-1}^1 |\mu|\psi(0,\mu)d\mu \ . \end{aligned} \tag{2.5b}$$

Similarly, operating on Eq. (2.1c) by $\int_{-1}^0 2|\mu|(\cdot)d\mu$ and using Eqs. (2.2) and (2.4), we

obtain:

$$
\begin{aligned}
0 &= \int_{-1}^{0} 2|\mu|\psi(X,\mu)d\mu \\
&= -\int_{-1}^{1} \mu\psi(X,\mu)d\mu \; + \int_{-1}^{1} |\mu|\psi(X,\mu)d\mu \\
&= -\phi_1(X) + \int_{-1}^{1} |\mu|\psi(X,\mu)d\mu \\
&= \frac{1}{\Sigma_t(X)}\frac{d\phi_2}{dx}(X) + \int_{-1}^{1} |\mu|\psi(X,\mu)d\mu \; . \qquad (2.5c)
\end{aligned}
$$

The *Eddington factor* is defined as:

$$
\begin{aligned}
E(x) &= \frac{\phi_2(x)}{\phi_0(x)} \\
&= \frac{\int_{-1}^{1} \mu^2\psi(x,\mu)d\mu}{\int_{-1}^{1} \psi(x,\mu)d\mu} \\
&= \langle\mu^2\rangle(x) \; , \quad 0 \le x \le X \; , \qquad (2.6a)
\end{aligned}
$$

and the *boundary Eddington factors* are defined as:

$$
\begin{aligned}
B(x) &= \frac{\int_{-1}^{1} |\mu|\psi(x,\mu)d\mu}{\int_{-1}^{1} \psi(x,\mu)d\mu} \\
&= \langle|\mu|\rangle(x) \; , \; x = 0, X \; . \qquad (2.6b)
\end{aligned}
$$

From Eqs. (2.6), we obtain:

$$\phi_2(x) = E(x)\phi_0(x) \; ,$$

and

$$\int_{-1}^{1} |\mu|\psi(x,\mu)d\mu = B(x)\phi_0(x) \, .$$

We may then write Eqs. (2.5) as the following *quasidiffusion* problem:

$$-\frac{d}{dx}\frac{1}{\Sigma_t(x)}\frac{d}{dx}E(x)\phi_0(x)+\Sigma_a(x)\phi_0(x)=\frac{\nu\Sigma_f(x)}{k}\phi_0(x)\ ,\quad 0<x<X\ , \tag{2.7a}$$

$$0=B(0)\phi_0(0)-\frac{1}{\Sigma_t(0)}\frac{dE\phi_0}{dx}(0)\ , \tag{2.7b}$$

$$0=B(X)\phi_0(X)+\frac{1}{\Sigma_t(X)}\frac{dE\phi_0}{dx}(X)\ . \tag{2.7c}$$

The *Quasidiffusion* method employs the following iteration scheme:

1. Starting with estimates $\phi^n(x)$ and k^n, an updated angular flux $\psi^{(n+1/2)}(x,\mu)$ is obtained by solving the "high-order" transport problem:

$$\mu\frac{\partial\psi^{(n+1/2)}}{\partial x}(x,\mu)+\Sigma_t(x)\psi^{(n+1/2)}(x,\mu) = \frac{1}{2}\left(\Sigma_s(x)+\frac{\nu\Sigma_f(x)}{k^{(n)}}\right)\phi^{(n)}(x)\ ,\ 0<x<X\ , \tag{2.8a}$$

$$\psi^{(n+1/2)}(0,\mu)=0\ ,\quad 0<\mu\le 1\,, \tag{2.8b}$$

$$\psi^{(n+1/2)}(X,\mu)=0\ ,\quad -1\le\mu<0\,. \tag{2.8c}$$

2. The updated angular flux $\psi^{(n+1/2)}(x,\mu)$ is then used to estimate the Eddington factors:

$$E^{(n+1/2)}(x)=\frac{\int_{-1}^{1}\mu^2\psi^{(n+1/2)}(x,\mu)d\mu}{\int_{-1}^{1}\psi^{(n+1/2)}(x,\mu)d\mu}\ ,\ 0<x<X\ , \tag{2.9a}$$

$$B^{(n+1/2)}(x)=\frac{\int_{-1}^{1}|\mu|\psi^{(n+1/2)}(x,\mu)d\mu}{\int_{-1}^{1}\psi^{(n+1/2)}(x,\mu)d\mu}\ ,\ x=0,X\ . \tag{2.9b}$$

3. The following "low-order" quasidiffusion problem is solved for the new eigenfunction

and eigenvalue estimates $\phi^{(n+1)}(x)$ and $k^{(n+1)}$.

$$-\frac{d}{dx}\frac{1}{\Sigma_t(x)}\frac{d}{dx}E^{(n+1/2)}(x)\phi^{(n+1)}(x)+\Sigma_a(x)\phi^{(n+1)}(x)$$
$$=\frac{\nu\Sigma_f(x)}{k^{(n+1)}}\phi^{(n+1)}(x)\ ,\ 0<x<X\,, \tag{2.10a}$$
$$0=B^{(n+1/2)}(0)\phi^{(n+1)}(0)-\frac{1}{\Sigma_t(0)}\frac{dE^{(n+1/2)}\phi^{(n+1)}}{dx}(0)\ , \tag{2.10b}$$
$$0=B^{(n+1/2)}(X)\phi^{(n+1)}(X)-\frac{1}{\Sigma_t(X)}\frac{dE^{(n+1/2)}\phi^{(n+1)}}{dx}(X)\ . \tag{2.10c}$$

Eqs. (2.8)–(2.10) have been solved previously using deterministic methods [1; 12]. With Cooper's work in mind, we develop a hybrid technique for eigenvalue problems by: (i) using the Monte Carlo method to solve Eqs. (2.8) for $\psi^{(n+1/2)}$ and Eqs. (2.9) for $E^{(n+1/2)}$ and $B^{(n+1/2)}$, and (ii) using a standard cell-average discretization to solve a discretized form of Eqs. (2.10). We describe this hybrid technique as the Monte Carlo quasidiffusion method (MCQD).

To accomplish this, we assume a spatial grid of J cells with cell-edges

$$0=x_{1/2}<x_{3/2}<\ldots<x_{j-1/2}<x_{j+1/2}<\ldots x_{J+1/2}=X\ . \tag{2.11}$$

The j^{th} spatial cell is $x_{j-1/2}<x<x_{j+1/2}$, with width $h_j=x_{j+1/2}-x_{j-1/2}$. We assume that within each j^{th} cell, the cross sections are constant.

At the beginning of the $(n+1)^{st}$ iteration, $\phi^{(n)}(x)$ and $k^{(n)}$ are known from having solved a cell-averaged discretization of Eqs. (2.10) in the previous iteration. We use Monte Carlo to simulate Eqs. (2.8) and determine $\psi^{(n+1/2)}(x,\mu)$. The results of this Monte Carlo simulation are used to estimate the integrals in Eqs. (2.6), and these are used to estimate the Eddington

factors in Eqs. (2.9), e.g.

$$E_j^{(n+1/2)} = \frac{\int_{-1}^{1}\int_{x_{j-1/2}}^{x_{j+1/2}} \mu^2 \psi^{(n+1/2)}(x,\mu)\,dx d\mu}{\int_{-1}^{1}\int_{x_{j-1/2}}^{x_{j+1/2}} \psi^{(n+1/2)}(x,\mu)\,dx d\mu},\ 1 \le j \le J\,, \tag{2.12a}$$

$$B_{1/2}^{(n+1/2)} = \frac{\int_{-1}^{1} |\mu| \psi^{(n+1/2)}(0,\mu) d\mu}{\int_{-1}^{1} \psi^{(n+1/2)}(0,\mu) d\mu}\,, \tag{2.12b}$$

$$B_{J+1/2}^{(n+1/2)} = \frac{\int_{-1}^{1} |\mu| \psi^{(n+1/2)}(X,\mu) d\mu}{\int_{-1}^{1} \psi^{(n+1/2)}(X,\mu) d\mu}\,. \tag{2.12c}$$

Finally, these Monte Carlo-generated Eddington factors are used in the standard cell-average discretization of Eqs. (2.10) on the grid defined by Eqs. (2.11). For the first ($j = 1$) spatial cell, we find:

$$-2\left(\frac{E_2^{(n+1/2)}\phi_2^{(n+1)} - E_1^{(n+1/2)}\phi_1^{(n+1)}}{\Sigma_{t2}h_2 + \Sigma_{t1}h_1}\right) + \left(\frac{B_{1/2}^{(n+1/2)}E_1^{(n+1/2)}}{E_{1/2}^{(n+1/2)} + \frac{\Sigma_{t,1}h_1}{2}B_{1/2}^{(n+1/2)}}\right)\phi_1^{(n+1)}$$
$$+ \Sigma_{a,1}h_1\phi_1^{(n+1)} = \frac{1}{k^{(n+1)}}\nu\Sigma_{f1}h_1\phi_1^{(n+1)}\,; \tag{2.13a}$$

for the interior ($2 \le j \le J-1$) spatial cells:

$$-2\left(\frac{E_{j+1}^{(n+1/2)}\phi_{j+1}^{(n+1)} - E_j^{(n+1/2)}\phi_j^{(n+1)}}{\Sigma_{t,j+1}h_{j+1} + \Sigma_{t,j}h_j}\right) + 2\left(\frac{E_j^{(n+1/2)}\phi_j^{(n+1)} - E_{j-1}^{(n+1/2)}\phi_{j-1}^{(n+1)}}{\Sigma_{t,j}h_j + \Sigma_{t,j-1}h_{j-1}}\right)$$
$$+ \Sigma_{a,j}h_j\phi_j^{(n+1)} = \frac{1}{k^{(n+1)}}\nu\Sigma_{f,j}h_j\phi_j^{(n+1)}\,; \tag{2.13b}$$

and for the last ($j = J$) spatial cell:

$$\left(\frac{B_{J+1/2}^{(n+1/2)}E_J^{(n+1/2)}}{E_{J+1/2}^{(n+1/2)} + \frac{\Sigma_{t,J}h_J}{2}B_{J+1/2}^{(n+1/2)}}\right)\phi_J^{(n+1)} + 2\left(\frac{E_J^{(n+1/2)}\phi_J^{(n+1)} - E_{J-1}^{(n+1/2)}\phi_{J-1}^{(n+1)}}{\Sigma_{t,J}h_J + \Sigma_{t,J-1}h_{J-1}}\right)$$
$$+ \Sigma_{a,J}h_J\phi_J^{(n+1)} = \frac{1}{k^{(n+1)}}\nu\Sigma_{f,J}h_J\phi_J^{(n+1)}\,. \tag{2.13c}$$

In Cooper's work [7] for deep shielding calculations, it was found that Monte Carlo

estimates of the Eddington factors Eqs. (2.6) are much more accurate and stable than the Monte Carlo estimates of ϕ. The reason for this is that the estimates of the Eddington factors depend only on the angular shape of the Monte Carlo estimate of ψ and not on its amplitude. We reasoned that for difficult eigenvalue problems, Monte Carlo could yield accurate Eddington factors, even if it could not yield accurate eigenfunctions, and that these Eddington factors could be used in Eqs. (2.13) to yield accurate estimates of ϕ and k.

The MCQD method described above has spatial truncation errors, because of the errors that occur in approximating Eqs. (2.10) by the discrete Eqs. (2.13). We may then inquire: is it possible to formulate equations of the general form of the QD equations above, but which have no truncation errors? If so, these equations could be adapted for use in Monte Carlo simulations by employing nonlinear functionals as in the QD method. One would then have a finite set of equations having the general form of a MCQD equation, but which in fact constitute a pure Monte Carlo method having only statistical errors that occur in the estimates of nonlinear functionals. The affirmative answer to this question is the newly-developed Functional Monte Carlo (FMC) method, which we describe next.

2.2 Analytical Formulation of the Functional Monte Carlo Method for the Monoenergetic k-Eigenvalue Problem

Here we consider a standard planar-geometry, monoenergetic k-eigenvalue problem with anisotropic scattering and vacuum boundaries:

$$\mu\frac{\partial\psi}{\partial x}(x,\mu)+\Sigma_t(x)\psi(x,\mu)-\int_{-1}^{1}\Sigma_s(x,\mu,\mu')\psi(x,\mu')d\mu' = \frac{\nu\Sigma_f(x)}{2k}\int_{-1}^{1}\psi(x,\mu')d\mu' \ , \ 0<x<X \ , \tag{2.14a}$$

$$\psi(0,\mu)=0 \ , \ 0<\mu\leq 1 \ , \tag{2.14b}$$

$$\psi(X,\mu)=0 \ , \ -1\leq\mu<0 \ , \tag{2.14c}$$

where:

$$\Sigma_s(x,\mu,\mu') = \sum_{n=0}^{\infty} \frac{2n+1}{2} \Sigma_{sn}(x) P_n(\mu) P_n(\mu') \; . \tag{2.15}$$

Eqs. (2.14) are the "high-order" transport equations for $\psi(x,\mu)$ and k. The "low-order" FMC equations are derived by the following procedure:

1. First, we construct specified angular moments of Eqs. (2.14). Specifically, we take the zero-th and first angular moments of Eq. (2.14a), multiply Eqs. (2.14b) and (2.14c) by μ, and integrate over the incident directions. No approximations are made in performing these operations, and the exact solution of Eqs. (2.14) satisfies the angularly-integrated equations. This step duplicates the first step of deriving the low-order QD equations.
2. Next, with the spatial grid of J cells from Eq. (2.11), we define $J+1$ "tent" functions on this grid [see Eqs. (2.21) and (2.22)]. Using the tent functions, we construct certain spatial moments of the angularly-integrated equations obtained in Step 1. Again, no approximations are made in performing these operations, and the exact solution of Eqs. (2.14) satisfies these spatially- and angularly-integrated equations. This step is not part of the QD method.
3. Introducing no approximations, we manipulate the spatially- and angularly-integrated equations from Step 2 to obtain a discrete system of "low-order" FMC equations, containing (i) nonlinear functionals of the exact solution, and (ii) spatial moments of the scalar flux around each of the $J+1$ grid points. Again, no approximations are made in performing these operations. If the nonlinear functionals are known exactly, the discrete system yields exactly (i) the spatial moments of the scalar flux around each of the $J+1$ grid points, and (ii) the k-eigenvalue.

After deriving the low-order FMC equations, the Monte Carlo simulation of Eqs. (2.14) can proceed. In this standard Monte Carlo simulation, the user specifies the number of Monte Carlo particles per generation, the simulation begins with a crude (flat) estimate of the fission source, "inactive" cycles (generations) are performed to converge the fission

source, and then "active" cycles (generations) are performed to estimate the eigenfunction and k. All of these operations are performed using conventional Monte Carlo procedures.

However, while performing these standard Monte Carlo simulations, information from the Monte Carlo particle histories is used to generate estimates of the scalar flux ϕ (the eigenfunction), and of the nonlinear functionals in the low-order FMC equations. More specifically: for each active generation, we calculate new estimates of the FMC functionals, using the new data generated from the Monte Carlo histories processed during that generation. At the end of each generation, after all the "fission" Monte Carlo particles have been processed, the FMC functionals are calculated and the discrete low-order FMC equations are solved. This yields the FMC estimates of the k-eigenfunction and k-eigenvalue for that generation. The process is repeated for each active generation. After a specified number of active generations, the mean value and standard deviation of the (standard Monte Carlo and FMC) generation-wise eigenvalues and eigenfunctions are calculated in the usual way.

We pursue two different approaches: (1) the Monte Carlo simulation of Eqs. (2.14) proceeds independently of the results of the FMC calculations. The FMC calculations are performed using information extracted from the conventional Monte Carlo particle histories, but none of this new information impacts the Monte Carlo simulation of Eqs. (2.14). The purpose of this approach is to describe the FMC method and show that even with a tilted or otherwise poorly-represented Monte Carlo fission source, this method is much more accurate than standard Monte Carlo. (2) A more sophisticated approach is the Monte Carlo simulation with FMC "feedback", i.e. use the (generally more accurate) estimate of the fission source from the low-order FMC calculations to modify the Monte Carlo fission source for the next generation.

Because the FMC functionals are weakly-dependent on the angular flux ψ, the Monte Carlo estimates of these functionals are less statistically noisy than those of ϕ, and the FMC estimates of the eigenvalue and eigenfunction generally have a smaller variance than the standard estimates. Also, because both the standard Monte Carlo and the FMC methods

have only statistical errors, in the limit of an infinite number of Monte Carlo particles per generation and an infinite number of generations, both methods will converge to the exact eigenvalue and eigenfunction.

We now begin the derivation of the low-order FMC equations. Following Step 1 described above, we take specific angular moments by operating on Eq. (2.14a) with $\int_{-1}^{1} \mu^n(\cdot)\, d\mu$ for $n = 0$ and 1. Defining:

$$\phi_n(x) = \int_{-1}^{1} \mu^n \psi(x,\mu) d\mu \ , \tag{2.16a}$$

$$\Sigma_a(x) = \Sigma_t(x) - \Sigma_{s0}(x) \ , \tag{2.16b}$$

$$\Sigma_{tr}(x) = \Sigma_t(x) - \Sigma_{s1}(x) \ , \tag{2.16c}$$

we obtain:

$$\frac{d\phi_1}{dx}(x) + \Sigma_a(x)\phi_0(x) = \frac{\nu\Sigma_f(x)}{k}\phi_0(x) \ , \tag{2.17a}$$

$$\frac{d\phi_2}{dx}(x) + \Sigma_{tr}(x)\phi_1(x) = 0 \ . \tag{2.17b}$$

Next, operating on Eq. (2.14b) by $\int_0^1 2\mu(\cdot)d\mu$ and on Eq. (2.1c) by $\int_{-1}^0 2\mu(\cdot)d\mu$, we get:

$$0 = \phi_1(0) + \int_{-1}^{1} |\mu|\psi(0,\mu)d\mu \ , \tag{2.18a}$$

$$0 = \phi_1(X) - \int_{-1}^{1} |\mu|\psi(X,\mu)d\mu \ . \tag{2.18b}$$

Solving Eq. (2.17b) for $\phi_1(x)$:

$$\phi_1(x) = -\frac{1}{\Sigma_{tr}(x)}\frac{d\phi_2}{dx}(x) \ . \tag{2.19}$$

Using Eq. (2.19) to eliminate ϕ_1 from Eqs. (2.17a) and (2.18), we obtain:

$$-\frac{d}{dx}\frac{1}{\Sigma_{tr}(x)}\frac{d\phi_2}{dx}(x)+\Sigma_a(x)\phi_0(x)=\frac{\nu\Sigma_f(x)}{k}\phi_0(x)\ , \tag{2.20a}$$

$$\frac{1}{\Sigma_{tr}(0)}\frac{d\phi_2}{dx}(0)=\int_{-1}^{1}|\mu|\psi(0,\mu)d\mu\ , \tag{2.20b}$$

$$\frac{1}{\Sigma_{tr}(X)}\frac{d\phi_2}{dx}(X)=-\int_{-1}^{1}|\mu|\psi(X,\mu)d\mu\ . \tag{2.20c}$$

Eqs. (2.20) are exactly satisfied by the solution of Eqs. (2.14). This completes Step 1 of the derivation of the FMC equations.

Next we perform Step 2 described above. We prescribe a spatial grid consisting of $J+1$ points $x_{j+1/2}$ satisfying $0=x_{1/2}<x_{3/2}<\cdots<x_{j-1/2}<x_{j+1/2}<\cdots<x_{J-1/2}<x_{J+1/2}=X$. The j^{th} spatial cell consists of the interval $x_{j-1/2}<x<x_{j+1/2}$; the width of this cell is $h_j=x_{j+1/2}-x_{j-1/2}$. Within each j^{th} spatial cell, the cross sections are assumed to be constant and are written as $\Sigma_{tr}(x)=\Sigma_{tr,j}$, $\Sigma_a(x)=\Sigma_{a,j}$, and $\nu\Sigma_f(x)=\nu\Sigma_{f,j}$. Later, we will discuss problems in which the cross sections are discontinuous within spatial cells.

For each grid point $x_{j+1/2}$ we define the functions $f(x)=f_{j+1/2}(x)$. For $0\le j\le J-1$, we let:

$$f^{+}_{j+1/2}(x)=\begin{cases}\frac{1}{h_{j+1}}(x_{j+3/2}-x) & ,\ 0=x_{j+1/2}<x<x_{j+3/2}\\ 0 & ,\ \text{otherwise}\ .\end{cases} \tag{2.21a}$$

For $1\le j\le J$, we let:

$$f^{-}_{j+1/2}(x)=\begin{cases}\frac{1}{h_j}(x-x_{j-1/2}) & ,\ 0=x_{j-1/2}<x<x_{j+1/2}\\ 0 & ,\ \text{otherwise}\ .\end{cases} \tag{2.21b}$$

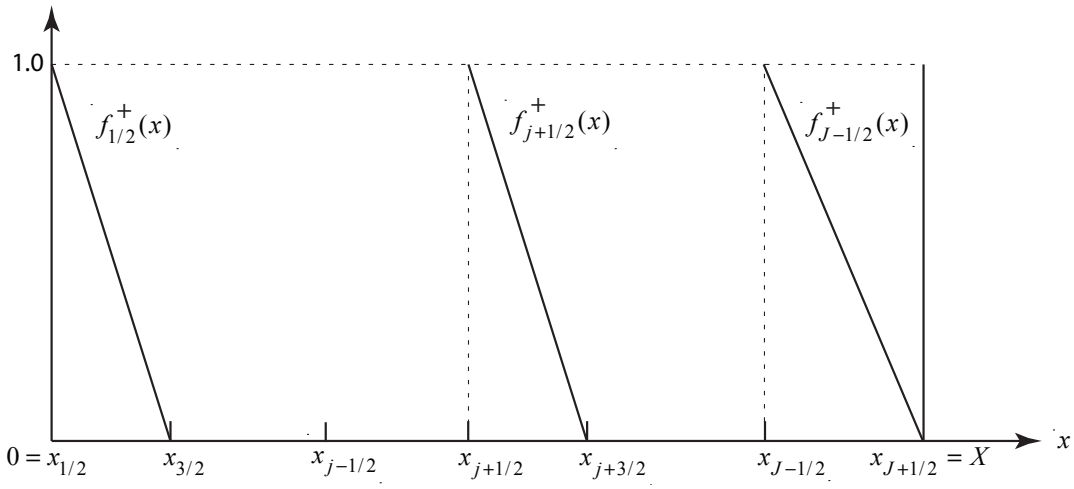

Figure 2.1 The functions $f^+_{j+1/2}(x)$.

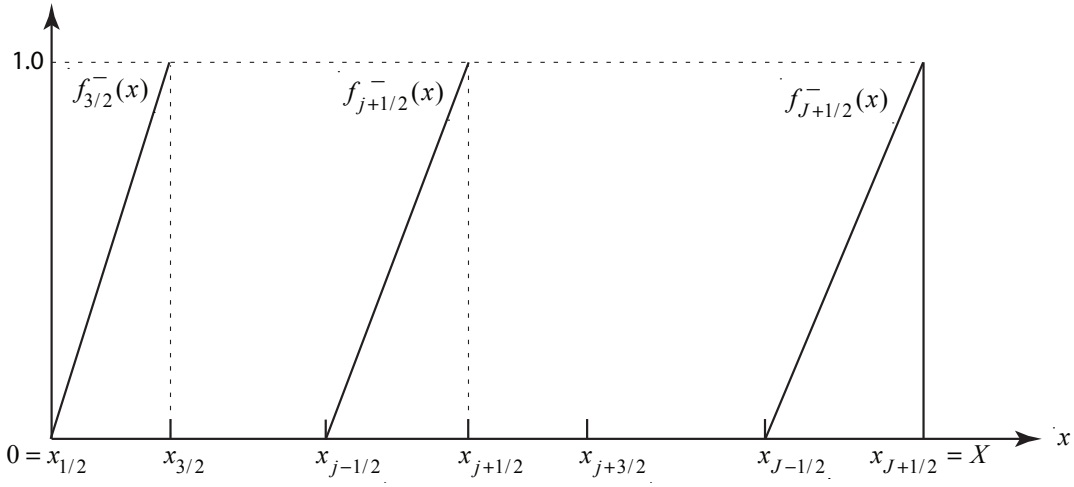

Figure 2.2 The functions $f^-_{j+1/2}(x)$.

Then we define the "tent" functions $f_{j+1/2}(x)$ by:

$$f_{j+1/2} = \begin{cases} f^+_{j+1/2}(x) & , \ j = 0 \\ f^+_{j+1/2}(x) + f^-_{j+1/2}(x) & , \ 1 \le j \le J-1 \\ f^-_{j+1/2}(x) & , \ j = J \, . \end{cases} \tag{2.22}$$

Since for $1 \leq j \leq J$,

$$f^{+}_{j-1/2}(x) + f^{-}_{j+1/2}(x) = \begin{cases} 1 & , \quad x_{j-1/2} \leq x \leq x_{j+1/2} \, , \\ 0 & , \quad \text{otherwise} \, , \end{cases}$$

the tent functions satisfy the condition:

$$\sum_{j=1}^{J} f_{j+1/2}(x) = 1 \, , 0 \leq x \leq X \, . \tag{2.23}$$

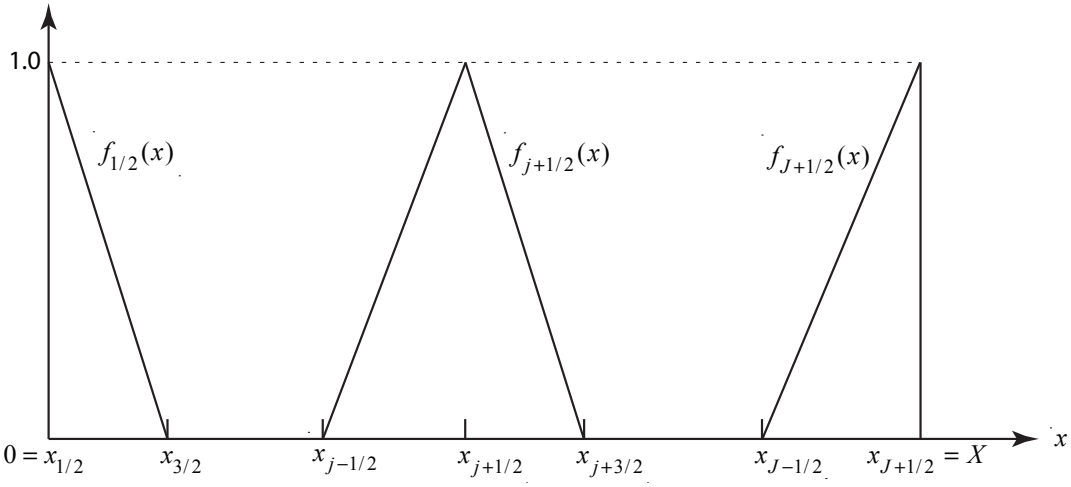

Figure 2.3 The tent functions.

Next, we multiply Eq. (2.20a) by $f_{j+1/2}(x)$ and integrate over $0 \leq x \leq X$. For $j = 0$ we obtain:

$$\begin{aligned} -\int_{x_{1/2}}^{x_{3/2}} f_{1/2}(x) \left[\frac{d}{dx} \frac{1}{\Sigma_{tr}(x)} \frac{d\phi_2}{dx}(x) \right] dx + \int_{x_{1/2}}^{x_{3/2}} f_{1/2}(x) \Sigma_a(x) \phi_0(x) dx \\ = \frac{1}{k} \int_{x_{1/2}}^{x_{3/2}} f_{1/2}(x) \nu\Sigma_f(x) \phi_0(x) dx \, . \end{aligned}$$

Integrating the first term by parts and using Eq. (2.20b), we get:

$$\begin{aligned}
&\int_{x_{1/2}}^{x_{3/2}} f_{1/2}(x)\left[\frac{d}{dx}\frac{1}{\Sigma_{tr}(x)}\frac{d\phi_2}{dx}(x)\right]dx \\
&\qquad = f_{1/2}(x)\frac{1}{\Sigma_{tr,1}}\frac{d\phi_2}{dx}(x)\Big|_{x_{1/2}}^{x_{3/2}} - \int_{x_{1/2}}^{x_{3/2}}\frac{df_{1/2}}{dx}(x)\frac{1}{\Sigma_{tr,1}}\frac{d\phi_2}{dx}(x)dx \\
&\qquad = -\frac{1}{\Sigma_{tr,1}}\frac{d\phi_2}{dx}(0) + \frac{1}{\Sigma_{tr,1}h_1}\int_{x_{1/2}}^{x_{3/2}}\frac{d\phi_2}{dx}(x)dx \\
&\qquad = -\int_{-1}^{1}|\mu|\psi(x_{1/2},\mu)d\mu + \frac{1}{\Sigma_{tr,1}h_1}\left[\phi_2(x_{3/2})-\phi_2(x_{1/2})\right].
\end{aligned}$$

Thus, the preceding equation can be written:

$$\begin{aligned}
&\int_{-1}^{1}|\mu|\psi(x_{1/2},\mu)d\mu - \frac{1}{\Sigma_{tr,1}h_1}\left[\phi_2(x_{3/2})-\phi_2(x_{1/2})\right] \\
&\qquad + \int_{x_{1/2}}^{x_{3/2}} f_{1/2}(x)\Sigma_{a,1}\phi_0(x)dx = \frac{1}{k}\int_{x_{1/2}}^{x_{3/2}} f_{1/2}(x)\nu\Sigma_{f,1}\phi_0(x)dx\,. \qquad (2.24a)
\end{aligned}$$

For $1 \le j \le J-1$, we obtain:

$$\begin{aligned}
&-\int_{x_{j-1/2}}^{x_{j+3/2}} f_{j+1/2}(x)\left[\frac{d}{dx}\frac{1}{\Sigma_{tr}(x)}\frac{d\phi_2}{dx}(x)\right]dx + \int_{x_{j-1/2}}^{x_{j+3/2}} f_{j+1/2}(x)\Sigma_a(x)\phi_0(x)dx \\
&\qquad = \frac{1}{k}\int_{x_{j-1/2}}^{x_{j+3/2}} f_{j+1/2}(x)\nu\Sigma_f(x)\phi_0(x)dx\,.
\end{aligned}$$

Integrating the first term by parts, we get:

$$\begin{aligned}
&\int_{x_{j-1/2}}^{x_{j+3/2}} f_{j+1/2}(x)\left[\frac{d}{dx}\frac{1}{\Sigma_{tr}(x)}\frac{d\phi_2}{dx}(x)\right]dx \\
&\qquad = -\int_{x_{j-1/2}}^{x_{j+3/2}}\frac{df_{j+1/2}}{dx}(x)\frac{1}{\Sigma_{tr}(x)}\frac{d\phi_2}{dx}(x)dx \\
&\qquad = -\int_{x_{j-1/2}}^{x_{j+1/2}}\frac{1}{h_j\Sigma_{tr,j}}\frac{d\phi_2}{dx}(x)dx + \int_{x_{j+1/2}}^{x_{j+3/2}}\frac{1}{h_{j+1}\Sigma_{tr,j+1}}\frac{d\phi_2}{dx}(x)dx \\
&\qquad = \frac{1}{\Sigma_{tr,j+1}h_{j+1}}\left[\phi_2(x_{j+3/2})-\phi_2(x_{j+1/2})\right] \\
&\qquad\qquad - \frac{1}{\Sigma_{tr,j}h_j}\left[\phi_2(x_{j+1/2})-\phi_2(x_{j-1/2})\right].
\end{aligned}$$

Thus, the preceding equation can be written:

$$-\frac{1}{\Sigma_{tr,j+1}h_{j+1}}\left[\phi_2(x_{j+3/2})-\phi_2(x_{j+1/2})\right]+\frac{1}{\Sigma_{tr,j}h_j}\left[\phi_2(x_{j+1/2})-\phi_2(x_{j-1/2})\right]$$
$$+\int_{x_{j-1/2}}^{x_{j+3/2}} f_{j+1/2}(x)\Sigma_a(x)\phi_0(x)dx=\frac{1}{k}\int_{x_{j-1/2}}^{x_{j+3/2}} f_{j+1/2}(x)\nu\Sigma_f(x)\phi_0(x)dx\,. \qquad (2.24b)$$

For $j=J$ we follow similar steps as for $j=0$ and get:

$$\int_{-1}^{1}|\mu|\psi(x_{J+1/2},\mu)d\mu+\frac{1}{\Sigma_{tr,J}h_J}\left[\phi_2(x_{J+1/2})-\phi_2(x_{J-1/2})\right]$$
$$+\int_{x_{J-1/2}}^{x_{J+1/2}} f_{J+1/2}(x)\Sigma_{a,J}\phi_0(x)dx=\frac{1}{k}\int_{x_{J-1/2}}^{x_{J+1/2}} f_{J+1/2}(x)\nu\Sigma_{f,J}\phi_0(x)dx\,. \qquad (2.24c)$$

Eqs. (2.24) are a system of $J+1$ discrete equations, which are exactly satisfied by the solution $\psi(x,\mu)$ and k of Eqs. (2.14). This completes Step 2 of the derivation of the FMC equations.

Next we perform Step 3 described above. For each $0\le j\le J$, we introduce new functions $g_{j+1/2}(x)$ that are nonzero only where $f_{j+1/2}(x)$ are nonzero. These functions are not uniquely defined; there is considerable flexibility in choosing them. We use two definitions of $g_{j+1/2}(x)$. First, we use a "delta-function" definition:

$$g_{j+1/2}(x)=\delta(x-x_{j+1/2})\ ,\ 0\le j\le J\,. \qquad (2.25)$$

We also use a "histogram" definition. With $x_j=(x_{j+1/2}+x_{j-1/2})/2$ = midpoint of the j^{th} spatial cell, we define: for $j=0$,

$$g_{1/2}(x)=\begin{cases}\frac{2}{h_1} & ,\quad x_{1/2}\le x\le x_1\,,\\ 0 & ,\quad \text{otherwise}\,,\end{cases} \qquad (2.26a)$$

for $1 \leq j \leq J-1$,

$$g_{j+1/2}(x) = \begin{cases} \frac{2}{h_j + h_{j+1}} & , \quad x_j \leq x \leq x_{j+1} \, , \\ 0 & , \quad \text{otherwise} \, , \end{cases} \tag{2.26b}$$

and for $j = J$,

$$g_{J+1/2}(x) = \begin{cases} \frac{2}{h_J} & , \quad x_J \leq x \leq x_{J+1/2} \, , \\ 0 & , \quad \text{otherwise} \, . \end{cases} \tag{2.26c}$$

Other definitions of $g_{j+1/2}$ are possible; for example, $g_{j+1/2} = f_{j+1/2}$. However, these will not be considered in this dissertation.

For $0 \leq j \leq J$, we define:

$$\Phi_{j+1/2} = \int_{x_{j-1/2}}^{x_{j+3/2}} g_{j+1/2}(x) \phi_0(x) dx \, , \tag{2.27}$$

where $\phi_0(x)$ is the scalar flux, $x_{-1/2} = x_{1/2} = 0$, and $x_{J+3/2} = x_{J+1/2} = X$. The quantities $\Phi_{j+1/2}$ will be the "flux" unknowns in the low-order FMC equations. If Eq. (2.25) is used to define $g_{j+1/2}(x)$, then for $0 \leq j \leq J$,

$$\begin{aligned} \Phi_{j+1/2} &= \phi_0(x_{j+1/2}) \\ &= \text{ pointwise (cell-edge) scalar flux at } x_{j+1/2} \, . \end{aligned}$$

If Eqs. (2.26) are used to define $g_{j+1/2}(x)$, then for $1 \leq j \leq J-1$,

$$\begin{aligned} \Phi_{j+1/2} &= \frac{2}{h_j + h_{j+1}} \int_{x_j}^{x_{j+1}} \phi_0(x) dx \\ &= \text{ scalar flux averaged between the midpoints of the } j^{th} \text{ and } (j+1)^{st} \text{ cells.} \end{aligned}$$

In the remainder of this dissertation we refer to the $\Phi_{j+1/2}$ obtained using $g_{j+1/2}$ defined by Eq. (2.25) as the *edge* unknowns, and to the $\Phi_{j+1/2}$ obtained using $g_{j+1/2}$ defined by Eq. (2.26) as the *average* unknowns.

To proceed, we multiply and divide each of the terms in Eqs. (2.24) by a suitable $\Phi_{j+1/2}$ to obtain the following equivalent system of $J+1$ equations:

$$\left[\frac{\int_{-1}^{1}|\mu|\psi(x_{1/2},\mu)d\mu}{\Phi_{1/2}}+\frac{1}{\Sigma_{tr,1}h_1}\frac{\phi_2(x_{1/2})}{\Phi_{1/2}}+\frac{\int_{x_{1/2}}^{x_{3/2}}f_{1/2}(x)\Sigma_{a,1}\phi_0(x)dx}{\Phi_{1/2}}\right]\Phi_{1/2}$$
$$-\left[\frac{1}{\Sigma_{tr,1}h_1}\frac{\phi_2(x_{3/2})}{\Phi_{3/2}}\right]\Phi_{3/2}=\frac{1}{k}\left[\frac{\int_{x_{1/2}}^{x_{3/2}}f_{1/2}(x)\nu\Sigma_{f,1}\phi_0(x)dx}{\Phi_{1/2}}\right]\Phi_{1/2}\,, \tag{2.28a}$$

$$\left[\left(\frac{1}{\Sigma_{tr,j+1}h_{j+1}}+\frac{1}{\Sigma_{tr,j}h_j}\right)\frac{\phi_2(x_{j+1/2})}{\Phi_{j+1/2}}+\frac{\int_{x_{j-1/2}}^{x_{j+3/2}}f_{j+1/2}(x)\Sigma_a(x)\phi_0(x)dx}{\Phi_{j+1/2}}\right]\Phi_{j+1/2}$$
$$-\left[\frac{1}{\Sigma_{tr,j}h_j}\frac{\phi_2(x_{j-1/2})}{\Phi_{j-1/2}}\right]\Phi_{j-1/2}-\left[\frac{1}{\Sigma_{tr,j+1}h_{j+1}}\frac{\phi_2(x_{j+3/2})}{\Phi_{j+3/2}}\right]\Phi_{j+3/2}$$
$$=\frac{1}{k}\left[\frac{\int_{x_{j-1/2}}^{x_{j+3/2}}f_{j+1/2}(x)\nu\Sigma_f(x)\phi_0(x)dx}{\Phi_{j+1/2}}\right]\Phi_{j+1/2}\ ,\ \ 1\le j\le J-1\,, \tag{2.28b}$$

$$\left[\frac{\int_{-1}^{1}|\mu|\psi(x_{J+1/2},\mu)d\mu}{\Phi_{J+1/2}}+\frac{1}{\Sigma_{tr,J}h_J}\frac{\phi_2(x_{J+1/2})}{\Phi_{J+1/2}}+\frac{\int_{x_{J-1/2}}^{x_{J+1/2}}f_{J+1/2}(x)\Sigma_{a,J}\phi_0(x)dx}{\Phi_{J+1/2}}\right]\Phi_{J+1/2}$$
$$-\left[\frac{1}{\Sigma_{tr,J}h_J}\frac{\phi_2(x_{J-1/2})}{\Phi_{J-1/2}}\right]\Phi_{J-1/2}=\frac{1}{k}\left[\frac{\int_{x_{J-1/2}}^{x_{J+1/2}}f_{J+1/2}(x)\nu\Sigma_{f,J}\phi_0(x)dx}{\Phi_{J+1/2}}\right]\Phi_{J+1/2}\,. \tag{2.28c}$$

Equivalently, if we define the following nonlinear functionals of ψ:

$$B_{1/2} = \frac{\int_{-1}^{1} |\mu| \psi(x_{1/2}, \mu) d\mu}{\int_{x_{1/2}}^{x_{3/2}} \int_{-1}^{1} g_{1/2}(x) \psi(x, \mu) d\mu dx} , \tag{2.29a}$$

$$B_{J+1/2} = \frac{\int_{-1}^{1} |\mu| \psi(x_{J+1/2}, \mu) d\mu}{\int_{x_{J-1/2}}^{x_{J+1/2}} \int_{-1}^{1} g_{J+1/2}(x) \psi(x, \mu) d\mu dx} , \tag{2.29b}$$

$$E_{j+1/2} = \frac{\int_{-1}^{1} \mu^2 \psi(x_{j+1/2}, \mu) d\mu}{\int_{x_{j-1/2}}^{x_{j+3/2}} \int_{-1}^{1} g_{j+1/2}(x) \psi(x, \mu) d\mu dx} , \tag{2.29c}$$

$$A_{j+1/2} = \frac{\int_{x_{j-1/2}}^{x_{j+3/2}} f_{j+1/2}(x) \Sigma_a(x) \phi_0(x) dx}{\int_{x_{j-1/2}}^{x_{j+3/2}} g_{j+1/2}(x) \phi_0(x) dx} , \tag{2.29d}$$

$$F_{j+1/2} = \frac{\int_{x_{j-1/2}}^{x_{j+3/2}} f_{j+1/2}(x) \nu \Sigma_f(x) \phi_0(x) dx}{\int_{x_{j-1/2}}^{x_{j+3/2}} g_{j+1/2}(x) \phi_0(x) dx} , \tag{2.29e}$$

then Eqs. (2.28) can be written more compactly as:

$$\left[B_{1/2} + \frac{1}{\Sigma_{tr,1} h_1} E_{1/2} + A_{1/2} \right] \Phi_{1/2} - \left[\frac{1}{\Sigma_{tr,1} h_1} E_{3/2} \right] \Phi_{3/2} = \frac{1}{k} \left[F_{1/2} \right] \Phi_{1/2} , \tag{2.30a}$$

$$\left[\left(\frac{1}{\Sigma_{tr,j} h_j} + \frac{1}{\Sigma_{tr,j+1} h_{j+1}} \right) E_{j+1/2} + A_{j+1/2} \right] \Phi_{j+1/2} - \left[\frac{1}{\Sigma_{tr,j} h_j} E_{j-1/2} \right] \Phi_{j-1/2} - \left[\frac{1}{\Sigma_{tr,j+1} h_{j+1}} E_{j+3/2} \right] \Phi_{j+3/2} = \frac{1}{k} \left[F_{j+1/2} \right] \Phi_{j+1/2} \ , \ 1 \le j \le J-1 , \tag{2.30b}$$

$$\left[B_{J+1/2} + \frac{1}{\Sigma_{tr,J} h_J} E_{J+1/2} + A_{J+1/2} \right] \Phi_{J+1/2} - \left[\frac{1}{\Sigma_{tr,J} h_J} E_{J-1/2} \right] \Phi_{J-1/2} = \frac{1}{k} \left[F_{J+1/2} \right] \Phi_{J+1/2} . \tag{2.30c}$$

Eqs. (2.29) and (2.30) are exactly satisfied by solution $\psi(x, \mu)$ and k of Eqs. (2.14). However, the following is also true: if the functionals in Eqs. (2.29) are evaluated using the exact eigenfunction $\psi(x, \mu)$, and Eqs. (2.30) are then solved for $\Phi_{j+1/2}$ and k, then the resulting

$\Phi_{j+1/2}$ and k are *exact*, i.e. k is the exact eigenvalue, and $\Phi_{j+1/2}$ are the exact appropriate space-angle moments of ψ. We remark that the QD method has "boundary" and "Eddington factor" functionals Eqs. (2.9) that are closely related to the B and E functionals in Eqs. (2.29).

To summarize the FMC procedure used here: Eqs. (2.14) are simulated using the standard Monte Carlo method of processing fission particles from one cycle to the next. The standard Monte Carlo k-eigenvalue is estimated for each cycle, and the final (standard Monte Carlo) estimate of k is obtained by averaging k over all active cycles. During this process, additional information is processed and stored beyond what is needed to perform the standard simulation. Specifically, Monte Carlo estimates of each of the integrals in the numerators and denominators of Eqs. (2.29) are obtained. At the end of each active cycle, the functionals in Eqs. (2.29) are calculated and Eqs. (2.30) are solved to obtain the FMC cycle-wise estimates of $\Phi_{j+1/2}$ and k. After the active cycles are completed, the FMC eigenvalues and eigenfunctions are averaged over the active cycles to obtain the final FMC estimates of k and ϕ.

Remarks

1. The FMC method is based on two assumptions:
   (a) The functionals in Eqs. (2.29) depend weakly on ψ and can be evaluated with Monte Carlo more accurately than direct Monte Carlo estimates of ϕ_0.
   (b) If Eqs. (2.30) are solved with small errors in the functionals, the resulting errors in $\Phi_{j+1/2}$ and k will be small.

   To argue the first point, we note that the functionals in Eqs. (2.29) are all *local*, e.g. $E_{j+1/2}$ depends on estimates of ψ only in the $j^{th}$and $(j+1)^{th}$ spatial cells. Also, these functionals depend only on low-order spatial and angular moments of ψ, and because of their nonlinear character, they are only weakly-dependent on the amplitude of ψ. Therefore, if a Monte Carlo estimate of ψ yield a poor estimate of the ampli-

tude but a reasonably good estimate of the spatial and angular shape of ψ, then the functionals in Eqs. (2.29) should be evaluated accurately.

To argue the second point, if we use the crude estimate of ψ:

$$\psi(x,\mu) \approx \frac{\phi_{0,j+1/2}}{2} \quad , \quad x_{j-1/2} < x < x_{j+1/2}$$

in Eqs. (2.29), we obtain:

$$B_{1/2} = B_{J+1/2} = \frac{1}{2} \, , \tag{2.31a}$$

$$E_{j+1/2} = \frac{1}{3} \, , \tag{2.31b}$$

$$A_{j+1/2} = \begin{cases} \frac{1}{2}\Sigma_{a,1}h_1 & , \quad j = 0 \\ \frac{1}{2}\left(\Sigma_{a,j}h_j + \Sigma_{a,j+1}h_{j+1}\right) & , \quad 1 \le j \le J-1 \\ \frac{1}{2}\Sigma_{a,J}h_J & , \quad j = J \, , \end{cases} \tag{2.31c}$$

$$F_{j+1/2} = \begin{cases} \frac{1}{2}\nu\Sigma_{f,1}h_1 & , \quad j = 0 \\ \frac{1}{2}\left(\nu\Sigma_{f,j}h_j + \nu\Sigma_{f,j+1}h_{j+1}\right) & , \quad 1 \le j \le J-1 \\ \frac{1}{2}\nu\Sigma_{f,J}h_J & , \quad j = J \, . \end{cases} \tag{2.31d}$$

When these functional values – all of which are independent of $\phi_{0,j+1/2}$ – are introduced into Eqs. (2.29), we obtain the standard cell-edge diffusion discretization of the diffusion approximation to Eqs. (2.14).

Thus, the discrete system of Eqs. (2.29) is closely related to the classic diffusion approximation to Eqs. (2.14). If the underlying physical transport problem has eigenfunctions and eigenvalues that are weakly-sensitive to small perturbations in the fuel or moderator, then small statistical errors in the FMC functionals should produce comparably small statistical errors in the FMC estimates of the eigenfunction and eigenvalue.

2. We give our argument for choosing "tent functions" as in Step 2. Let $f_{j+1/2}(x)$ be an arbitrary local function, which involves the spatial grid point it is identified with and adjacent spatial grid points. We shall see what conditions the function $f_{j+1/2}(x)$ needs to satisfy. Again operating on Eq. (2.20a) by

$$\int_{x_{j-1/2}}^{x_{j+3/2}} f_{j+1/2}(x)\,[\cdot]\,dx$$

we get:

$$-\int_{x_{j-1/2}}^{x_{j+3/2}} f_{j+1/2}(x)\left[\frac{d}{dx}\frac{1}{\Sigma_{tr}(x)}\frac{d\phi_2}{dx}(x)\right]dx+\int_{x_{j-1/2}}^{x_{j+3/2}} f_{j+1/2}(x)\Sigma_a(x)\phi_0(x)dx$$
$$=\frac{1}{k}\int_{x_{j-1/2}}^{x_{j+3/2}} f_{j+1/2}(x)\nu\Sigma_f(x)\phi_0(x)dx\,. \tag{2.32}$$

Using integration by parts, the leakage term becomes:

$$\int_{x_{j-1/2}}^{x_{j+3/2}} f_{j+1/2}(x)\left[\frac{d}{dx}\frac{1}{\Sigma_{tr}(x)}\frac{d\phi_2}{dx}(x)\right]dx$$
$$=f_{j+1/2}(x)\frac{1}{\Sigma_{tr}(x)}\frac{d\phi_2}{dx}(x)\Big|_{x_{j-1/2}}^{x_{j+3/2}}-\int_{x_{j-1/2}}^{x_{j+3/2}}\frac{df_{j+1/2}}{dx}(x)\frac{1}{\Sigma_{tr}(x)}\frac{d\phi_2}{dx}(x)dx\,.$$

If the function $f_{j+1/2}(x)$ satisfies $f_{j+1/2}(x_{j-1/2})=f_{j+1/2}(x_{j+3/2})=0$, then the first term is zero and the leakage term is simplified to:

$$=-\int_{x_{j-1/2}}^{x_{j+3/2}}\frac{df_{j+1/2}}{dx}(x)\frac{1}{\Sigma_{tr}(x)}\frac{d\phi_2}{dx}(x)dx\,.$$

Here we require that function $f_{j+1/2}(x)$ is continuous but need not possess a derivative at the spatial grid point it is identified with. If we also assume that $df_{j+1/2}(x)/dx$ is a constant between adjacent spatial grid points, then the integral above can be further simplified. The "tent functions" satisfy all the conditions discussed above. By defining $f_{j+1/2}(x)$ as a tent function at spatial grid point $x_{j+1/2}$, the above integral

can now be easily carried out, yielding

$$
\begin{aligned}
&= -\int_{x_{j-1/2}}^{x_{j+1/2}} \frac{1}{h_j \Sigma_{tr,j}} \frac{d\phi_2}{dx}(x)dx + \int_{x_{j+1/2}}^{x_{j+3/2}} \frac{1}{h_{j+1}\Sigma_{tr,j+1}} \frac{d\phi_2}{dx}(x)dx \\
&= \frac{1}{\Sigma_{tr,j+1}h_{j+1}} \left[\phi_2(x_{j+3/2}) - \phi_2(x_{j+1/2})\right] \\
&\qquad - \frac{1}{\Sigma_{tr,j}h_j} \left[\phi_2(x_{j+1/2}) - \phi_2(x_{j-1/2})\right] .
\end{aligned}
$$

The "tent function" is not the only possible choice here. However, it is certainly a straightforward one. We note that the tent function is also used in the finite element method as a first-order basis function. However the finite element method has truncation errors, but in the present context, the use of the tent function does not lead to any truncation error.

3. We give a brief discussion of attempts to develop an FMC method in which the functionals depend on the neutron current. (We were not able to obtain a satisfactory method of this type, for reasons discussed below.)

   For simplicity, without considering the spatial dependence, we write the Monte Carlo estimate of the angular flux as

$$\psi_{est}(\mu) = \psi(\mu) + \delta\psi(\mu) ,$$

   where $\psi(\mu)$ is the true angular flux, and $\delta\psi(\mu)$ is a small perturbation.
   If we define the nonlinear functional

$$f_n = \frac{\int_{-1}^{1} \mu^n \psi(\mu) d\mu}{\int_{-1}^{1} \psi(\mu) d\mu} \ , \ n = 1,2 \ , \tag{2.33}$$

then the Monte Carlo estimate of the nonlinear functional becomes:

$$
\begin{aligned}
f_{n,est} &= f_n + \delta f_n \\
&= \frac{\int_{-1}^{1} \mu^n \left[\psi(\mu) + \delta\psi(\mu)\right] d\mu}{\int_{-1}^{1} \left[\psi(\mu) + \delta\psi(\mu)\right] d\mu} \\
&= \frac{\int_{-1}^{1} \mu^n \psi(\mu) d\mu + \int_{-1}^{1} \mu^n \delta\psi(\mu) d\mu}{\int_{-1}^{1} \psi(\mu) d\mu + \int_{-1}^{1} \delta\psi(\mu) d\mu} \\
&= \frac{\int_{-1}^{1} \mu^n \psi(\mu) d\mu \left[1 + \frac{\int_{-1}^{1} \mu^n \delta\psi(\mu) d\mu}{\int_{-1}^{1} \mu^n \psi(\mu) d\mu}\right]}{\int_{-1}^{1} \psi(\mu) d\mu \left[1 + \frac{\int_{-1}^{1} \delta\psi(\mu) d\mu}{\int_{-1}^{1} \psi(\mu) d\mu}\right]} \\
&= f_n \left[1 + \frac{\int_{-1}^{1} \mu^n \delta\psi(\mu) d\mu}{\int_{-1}^{1} \mu^n \psi(\mu) d\mu}\right] \left[1 - \frac{\int_{-1}^{1} \delta\psi(\mu) d\mu}{\int_{-1}^{1} \psi(\mu) d\mu} + \cdots\right] \\
&= f_n \left[1 + \left(\frac{\int_{-1}^{1} \mu^n \delta\psi(\mu) d\mu}{\int_{-1}^{1} \mu^n \psi(\mu) d\mu} - \frac{\int_{-1}^{1} \delta\psi(\mu) d\mu}{\int_{-1}^{1} \psi(\mu) d\mu}\right) + \cdots\right] . \qquad (2.34)
\end{aligned}
$$

The relative error in the nonlinear functional can expressed as:

$$
\frac{\delta f_n}{f_n} = \frac{\int_{-1}^{1} \mu^n \delta\psi(\mu) d\mu}{\int_{-1}^{1} \mu^n \psi(\mu) d\mu} - \frac{\int_{-1}^{1} \delta\psi(\mu) d\mu}{\int_{-1}^{1} \psi(\mu) d\mu} . \qquad (2.35)
$$

When $n = 1$ (odd), $\int_{-1}^{1} \mu\psi(\mu) d\mu$ can be very small for diffusive problems where ψ is nearly isotropic, thus the relative error in f_n can be very large. This is not true when $n = 2$ $(even)$, since $\int_{-1}^{1} \mu^2\psi(\mu) d\mu$ is always positive.

Our conclusion is that the "functional" approach is likely to be advantageous when the FMC method is based on low-order equations in which the current- related ($n = 1$) term is algebraically eliminated. This does not mean that efficient methods containing current do not exist; but it does mean that methods containing these terms are more likely to be problematic.

4. The FMC method does not have the conventional standard neutron balance equation for each cell. Integrating Eq.(2.17a) over $[x_{j-1/2},\ x_{j+1/2}]$, we obtain the standard

neutron balance equation for cell j:

$$\phi_1(x_{j+1/2}) - \phi_1(x_{j-1/2}) + \int_{x_{j-1/2}}^{x_{j+1/2}} \Sigma_a(x)\phi_0(x)dx = \int_{x_{j-1/2}}^{x_{j+1/2}} \frac{\nu\Sigma_f(x)}{k}\phi_0(x)dx \;\; 1 \le j \le J \,. \tag{2.36}$$

However, operating on Eq. (2.36) by $\sum_{j=1}^{J}(\cdot)$, we get

$$\phi_1(x_{J+1/2}) - \phi_1(x_{1/2}) + \int_0^X \Sigma_a(x)\phi_0(x)dx = \int_0^X \frac{\nu\Sigma_f(x)}{k}\phi_0(x)dx \,. \tag{2.37}$$

Eq. (2.37) is a statement of neutron conservation over the system. Eq. (2.37) is also an ingredient of the FMC method, because the FMC method is based on :

$$\int_0^X f_{j+1/2}(x)[Eq.(2.20)]dx \,, \tag{2.38}$$

and operating on Eq. (2.38) by $\sum_{j=1}^{J}(\cdot)$, we have

$$\begin{aligned} &\sum_{j=1}^{J}\Big[\int_0^X f_{j+1/2}(x)[Eq.(2.20)]dx\Big] \\ &= \int_0^X \Big(\sum_{j=1}^{J} f_{j+1/2}(x)\Big)[Eq.(2.20)]dx \\ &= \int_0^X [Eq.(2.20)]dx \,, \end{aligned} \tag{2.39}$$

which states that the FMC method satisfies neutron conservation over the system.

5. In this section, the tent functions are defined on a spatial grid having J spatial cells. The eigenfunctions obtained from the low order FMC equations are defined either "at" the cell edges [Eq.(2.23)] or averaged on a "staggered" grid [Eqs.(2.24)] as shown in Figure 2.4, rather than averaged over the spatial cells. We may inquire: is it possible to make accurate estimates of ϕ over the spatial cells? The answer to this question is discussed next.

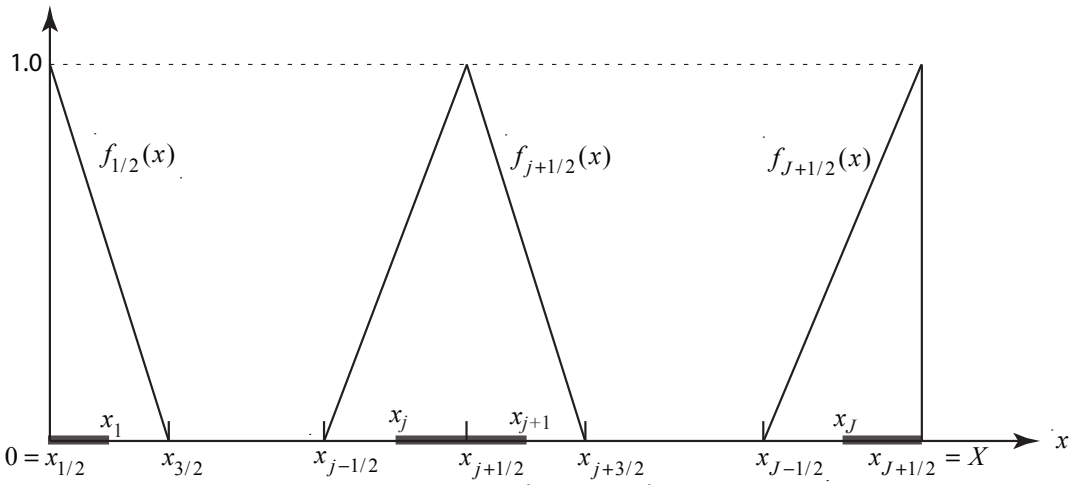

Figure 2.4 The FMC eigenfunctions are averaged on a "staggered" grid as shown.

2.3 Cross Sections that are Discontinuous within a Cell

In Section 2.2, we have assumed that each spatial cell only contains one kind of material. Here we adopt the assumption that each interior spatial cell may consist of two regions with different cross sections except at the boundary layers. For boundary layers, we assume that each layer only contains one kind of material. The case of a spatial cell containing multiple regions is discussed later in Chapter 5.

2.3.1 Procedure to Generate Low-order Equations with Material Discontinuities within a Cell

Again, we prescribe a spatial grid, consisting of $J+1$ points $x_{j+1/2}$ satisfying $0 = x_{1/2} < x_{3/2} < \cdots < x_{j-1/2} < x_{j+1/2} < \cdots < x_{J-1/2} < x_{J+1/2} = X$. The j^{th} spatial cell consists of the interval $x_{j-1/2} < x < x_{j+1/2}$; the width of this cell is $h_j = x_{j+1/2} - x_{j-1/2}$.

To obtain the flux average over a spatial cell:

$$\begin{aligned}\Phi_j &= \frac{1}{x_{j+1/2} - x_{j-1/2}} \int_{x_{j-1/2}}^{x_{j+1/2}} \phi_0(x)dx \\ &= \frac{1}{h_j} \int_{x_{j-1/2}}^{x_{j+1/2}} \phi_0(x)dx \qquad 1 \le j \le J \ , \end{aligned} \tag{2.40}$$

we introduce a *staggered grid point* x_j such that $x_{j-1/2} < x_j < x_{j+1/2}$ for $2 \le j \le J-1$. There are two ways to choose staggered grid points: (1) x_j is chosen as the material interface if the spatial cell contains two material regions; (2) x_j is chosen to be the midpoint if the cell only contains one kind of material. Let $h_j^L = x_j - x_{j-1/2}$, and $h_j^R = x_{j+1/2} - x_j$. Clearly the width of the j^{th} cell $h_j = h_j^L + h_j^R$.

For $1 \le j \le J$, we define tent functions $f_j(x)$ at the staggered grid point x_j.

For $j = 1$:

$$f_1(x) = \begin{cases} \frac{1}{h_1 + h_2^L}(x_2 - x) & , \ 0 = x_1 < x < x_2 \\ 0 & , \ \text{otherwise} \ . \end{cases} \tag{2.41a}$$

For $2 \le j \le J-1$:

$$f_j(x) = \begin{cases} \frac{1}{h_{j-1}^R + h_j^L}(x - x_{j-1}) & , \ x_{j-1} < x < x_j \\ \frac{1}{h_j^R + h_{j+1}^L}(x_{j+1} - x) & , \ x_j < x < x_{j+1} \\ 0 & , \ \text{otherwise} \ . \end{cases} \tag{2.41b}$$

And for $j = J$:

$$f_J(x) = \begin{cases} \frac{1}{h_{J-1}^R + h_J}(x - x_{J-1}) & , \ x_{J-1} < x < x_J = X \\ 0 & , \ \text{otherwise} \ . \end{cases} \tag{2.41c}$$

The tent functions defined on a staggered grid are displayed in Figure 2.5, while detailed information for a staggered grid point x_j is shown in Figure 2.6. We note that the number of tent functions is equal to the number of spatial cells.

We now begin the derivation of the low-order FMC equations. We multiply Eq. (2.20a) by $f_j(x)$ and integrate over $0 \le x \le X$.

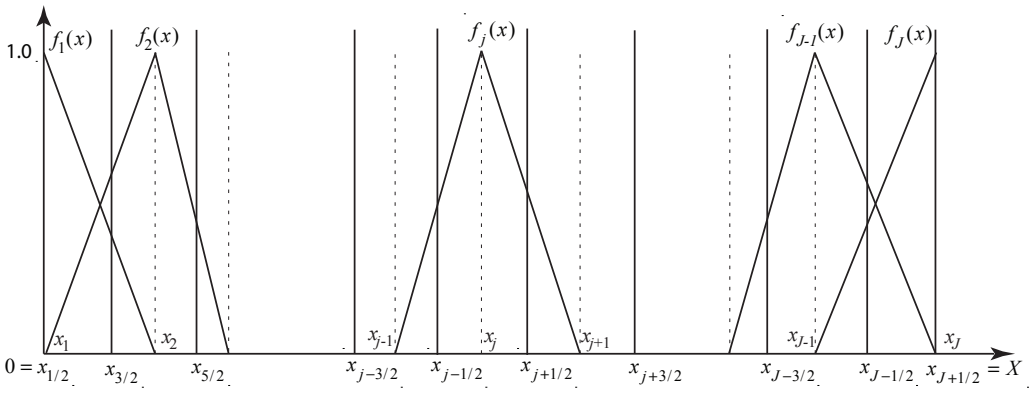

Figure 2.5 The tent functions defined on a staggered grid.

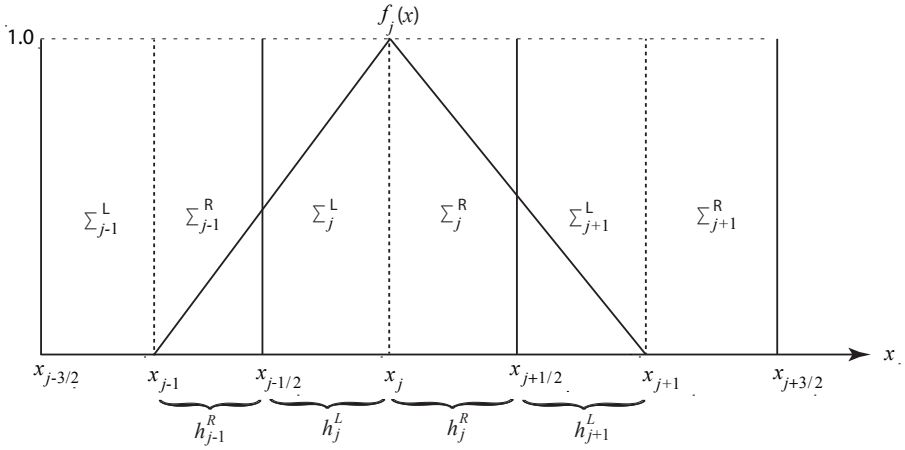

Figure 2.6 Detailed information for a staggered grid point x_j.

For $2 \leq j \leq J-1$, we obtain:

$$-\int_{x_{j-1}}^{x_{j+1}} f_j(x)\left[\frac{d}{dx}\frac{1}{\Sigma_{tr}(x)}\frac{d\phi_2}{dx}(x)\right]dx+\int_{x_{j-1}}^{x_{j+1}} f_j(x)\Sigma_a(x)\phi_0(x)dx$$
$$=\frac{1}{k}\int_{x_{j-1}}^{x_{j+1}} f_j(x)\nu\Sigma_f(x)\phi_0(x)dx\,. \tag{2.42}$$

Using integration by parts, we write the first term of Eq. (2.42) explicitly as:

$$
\begin{aligned}
&-\int_{x_{j-1}}^{x_{j+1}} f_j(x)\left[\frac{d}{dx}\frac{1}{\Sigma_{tr}(x)}\frac{d\phi_2}{dx}(x)\right]dx \\
&\quad=\int_{x_{j-1}}^{x_{j+1}}\frac{df_j}{dx}(x)\frac{1}{\Sigma_{tr}(x)}\frac{d\phi_2}{dx}(x)dx \\
&\quad=\frac{1}{h_{j-1}^R+h_j^L}\int_{x_{j-1}}^{x_j}\frac{1}{\Sigma_{tr}(x)}\frac{d\phi_2}{dx}(x)dx-\frac{1}{h_j^R+h_{j+1}^L}\int_{x_j}^{x_{j+1}}\frac{1}{\Sigma_{tr}(x)}\frac{d\phi_2}{dx}(x)dx \\
&\quad=\frac{1}{h_{j-1}^R+h_j^L}\left[\frac{\phi_2(x_{j-1/2})-\phi_2(x_{j-1})}{\Sigma_{tr,j-1}^R}+\frac{\phi_2(x_j)-\phi_2(x_{j-1/2})}{\Sigma_{tr,j}^L}\right] \\
&\quad-\frac{1}{h_j^R+h_{j+1}^L}\left[\frac{\phi_2(x_{j+1/2})-\phi_2(x_j)}{\Sigma_{tr,j}^R}+\frac{\phi_2(x_{j+1})-\phi_2(x_{j+1/2})}{\Sigma_{tr,j+1}^L}\right]. \qquad (2.43)
\end{aligned}
$$

To simplify notation in Eq. (2.43), we define the contents of the second square bracket as

$$
G_j=\frac{1}{\Sigma_{tr,j}^R}\left[\phi_2(x_{j+1/2})-\phi_2(x_j)\right]+\frac{1}{\Sigma_{tr,j+1}^L}\left[\phi_2(x_{j+1})-\phi_2(x_{j+1/2})\right]. \qquad (2.44)
$$

In Section 2.3.2, the function G_j is rewritten in terms of $\phi_2(x_j)$ and $\phi_2(x_{j+1})$:

$$
\begin{aligned}
G_j&=\left[\frac{1}{\overline{\Sigma}_{tr,j}}+\frac{1}{2}\frac{|\mathscr{E}_j|+\mathscr{E}_j}{\phi_2(x_{j+1})}\right]\phi_2(x_{j+1}) \\
&\quad-\left[\frac{1}{\overline{\Sigma}_{tr,j}}+\frac{1}{2}\frac{|\mathscr{E}_j|-\mathscr{E}_j}{\phi_2(x_j)}\right]\phi_2(x_j) \\
&=L_{1,j}\phi_2(x_{j+1})-L_{2,j}\phi_2(x_j), \qquad (2.45)
\end{aligned}
$$

where

$$
\begin{aligned}
\frac{1}{\overline{\Sigma}_{tr,j}}&=\frac{1}{h_j^R+h_{j+1}^L}\left(\frac{h_j^R}{\Sigma_{tr,j}^R}+\frac{h_{j+1}^L}{\Sigma_{tr,j+1}^L}\right), \\
\mathscr{E}_j&=\left(\frac{1}{\Sigma_{tr,j}^R}-\frac{1}{\Sigma_{tr,j+1}^L}\right)E_j, \\
E_j&=\phi_2(x_{j+1/2})-\phi_2(x_j)\frac{h_{j+1}^L}{h_j^R+h_{j+1}^L}-\phi_2(x_{j+1})\frac{h_j^R}{h_j^R+h_{j+1}^L}, \qquad (2.46)
\end{aligned}
$$

and

$$L_{1,j} = \frac{1}{\overline{\Sigma}_{tr,j}} + \frac{1}{2}\frac{|\mathscr{E}_j| + \mathscr{E}_j}{\phi_2(x_{j+1})} ,$$
$$L_{2,j} = \frac{1}{\overline{\Sigma}_{tr,j}} + \frac{1}{2}\frac{|\mathscr{E}_j| - \mathscr{E}_j}{\phi_2(x_{j+1})} . \tag{2.47}$$

Using Eq. (2.45), Eq. (2.43) can be written:

$$\begin{aligned}
&-\int_{x_{j-1}}^{x_{j+1}} f_j(x)\left[\frac{d}{dx}\frac{1}{\Sigma_{tr}(x)}\frac{d\phi_2}{dx}(x)\right]dx \\
&= \frac{1}{h_{j-1}^R + h_j^L} G_{j-1} - \frac{1}{h_j^R + h_{j+1}^L} G_j \\
&= \frac{1}{h_{j-1}^R + h_j^L}\left[L_{1,j-1}\,\phi_2(x_j) - L_{2,j-1}\,\phi_2(x_{j-1})\right] \\
&- \frac{1}{h_j^R + h_{j+1}^L}\left[L_{1,j}\,\phi_2(x_{j+1}) - L_{2,j}\,\phi_2(x_j)\right] \\
&= -\frac{L_{2,j-1}}{h_{j-1}^R + h_j^L}\phi_2(x_{j-1}) + \left[\frac{L_{1,j-1}}{h_{j-1}^R + h_j^L} + \frac{L_{2,j}}{h_j^R + h_{j+1}^L}\right]\phi_2(x_j) \\
&\quad - \frac{L_{1,j}}{h_j^R + h_{j+1}^L}\,\phi_2(x_{j+1}) ,
\end{aligned} \tag{2.48}$$

where the second moments defined at the spatial grid points $\phi_2(x_{j\pm 1/2})$ have been collapsed into the parameters $L_{1,j}$ and $L_{2,j}$.

Using Eq. (2.48), for $2 \le j \le J-1$, Eq. (2.42) becomes:

$$\begin{aligned}
&-\frac{L_{2,j-1}}{h_{j-1}^R + h_j^L}\phi_2(x_{j-1}) + \left[\frac{L_{1,j-1}}{h_{j-1}^R + h_j^L} + \frac{L_{2,j}}{h_j^R + h_{j+1}^L}\right]\phi_2(x_j) - \frac{L_{1,j}}{h_j^R + h_{j+1}^L}\,\phi_2(x_{j+1}) \\
&\quad + \int_{x_{j-1}}^{x_{j+1}} f_j(x)\Sigma_a(x)\phi_0(x)dx = \frac{1}{k}\int_{x_{j-1}}^{x_{j+1}} f_j(x)\nu\Sigma_f(x)\phi_0(x)dx .
\end{aligned} \tag{2.49}$$

Similarly, for $j = 1$ (left boundary, Figure 2.7) we multiply Eq. (2.20a) by $f_1(x)$ and

integrate to obtain

$$-\int_{x_1}^{x_2} f_1(x)\left[\frac{d}{dx}\frac{1}{\Sigma_{tr}(x)}\frac{d\phi_2}{dx}(x)\right]dx+\int_{x_1}^{x_2} f_1(x)\Sigma_a(x)\phi_0(x)dx$$
$$=\frac{1}{k}\int_{x_1}^{x_2} f_1(x)\nu\Sigma_f(x)\phi_0(x)dx\,. \tag{2.50}$$

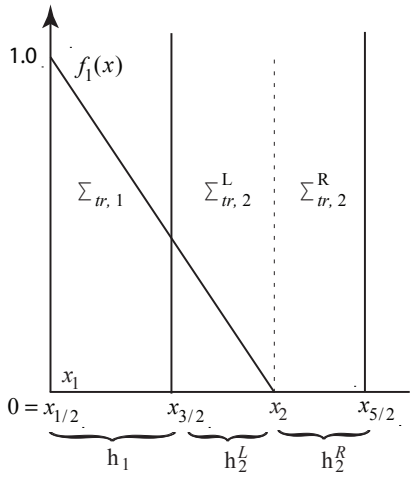

Figure 2.7 Detailed information on the left boundary.

Integrating the first term of Eq. (2.50) by parts, we get:

$$\begin{aligned}
&-\int_{x_1}^{x_2} f_1(x)\left[\frac{d}{dx}\frac{1}{\Sigma_{tr}(x)}\frac{d\phi_2}{dx}(x)\right]dx\\
&=\int_{-1}^{1}|\mu|\psi(0,\mu)d\mu-\frac{1}{h_1+h_2^L}\left[\frac{\phi_2(x_{3/2})-\phi_2(x_1)}{\Sigma_{tr,1}}+\frac{\phi_2(x_2)-\phi_2(x_{3/2})}{\Sigma_{tr,2}^L}\right]\\
&=\int_{-1}^{1}|\mu|\psi(0,\mu)d\mu-\frac{1}{h_1+h_2^L}G_1\\
&=\int_{-1}^{1}|\mu|\psi(0,\mu)d\mu-\frac{1}{h_1+h_2^L}\left[L_{1,1}\,\phi_2(x_2)-L_{2,1}\,\phi_2(x_1)\right]\,.
\end{aligned} \tag{2.51}$$

Thus, the preceding Eq. (2.50) for $j=1$ can be written:

$$\int_{-1}^{1}|\mu|\psi(0,\mu)d\mu+\frac{L_{2,1}}{h_1+h_2^L}\,\phi_2(x_1)-\frac{L_{1,1}}{h_1+h_2^L}\,\phi_2(x_2)$$
$$+\int_{x_1}^{x_2} f_1(x)\Sigma_a(x)\phi_0(x)dx=\frac{1}{k}\int_{x_1}^{x_2} f_1(x)\nu\Sigma_f(x)\phi_0(x)dx\,. \tag{2.52}$$

For $j = J$ (right boundary, Figure 2.8), We follow similar steps as for $j = 1$ by multiplying Eq. (2.20a) with $f_J(x)$ and integrate to obtain

$$-\int_{x_{J-1}}^{x_J} f_J(x)\left[\frac{d}{dx}\frac{1}{\Sigma_{tr}(x)}\frac{d\phi_2}{dx}(x)\right]dx+\int_{x_{J-1}}^{x_J} f_J(x)\Sigma_a(x)\phi_0(x)dx$$
$$=\frac{1}{k}\int_{x_{J-1}}^{x_J} f_J(x)\nu\Sigma_f(x)\phi_0(x)dx\,. \tag{2.53}$$

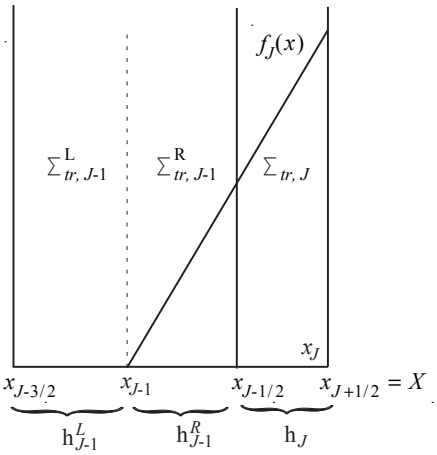

Figure 2.8 Detailed information on the right boundary.

Integrating the first term of Eq. (2.53) by parts, we get:

$$-\int_{x_{J-1}}^{x_J} f_J(x)\left[\frac{d}{dx}\frac{1}{\Sigma_{tr}(x)}\frac{d\phi_2}{dx}(x)\right]dx$$
$$=\int_{-1}^{1}|\mu|\psi(X,\mu)d\mu-\frac{1}{h^R_{J-1}+h_J}\left[L_{1,J-1}\,\phi_2(x_J)-L_{2,J-1}\,\phi_2(x_{J-1})\right]. \tag{2.54}$$

Thus, the preceding Eq. (2.53) for $j = J$ can be written:

$$\int_{-1}^{1}|\mu|\psi(X,\mu)d\mu+\frac{L_{1,J-1}}{h^R_{J-1}+h_J}\,\phi_2(x_J)-\frac{L_{2,J-1}}{h^R_{J-1}+h_J}\,\phi_2(x_{J-1})$$
$$+\int_{x_{J-1}}^{x_J} f_J(x)\Sigma_a(x)\phi_0(x)dx=\frac{1}{k}\int_{x_{J-1}}^{x_J} f_J(x)\nu\Sigma_f(x)\phi_0(x)dx\,. \tag{2.55}$$

Next, for $1 \leq j \leq J$, we introduce functions $g_j(x)$ that are to satisfy:

$$g_j(x) = \begin{cases} \frac{1}{h_j} & x_{j-1/2} < x < x_{j+1/2} \\ 0 \quad , \quad \text{otherwise} \ . \end{cases}$$

For $1 \leq j \leq J$, we define:

$$\Phi_j = \int_{x_{j-1}}^{x_{j+1}} g_j(x)\phi_0(x)dx \, , \tag{2.56}$$

where $x_0 = x_{1/2} = x_1 = 0$, and $x_{J+1} = x_{J+1/2} = x_J = X$. The quantities Φ_j are the flux average over spatial cells, which are also unknowns for the low-order FMC equations as indicated in Figure 2.9. We note that Eq. (2.56) is equivalent to Eq. (2.40).

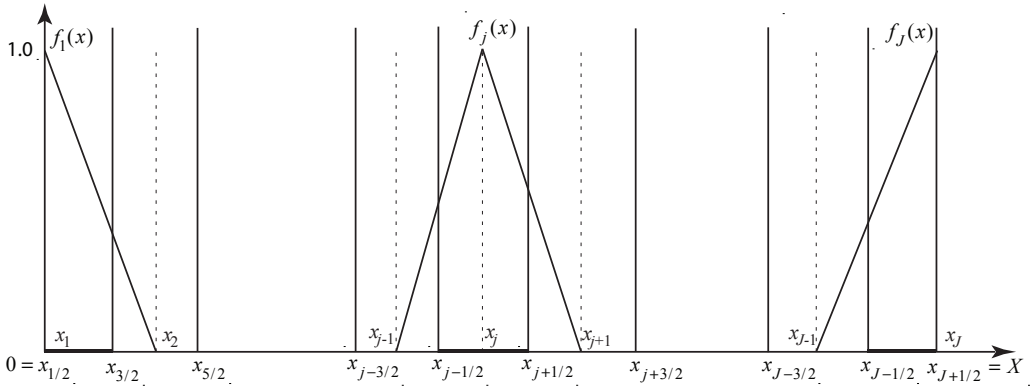

Figure 2.9 The heavy line (spatial cell) intervals show the regions where the Φ_j are averaged using tent functions defined on a staggered grid.

In the next step, we define the nonlinear functionals, which are similar to the monoenergetic case, as follows:

$$
\begin{aligned}
B_1 &= \frac{\int_{-1}^{1} |\mu| \psi(0,\mu) d\mu}{\int_{x_1}^{x_2} g_1(x) \phi_0(x) dx} \,, \\
B_J &= \frac{\int_{-1}^{1} |\mu| \psi(X,\mu) d\mu}{\int_{x_{J-1}}^{x_J} g_J(x) \phi_0(x) dx} \,, \\
E_j &= \frac{\int_{-1}^{1} \mu^2 \psi(x_j,\mu) d\mu}{\int_{x_{j-1}}^{x_{j+1}} g_j(x) \phi_0(x) dx} \,, \\
A_j &= \frac{\int_{x_{j-1}}^{x_{j+1}} f_j(x) \Sigma_a(x) \phi_0(x) dx}{\int_{x_{j-1}}^{x_{j+1}} g_j(x) \phi_0(x) dx} \,, \\
F_j &= \frac{\int_{x_{j-1}}^{x_{j+1}} f_j(x) \nu\Sigma_f(x) \phi_0(x) dx}{\int_{x_{j-1}}^{x_{j+1}} g_j(x) \phi_0(x) dx} \,.
\end{aligned} \tag{2.57}
$$

In terms of nonlinear functionals, Eqs. (2.49), (2.52), and (2.55) can be written as:

$$
\begin{aligned}
\left[B_1 + \frac{L_{2,1}}{h_1 + h_2^L} E_1 + A_1 \right] \Phi_1 - \left[\frac{L_{1,1}}{h_1 + h_2^L} E_2 \right] \Phi_2 \\
= \frac{1}{k} \left[F_1 \right] \Phi_1 \,,
\end{aligned} \tag{2.58a}
$$

$$
\begin{aligned}
- \left[\frac{L_{2,j-1}}{h_{j-1}^R + h_j^L} E_{j-1} \right] \Phi_{j-1} + \left[\left(\frac{L_{1,j-1}}{h_{j-1}^R + h_j^L} + \frac{L_{2,j}}{h_j^R + h_{j+1}^L} \right) E_j + A_j \right] \Phi_j \\
- \left[\frac{L_{1,j}}{h_j^R + h_{j+1}^L} E_{j+1} \right] \Phi_{j+1} = \frac{1}{k} \left[F_j \right] \Phi_j \,, \quad 2 \le j \le J-1
\end{aligned} \tag{2.58b}
$$

$$
\begin{aligned}
- \left[\frac{L_{2,J-1}}{h_{J-1}^R + h_J} E_{J-1} \right] \Phi_{J-1} + \left[B_J + \frac{L_{1,J-1}}{h_{J-1}^R + h_J} E_J + A_J \right] \Phi_J \\
= \frac{1}{k} \left[F_J \right] \Phi_J
\end{aligned} \tag{2.58c}
$$

Eqs. (2.58) are the FMC low-order equations, which are solved to obtain the FMC eigenfunctions averaged over spatial cells. To summarize the FMC procedure used here with material discontinuities within spatial cells, Eqs. (2.14) are simulated using the standard Monte Carlo method of processing fission particles over a series of cycles. The standard Monte Carlo k-eigenvalue is estimated for each cycle, and the final (standard Monte Carlo)

estimate of k is obtained by averaging k over all active cycles. During this process, Monte Carlo estimates of each of the integrals in the numerators and denominators of Eqs. (2.57) and the remainder term $\mathscr{E}$ Eq. (2.46) are obtained. At the end of each active cycle, the functionals in Eqs. (2.57) and the terms $L_{1,j}$ and $L_{2,j}$ in Eqs. (2.47) are calculated. Eqs. (2.58) are solved to obtain the FMC cycle-wise estimates of Φ_j and k. The FMC cycle-wise estimates of Φ_j are averaged over spatial cells. This information can be used to update the Monte Carlo fission source distribution.

It remains to evaluate the G_j function defined in Eq. (2.44). A detailed procedure to accomplish this is described next.

2.3.2 Procedure for Evaluating the G_j function

We recall from Section 2.3.1, the G_j function is defined as:

$$G_j = \frac{1}{\Sigma^R_{tr,j}} \left[\phi_2(x_{j+1/2}) - \phi_2(x_j)\right] + \frac{1}{\Sigma^L_{tr,j+1}} \left[\phi_2(x_{j+1}) - \phi_2(x_{j+1/2})\right] \ , \tag{2.59}$$

where x_j and x_{j+1} are staggered grid points, $x_{j+1/2}$ is the spatial grid point (Figure 2.10). Let $h^R_j = x_{j+1/2} - x_j$, $\quad h^L_{j+1} = x_{j+1} - x_{j+1/2}$, and $\Delta_j = h^R_j + h^L_{j+1}$. For region $[x_j,\, x_{j+1/2}]$, the cross section is assumed to be constant and is written as Σ^R_j, while for region $[x_{j+1/2},\, x_{j+1}]$, the cross section is assumed to be constant and is written as Σ^L_{j+1}.

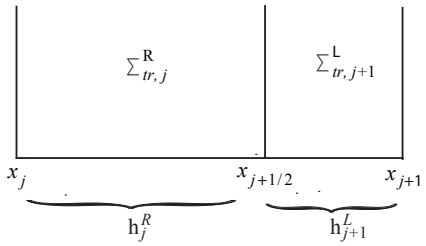

Figure 2.10 G_j function is defined on two neighboring staggered grid points.

We want to rewrite G_j in Eq. (2.59) so as to eliminate $\phi_2(x_{j+1/2})$. The second moment

$\phi_2(x)$ can be approximated using linear interpolation:

$$\phi_2(x) \approx \phi_2(x_j)\frac{(x_{j+1}-x)}{\Delta_j} + \phi_2(x_{j+1})\frac{(x-x_j)}{\Delta_j} \ .$$

Pursuing this approximation, we define E_j to satisfy the following equation:

$$\phi_2(x_{j+1/2}) = \phi_2(x_j)\frac{h^L_{j+1}}{\Delta_j} + \phi_2(x_{j+1})\frac{h^R_j}{\Delta_j} + E_j \ , \tag{2.60}$$

then $E_j = O(\Delta_j^2)$.

Next, using Eq. (2.60) to eliminate $\phi_2(x_{j+1/2})$ from Eq. (2.59), we obtain:

$$\begin{aligned}
G_j &= \frac{1}{\Sigma^L_{tr,j+1}}\phi_2(x_{j+1}) - \frac{1}{\Sigma^R_{tr,j}}\phi_2(x_j) + \left(\frac{1}{\Sigma^R_{tr,j}} - \frac{1}{\Sigma^L_{tr,j+1}}\right)\phi_2(x_{j+1/2}) \\
&= \frac{1}{\Sigma^L_{tr,j+1}}\phi_2(x_{j+1}) - \frac{1}{\Sigma^R_{tr,j}}\phi_2(x_j) + \left(\frac{1}{\Sigma^R_{tr,j}} - \frac{1}{\Sigma^L_{tr,j+1}}\right)\left[\phi_2(x_j)\frac{h^L_{j+1}}{\Delta_j} + \phi_2(x_{j+1})\frac{h^R_j}{\Delta_j} + E_j\right] \\
&= \phi_2(x_{j+1})\left[\frac{1}{\Sigma^L_{tr,j+1}} + \left(\frac{1}{\Sigma^R_{tr,j}} - \frac{1}{\Sigma^L_{tr,j+1}}\right)\frac{h^R_j}{\Delta_j}\right] - \phi_2(x_j)\left[\frac{1}{\Sigma^R_{tr,j}} - \left(\frac{1}{\Sigma^R_{tr,j}} - \frac{1}{\Sigma^L_{tr,j+1}}\right)\frac{h^L_{j+1}}{\Delta_j}\right] \\
&\qquad + \left(\frac{1}{\Sigma^R_{tr,j}} - \frac{1}{\Sigma^L_{tr,j+1}}\right)E_j \\
&= \phi_2(x_{j+1})\left[\frac{h^L_{j+1}}{\Sigma^L_{tr,j+1}} + \frac{h^R_j}{\Sigma^R_{tr,j}}\right]\frac{1}{\Delta_j} - \phi_2(x_j)\left[\frac{h^R_j}{\Sigma^R_{tr,j}} + \frac{h^L_{j+1}}{\Sigma^L_{tr,j+1}}\right]\frac{1}{\Delta_j} + \left(\frac{1}{\Sigma^R_{tr,j}} - \frac{1}{\Sigma^L_{tr,j+1}}\right)E_j \ .
\end{aligned} \tag{2.61}$$

To simplify Eq. (2.61), we define

$$\begin{aligned}
\frac{1}{\overline{\Sigma}_{tr,j}} &= \left(\frac{h^R_j}{\Sigma^R_{tr,j}} + \frac{h^L_{j+1}}{\Sigma^L_{tr,j+1}}\right)\frac{1}{h^R_j + h^L_{j+1}} \\
&= \left(\frac{h^R_j}{\Sigma^R_{tr,j}} + \frac{h^L_{j+1}}{\Sigma^L_{tr,j+1}}\right)\frac{1}{\Delta_j} \ .
\end{aligned} \tag{2.62}$$

Thus, Eq. (2.61) becomes

$$G_j = \frac{1}{\overline{\Sigma}_{tr,j}} \left[\phi_2(x_{j+1}) - \phi_2(x_j)\right] + \left(\frac{1}{\Sigma^R_{tr,j}} - \frac{1}{\Sigma^L_{tr,j+1}}\right) E_j \,. \tag{2.63}$$

Let:

$$\mathscr{E}_j = \left(\frac{1}{\Sigma^R_{tr,j}} - \frac{1}{\Sigma^L_{tr,j+1}}\right) E_j = \text{remainder term.} \tag{2.64}$$

Rewriting the remainder term and combining it with the first term in Eq. (2.63), we get

$$\begin{aligned}
G_j &= \frac{1}{\overline{\Sigma}_{tr,j}} \left[\phi_2(x_{j+1}) - \phi_2(x_j)\right] + \mathscr{E}_j \\
&= \frac{1}{\overline{\Sigma}_{tr,j}} \left[\phi_2(x_{j+1}) - \phi_2(x_j)\right] + \frac{1}{2}\left(|\mathscr{E}_j| + \mathscr{E}_j\right) - \frac{1}{2}\left(|\mathscr{E}_j| - \mathscr{E}_j\right) \\
&= \left[\frac{1}{\overline{\Sigma}_{tr,j}}\phi_2(x_{j+1}) + \frac{1}{2}\left(|\mathscr{E}_j| + \mathscr{E}_j\right)\right] - \left[\frac{1}{\overline{\Sigma}_{tr,j}}\phi_2(x_j) + \frac{1}{2}\left(|\mathscr{E}_j| - \mathscr{E}_j\right)\right] \\
&= \left[\frac{1}{\overline{\Sigma}_{tr,j}} + \frac{1}{2}\frac{|\mathscr{E}_j| + \mathscr{E}_j}{\phi_2(x_{j+1})}\right]\phi_2(x_{j+1}) - \left[\frac{1}{\overline{\Sigma}_{tr,j}} + \frac{1}{2}\frac{|\mathscr{E}_j| - \mathscr{E}_j}{\phi_2(x_j)}\right]\phi_2(x_j) \,,
\end{aligned} \tag{2.65}$$

where $\frac{1}{2}\left(|\mathscr{E}_j| + \mathscr{E}_j\right) \geq 0$ and $\frac{1}{2}\left(|\mathscr{E}_j| - \mathscr{E}_j\right) \geq 0$.

We further define

$$\begin{aligned}
L_{1,j} &= \frac{1}{\overline{\Sigma}_{tr,j}} + \frac{1}{2}\frac{|\mathscr{E}_j| + \mathscr{E}_j}{\phi_2(x_{j+1})} \\
L_{2,j} &= \frac{1}{\overline{\Sigma}_{tr,j}} + \frac{1}{2}\frac{|\mathscr{E}_j| - \mathscr{E}_j}{\phi_2(x_{j+1})} \,,
\end{aligned} \tag{2.66}$$

which yields

$$G_j = L_{1,j}\phi_2(x_{j+1}) - L_{2,j}\phi_2(x_j) \,. \tag{2.67}$$

Note that if $\mathscr{E}_j > 0$,

$$\begin{aligned}
\frac{1}{2}\frac{|\mathscr{E}_j| + \mathscr{E}_j}{\phi_2(x_{j+1})} &= \frac{\mathscr{E}_j}{\phi_2(x_{j+1})} \\
&= \frac{1}{\phi_2(x_{j+1})}\left(\frac{1}{\Sigma^R_{tr,j}} - \frac{1}{\Sigma^L_{tr,j+1}}\right) E_j \\
&= \left(\frac{1}{\Sigma^R_{tr,j}} - \frac{1}{\Sigma^L_{tr,j+1}}\right) \frac{1}{\phi_2(x_{j+1})} \left[\phi_2(x_{j+1/2}) - \phi_2(x_j)\frac{h^L_{j+1}}{\Delta_j} - \phi_2(x_{j+1})\frac{h^R_j}{\Delta_j}\right] \\
&= \left(\frac{1}{\Sigma^R_{tr,j}} - \frac{1}{\Sigma^L_{tr,j+1}}\right) \left[\frac{\phi_2(x_{j+1/2})}{\phi_2(x_{j+1})} - \frac{\phi_2(x_j)}{\phi_2(x_{j+1})}\frac{h^L_{j+1}}{\Delta_j} - \frac{h^R_j}{\Delta_j}\right] .
\end{aligned}$$

In this way, we show how the remainder term $\mathscr{E}_j$ and the $L_{1,j}, L_{2,j}$ in Eq. (2.66) are evaluated using MC simulation.

2.4 MC Fission Source with FMC feedback

A longstanding problem for Monte Carlo criticality calculations is the slow convergence of the fission source distribution for systems with a high dominance ratio (DR). Since the resulting FMC eigenfunction estimates from the low-order equations are more accurate than the standard MC estimates, the MC fission source distribution can be improved by utilization of the FMC fission source distribution. We now list the steps involved in the straightforward feedback algorithm.

1. Calculate the fraction of fission source distribution occurring in each cell j,

$$P_j = \frac{\nu\Sigma_{f,j}\phi_j}{\sum_{j'=1}^{J} \nu\Sigma_{f,j'}\phi_{j'}} \qquad \text{for} \quad 1 \le j \le J \ ,$$

   where ϕ_j is the resulting eigenfunction estimate for cell j from the low-order FMC equations.

2. The expected number of fission neutrons in cell j can then be calculated as

$$n_j = \text{total number of neutrons/cycle} * P_j \ .$$

3. Finally, we adjust the number of fission neutrons in cell j according to the following ratio

$$r_j = \frac{\text{expected number of fission neutrons } n_j}{\text{actual number of MC fission neutrons in cell } j} .$$

We do this by randomly deleting particles in cell j if there are too many, or randomly duplicating in the cell if there are too few.

2.5 Analog Monte Carlo method

2.5.1 Path Length Estimator and Related Functions Tally

The Monte Carlo method can be used to solve the transport equation by following each of many MC particles from its birth to its death. We can then obtain the information of interest by tabulating the average behavior of the simulated particles. Quantities we are interested in here are the scalar flux and FMC nonlinear functionals. The most widely used method for estimating the scalar flux is the path length estimator. For each MC particle, we record the path lengths of its tracks from its birth to its death. The scalar flux is defined as the mean path length generated per MC particle per unit volume, i.e. the scalar flux is in units of per MC particle per unit area:

$$\phi = \frac{1}{VN} \sum_{n=1}^{N} \Big(\sum_{j=1}^{N_n} l_{n,j} \Big) , \tag{2.68}$$

where V is the volume of tallied region, N is the total number of simulated MC particles, N_n is the total number of track lengths generated by the n^{th} history, and $l_{n,j}$ is the j^{th} path length tracked by the n^{th} history in tallied region V.

To evaluate FMC nonlinear functionals, we need to estimate integrals of the type

$$\int_{x_{j-1/2}}^{x_{j+1/2}} (ax+b)\phi(x)dx . \tag{2.69}$$

To do this, let x_s be a MC particle initial position and x_e be the ending position within the tallied region $[x_{j-1/2}, x_{j+1/2}]$. Then the path length the MC particle traverses equals $l = |(x_e - x_s)/\mu|$, where μ is the direction cosine of the MC particle. The integrals of type $\int_{x_{j-1/2}}^{x_{j+1/2}} (ax+b)\phi(x)dx$ can be evaluated as the average of $\hat{l}$:

$$\int_{x_{j-1/2}}^{x_{j+1/2}} (ax+b)\phi(x)dx = \frac{1}{N}\sum \hat{l}\,, \tag{2.70}$$

where

$$\begin{aligned}\hat{l} &= \frac{1}{\mu}\int_{x_s}^{x_e} (ax+b)dx \\ &= \frac{1}{\mu}(x_e - x_s)\big[\frac{1}{2}a(x_s+x_e)+b\big] \\ &= \big[\frac{1}{2}a(x_s+x_e)+b\big]l\,. \end{aligned} \tag{2.71}$$

2.5.2 Surface Crossing Estimator

The scalar flux on a planar surface at depth x can be evaluated as

$$\phi(x) = \frac{1}{N}\sum_{n=1}^{N}\big(\sum_{j=1}^{N_n}\frac{1}{|\mu_{n,j}|}\big) \tag{2.72}$$

where

$\mu_{n,j}$ = direction cosine of the n^{th} particle, the j^{th} time it crosses the surface at depth x;

N_n = number of times the n^{th} particle crosses the surface at depth x.

The surface flux also has the unit of per particle per unit area.

The second moment can be evaluated as

$$\begin{aligned}\phi_2(x) &= \frac{1}{N}\sum_{n=1}^{N}\big(\sum_{j=1}^{N_n}\frac{1}{|\mu_{n,j}|}|\mu_{n,j}|^2\big) \\ &= \frac{1}{N}\sum_{n=1}^{N}\big(\sum_{j=1}^{N_n}|\mu_{n,j}|\big)\,. \end{aligned} \tag{2.73}$$

2.5.3 Estimators for the k-eigenvalue

The following information is required to set up a criticality calculation using Monte Carlo simulation [27]:

1. initial guesses of k_{eff} and the initial fission source distribution;
2. number of histories N per k_{eff} cycle (generation);
3. the number of inactive cycles;
4. the number of active cycles M.

With the initial guess for the fission source distribution, N Monte Carlo particles are simulated. Both eigenvalue and eigenfunction are estimated, and the fission sites for the next cycle are generated. This iterative process is continued until all active cycles are completed. The criticality eigenvalue for any active cycle is estimated using the following three estimators.

k-eigenvalue definition

k_{eff} is estimated using its definition:

$$k_{eff} = \frac{\text{number of fission neutrons in generation } \ i+1}{\text{number of fission neutrons in generation } \ i} \ . \tag{2.74}$$

Path Length Estimator

The rate of fission neutron production is given by

$$\int_V \nu\Sigma_f(x)\phi(x)dx \ . \tag{2.75}$$

Thus the path length estimator of k_{eff} can be accumulated when a MC particle traverses a distance l in a fissionable material region with fission cross section Σ_f:

$$k_{eff} = \frac{1}{N} \sum_{n=1}^{N} \nu\Sigma_f \, l \, . \tag{2.76}$$

Collision Estimator

The collision estimator of k_{eff} takes account the collisions which occur. It is a summation of the probability of fission occurring over all collisions.

$$\begin{aligned} k_{eff} &= \frac{1}{N} \sum_{n=1}^{N} \frac{\nu\Sigma_f}{\Sigma_s + \Sigma_\gamma + \Sigma_f} \\ &= \frac{1}{N} \sum_{n=1}^{N} \frac{\nu\Sigma_f}{\Sigma_t} \, . \end{aligned} \tag{2.77}$$

2.5.4 Mean, Variance and Relative Standard Deviation

The Monte Carlo estimate of the mean value (*sample mean*) is calculated as

$$\bar{x} = \frac{1}{M} \sum_{i=1}^{M} x_i \, , \tag{2.78}$$

where x_i is the estimated value for the i^{th} active cycle and M is the total active cycles simulated in the problem.

The unbiased Monte Carlo *estimate of variance* of the x values can be estimated as

$$\sigma_x^2 = \frac{\sum_{i=1}^{M} (x_i - \bar{x})^2}{M - 1} \, . \tag{2.79}$$

The Monte Carlo *estimate of variance of the sample mean* $\bar{x}$ is given by

$$\begin{aligned}\sigma_{\bar{x}}^2 &= \frac{1}{M}\sigma_x^2 \\ &= \frac{1}{M}\frac{\sum_{i=1}^{M}(x_i-\bar{x})^2}{M-1} \,.\end{aligned} \tag{2.80}$$

The square root of the variance is called the *standard deviation*. We define the *relative standard deviation* of x values as

$$\sigma_{rel} = \frac{\sigma_x}{\bar{x}} \,, \tag{2.81}$$

and the *relative standard deviation of the sample mean* $\bar{x}$ as

$$\begin{aligned}\mathrm{RSD} &= \frac{\sigma_{\bar{x}}}{\bar{x}} \\ &= \frac{1}{\sqrt{M}}\frac{\sigma_x}{\bar{x}} \,.\end{aligned} \tag{2.82}$$

The relative standard deviation in population σ_{rel} is a dimensionless quantity, while the relative standard deviation of sample mean RSD is inversely proportional to $\sqrt{M}$. In this thesis, the *sample mean* and the *relative standard deviation of the sample mean* are compared in eigenvalue and eigenfunction calculations for all different methods.

For a single MC run with M active cycles, the *apparent relative standard deviation of the sample mean* (apparent RSD) is obtained using Eqs. (2.80) and (2.82). The *true relative standard deviation of the sample mean* (true RSD) is estimated from L independent MC runs (with the same M active cycles, and different random number seeds). We then obtain L estimates of the value of $\bar{x}$. The estimated true RSD of $\bar{x}$ is obtained using equations analogous to Eqs. (2.79) and (2.81):

$$\sigma_{\bar{x}}^2(\mathrm{true}) = \frac{1}{L-1}\sum_{i=1}^{L}((\bar{x})_i - \bar{\bar{x}})^2 \,, \tag{2.83}$$

and

$$\sigma_{rel}(\text{true}) = \frac{\sigma_{\bar{x}}(\text{true})}{\bar{\bar{x}}} \ . \tag{2.84}$$

$L = 25$ independent MC runs are used in obtaining the estimated true RSD. The central limit theorem states that we can use the normal distribution to approximate the sampling distribution of the sample mean. For the uniform, normal, and exponential population distributions, the sample distribution of the sample mean tends to become very nearly normal for sample size as small as $L = 25$.

Due to inter-cycle correlation, the MC estimates of the apparent relative standard deviation of the eigenfuntion are much smaller than the MC estimates of the true relative standard deviations. This is particularly true for problems with high dominance ratios.

2.5.5 Shannon Entropy

The Shannon entropy [29; 30; 28] of a source distribution is defined as

$$H = -\sum_{j=1}^{J} P_j \ln(P_j) \tag{2.85}$$

where P_j is the source fraction in region j.

Shannon entropy can be used as an index to judge whether the fission source distribution has converged. (The Shannon entropy fluctuates when equilibrium of the fission source distribution has not been achieved, but becomes nearly constant when the fission source is converged.)

Chapter 3

Monoenergetic k-Eigenvalue Problems: Numerical Results

In this Chapter, we numerically test the FMC method as described in Chapter 2 on four problems for which the standard Monte Carlo method is problematic. These problems were chosen to highlight the strengths and the weaknesses of the FMC method.

3.1 Monoenergetic Problem 1: A Large, Homogeneous Fissile Region

First, we consider the relatively straightforward problem of a large homogeneous fissile region surrounded by a thin reflector. The physical data is given in Table 3.1.

Table 3.1 Data for Problem 1.

Region	Location	Σ_t	$\Sigma_{s,0}$	$\Sigma_{s,n}$	$\nu\Sigma_f$
1	$0 < x < 5$	1.0	0.856	0.1	0
2	$5 < x < 205$	1.0	0.856	0.1	0.144
3	$205 < x < 210$	1.0	0.856	0.1	0

Here x has units of cm, Σ has units of cm^{-1}, in column 5 of the data Table 3.1 $n = 1,2,3$, and $\Sigma_{s,n} = 0$ for $n \geq 4$. We consider anisotropic P_3 scattering. The exact eigenfunction of Problem 1 has a basic "cosine" shape in the central fissile region. Our fine-mesh S_N solution of this problem, which used the S_{32} Gauss-Legendre quadrature set with $h = 0.01$, produced $k = 0.999384$. The dominance ratio (DR) of this problem is 0.995, which is obtained by

using the the S_{32} Gauss-Legendre quadrature set with 50 inner iterations.

3.1.1 Flat Initial Fission Source without FMC Feedback

We now present results of Problem 1 for a flat initial fission source guess and without FMC feedback. Our Monte Carlo simulations use 50,000 histories per cycle with a uniform grid $h = 1.0$.

In Figures 3.1-3.3 we display for Problem 1 the S_N eigenfunction and averaged estimates of the eigenfunction from (i) standard Monte Carlo (MC), (ii) Functional Monte Carlo using the "edge" unknowns (FMC edg), and (iii) Functional Monte Carlo using the "averaged" unknowns (FMC avg). As is indicated in the figures, these plots are obtained by averaging the Monte Carlo estimates of the eigenfunction over nine 100-cycle spans, i.e. cycles 101-200, 201-300, 301-400, 401-500, 501-600, 601-700,701-800,801-900, and 901-100.

Figures 3.1-3.3 show that the S_N and FMC estimates of the eigenfunction are virtually coincident and are much more accurate than the MC estimates. The MC eigenfunction appears to be trying to converge to the correct "cosine" shape, but it slowly "wobbles" around it. This "wobbling" is caused by undersampling of the fission source and can be suppressed by increasing the number of Monte Carlo particles per cycle.

Figure 3.4 shows the estimates of the eigenfunction, averaged over the last 500 cycles (501-1000), and the estimated apparent relative standard deviations and true relative standard deviations in the Monte Carlo, FMC edge, and FMC average scalar fluxes over the cycles. The apparent relative standard deviations are obtained from a single 1000-cycle (500 inactive cycles, and 500 active cycles) run; the true relative standard deviations are obtained from 25 independent 1000-cycle runs. A detailed procedure is given in Chapter 2, Section 2.5.4.

The figure shows that, even though it is averaged over a large number of cycles, the MC estimate of the eigenfunction is inaccurate and "tilted." The estimated relative standard deviations (both apparent and true) in the FMC eigenfunctions are smaller than those of the MC eigenfunction, and the FMC eigenfunction estimates are clearly much more accurate. A

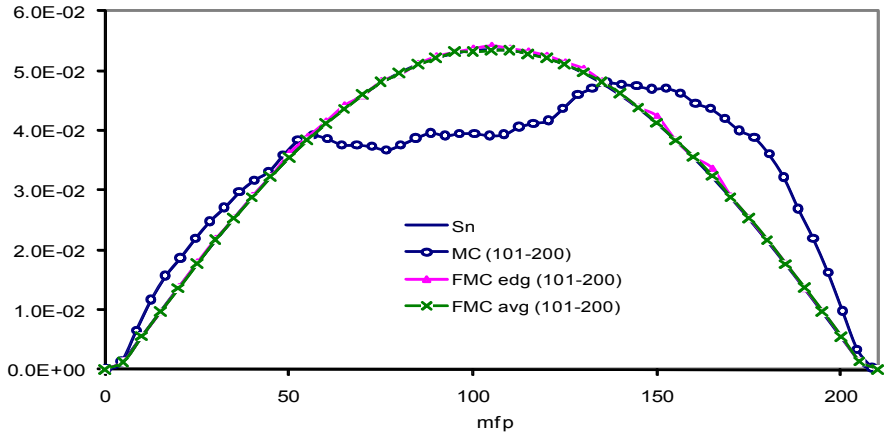

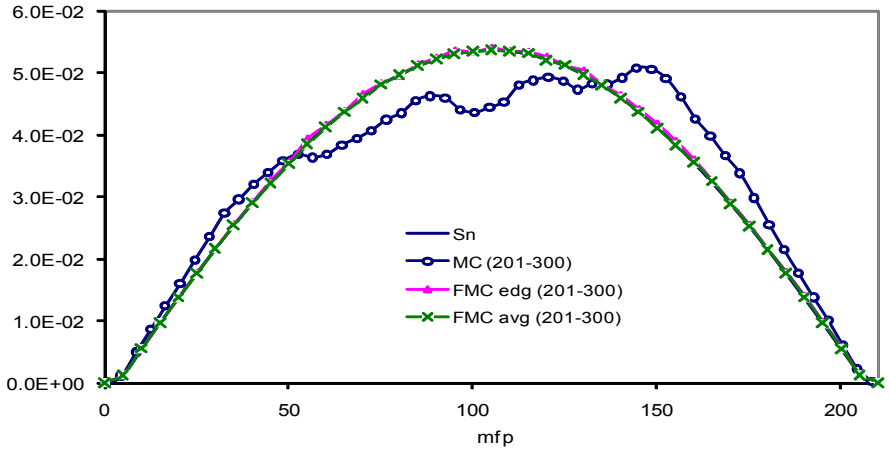

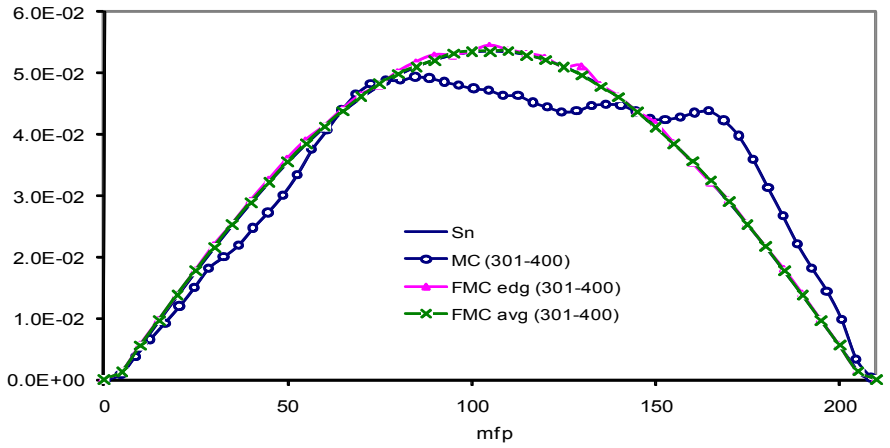

Figure 3.1 Problem 1 averaged eigenfunction estimates during cycles 101-400.

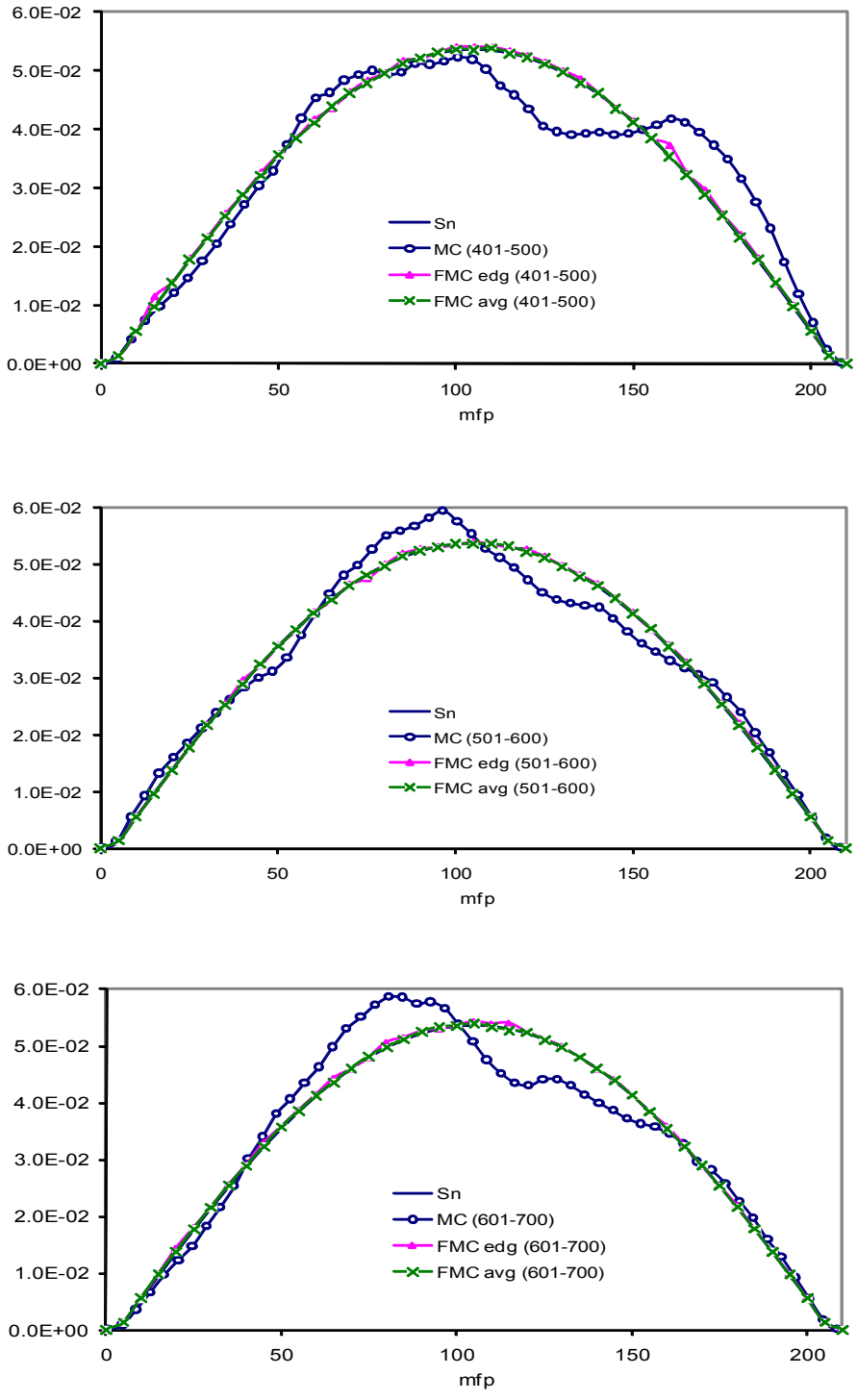

Figure 3.2 Problem 1 averaged eigenfunction estimates during cycles 401-700.

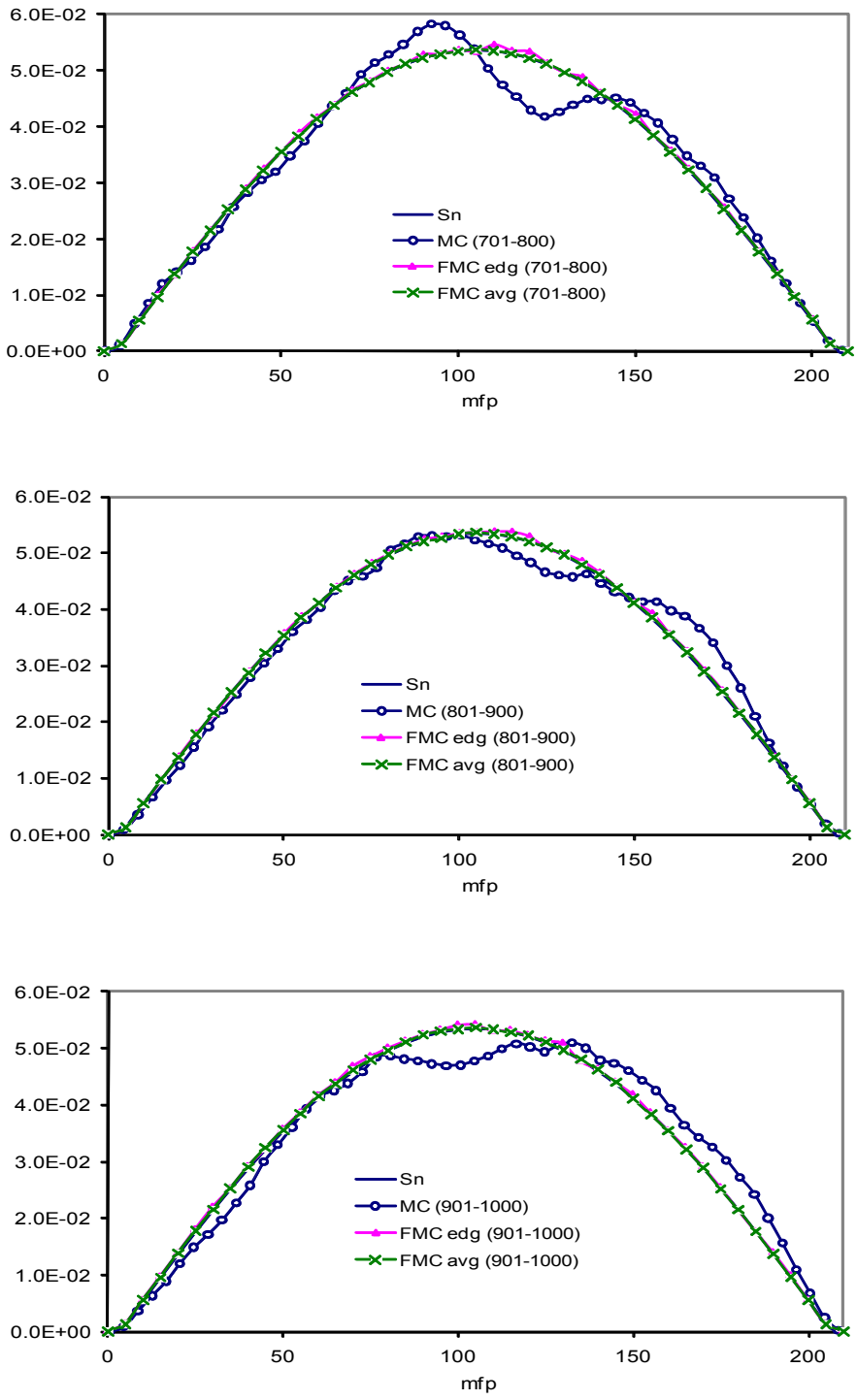

Figure 3.3 Problem 1 averaged eigenfunction estimates during cycles 701-1000.

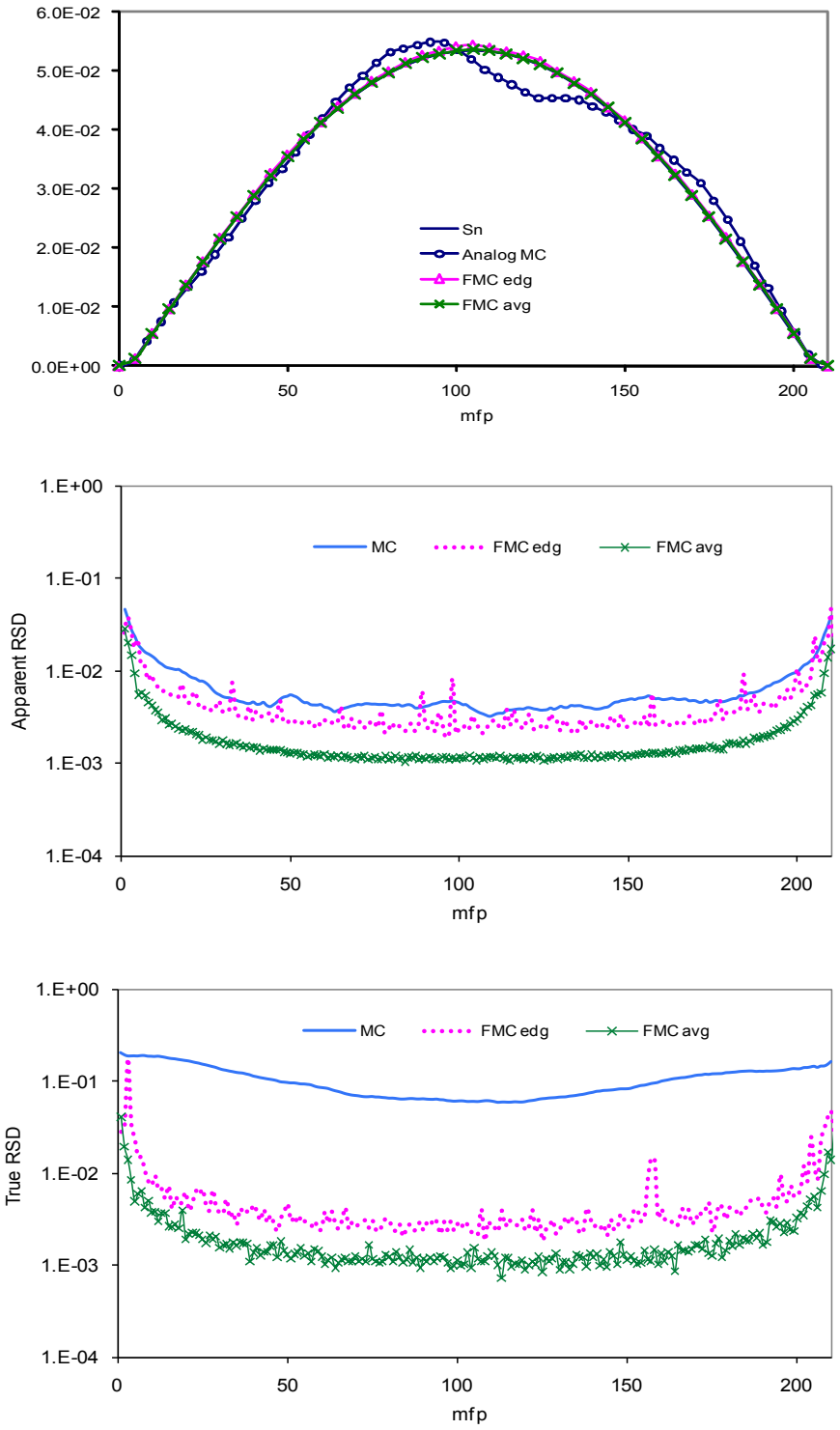

Figure 3.4 Problem 1 averaged eigenfunctions and their RSDs over 501-1000 cycles.

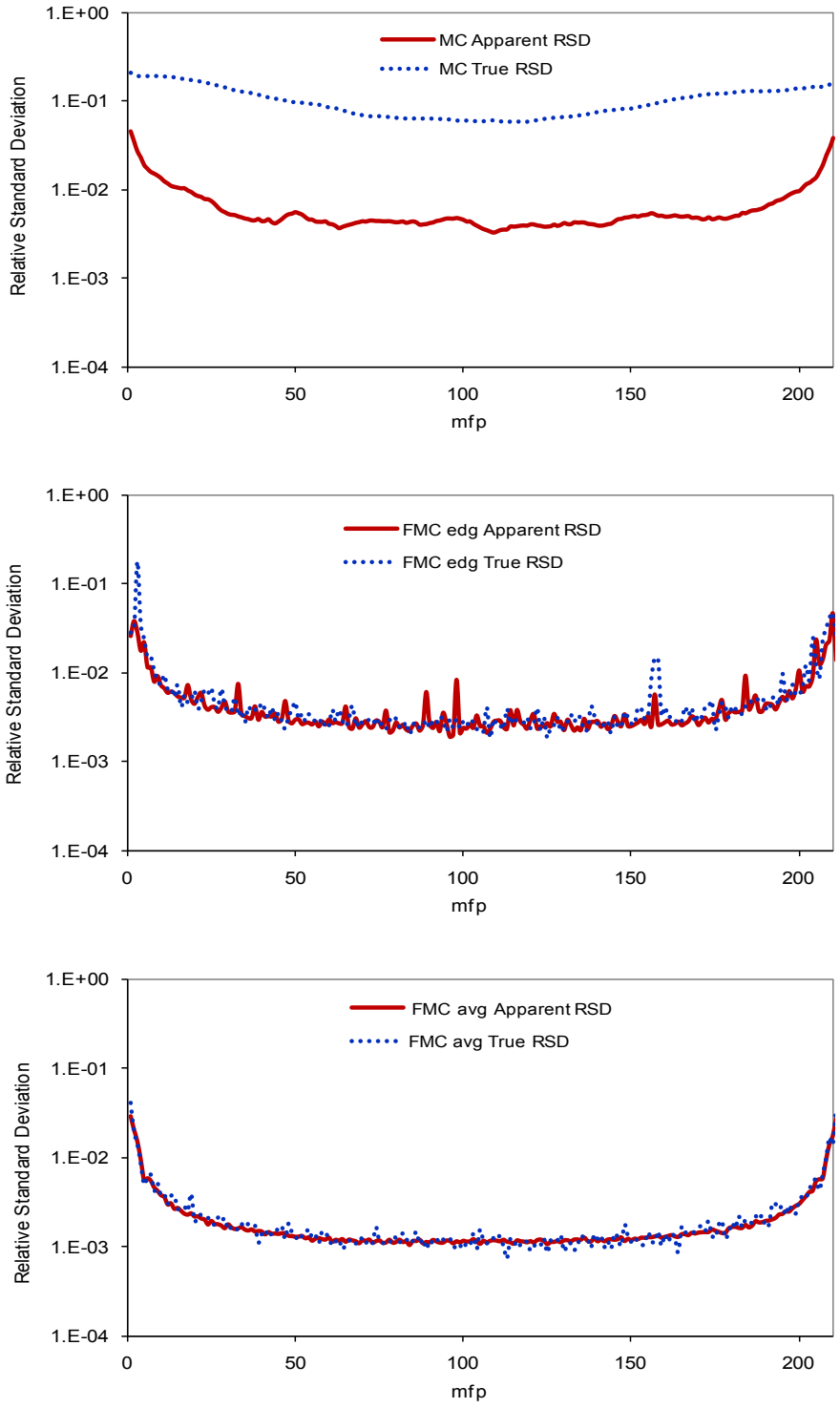

Figure 3.5 Comparison for Problem 1 of apparent RSDs and true RSDs in MC, FMC edge, and FMC average eigenfunction estimates.

detailed comparison between the apparent relative standard deviation and the true relative standard deviation in the MC, FMC edge, FMC average eigenfunction estimates is given in Figure 3.5. This figure shows that the true relative standard deviation is more than a factor of 10 greater than the apparent relative standard deviation in the MC eigenfunction estimate. This is because of the correlations in the fission source between one cycle and the next. Figure 3.5 also shows that the true relative standard deviations in FMC edge and FMC average eigenfunction estimates are approximately the same as the apparent relative standard deviations. Thus, fission source correlations do not seem to affect the FMC estimates. We conclude that the estimated relative standard deviations in the FMC eigenfunctions from a single 1000-cycle run can be trusted.

Figure 3.6 gives the apparent relative standard deviations and the true relative standard deviations in the nonlinear functionals E and A, and in the MC, FMC edge, FMC average scalar fluxes. The figure shows that the true relative standard deviations in the nonlinear functionals E and A are approximately the same as the apparent relative standard deviations. As expected, the MC estimates of the nonlinear functionals E and A are much more accurate than the direct MC estimates of the eigenfunction. Also, the relative standard deviations in the "average" FMC functionals are smaller than the relative standard deviations in the "edge" functionals.

Figures 3.7-3.8 display results for eigenfunction estimates at the 100^{th}, and 500^{th} cycles. These figures show that the MC eigenfunction estimate is noisier than the FMC "edge" eigenfunction estimate, which in turn is noisier than the FMC "average" eigenfunction estimate. These figures also show that the "average" FMC functionals are less noisy than the "edge" functionals.

We note from Figures 3.7-3.8 that for individual cycles, the MC and FMC estimates of the eigenfunction all contain high-frequency spatial errors, and from Figures 3.1-3.4 that by averaging these eigenfunction estimates over 100 or more cycles, the high-frequency errors are greatly suppressed. However, the MC eigenfunction estimates contain much

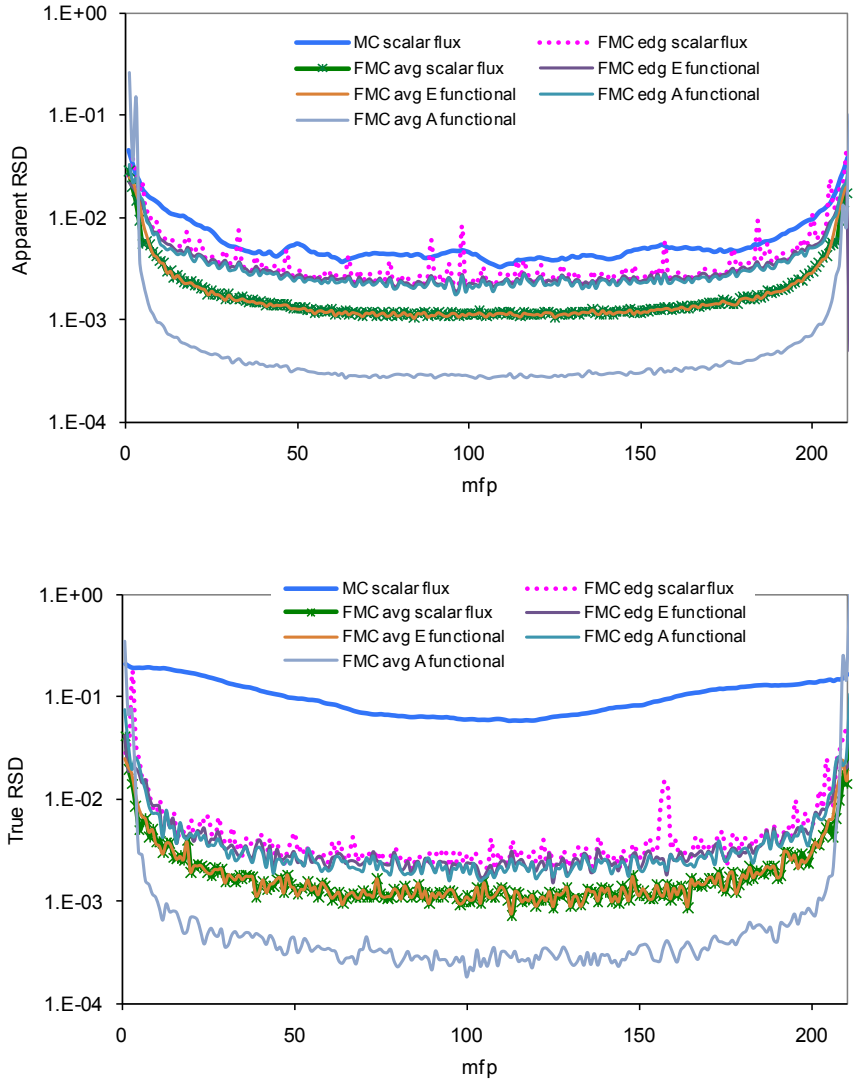

Figure 3.6 Comparison for Problem 1 of apparent RSDs and true RSDs in MC, FMC edge, FMC average scalar fluxes, and the nonlinear functionals E and A.

larger low-frequency errors than the FMC eigenfunction estimates, and these are not greatly suppressed by averaging over active cycles.

In Table 3.2 we display the estimates of the Problem 1 eigenvalue and the relative standard deviation during each of the ten 100-cycle spans that we ran.

This table shows that the FMC estimates of k are several orders of magnitude more accurate than the MC estimates; this is due to (i) the insensitivity of the nonlinear functionals to statistical errors in the flux estimates, (ii) the insensitivity of the low order FMC equations to

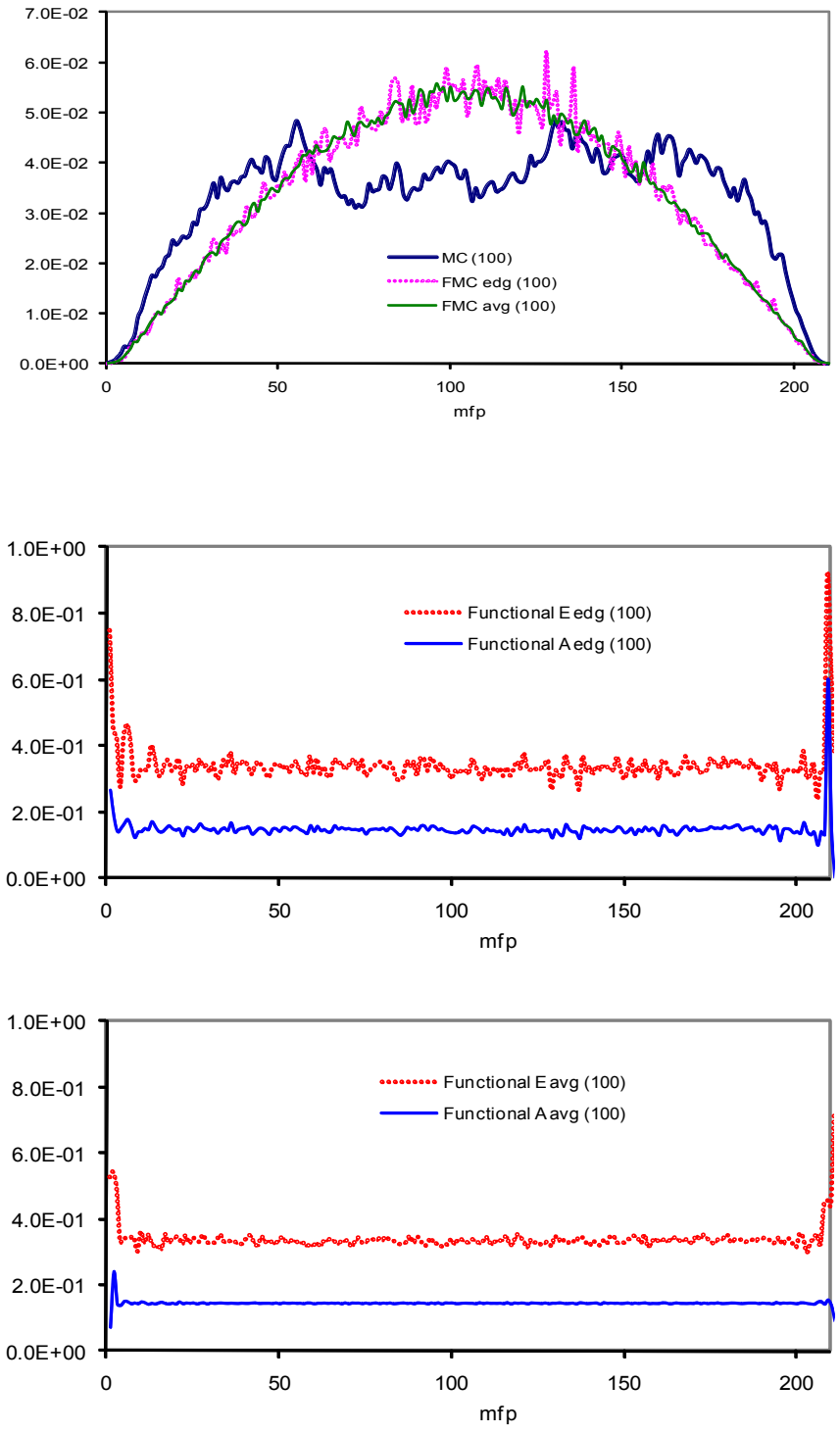

Figure 3.7 Problem 1 eigenfunction and nonlinear functional estimates for cycle 100.

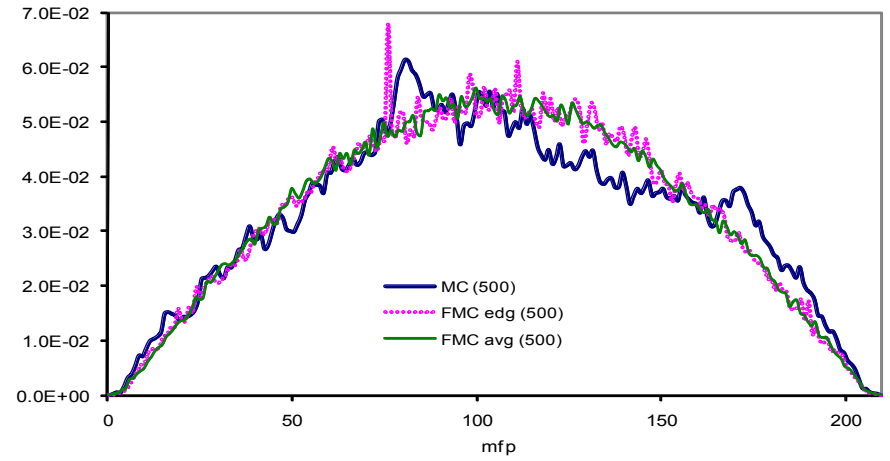

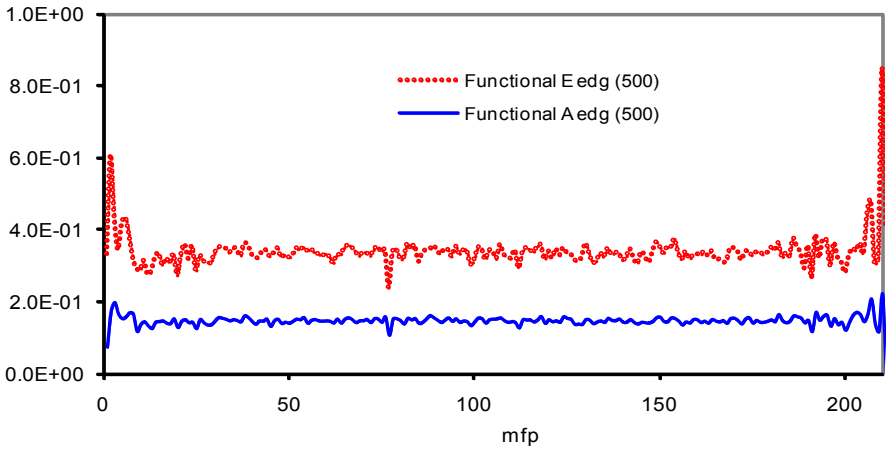

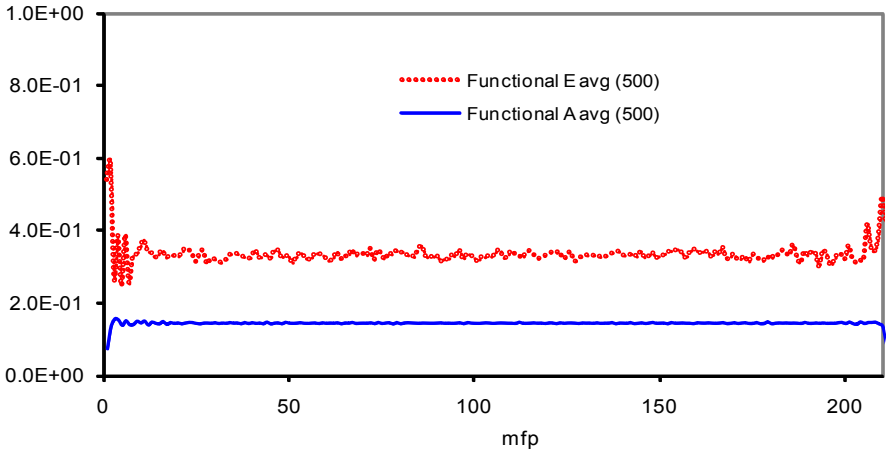

Figure 3.8 Problem 1 eigenfunction and nonlinear functional estimates for cycle 500.

Table 3.2 Estimates of k and its Relative Standard Deviation for Problem 1.

Cycles	Standard MC	FMC edge	FMC average
1-100	0.998050 (0.0007701)	0.999385 (0.0000002)	0.999385 (0.0000002)
101-200	0.998768 (0.0005659)	0.999385 (0.0000002)	0.999385 (0.0000002)
201-300	0.999546 (0.0005243)	0.999385 (0.0000002)	0.999385 (0.0000002)
301-400	0.998978 (0.0005663)	0.999385 (0.0000002)	0.999385 (0.0000002)
401-500	0.997939 (0.0005906)	0.999385 (0.0000002)	0.999385 (0.0000002)
501-600	0.998691 (0.0004900)	0.999385 (0.0000002)	0.999385 (0.0000002)
601-700	0.999997 (0.0005218)	0.999385 (0.0000002)	0.999385 (0.0000002)
701-800	0.998958 (0.0006221)	0.999385 (0.0000002)	0.999385 (0.0000002)
801-900	0.999819 (0.0005835)	0.999385 (0.0000002)	0.999385 (0.0000002)
901-1000	0.999810 (0.0005316)	0.999385 (0.0000002)	0.999385 (0.0000002)

small errors in the functionals, and (iii) the relative geometric simplicity of the problem. An unexpected result is that even though the FMC-edge eigenfunction estimate is noisier than the FMC-average eigenfunction estimates, the two eigenvalue estimates are of comparable quality.

Since the S_N solution of Problem 1 is known, we can calculate the true relative standard deviation using the "exact" (S_N) k_{eff} value. Our calculation results show that the true relative standard deviations are identical to the apparent relative standard deviations in the FMC estimates of k_{eff}. Also, the ratios of the true relative standard deviations to the apparent relative standard deviations for the MC estimates of k_{eff} for ten 100-cycle spans are given in Table 3.3. From this table, we note that the true relative standard deviations are only slightly greater than the apparent relative standard deviations (difference in the 5th digits). These ratios are approximately equal to one. Thus the Monte Carlo estimates of the eigenvalues

can be trusted.

Table 3.3 MC estimates of Relative Standard Deviation of k for Problem 1.

Cycles	True Rel. Std. Dev.	Apparent Rel. Std. Dev.	Ratio
1-100	0.0007807	0.0007701	1.0138
101-200	0.0005689	0.0005659	1.0053
201-300	0.0005246	0.0005243	1.0006
301-400	0.0005675	0.0005663	1.0021
401-500	0.0006074	0.0005906	1.0284
501-600	0.0004946	0.0004900	1.0094
601-700	0.0005257	0.0005218	1.0075
701-800	0.0006233	0.0006221	1.0019
801-900	0.0005854	0.0005835	1.0033
901-1000	0.0005335	0.0005316	1.0036

3.1.2 Flat Initial Fission Source with FMC Feedback

In Section 3.1.1, it is seen that the MC estimates of the eigenfunction do not converge to the correct "cosine" shape during a 1000 cycle test run. On the other hand, the resulting FMC eigenfunction estimates from the low-order equations are seen to converge almost immediately and remain stable in all 100-cycle spans. A more sophisticated approach to this problem is the MC simulation with FMC feedback, in which the MC fission source distribution is improved by utilization of the FMC fission source distribution. A detailed procedure is given in Chapter 2, Section 2.4.

Figure 3.9 shows estimates of the eigenfunction from standard Monte Carlo (MC) with FMC feedback, and the consequent Functional Monte Carlo (FMC avg). This figure is obtained by averaging the Monte Carlo estimates of the eigenfunction over 100-cycle spans, i.e. cycles 1-100, 101-200, and 201-300. Examining Figure 3.9 we see that Monte Carlo estimates of the eigenfunction with FMC feedback converge within the first 100-cycle average.

The Shannon entropy behavior of the fission source for Problem 1 without FMC feed-

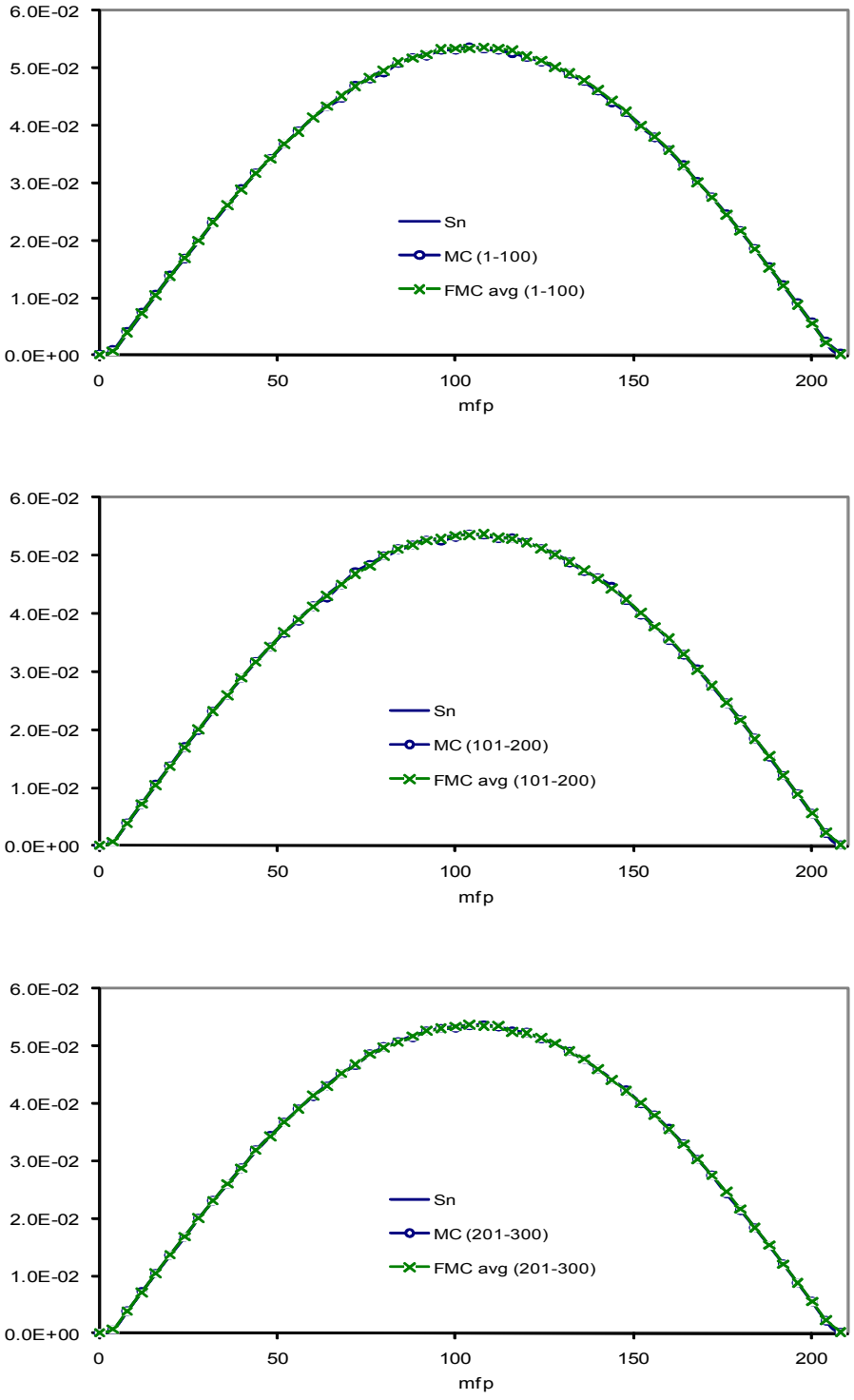

Figure 3.9 Problem 1 averaged eigenfunction estimates during cycles 1-300 with FMC feedback.

back is shown in Figure 3.10, while the Shannon entropy behavior of the fission source for Problem 1 with FMC feedback is shown in Figure 3.11. Figure 3.11 shows that the Monte Carlo estimates of the eigenfunction with FMC feedback converges almost immediately.

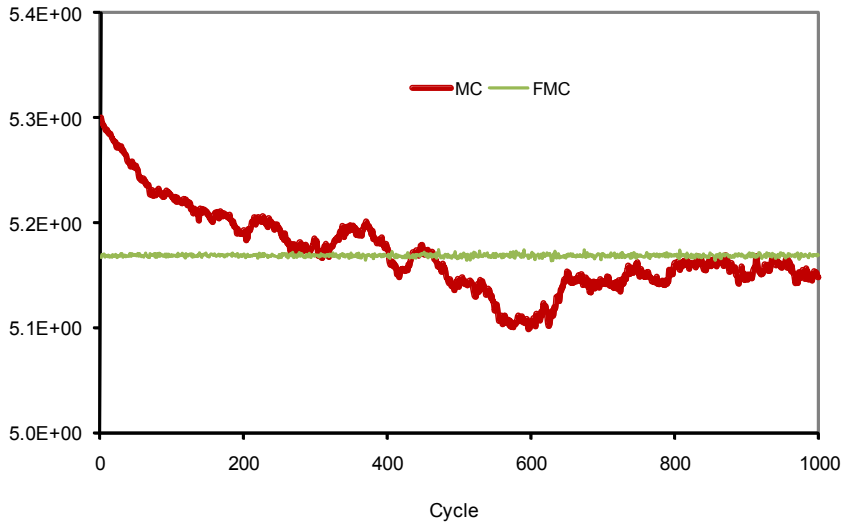

Figure 3.10 Shannon entropy behavior of the fission source for Problem 1 without FMC feedback.

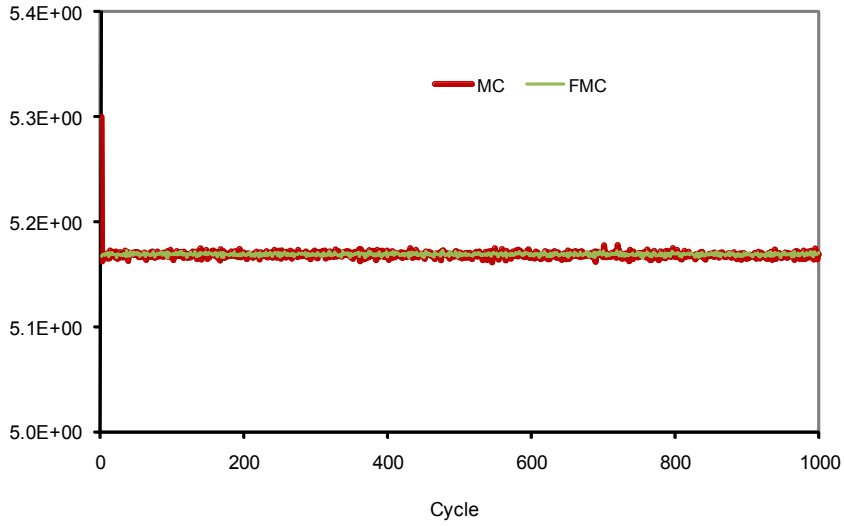

Figure 3.11 Shannon entropy behavior of the fission source for Problem 1 with FMC feedback.

With FMC feedback, the estimates of the Problem 1 eigenvalue with their estimated relative standard deviations over ten 100-cycle spans are given in Table 3.4 for the standard Monte Carlo and FMC average. We note that with FMC feedback (Table 3.4) or without

FMC feedback (Table 3.2), the estimates of the eigenvalue are identical for the FMC average simulations, and the estimates of eigenvalue agree within statistical errors for the standard Monte Carlo simulations. Therefore, the use of feedback can greatly improve the MC eigenfunction estimates, but not the MC eigenvalue estimates.

Table 3.4 Estimates of k and its Relative Standard Deviation for Problem 1 with FMC Feedback.

Cycles	Standard MC	FMC average
1-100	0.998977 (0.0007465)	0.999385 (0.0000002)
101-200	0.999337 (0.0005985)	0.999385 (0.0000002)
201-300	0.999038 (0.0006221)	0.999385 (0.0000002)
301-400	0.999360 (0.0005173)	0.999385 (0.0000002)
401-500	0.999587 (0.0005406)	0.999385 (0.0000002)
501-600	0.999293 (0.0005925)	0.999385 (0.0000002)
601-700	0.999616 (0.0005773)	0.999385 (0.0000002)
701-800	1.000814 (0.0005949)	0.999385 (0.0000002)
801-900	0.999419 (0.0005751)	0.999385 (0.0000002)
901-1000	0.999264 (0.0005360)	0.999385 (0.0000002)

3.1.3 Asymmetric Initial Fission Source, with and without FMC Feedback

Next, we further demonstrate the strengths of FMC by considering an asymmetric initial fission source guess. We assume that the initial source sample probability of the left half fissile region (5cm-105cm) is 85%, while the initial source sample probability of the right half fissile region (105cm-200cm) is 15%.

First, we run for 1000 cycles, using 50,000 histories/cyc without FMC feedback. In Figures 3.12-3.14, we compare results for the estimated flux, averaged over 100 cycle intervals (from a 1000-cycle sequence) for (a) standard Monte Carlo and (b) FMC average. Although the initial fission source is extremely asymmetric, the FMC results are seen to have only small fluctuations for the first 100-cycle average, and the fluctuations die out by the fourth 100-cycle (301-400) average. The MC results are far from the symmetric "cosine" shape for all 100 cycle averages (from a 1000-cycle sequence).

We also ran this asymmetric initial fission source problem with FMC feedback. Figure 3.15 is obtained by averaging the Monte Carlo estimates of the eigenfunction over 100-cycle spans, i.e. cycles 1-100, 101-200, and 201-300. This figure shows that the Monte Carlo estimates of the eigenfunction with FMC feedback converge within the first 100 cycle average. We investigate the convergent behavior further by averaging the Monte Carlo estimates of the eigenfunction over 10-cycle spans, i.e. cycles 1-10, 11-20, and 21-30. Figure 3.16 shows that the Monte Carlo estimates of the eigenfunction with FMC feedback converge within the second 10-cycle span.

The Shannon entropy behavior of the fission source without FMC feedback during 1000 cycles is shown in Figure 3.17, while the Shannon entropy behavior of the fission source with FMC feedback is shown in Figure 3.18. Again, the figures show that the MC estimates of the eigenfunction with FMC feedback converge almost immediately.

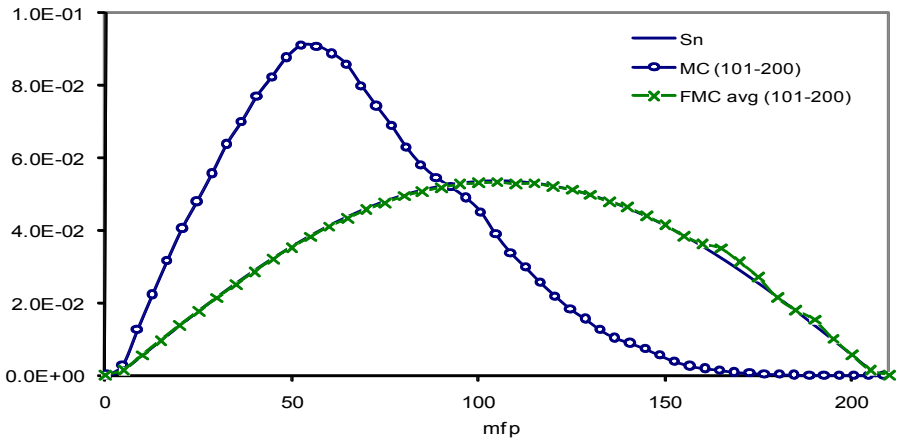

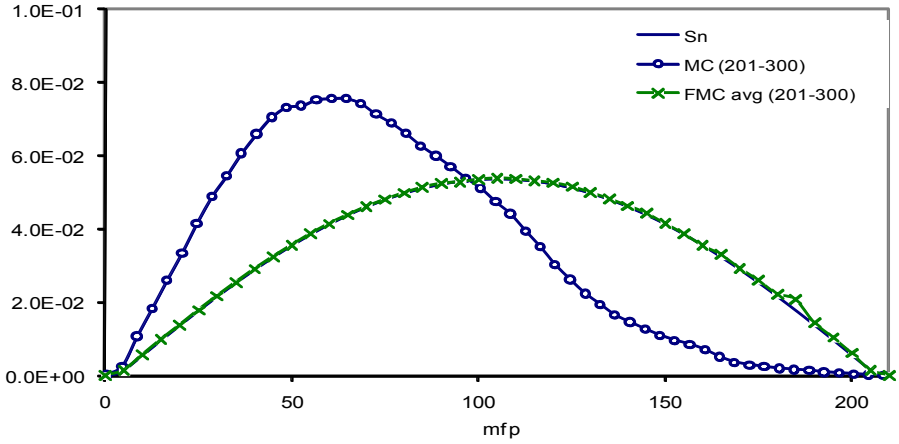

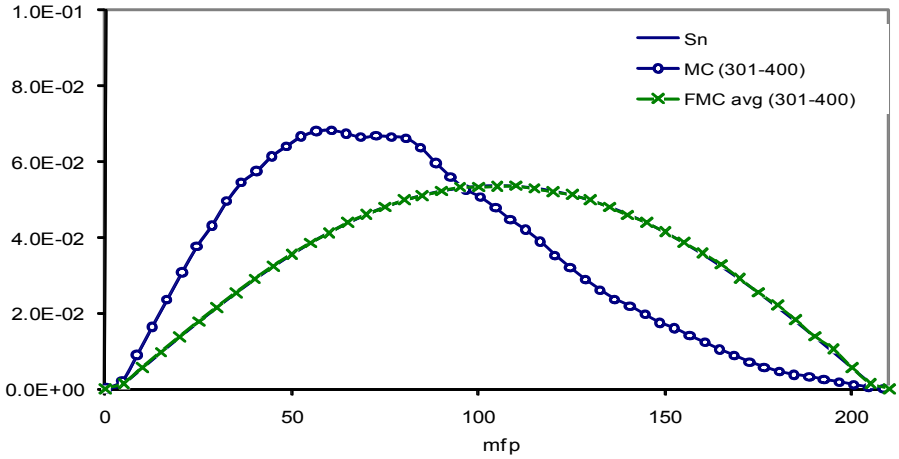

Figure 3.12 Problem 1 averaged eigenfunction estimates during cycles 101-400 for asymmetric initial fission source without FMC feedback.

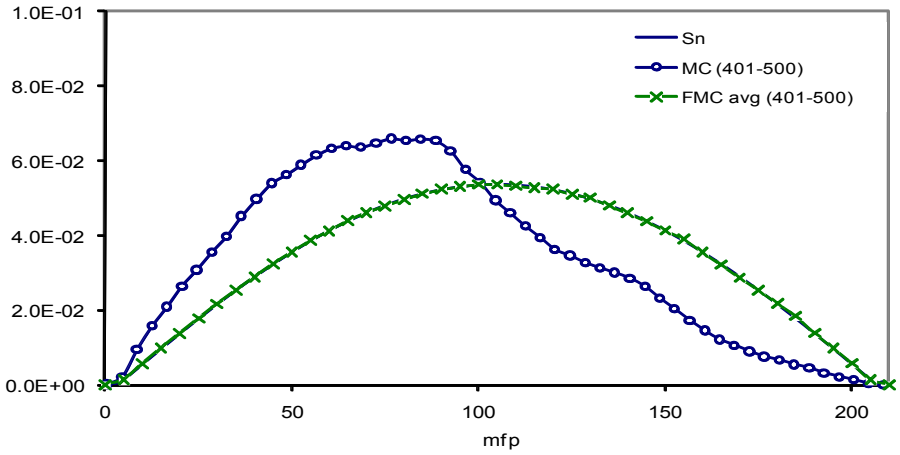

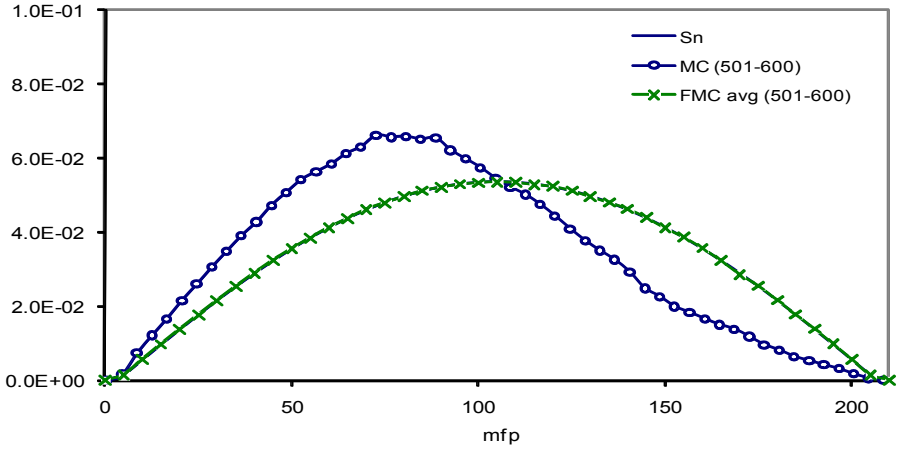

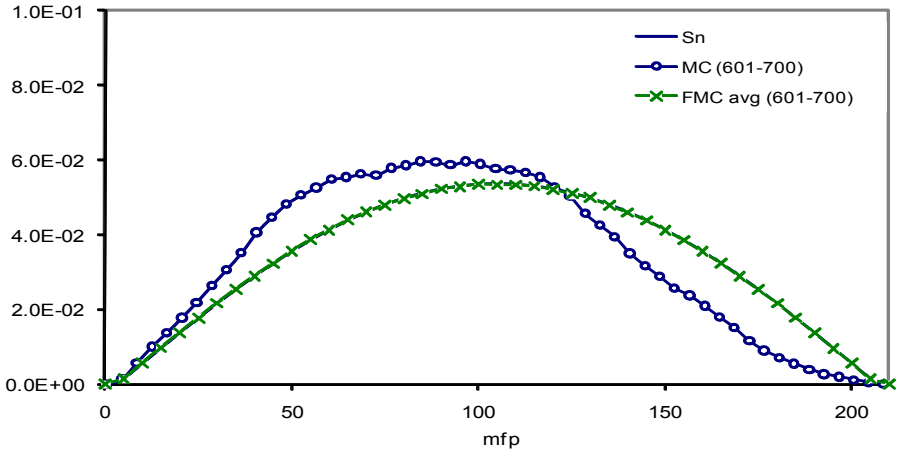

Figure 3.13 Problem 1 averaged eigenfunction estimates during cycles 401-700 for asymmetric initial fission source without FMC feedback.

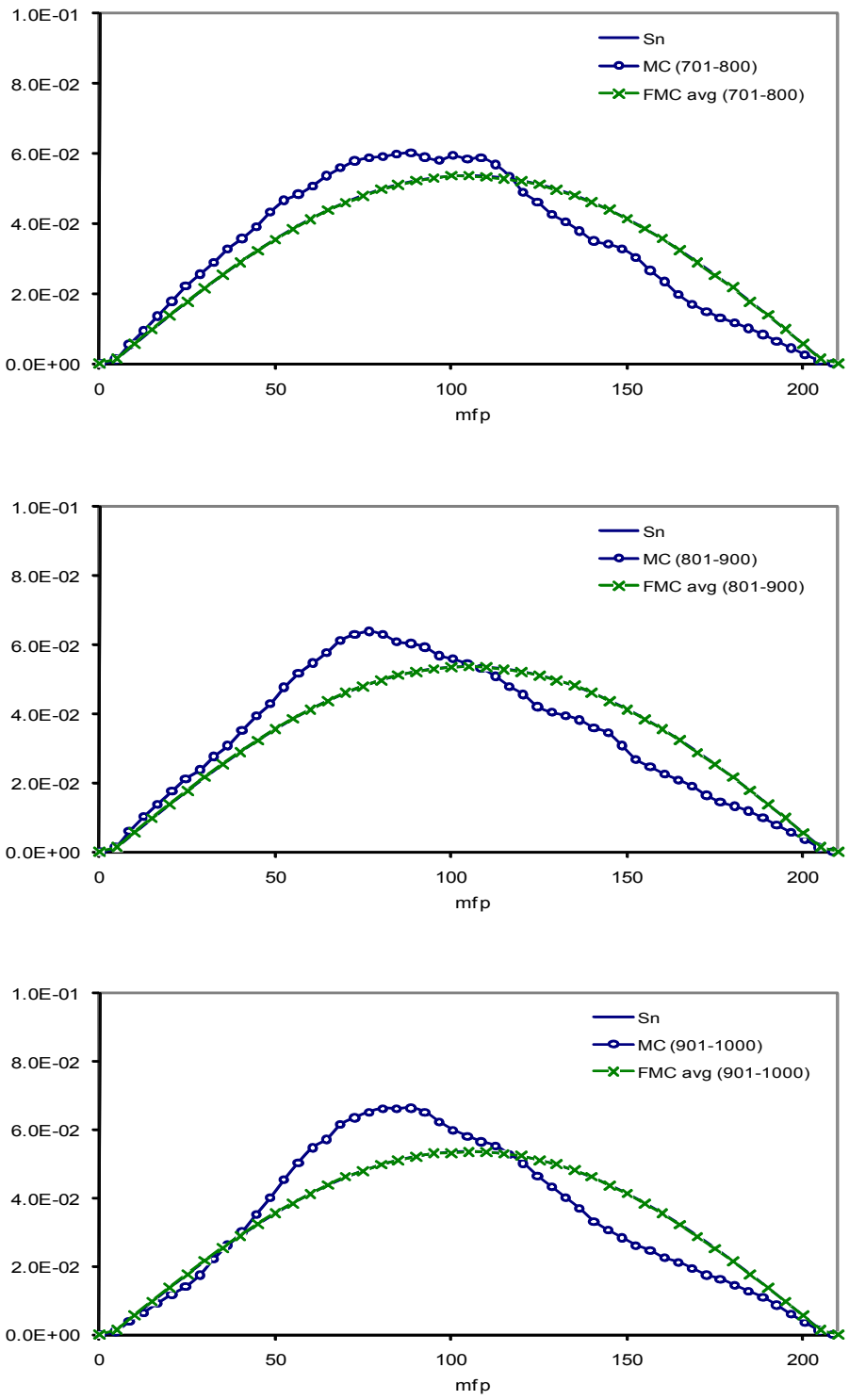

Figure 3.14 Problem 1 averaged eigenfunction estimates during cycles 701-1000 for asymmetric initial fission source without FMC feedback.

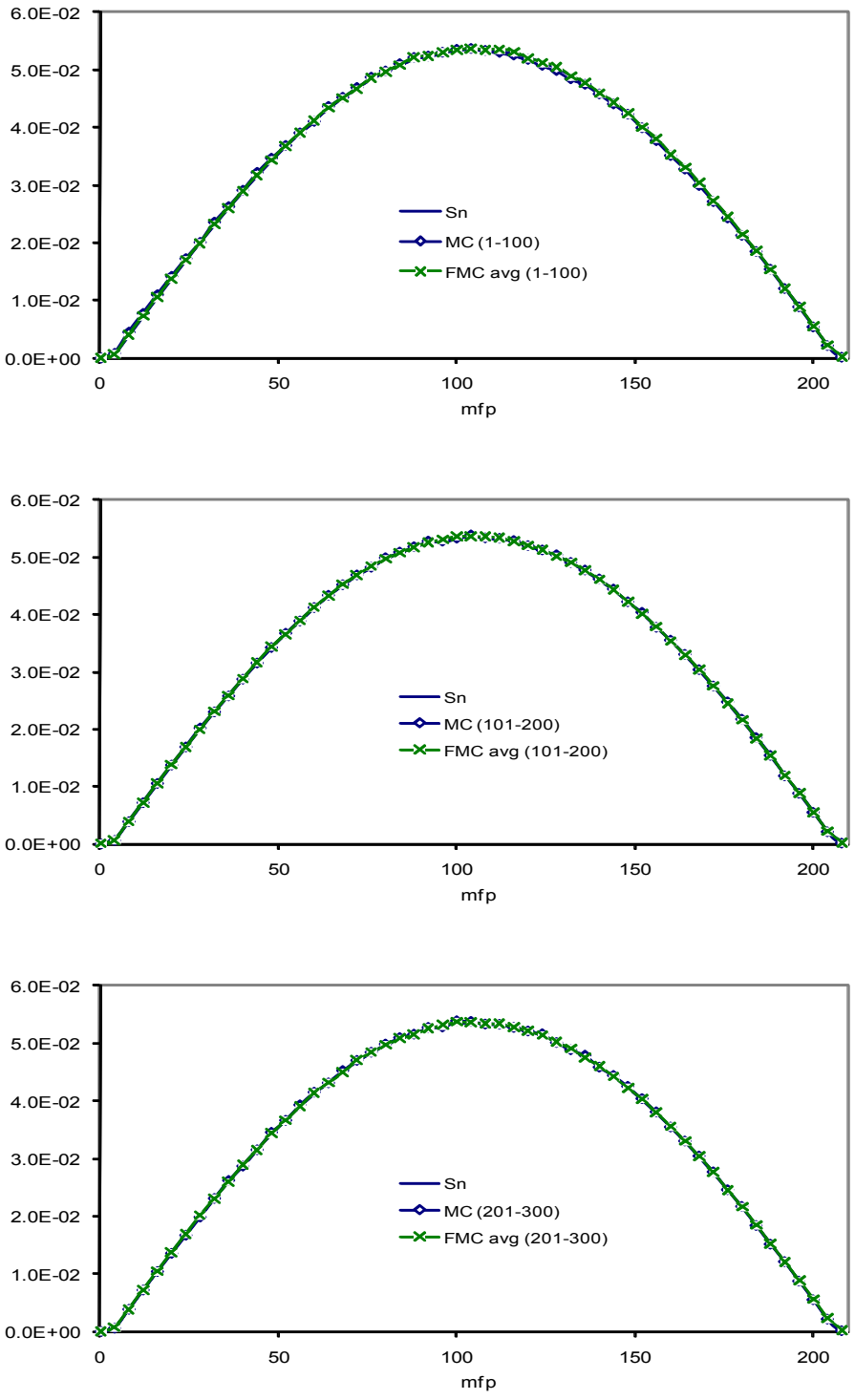

Figure 3.15 Problem 1 averaged eigenfunction estimates during cycles 1-300 for asymmetric initial fission source with FMC feedback.

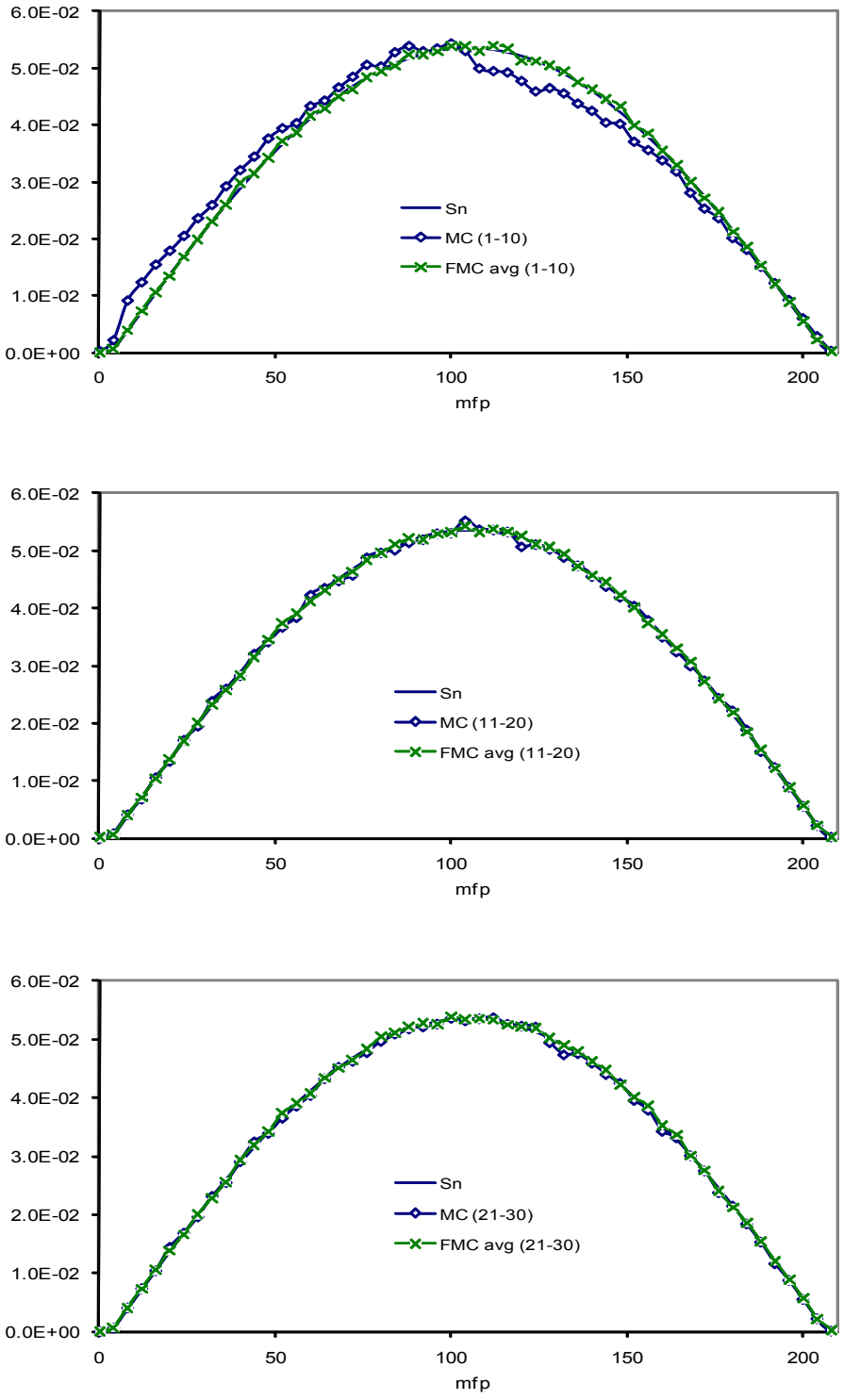

Figure 3.16 Problem 1 averaged eigenfunction estimates during cycles 1-30 for asymmetric initial fission source with FMC feedback.

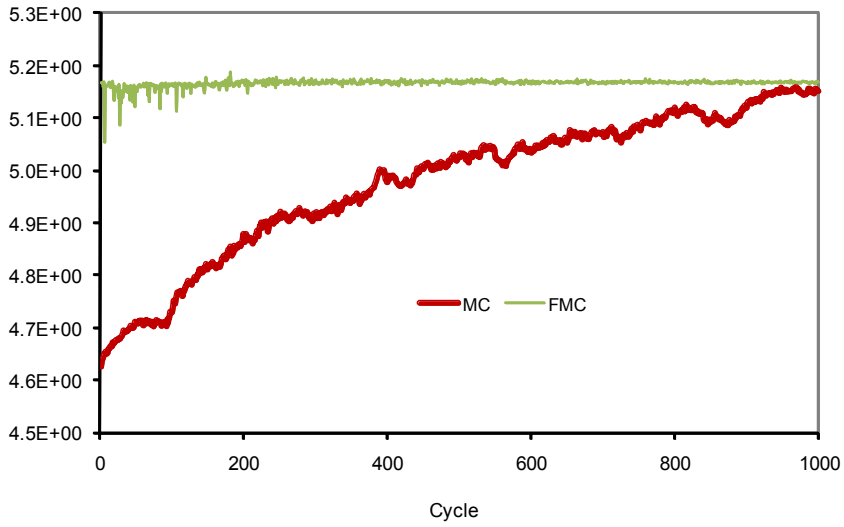

Figure 3.17 Shannon entropy behavior of the fission source in Problem 1 for asymmetric initial fission source without FMC feedback.

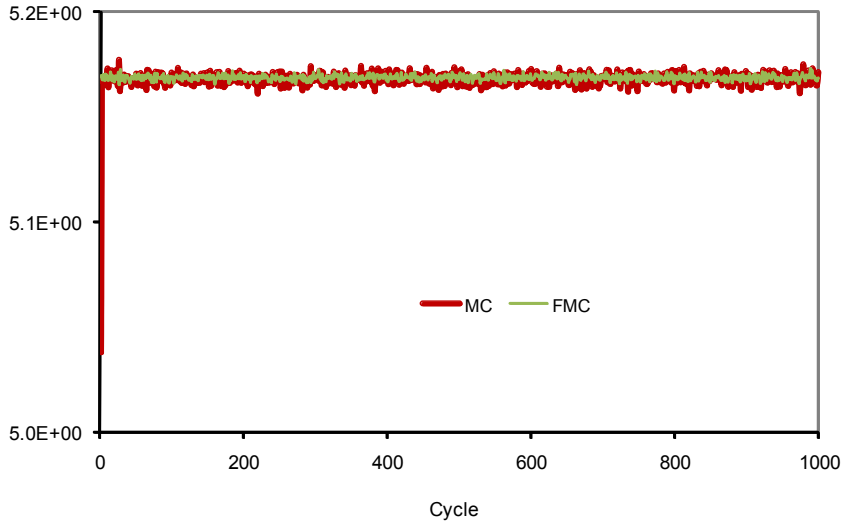

Figure 3.18 Shannon entropy behavior of the fission source in Problem 1 for asymmetric initial fission source with FMC feedback.

Next we consider two related problems, each having two slightly different fissile regions separated and surrounded by an absorbing moderator. The purpose of these problems is to examine the MC and FMC methods when fissile regions begin to decouple.

3.2 Monoenergetic Problem 2: Two Separated Fissile Regions

In Problem 2, two nearly identical 5.0 cm wide fissile regions are (i) separated by a 7-cm moderator, and (ii) surrounded by equivalent 5.0-cm moderators. This problem differs from Problem 1 because there are now two local maxima in the scalar flux (corresponding to the two separated fissile regions), and the amplitude of the scalar flux at these two maxima depends sensitively on the problem details (the width and values of $\nu\Sigma_f$ in the two fissile regions, the optical distance between the two regions, etc.). The data for this problem is given in Table 3.5.

Table 3.5 Data for Problem 2.

Region	Location	Σ_t	$\Sigma_{s,0}$	$\Sigma_{s,n}$	$\nu\Sigma_f$
1	$0 < x < 5$	1.0	0.856	0.1	0.0
2	$5 < x < 10$	1.0	0.856	0.1	0.19680
3	$10 < x < 17$	1.0	0.856	0.1	0.0
4	$17 < x < 22$	1.0	0.856	0.1	0.19764
5	$22 < x < 27$	1.0	0.856	0.1	0.0

As in Problem 1, column 5 holds for $n = 1, 2$, and 3, with $\Sigma_{s,n} = 0$ for $n \geq 4$. The entire system is 27 cm thick. The S_{32} solution, obtained with $h = 0.01$, yields $k = 0.992429$. The dominance ratio (DR) of this problem is 0.993, which is obtained by using the the S_{32} Gauss-Legendre quadrature set with 50 inner iterations. Because of the slight (0.43%) asymmetry in $\nu\Sigma_f$, the S_N eigenfunction is asymmetric about the midpoint of the system; the peak of the eigenfunction in the right (slightly more fissile) region is nearly double that in the left (slightly less fissile) region. Our Monte Carlo simulations used 100,000 histories per cycle with a uniform grid $h = 0.1$.

In Figure 3.19, we show plots obtained by averaging the MC and FMC estimates of the eigenfunction over cycles 101-200, 201-300, and 301-400. As in Problem 1, the S_N and FMC eigenfunction estimates are virtually coincident. However, the MC eigenfunction does not converge during the first 400 cycles.

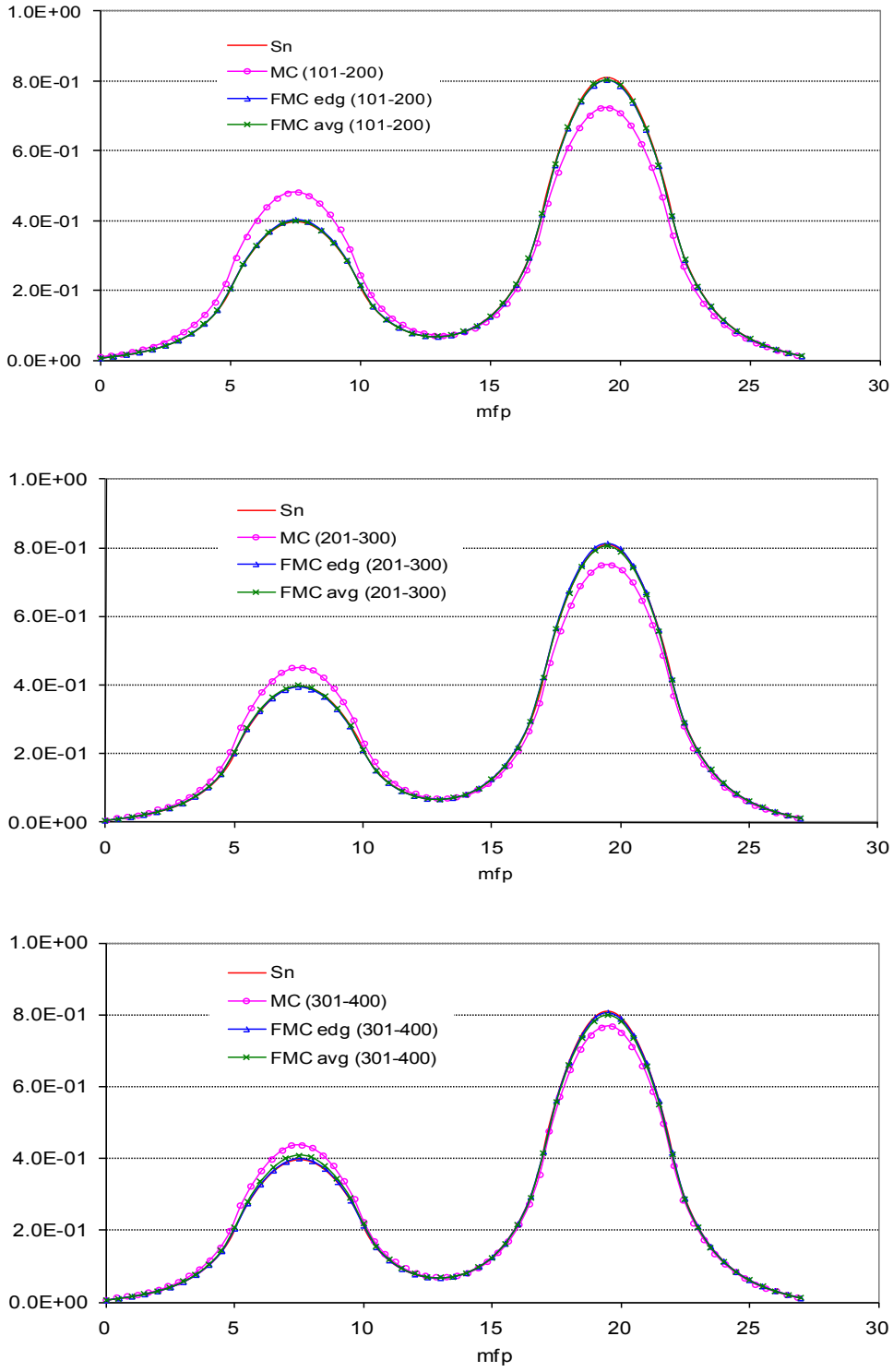

Figure 3.19 Problem 2 averaged eigenfunction estimates during cycles 101 to 400 without FMC feedback.

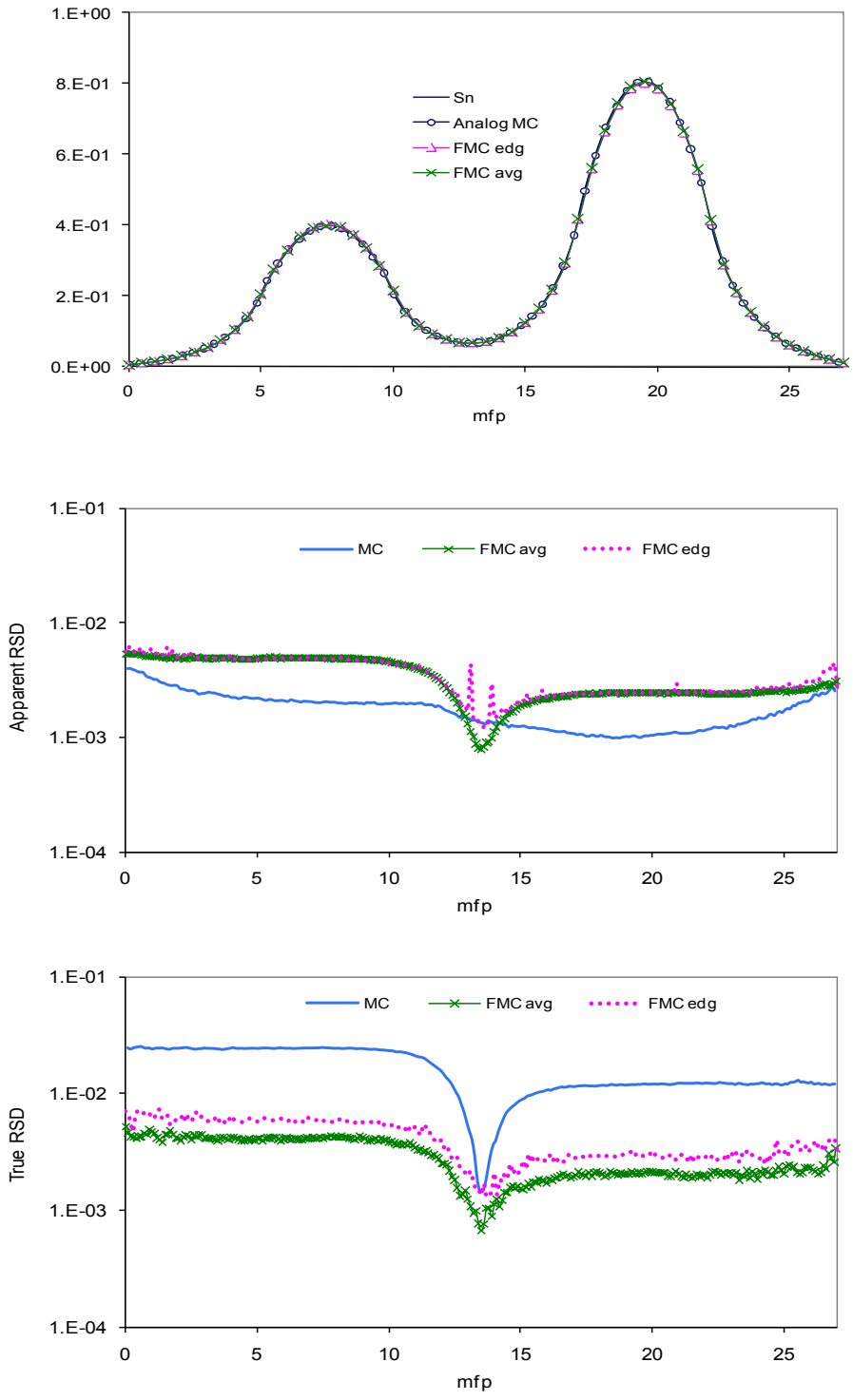

Figure 3.20 Problem 2 averaged eigenfunctions and their RSDs over 501-1000 cycles.

Figure 3.20 shows the MC estimates of the eigenfunction, averaged over 500 active cycles (501-1000), and the estimated apparent relative standard deviations and true relative standard deviations in the MC, FMC edge, and FMC average scalar fluxes over the cycles. As in Problem 1, the apparent relative standard deviations are obtained from a single 1000-cycle (500 inactive cycles, and 500 active cycles) run; the true relative standard deviations are obtained from 25 independent 1000-cycle runs. The figure shows that the apparent relative standard deviation in the MC eigenfunction estimate is smaller than the apparent relative standard deviation in the FMC eigenfunction estimates, but the true relative standard deviation in the MC eigenfunction estimate is noticeably greater than the relative standard deviation in the FMC eigenfunction estimates. A detailed comparison between the apparent relative standard deviation and the true relative standard deviation in the MC, FMC edge, FMC average eigenfunction estimates is given in Figure 3.21.

Figure 3.22 displays the apparent relative standard deviations and the true relative standard deviations in the nonlinear functionals E and A, and in the MC, FMC edge, FMC average scalar fluxes. The figure shows that the MC estimates of the nonlinear functionals E and A are much more accurate than the direct MC estimates of the eigenfunction, and the relative standard deviations in the "average" FMC functionals are smaller than the relative standard deviations in the "edge" functionals.

We show Problem 2 eigenfunction plots for individual cycles 100, 101, and 102 in Figure 3.23, and eigenfunction plots for individual cycles 500, 501, and 502 in Figure 3.24. As in Problem 1, the correlations that exist between cycles cause the MC estimate of the eigenfunction to change slowly from one cycle to the next. Because the eigenfunction is sensitive to perturbations in the cross sections (a 0.43% change in $\nu\Sigma_f$ in one region causes a factor of 2 change in the eigenfunction), the FMC estimates of the eigenfunction show considerable variation from cycle to cycle.

Figures 3.25-3.26 display information concerning eigenfunction estimates at the 100^{th}, and 500^{th} cycles. These figures show that the "average" FMC functionals are less noisy than

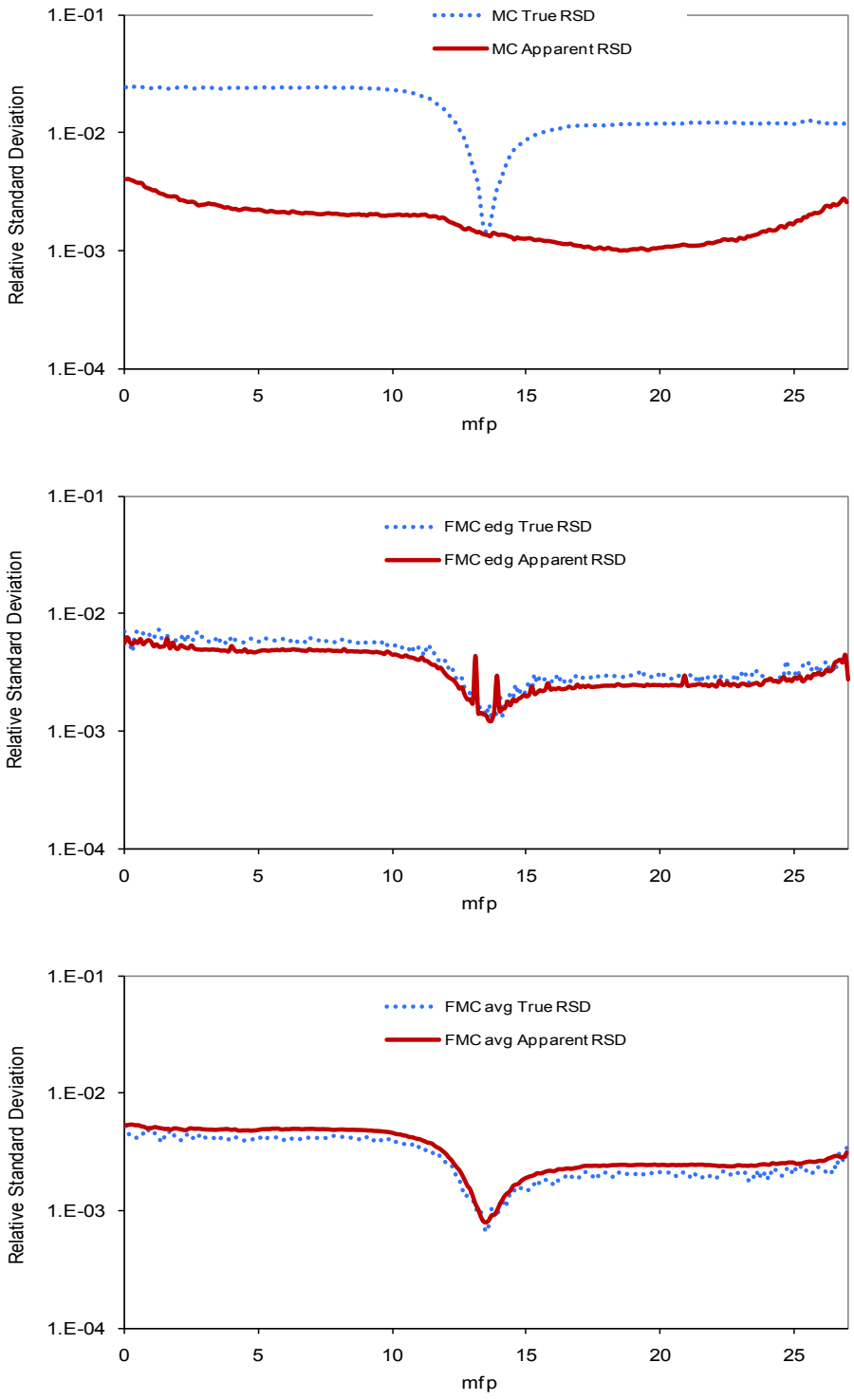

Figure 3.21 Comparison for Problem 2 of apparent RSDs and true RSDs in MC, FMC edge, and FMC average eigenfunction estimates.

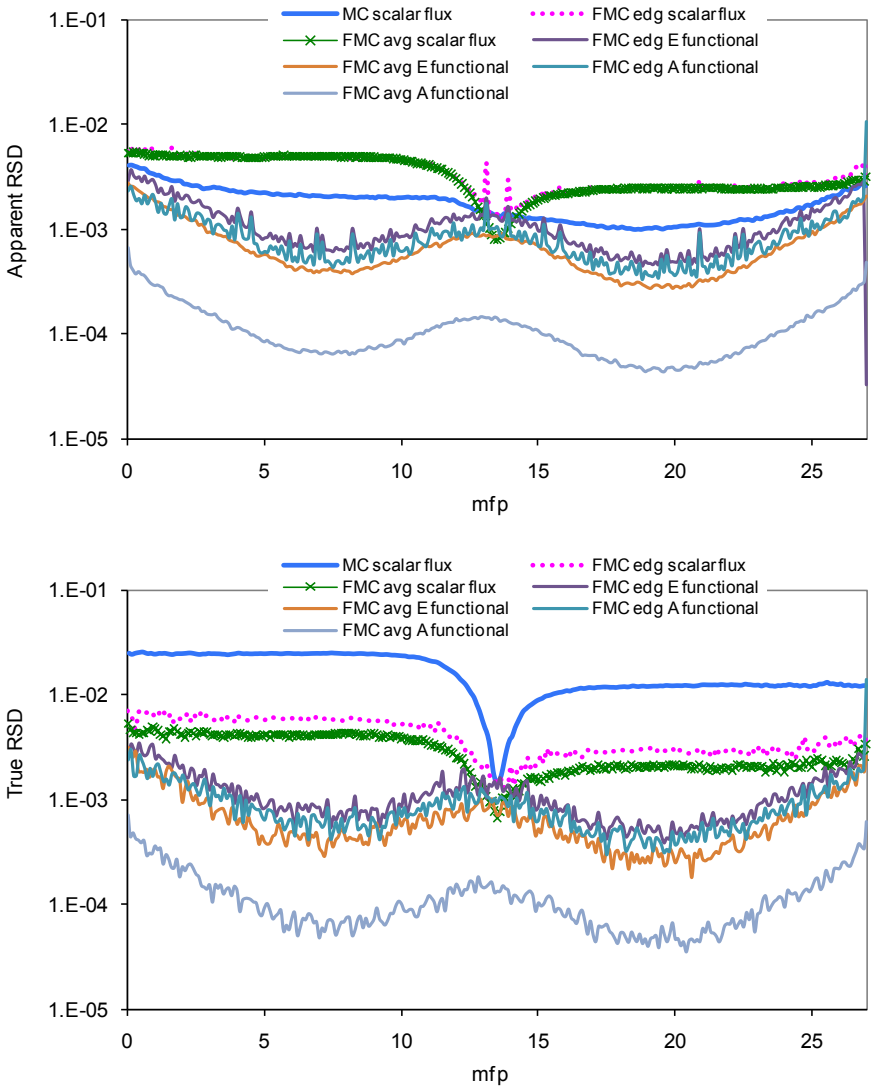

Figure 3.22 Comparison for Problem 2 of apparent RSDs and true RSDs in MC, FMC edge, FMC average scalar fluxes, and the nonlinear functionals E and A.

the "edge" functionals.

In Table 3.6, we present the estimates of the Problem 2 eigenvalue during each of the ten 100-cycle spans that we ran. This table shows that estimated relative standard deviations in the FMC estimates of k are about a factor of 6 smaller than the MC estimates. The true relative standard deviations in MC, FMC edge, FMC average (obtained by comparing to the S_N estimate) are given in Table 3.7, Table 3.8 and Table 3.9 respectively. From Table 3.7-3.9, we note that these ratios are approximately equal to one. Thus the estimated relative

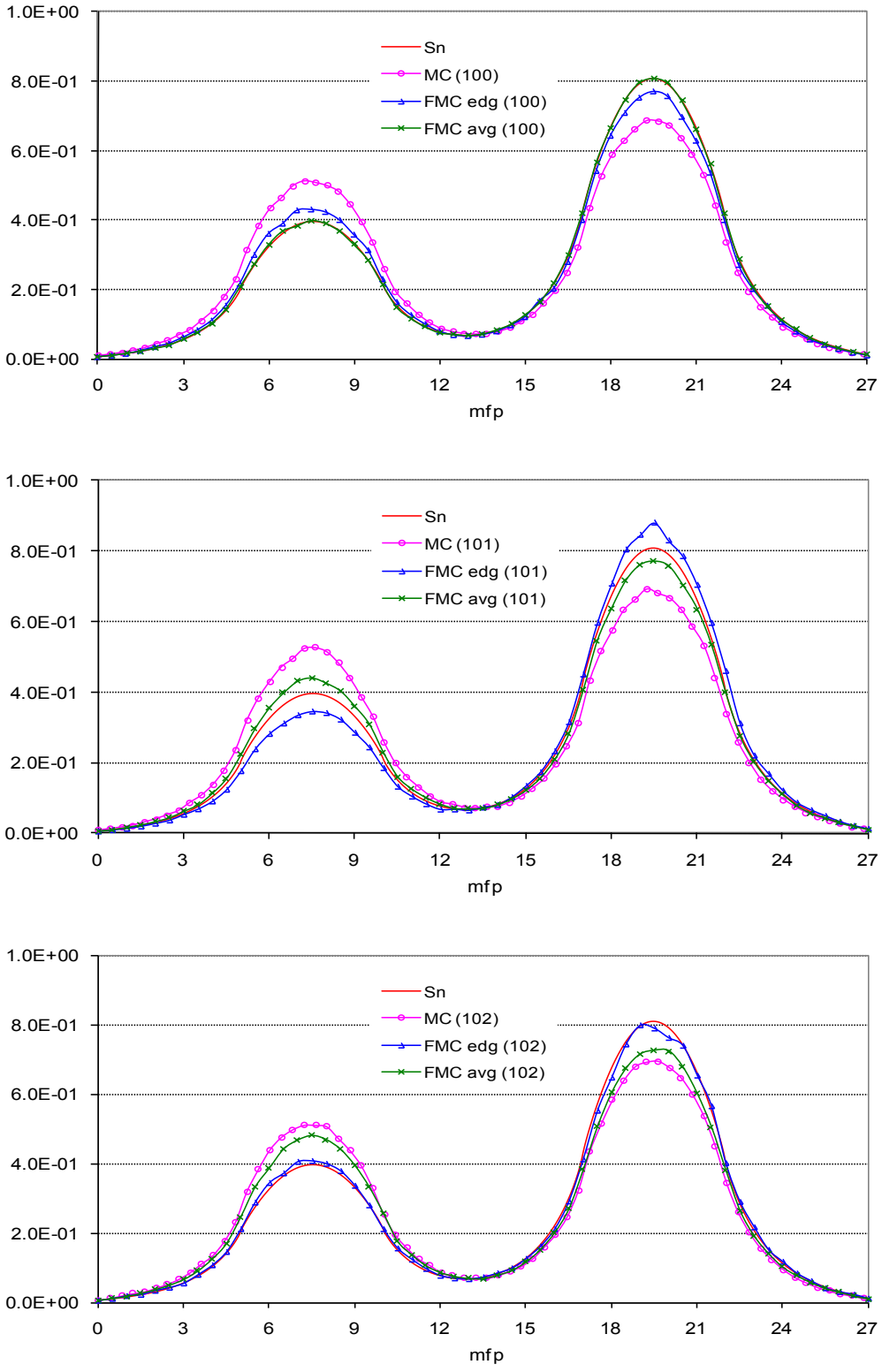

Figure 3.23 Problem 2 eigenfunction estimates for cycles 100, 101 to 102.

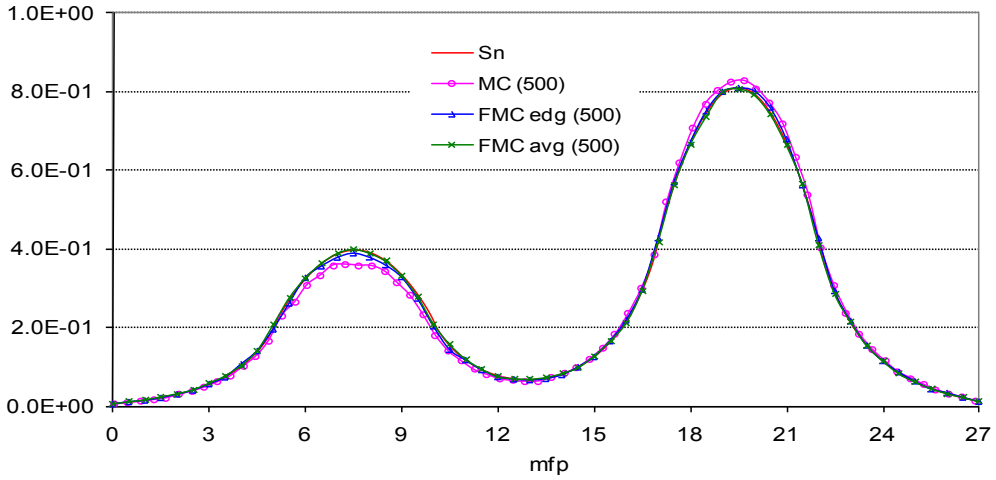

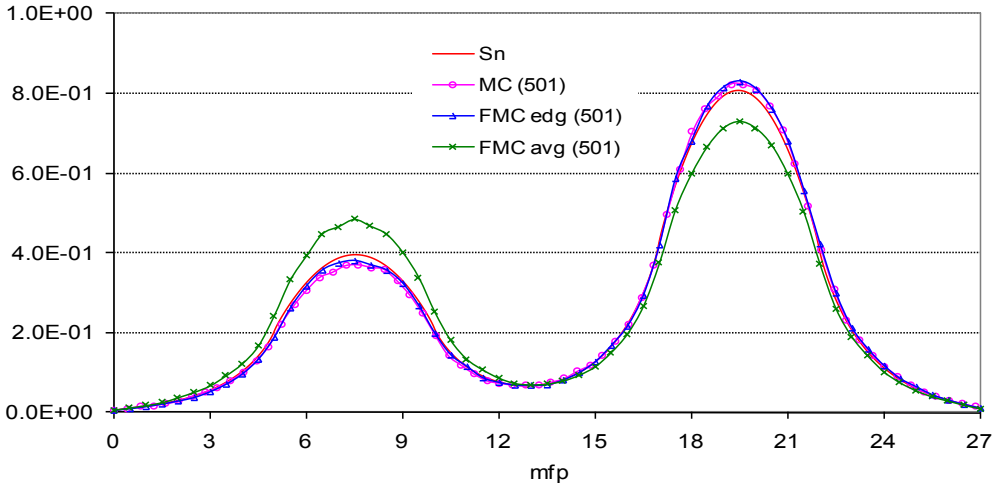

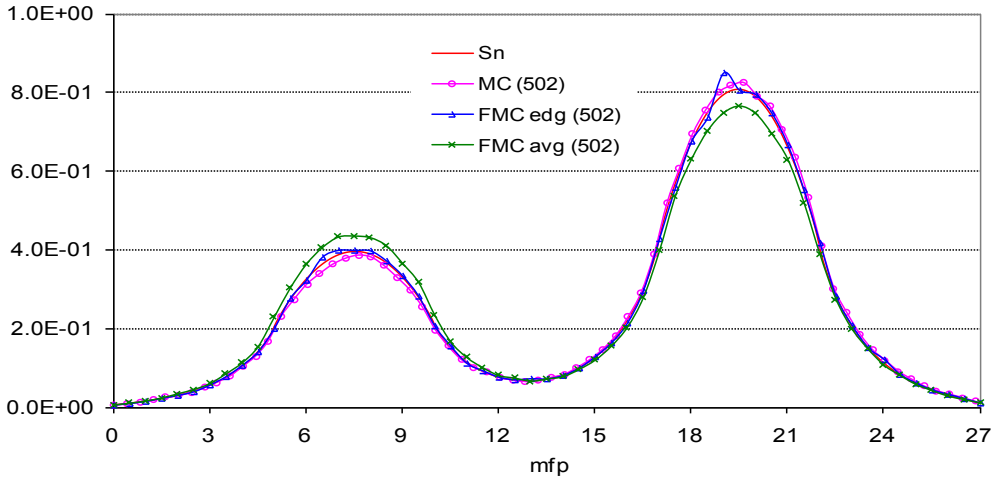

Figure 3.24 Problem 2 eigenfunction estimates for cycles 500, 501 to 502.

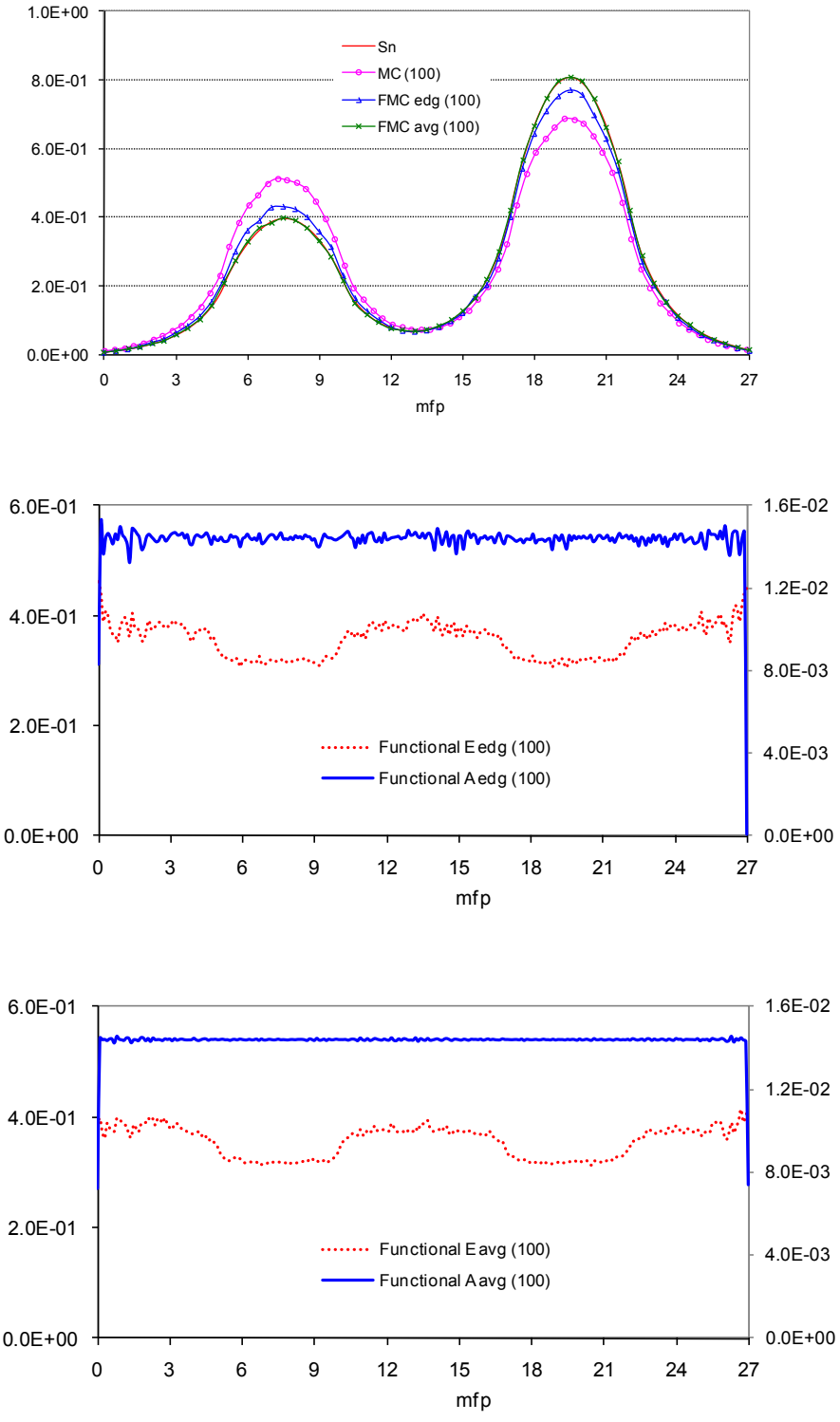

Figure 3.25 Problem 2 eigenfunction and nonlinear functional estimates for cycle 100.

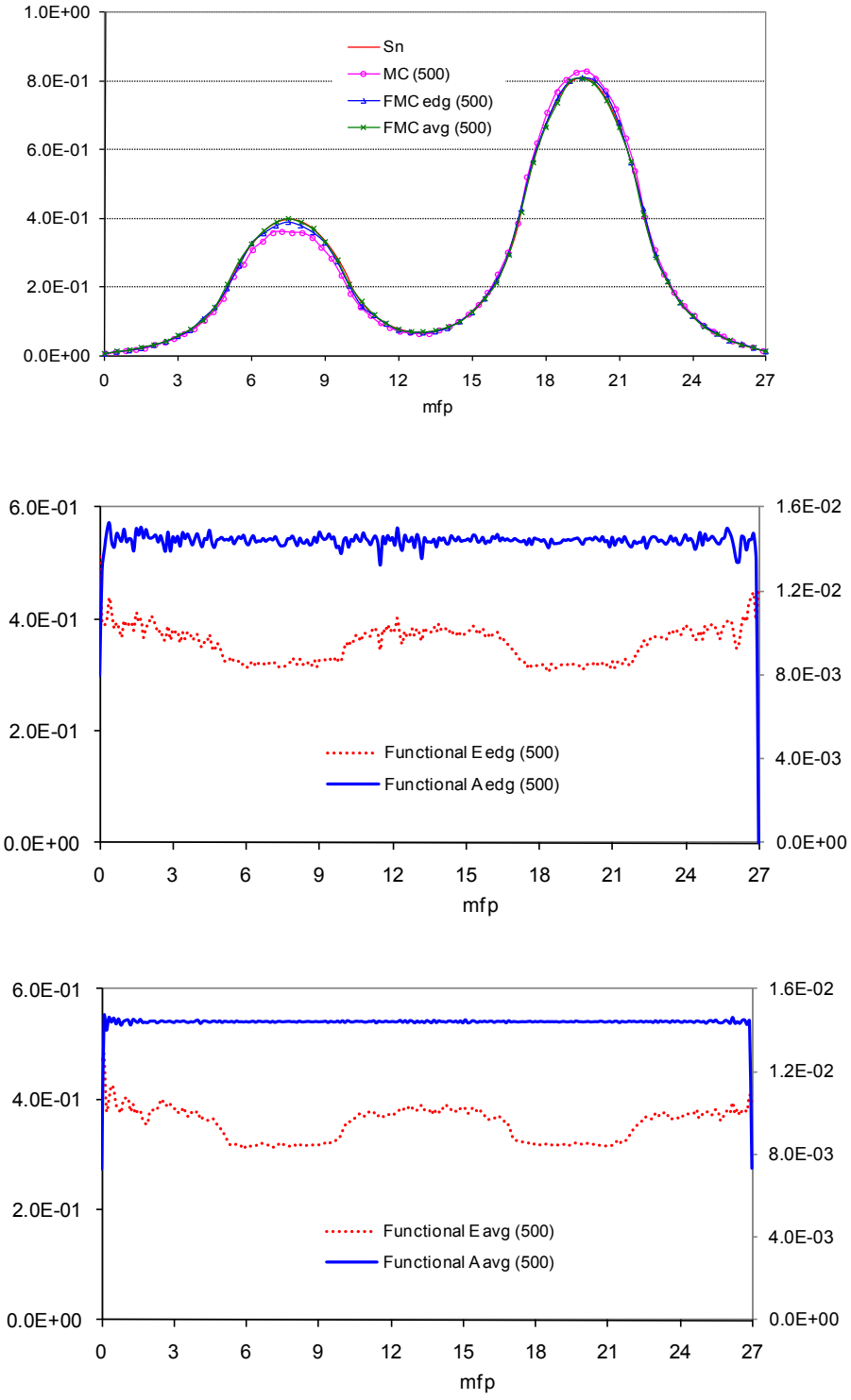

Figure 3.26 Problem 2 eigenfunction and nonlinear functional estimates for cycle 500.

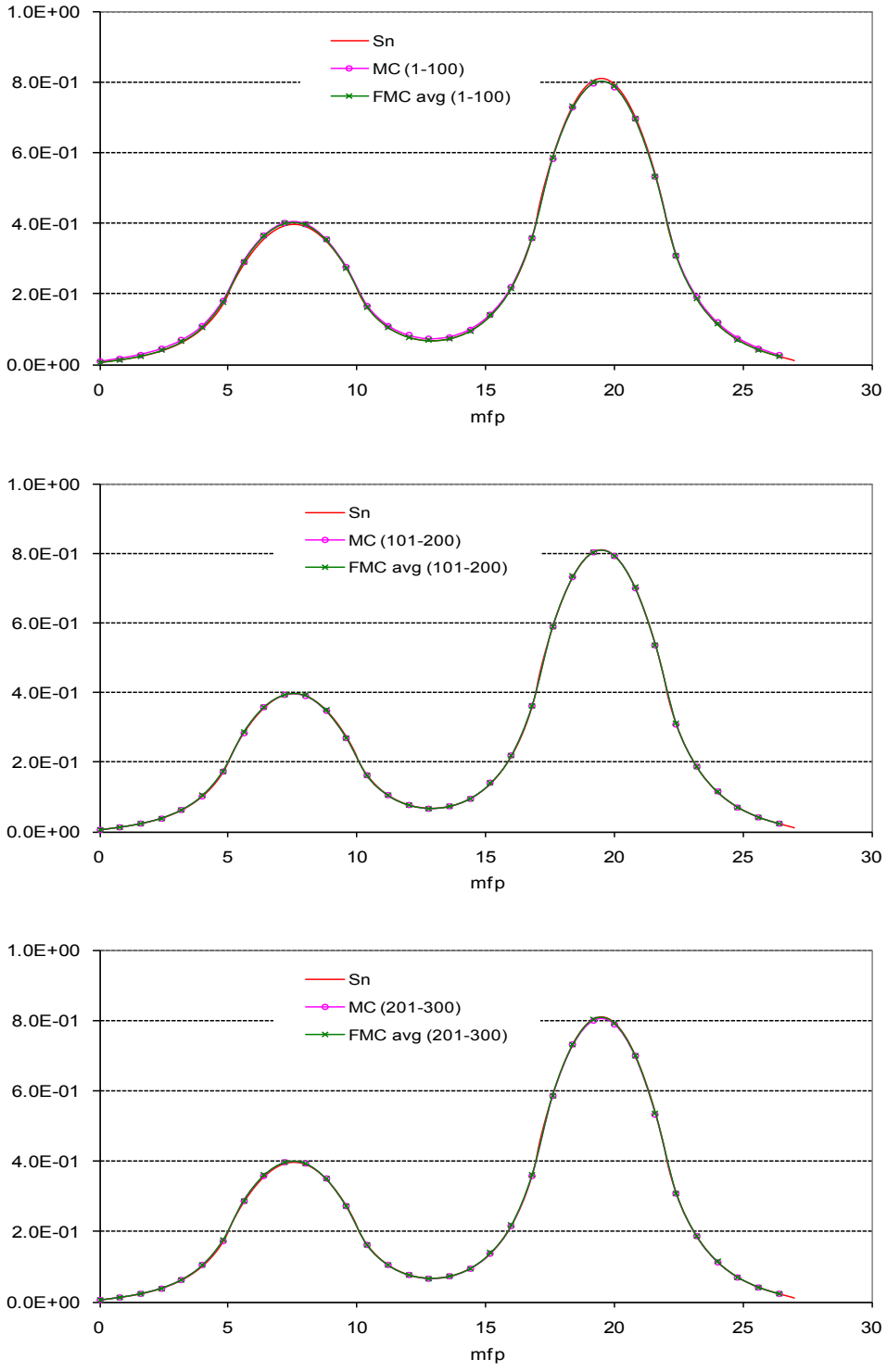

Figure 3.27 Problem 2 averaged eigenfunction estimates during cycles 1 to 300 with FMC feedback.

standard deviations in k for the MC, FMC edge, FMC average methods can be trusted.

As in Problem 1, we applied the FMC feedback to Problem 2. Figure 3.27 shows the estimates of the eigenfunction from standard Monte Carlo (MC) with FMC feedback, and the consequent Functional Monte Carlo (FMC avg). This figure is obtained by averaging the Monte Carlo estimates of the eigenfunction over 100-cycle spans, i.e. cycles 1-100, 101-200, and 201-300. Again, the Monte Carlo estimates of the eigenfunction with FMC feedback converge within the first 100-cycle span.

Table 3.6 Estimates of k and its Relative Standard Deviation for Problem 2.

Cycles	Standard MC	FMC edge	FMC average
1-100	0.987194 (0.0049541)	0.992272 (0.0002106)	0.992264 (0.0001965)
101-200	0.992240 (0.0003695)	0.992460 (0.0000524)	0.992441 (0.0000626)
201-300	0.993296 (0.0004312)	0.992540 (0.0000601)	0.992488 (0.0000545)
301-400	0.992658 (0.0003634)	0.992478 (0.0000554)	0.992529 (0.0000611)
401-500	0.993024 (0.0004106)	0.992477 (0.0000580)	0.992528 (0.0000503)
501-600	0.992746 (0.0004383)	0.992519 (0.0000525)	0.992460 (0.0000552)
601-700	0.992537 (0.0003638)	0.992527 (0.0000476)	0.992608 (0.0000580)
701-800	0.992988 (0.0004511)	0.992352 (0.0000554)	0.992395 (0.0000469)
801-900	0.992907 (0.0004164)	0.992490 (0.0000577)	0.992478 (0.0000594)
901-1000	0.992255 (0.0003977)	0.992496 (0.0000509)	0.992491 (0.0000532)

With FMC feedback, the estimates of the Problem 2 eigenvalue with their estimated relative standard deviations over ten 100-cycle spans are given in Table 3.10 for the standard Monte Carlo and the FMC average methods. We note that with FMC feedback (Table 3.10)

Table 3.7 MC Estimates of Relative Standard Deviation of k for Problem 2.

Cycles	True Rel. Std. Dev.	Apparent Rel. Std. Dev.	Ratio
1-100	0.0049564	0.0049541	1.0005
101-200	0.0003700	0.0003695	1.0014
201-300	0.0004404	0.0004312	1.0213
301-400	0.0003642	0.0003634	1.0022
401-500	0.0004153	0.0004106	1.0114
501-600	0.0004396	0.0004383	1.0030
601-700	0.0003640	0.0003638	1.0005
701-800	0.0004549	0.0004511	1.0084
801-900	0.0004194	0.0004164	1.0072
901-1000	0.0003980	0.0003977	1.0008

Table 3.8 FMC Edge Estimates of Relative Standard Deviation of k for Problem 2.

Cycles	True Rel. Std. Dev.	Apparent Rel. Std. Dev.	Ratio
1-100	0.0002112	0.0002106	1.0028
101-200	0.0000525	0.0000524	1.0019
201-300	0.0000611	0.0000601	1.0166
301-400	0.0000556	0.0000554	1.0036
401-500	0.0000582	0.0000580	1.0034
501-600	0.0000533	0.0000525	1.0152
601-700	0.0000486	0.0000476	1.0210
701-800	0.0000559	0.0000554	1.0090
801-900	0.0000580	0.0000577	1.0052
901-1000	0.0000514	0.0000509	1.0098

Table 3.9 FMC Average Estimates of Relative Standard Deviation of k for Problem 2.

Cycles	True Rel. Std. Dev.	Apparent Rel. Std. Dev.	Ratio
1-100	0.0001972	0.0001965	1.0036
101-200	0.0000626	0.0000626	1.0000
201-300	0.0000549	0.0000545	1.0073
301-400	0.0000620	0.0000611	1.0147
401-500	0.0000513	0.0000503	1.0199
501-600	0.0000553	0.0000552	1.0018
601-700	0.0000608	0.0000580	1.0483
701-800	0.0000470	0.0000469	1.0021
801-900	0.0000596	0.0000594	1.0034
901-1000	0.0000535	0.0000532	1.0056

or without feedback (Table 3.6), eigenvalue estimates agree within statistical errors in MC and FMC.

Table 3.10 Estimates of k and its Relative Standard Deviation for Problem 2 with FMC Feedback.

Cycles	Standard MC	FMC average
1-100	0.987645 (0.0050033)	0.992297 (0.0001963)
101-200	0.992661 (0.0004103)	0.992496 (0.0000486)
201-300	0.992969 (0.0003614)	0.992420 (0.0000553)
301-400	0.994029 (0.0004095)	0.992575 (0.0000601)
401-500	0.992368 (0.0003979)	0.992550 (0.0000511)
501-600	0.992851 (0.0003831)	0.992455 (0.0000538)
601-700	0.992706 (0.0003511)	0.992593 (0.0000565)
701-800	0.993234 (0.0003544)	0.992494 (0.0000532)
801-900	0.992830 (0.0003935)	0.992562 (0.0000508)
901-1000	0.993140 (0.0003766)	0.992575 (0.0000537)

The Shannon entropy behavior of the fission source without FMC feedback during 1000 cycles is shown in Figure 3.28. This figure shows that the FMC estimates of the eigenfunction have considerable variation from cycle to cycle, while the MC estimate of the eigenfunction changes slowly from one cycle to the next. Figure 3.29 shows the 10-cycle running average Shannon entropy behavior without FMC feedback. The FMC variations are now greatly reduced. The Shannon entropy behavior with FMC feedback in every cycle is shown in Figure 3.30.

As in Problem 1, these figures indicate that the FMC solution has a notably different character than the MC solution. Figure 3.28 depicts (i) the slow convergence of the MC fission source to the correct solution, caused by the correlations between sequential fission

sources. It also depicts (ii) the relatively rapid convergence of the FMC fission source to the approximate correct solution, but with a much large statistical variance about this solution than in Problem 1. This larger statistical variation is caused by the eigenfunction's inherent sensitivity to small perturbations in the details of the problem. For example, if the 7.0*cm* moderator region between the two fissile regions is increased, the problem will inherently become more sensitive, and the cycle-to-cycle variations in the FMC Shannon entropy will increase. Figure 3.29 shows that a 10-cycle running average of the eigenfunction yields nearly an identical MC result as in Figure 3.28, but a FMC result with greatly reduced statistical variance. This indicates that the relatively large-amplitude statistical variance in the FMC solution quickly cancels out when averaged over a small number of cycles. Finally, Figure 3.30 shows that when the MC method is used with FMC feedback, the resulting Shannon entropy has the same character as that of the FMC Shannon entropy depicted in Figure 3.28.

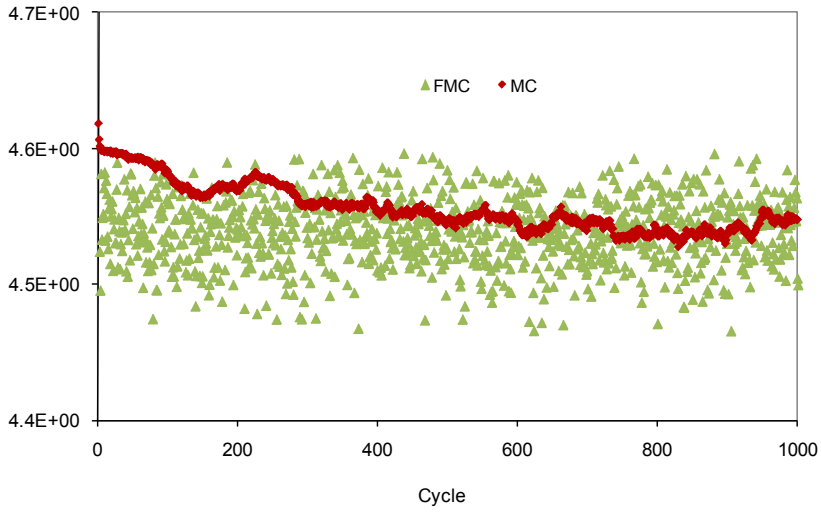

Figure 3.28 Shannon entropy behavior of the fission source for Problem 2 without FMC feedback.

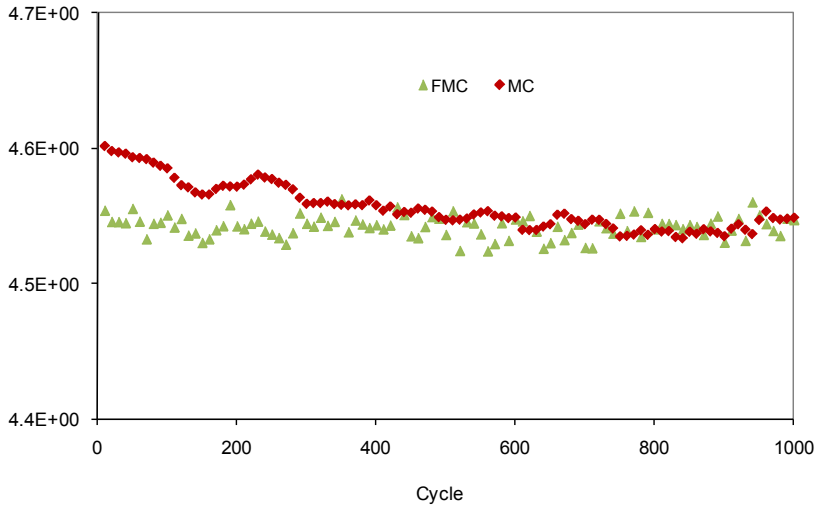

Figure 3.29 Shannon entropy (10 cycle running average) behavior of the fission source for Problem 2 without FMC feedback.

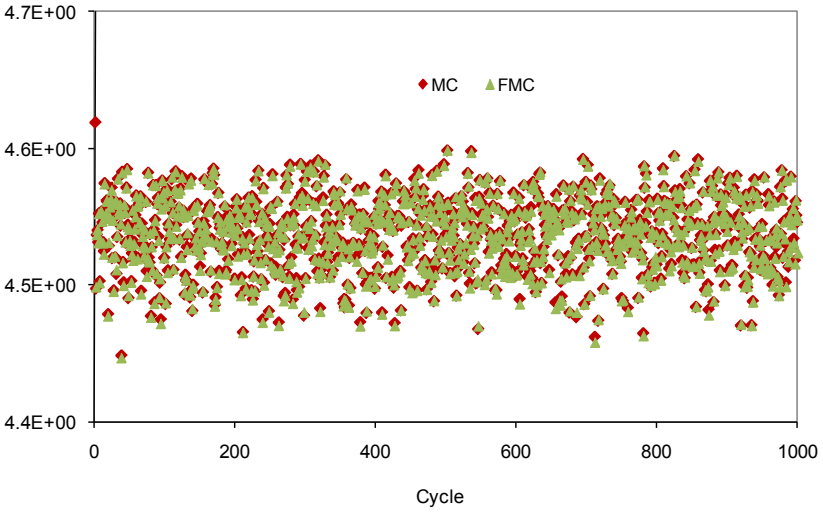

Figure 3.30 Shannon entropy behavior of the fission source for Problem 2 with FMC feedback.

3.3 Monoenergetic Problem 3: Two Loosely Coupled Fissile Regions

Problem 3 is similar to but more difficult than Problem 2. The two fissile regions are now separated by a wider 10 cm absorbing moderator, and now a smaller (0.073%) increase in $\nu\Sigma_f$ in the right fissile region yields an eigenfunction with a factor of 2 difference in the

peaks at the two fissile regions. The data for this problem is given in Table 3.11.

Table 3.11 Data for Problem 3.

Region	Location	Σ_t	$\Sigma_{s,0}$	$\Sigma_{s,n}$	$\nu\Sigma_f$
1	$0 < x < 5$	1.0	0.856	0.1	0
2	$5 < x < 10$	1.0	0.856	0.1	0.19680
3	$10 < x < 20$	1.0	0.856	0.1	0
4	$20 < x < 25$	1.0	0.856	0.1	0.196944
5	$25 < x < 30$	1.0	0.856	0.1	0

Again, column 5 holds for $n = 1, 2$, and 3; with $\Sigma_{s,n} = 0$ for $n \geq 4$. The entire system is 30 cm thick. The S_{32} solution, obtained with $h = 0.01$, yielded $k = 0.987828$. The dominance ratio for this problem is 0.999. Our Monte Carlo simulations of this problem used a uniform grid $h = 0.1$.

In Figure 3.31 we show plots obtained by averaging the MC and FMC estimates of the eigenfunction over cycles 201-300, 301-400, and 401-500 using 100,000 histories per cycle. For this problem the two FMC eigenfunction plots are very similar to each other but are not as close to the S_N eigenfunction as they were in Problem 2. However, the errors in the FMC eigenfunctions (compared to the S_N eigenfunction) are smaller than the errors in the MC eigenfunctions. In Figure 3.32, we show eigenfunction plots for individual cycles 500, 501, and 502. As in Problem 2, the MC eigenfunction estimate changes slowly from one cycle to the next, while now the FMC eigenfunction estimates vary more from cycle to cycle than in Problem 2. This happens because the system is more sensitive to perturbations in the cross sections than in Problem 2 (now only a 0.073% change in $\nu\Sigma_f$ in one fissile region causes a factor of 2 change in the eigenfunction). The Shannon entropy behavior without FMC feedback during 1000 cycles is shown in Figure 3.33. Again, the figure shows that the MC eigenfunction estimate changes very slowly from one cycle to the next, while the FMC eigenfunction estimates vary rapidly from cycle to cycle. The variation in the FMC Shannon entropy behavior indicates that the eigenfunction can not be trusted. Since Problem 3 is the most difficult eigenvalue problem with DR nearly equal to one,100,000 histories per cycle is

simply not sufficient.

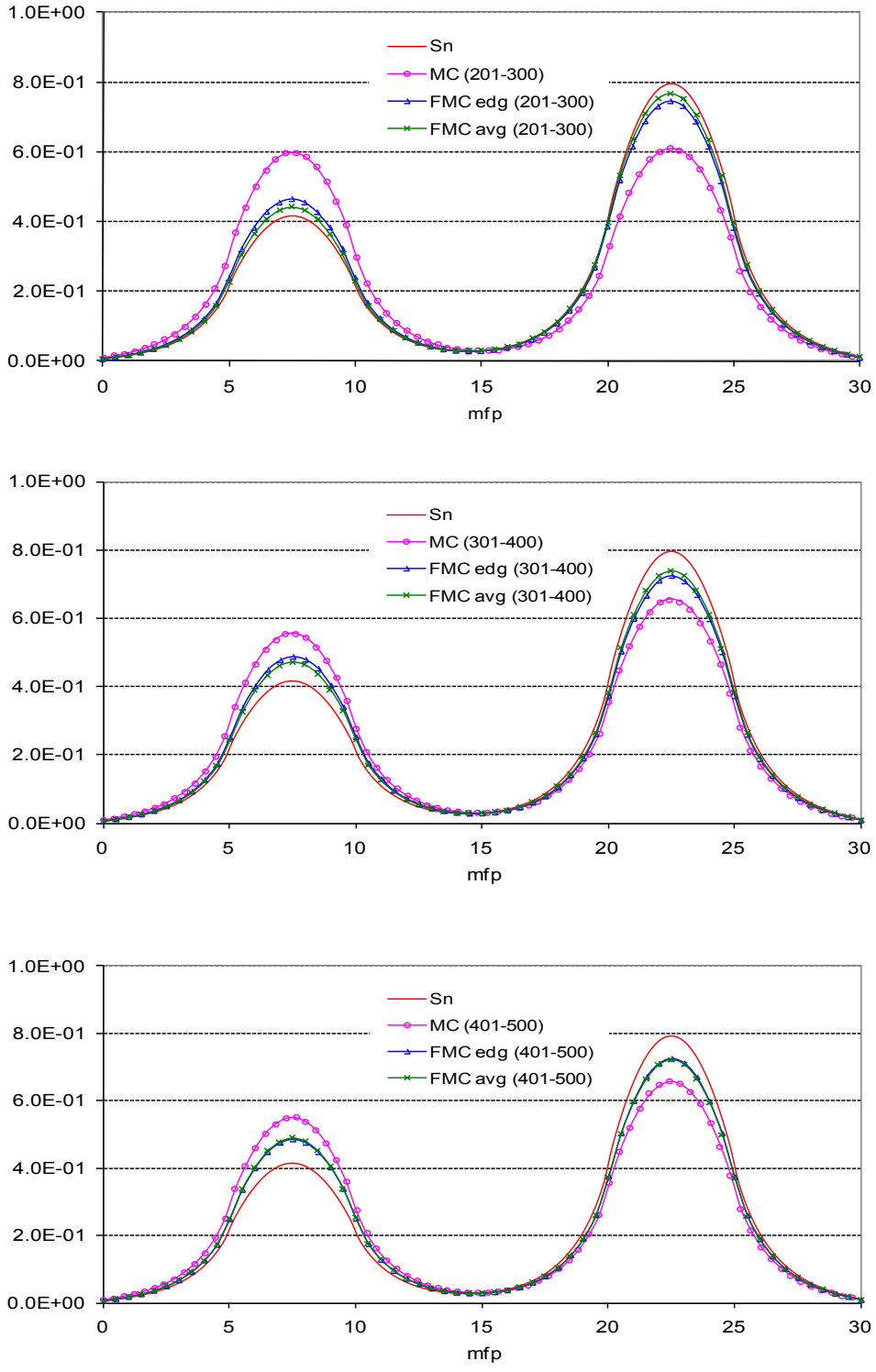

Figure 3.31 Problem 3 averaged eigenfunction estimates during cycles 201 to 500 without FMC feedback (100k histories/cycle).

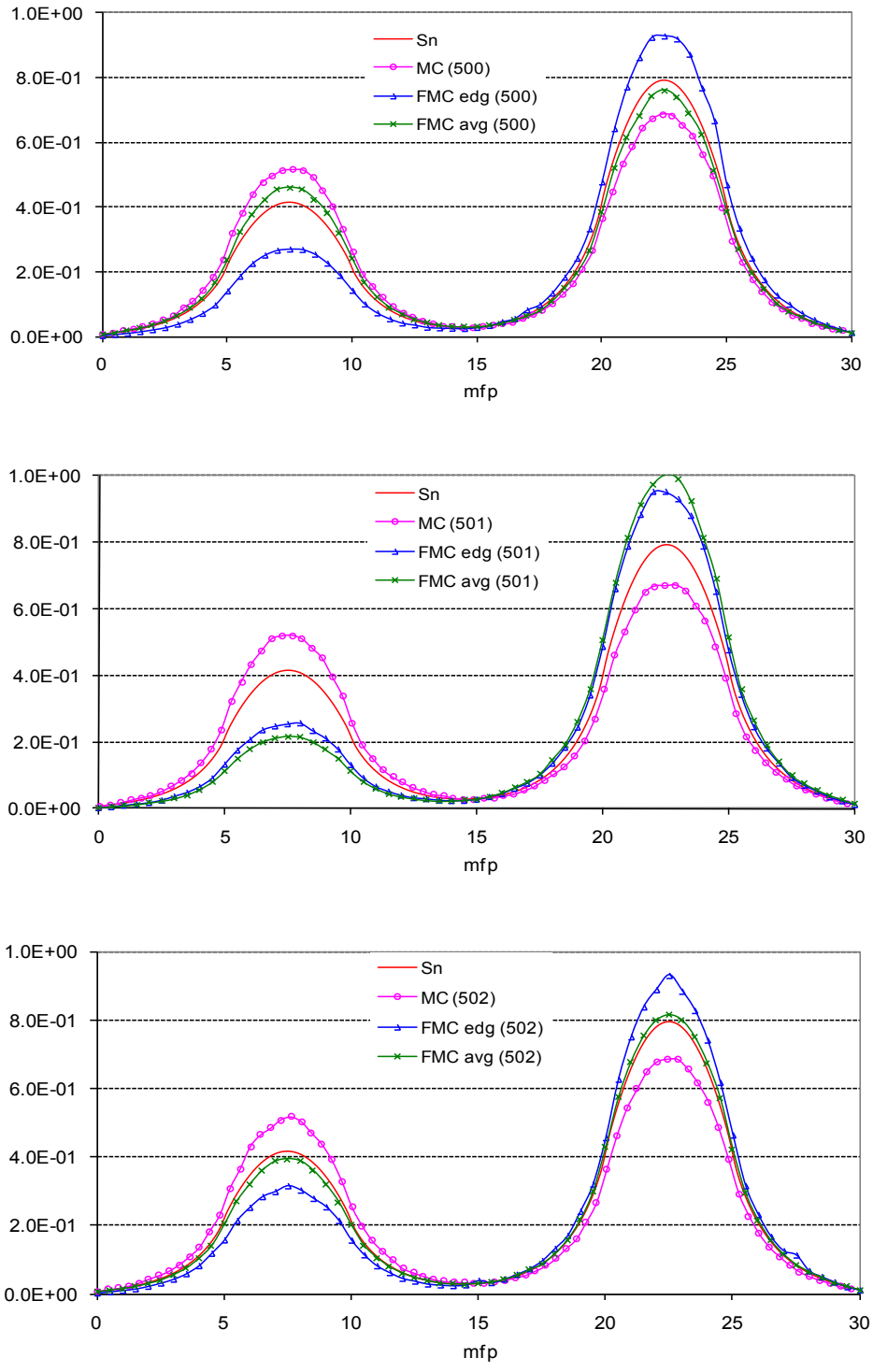

Figure 3.32 Problem 3 eigenfunction estimates for cycles 500, 501 to 502 (100k histories/cycle).

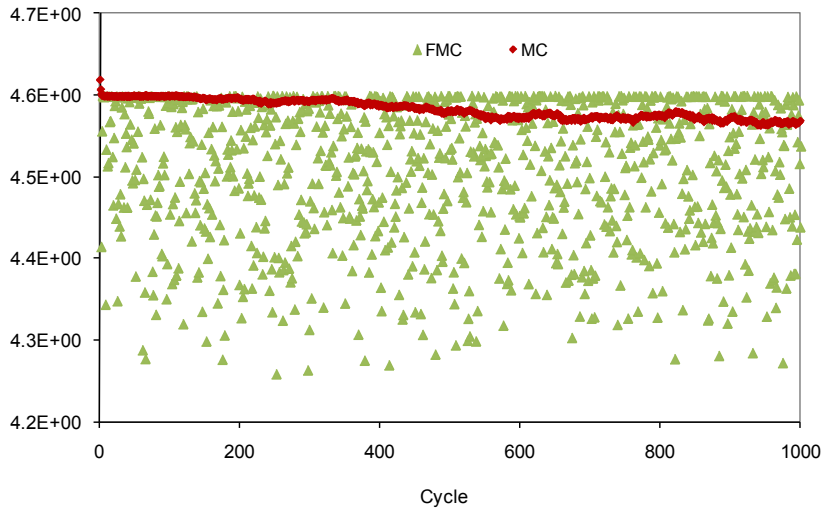

Figure 3.33 Shannon entropy behavior of the fission source for Problem 3 without FMC feedback (100k histories/cycle).

In Figure 3.34 we show plots obtained by averaging the MC and FMC estimates of the eigenfunction over cycles 201-300, 301-400, and 401-500 using 1,000,000 histories per cycle. The figure shows that the FMC estimates are almost converged to the S_N eigenfunction, while the MC estimates are still far from the S_N value.

We show eigenfunction plots for cycles 500, 501, and 502 in Figure 3.35. Again, the MC eigenfunction estimate changes slowly from one cycle to the next, while the FMC eigenfunction estimates vary significantly from cycle to cycle.

Figure 3.36 shows the MC estimates of the eigenfunction averaged over 500 active cycles (501-1000), its estimated apparent relative standard deviations, and the true relative standard deviations in the MC, and FMC average scalar fluxes over the cycles. The apparent relative standard deviations are obtained from a single 1000-cycle (500 inactive cycles, and 500 active cycles) run. The figure shows that the apparent relative standard deviation in the MC eigenfunction estimate appears to be smaller than the apparent relative standard deviation in the FMC eigenfunction estimates, but the true relative standard deviation in the MC eigenfunction estimate is noticeably greater than the relative standard deviation in the FMC average eigenfunction estimate as in Problem 2. A detailed comparison between the

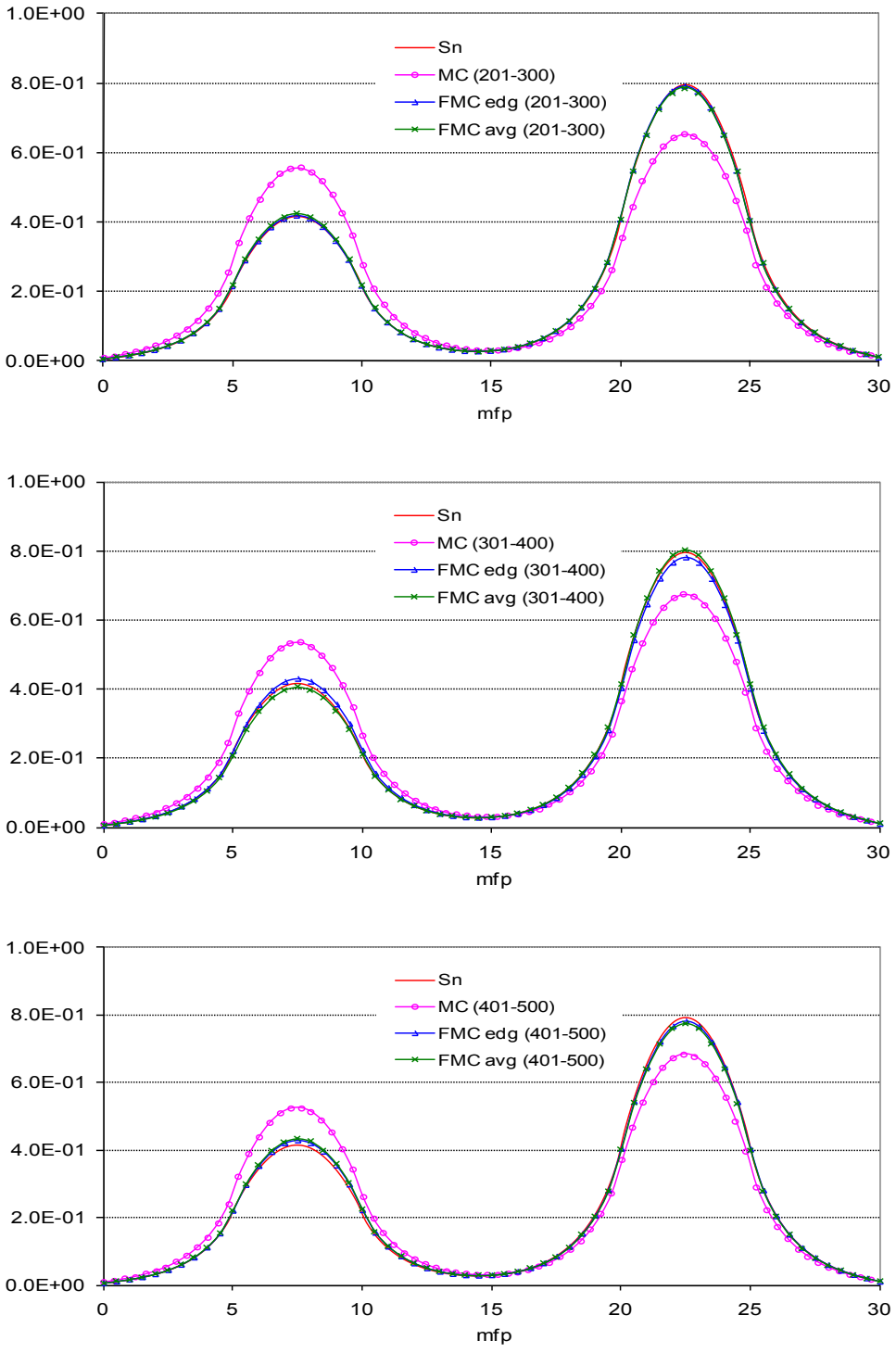

Figure 3.34 Problem 3 averaged eigenfunction estimates during cycles 201 to 500 without FMC feedback (1 million histories/cycle).

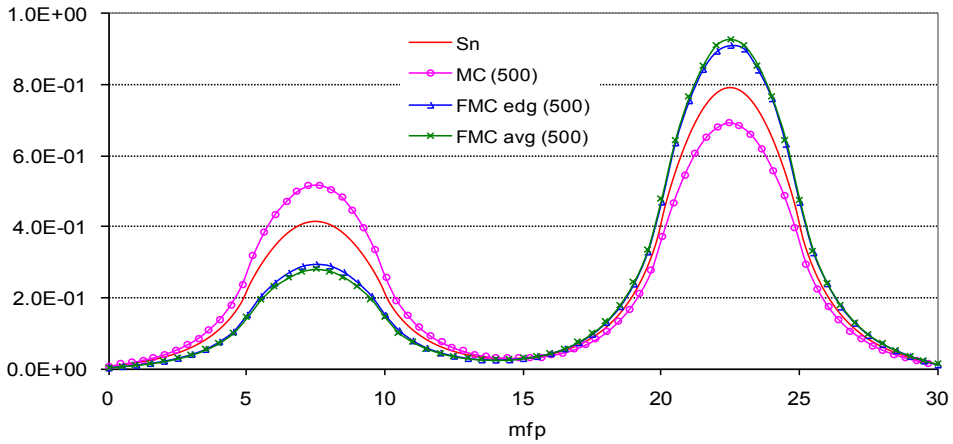

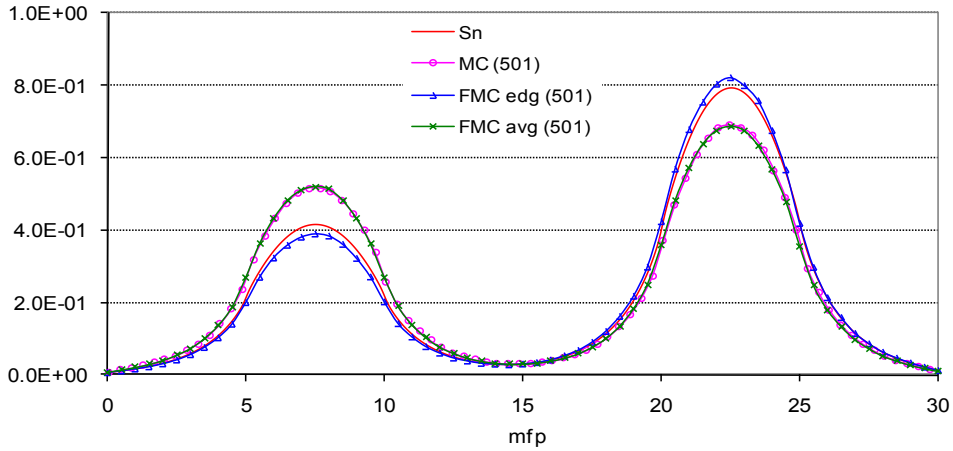

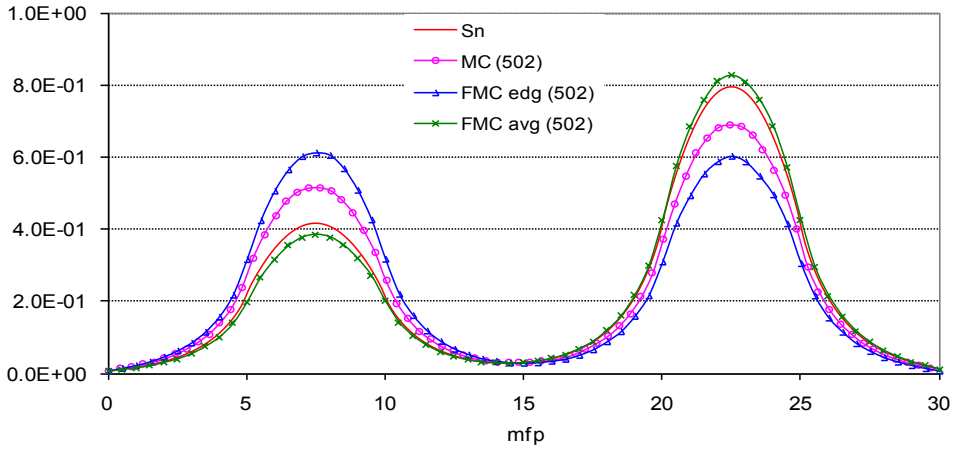

Figure 3.35 Problem 3 eigenfunction estimates for cycles 500, 501 to 502 (1 million histories/cycle).

apparent relative standard deviation and the true relative standard deviation in the MC, FMC average eigenfunction estimates is given in Figure 3.37.

The Shannon entropy behavior without FMC feedback during 1000 cycles (one million histories per cycle) is shown in Figure 3.38. This figure shows that the MC eigenfunction estimate changes very slowly from one cycle to the next, while the FMC eigenfunction estimates vary from cycle to cycle but with a smaller magnitude compared to that using 100,000 histories per cycle. Figure 3.39 shows the 10-cycle average Shannon entropy behavior. The variations are greatly reduced.

In Table 3.12 we present the estimates of the Problem 3 eigenvalue during each of the ten 100-cycle spans that we ran. As in Problem 2, the FMC estimated standard deviations in k are about a factor of 6 smaller than the MC estimates. The true relative standard deviations in MC, FMC edge, FMC average (obtained by comparing to the S_N estimate) are given in Table 3.13, Table 3.14 and Table 3.15 respectively. From Table 3.13-3.15, we note that these ratios are approximately equal to one. Thus the estimated relative standard deviations in k for the MC, FMC edge, FMC average methods can be trusted.

As in Problem 2, we applied the FMC feedback to Problem 3. The Shannon entropy behavior with FMC feedback is shown in Figure 3.40. Figure 3.41 shows the estimates of the eigenfunction from standard Monte Carlo (MC) with FMC feedback, and the consequent Functional Monte Carlo (FMC avg). This figure is obtained by averaging the Monte Carlo estimates of the eigenfunction over the first three 100-cycle spans. The Monte Carlo estimates of the eigenfunction with FMC feedback converges within the second 100-cycle span.

Problems 2 and 3 show that for systems with fissile regions that are becoming weakly-coupled, FMC estimates of the eigenfunction can vary significantly from one cycle to the next, and this variation increases as the fissile regions increasingly decouple. This happens because (i) the eigenfunction in such physical systems becomes increasingly sensititve to small perturbations in the cross sections, and (ii) the number of Monte Carlo particles

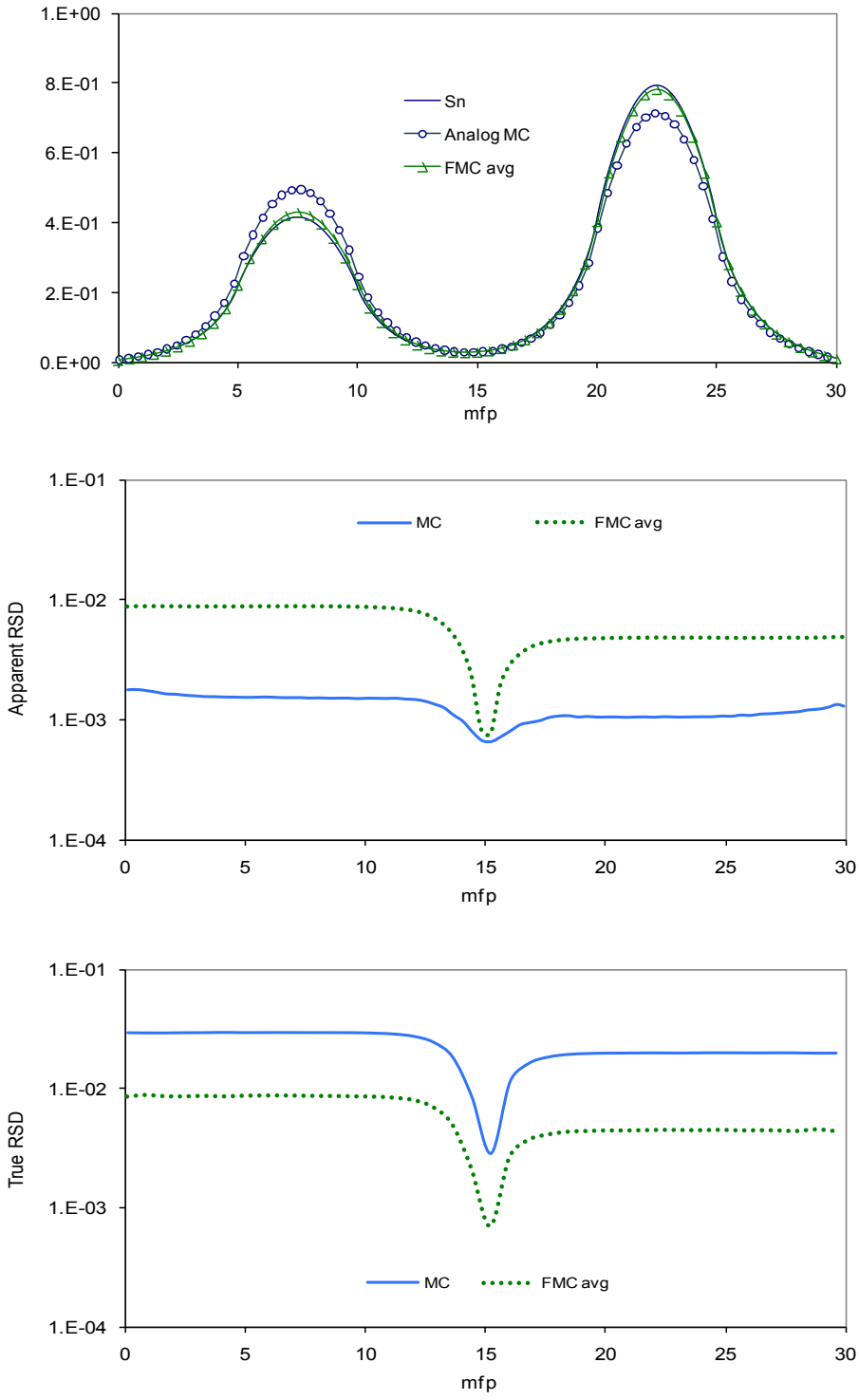

Figure 3.36 Problem 3 averaged eigenfunctions and their relative standard deviations over 501-1000 cycles (1 million histories/cycle).

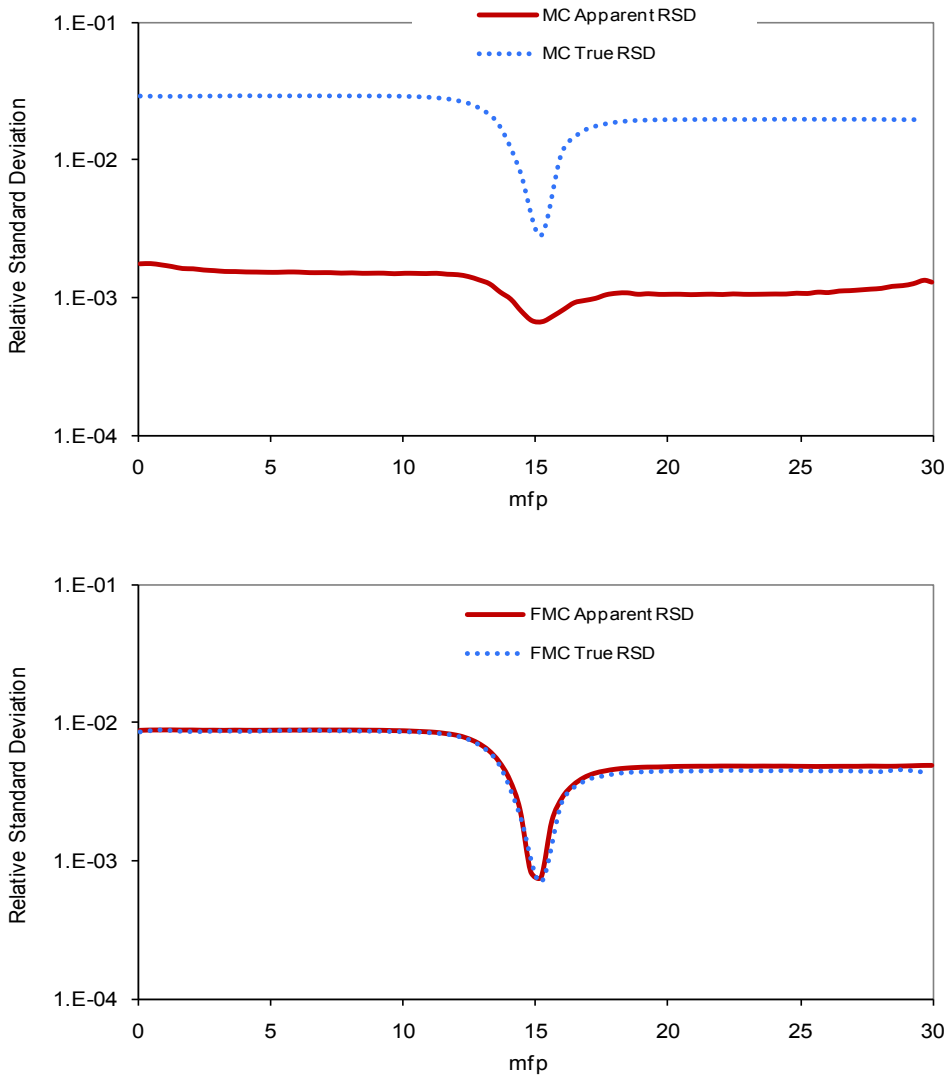

Figure 3.37 Comparison for Problem 3 of apparent RSDs and true RSDs in MC and FMC average eigenfunction estimates (1 million histories/cycle).

per cycle must be increased to avoid undersampling of the fission source. However, the eigenvalues in such systems are much less sensitive than the eigenfunctions, and indeed our FMC k-eigenvalue estimates for these problems are significantly more accurate than both the FMC eigenfunction estimates and the MC eigenvalue estimates. We note that a factor of 6 difference in the FMC and MC statistical errors in k (roughly seen in Problems 2 and 3) translates into a factor of $6^2 = 36$ computation time. That is, the MC code would have to run about 36 times as many particles or cycles to obtain an accuracy comparable to the

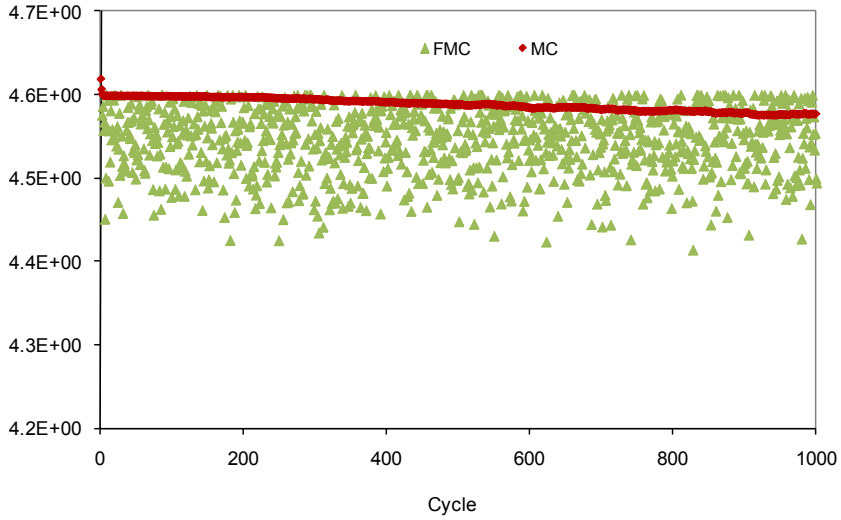

Figure 3.38 Shannon entropy behavior of the fission source for Problem 3 without FMC feedback (1 million histories/cycle).

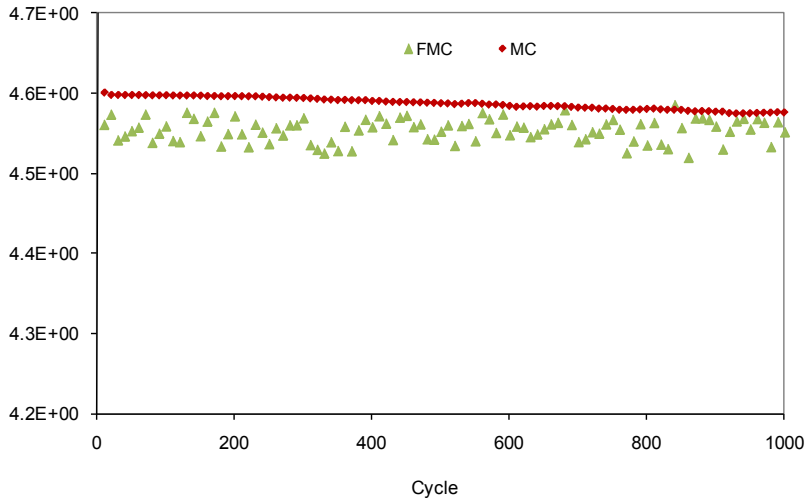

Figure 3.39 Shannon entropy behavior of the fission source for Problem 3 without FMC feedback (1 million histories/cycle, 10-cycle average).

FMC results.

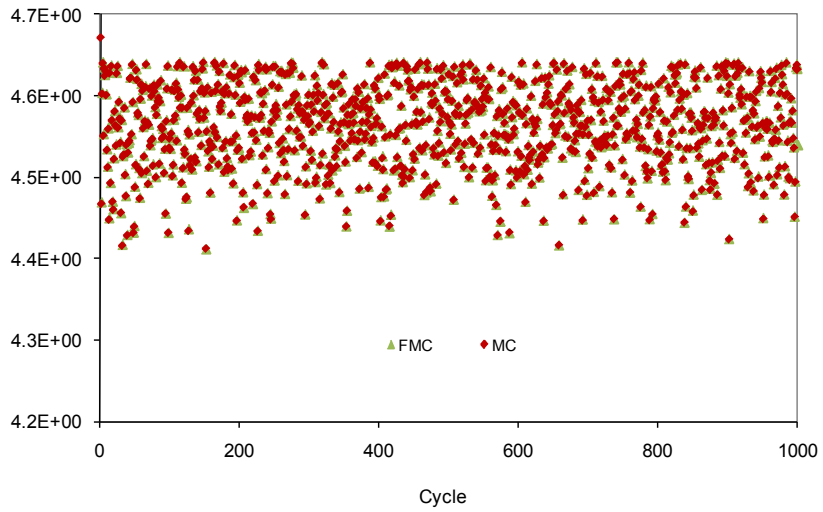

Figure 3.40 Shannon entropy behavior of the fission source for Problem 3 with FMC feedback (1 million histories/cycle).

Table 3.12 Estimates of k and its Standard Deviation for Problem 3.

Cycles	Standard MC	FMC edge	FMC average
1-100	0.982371 (0.0054625)	0.987647 (0.0001993)	0.987670 (0.0001894)
101-200	0.987948 (0.0001301)	0.987853 (0.0000191)	0.987877 (0.0000204)
201-300	0.988025 (0.0001428)	0.987864 (0.0000169)	0.987835 (0.0000187)
301-400	0.988036 (0.0001254)	0.987890 (0.0000169)	0.987854 (0.0000185)
401-500	0.988040 (0.0001438)	0.987851 (0.0000191)	0.987877 (0.0000179)
501-600	0.988071 (0.0001288)	0.987839 (0.0000177)	0.987854 (0.0000189)
601-700	0.988042 (0.0001142)	0.987851 (0.0000185)	0.987854 (0.0000165)
701-800	0.988069 (0.0001342)	0.987868 (0.0000175)	0.987821 (0.0000165)
801-900	0.988075 (0.0001187)	0.987851 (0.0000184)	0.987842 (0.0000179)
901-1000	0.988137 (0.0001294)	0.987864 (0.0000179)	0.987825 (0.0000177)

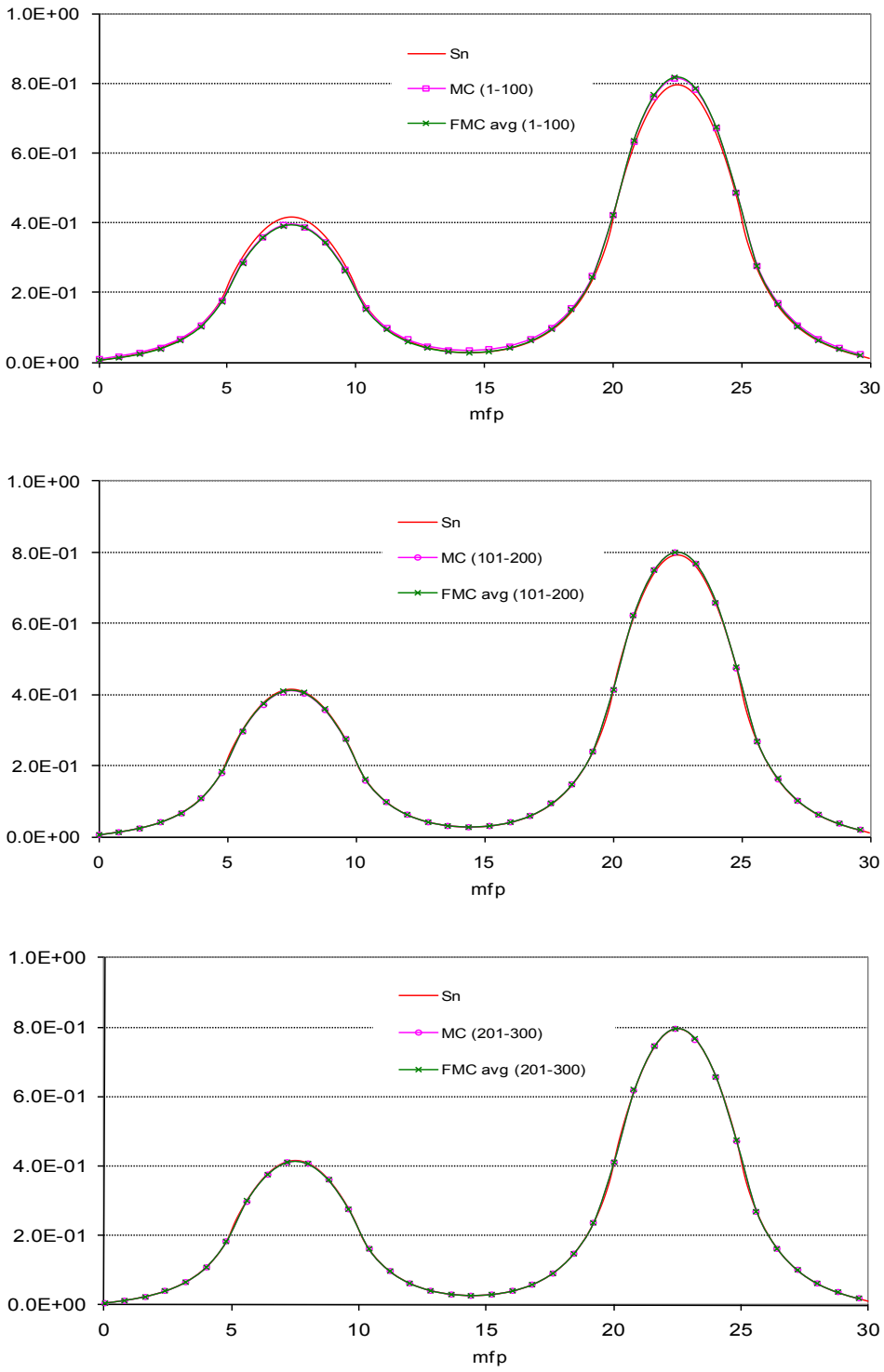

Figure 3.41 Problem 3 averaged eigenfunction estimates during cycles 1 to 300 with FMC feedback.

Table 3.13 MC Estimates of Relative Standard Deviation of k for Problem 3.

Cycles	True Rel. Std. Dev.	Apparent Rel. Std. Dev.	Ratio
1-100	0.0054606	0.0054625	0.9997
101-200	0.0001307	0.0001301	1.0046
201-300	0.0001442	0.0001428	1.0098
301-400	0.0001272	0.0001254	1.0144
401-500	0.0001455	0.0001438	1.0118
501-600	0.0001312	0.0001288	1.0186
601-700	0.0001163	0.0001142	1.0184
701-800	0.0001365	0.0001342	1.0171
801-900	0.0001214	0.0001187	1.0227
901-1000	0.0001332	0.0001294	1.0294

Table 3.14 FMC Edge Estimates of Relative Standard Deviation of k for Problem 3.

Cycles	True Rel. Std. Dev.	Apparent Rel. Std. Dev.	Ratio
1-100	0.0002001	0.0001993	1.0040
101-200	0.0000192	0.0000191	1.0052
201-300	0.0000173	0.0000169	1.0237
301-400	0.0000181	0.0000169	1.0710
401-500	0.0000193	0.0000191	1.0105
501-600	0.0000177	0.0000177	1.0000
601-700	0.0000187	0.0000185	1.0108
701-800	0.0000179	0.0000175	1.0229
801-900	0.0000185	0.0000184	1.0054
901-1000	0.0000182	0.0000179	1.0168

Table 3.15 FMC Average Estimates of Relative Standard Deviation of k for Problem 3.

Cycles	True Rel. Std. Dev.	Apparent Rel. Std. Dev.	Ratio
1-100	0.0001901	0.0001894	1.0037
101-200	0.0000210	0.0000204	1.0294
201-300	0.0000187	0.0000187	1.0000
301-400	0.0000187	0.0000185	1.0108
401-500	0.0000186	0.0000179	1.0391
501-600	0.0000191	0.0000189	1.0106
601-700	0.0000167	0.0000165	1.0121
701-800	0.0000165	0.0000165	1.0000
801-900	0.0000180	0.0000179	1.0056
901-1000	0.0000177	0.0000177	1.0000

3.4 Monoenergetic Problem 4: A 1-D PWR Full Reactor Core

Problems 1-3 are challenging problems with very high dominance ratios. Problem 4 however is a simplified 1-D PWR full reactor core. This problem was proposed by Professor Han Gyu Joo and his student Min-Jae Lee from Seoul National University. The core consists of 17 assemblies, in which 15 are fuel assemblies and 2 are reflectors. There are 4 different types of fuel assemblies in the core: fresh UO_2 fuel, MOX fuel, burnable poison GD fuel, and sightly low enrichment fresh UO_2 fuel. Each assembly consists of 16 pin cells, and each pin cell consists of 3 regions of $0.425cm$ in thickness. The detailed core descriptions are shown in Figures 3.42-3.44. The material cross sections are given in Table 3.16.

Figure 3.42 Problem 4 reactor core configuration.

R	1	1	1	1	1	1	1	1	1	1	1	1	1	1	1	1
C	2	2	2	6	2	2	2	2	2	2	2	2	6	2	2	2
M	3	3	3	6	3	3	3	3	3	3	3	3	6	3	3	3
B	2	2	4	6	2	2	2	2	2	2	2	2	6	4	2	2
A	5	5	5	6	5	5	5	5	5	5	5	5	6	5	5	5

Figure 3.43 Problem 4 five different type of assemblies' layout.

		0.425 cm	0.425 cm	0.425 cm
Pin 1	Reflector	m6	m6	m6
Pin 2	UO2 Fuel	m1	m2	m1
Pin 3	MOX Fuel	m1	m3	m1
Pin 4	GD Fuel	m1	m4	m1
Pin 5	UO2L Fuel	m1	m5	m1
Pin 6	Water Hole	m7	m7	m7

Figure 3.44 Problem 4 structure of the six pin cells.

Table 3.16 Material Cross Sections for Problem 4.

Material	Description	Σ_t	Σ_a	$\Sigma_{s,0}$	$\nu\Sigma_f$
m1	h_2O*0.69	1.74712E-01	9.33242E-04	1.73779E-01	0.00000E+00
m2	UO_2	3.32736E-01	5.78256E-02	2.74910E-01	3.32433E-02
m3	MOX*0.85	2.82549E-01	6.76607E-02	2.14888E-01	3.60099E-02
m4	UO_2BP*0.035	8.58461E-02	4.25733E-02	4.32728E-02	7.73288E-04
m5	UO_2L	3.33356E-01	5.78218E-02	2.75534E-01	3.31856E-02
m6	H_2O*0.25	7.85602E-02	7.65957E-04	7.77942E-02	0.00000E+00
m7	H_2O*0.35	9.01554E-02	5.25823E-04	8.96296E-02	0.00000E+00

We consider isotropic scattering in this problem. Our fine-mesh S_N solution, which used the S_{32} Gauss-Legendre quadrature set with $h = 0.0425cm$, produced $k = 1.212215$ and dominance ratio $DR = 0.989$. We ran this problem with a flat initial source guess. Our Monte Carlo simulations used 100,000 histories per cycle with a uniform grid $h = 0.425cm$ for total 200 cycles.

The Shannon entropy behavior without FMC feedback for the 200 cycles is shown in Figure 3.45. The figure shows that the FMC estimates of the eigenfunction converge immediately and the Monte Carlo estimates of the eigenfunction appears to be nearly converged after 20 cycles. This is due to the fact that the reactor is super critical. There are more fission sites available in each cycle, so that it is easier to establish the correct fission source distribution than a critical or sub-critical reactor. We also notice that the Shannon entropy behavior for the Monte Carlo estimates does not stay constant. It slowly "wobbles" around. This is due to the fact that Monte Carlo particles are not sufficient to keep the correct fission source distribution for an asymmetric core configuration. There is more fuel available at the left side of the core (3rd from left is a fresh UO_2 fuel assembly) than the right side (3rd from right is a low enrichment fresh UO_2 fuel assembly).

In Figure 3.46, we show plots of the MC and FMC estimates of the eigenfunction averaged over cycle 101-200, and the associated estimated relative standard deviations and true relative standard deviations. The S_N and FMC eigenfunction estimates are virtually coincident. And as expected, the MC eigenfunction is slightly tilted near both ends. The true

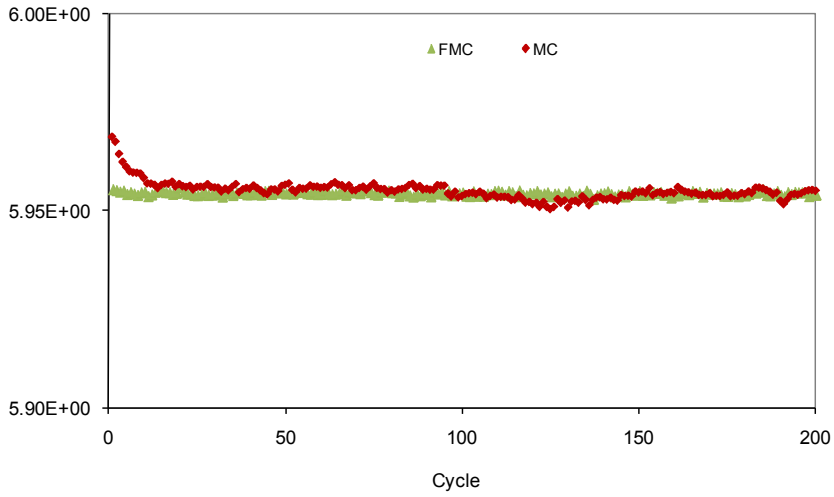

Figure 3.45 Shannon entropy behavior of the fission source for Problem 4 without FMC feedback.

relative standard deviations are obtained from 25 independent 200-cycle runs (100 inactive cycles, and 100 active cycles). The estimated relative standard deviations (both apparent and true) in the FMC eigenfunctions are smaller than those of the MC eigenfunction. A detailed comparison between the apparent relative standard deviation and the true relative standard deviation in the MC, FMC average eigenfunction estimates is given in Figure 3.47. This figure shows that the true relative standard deviation is at least a factor of 5 greater than the apparent relative standard deviation in the MC eigenfunction estimate. Figure 3.47 also shows that the true relative standard deviations in FMC average eigenfunction estimates are approximately the same as the apparent relative standard deviations as we observed in previous problems.

Table 3.17 displays estimates of the eigenvalue and the relative standard deviation for Problem 4 during each of the two 100-cycle spans that we ran. The results show that the FMC estimates of k are much more accurate than the MC estimates.

We ran this problem with FMC feedback for 30 cycles. Figure 3.48 is obtained by averaging the Monte Carlo estimates of the eigenfunction over 10-cycle spans. Figure 3.48 shows that the Monte Carlo estimates of the eigenfunction with FMC feedback converge

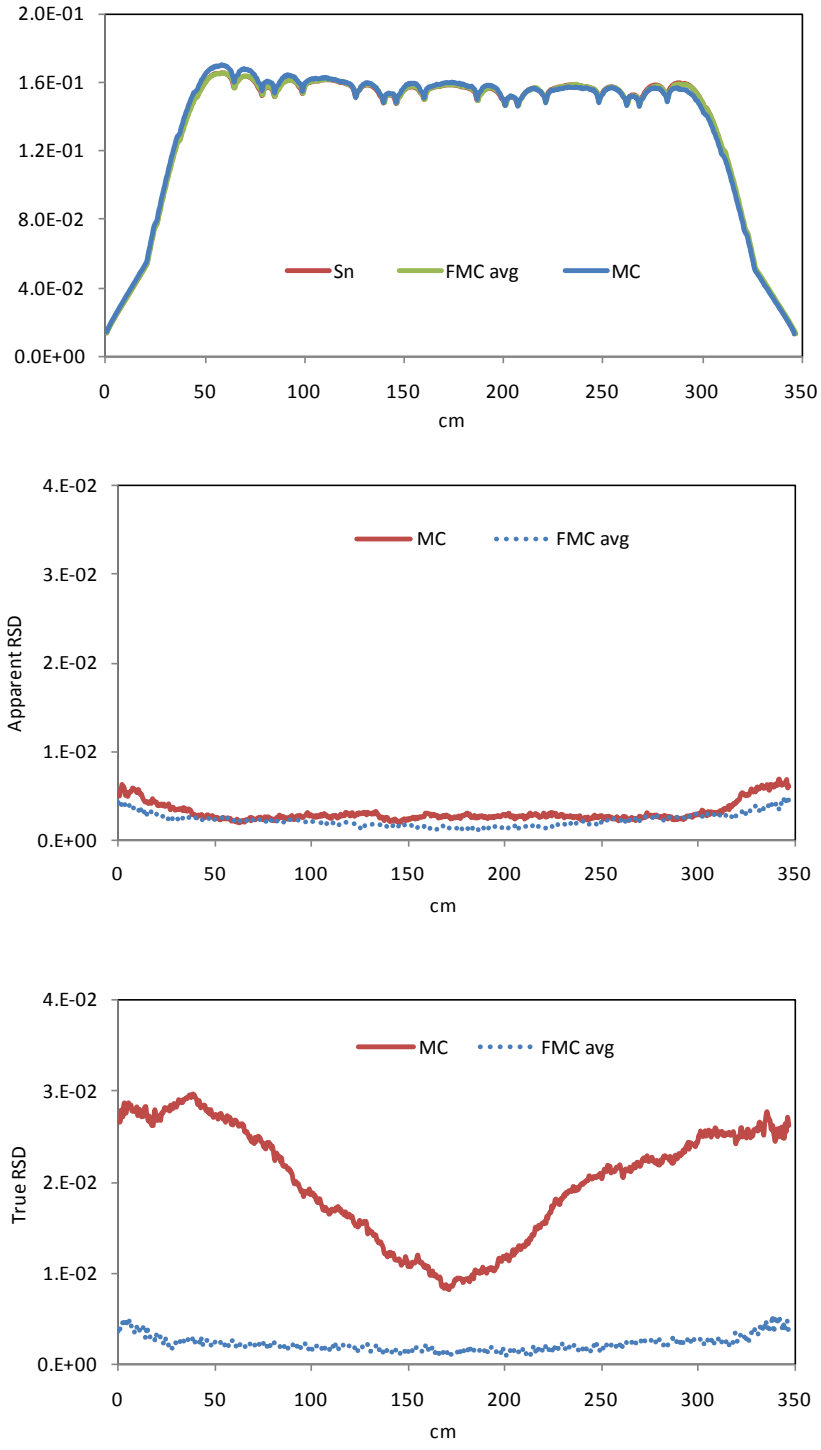

Figure 3.46 Problem 4 averaged eigenfunctions and their relative standard deviations over 101-200 cycles without FMC feedback.

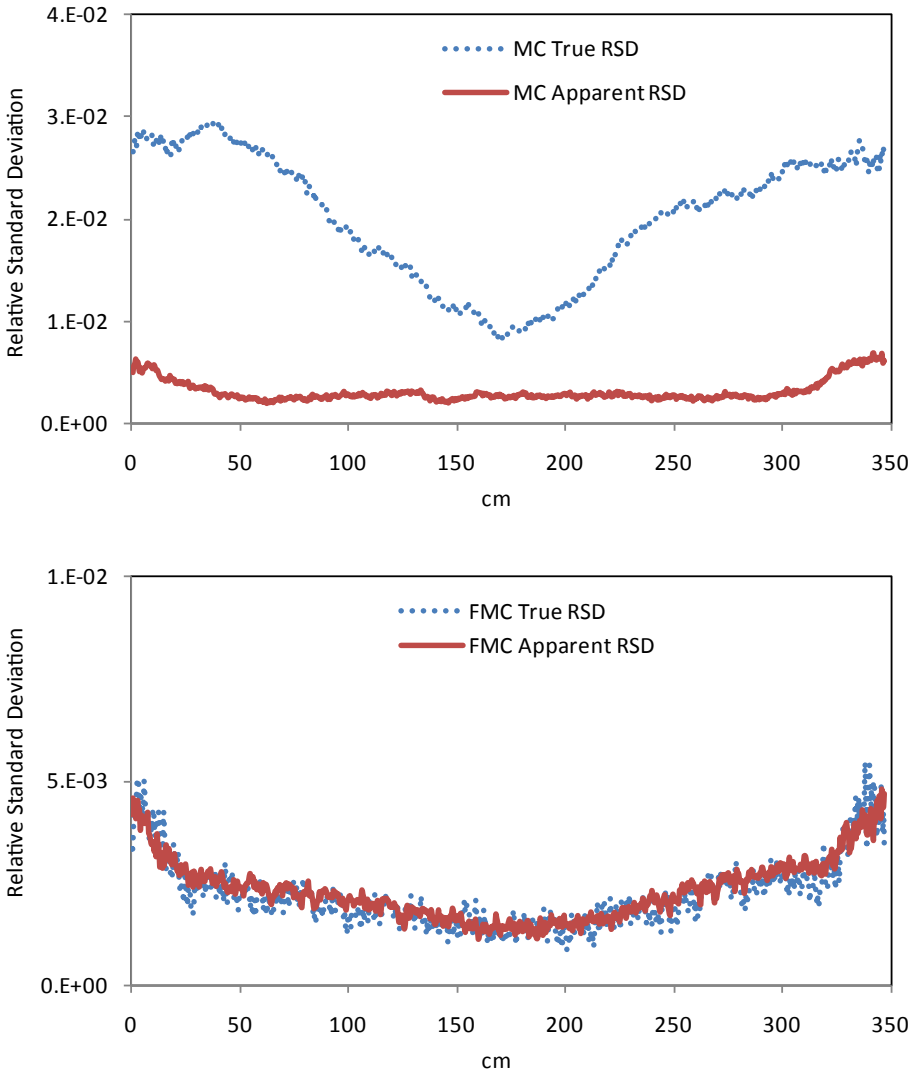

Figure 3.47 Comparison for Problem 4 of apparent RSDs and true RSDs in MC, and FMC average eigenfunction estimates.

within the second 10-cycle span. The Shannon entropy behavior with FMC feedback is shown in Figure 3.49. This figure shows that the MC estimates converge to the correct fission source distribution once the FMC feedback is applied.

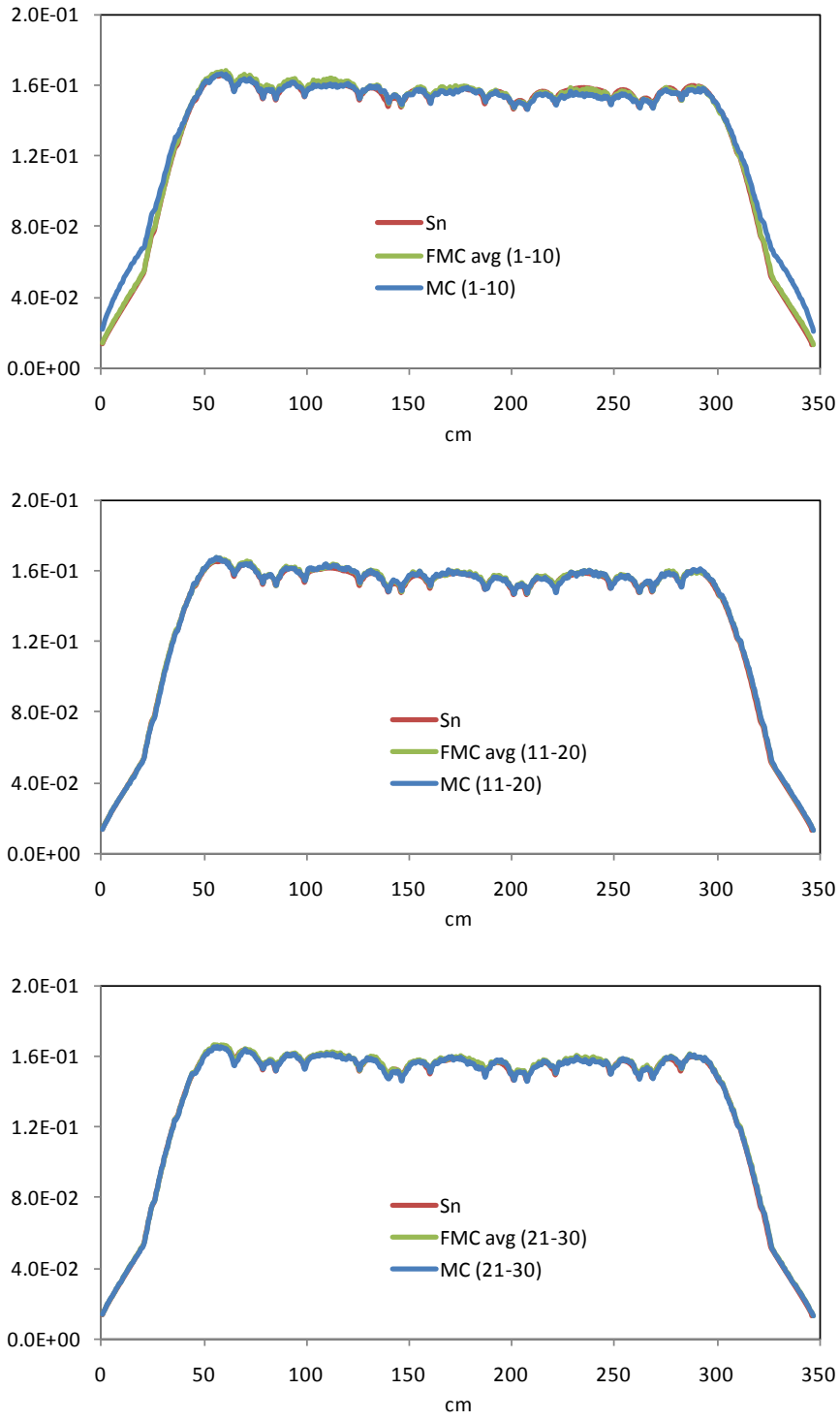

Figure 3.48 Problem 4 averaged eigenfunction estimates for 30 active cycles with FMC feedback.

Table 3.17 Estimates of k and its Standard Deviation for Problem 4.

Cycles	Standard MC	FMC average
1-100	1.211187 (0.0009683)	1.212480 (0.0000193)
101-200	1.212105 (0.0003376)	1.212480 (0.0000193)

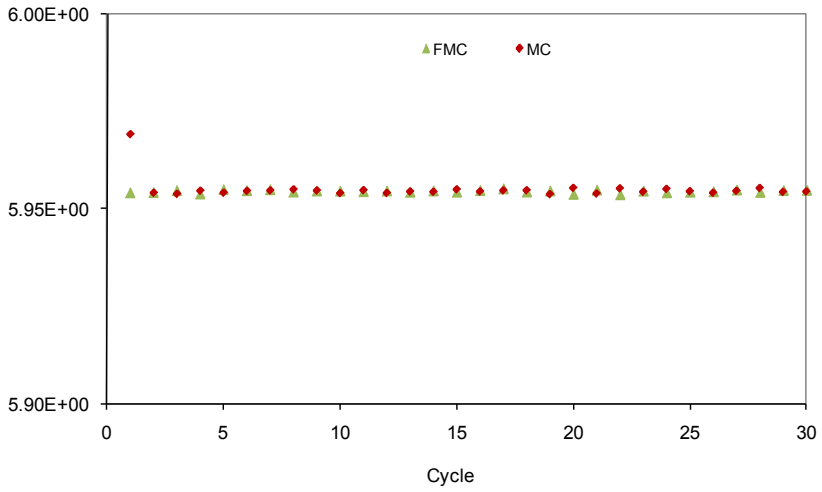

Figure 3.49 Shannon entropy behavior of the fission source for Problem 4 with FMC feedback.

3.5 Summary of the Mono-energetic Numerical Results

We have tested the FMC method on four problems for which the standard Monte Carlo method is problematic:

1. Accuracy in the estimates of the eigenvalue and eigenfunction.
2. Source convergence with a flat initial source guess or an extremely asymmetric initial fission source guess.
3. Inter-cycle correlation.
4. FMC feedback.

As expected, estimates of the eigenvalue and eigenfunction with the FMC method were more accurate and more rapidly convergent. For a large, homogeneous fissile region problem, the FMC estimates of the eigenfunction converged within the first 100-cycle averages

(50,000 histories per cycle) starting with a flat initial source guess. The FMC estimates of the eigenfunction also converged at the third 100-cycle averages with an extremely asymmetric initial fission source guess. However, the MC estimates of the eigenfunction did not converge after a test run with a total of 1000 cycles. Inter-cycle correlation is quite weak for the FMC method. The true relative standard deviations are about the same as the apparent relative standard deviations for the FMC method. The apparent relative standard deviations are more than a factor of 10 smaller than the true relative standard deviations for the MC method. With FMC feedback, the MC estimates of the eigenfunction converged after skipping only 20 cycles. We then tested two problems with loosely coupled fissile regions. The FMC method was shown to be highly efficient relative to the MC method. One of the heterogeneous problems has a DR = 0.999, which represents a very difficult problem in source convergence. With FMC feedback (1 million histories per cycle), the MC results were fully converged after only 100 inactive cycles. Finally, we tested the FMC method for a simplified 1-D full PWR reactor core. With FMC feedback, the performance of the Monte Carlo estimates of the eigenfunction improved significantly. The MC estimates converge to the correct fission source distribution promptly once the FMC feedback is applied.

Chapter 4

The FMC method for 1-D Multigroup Energy k-eigenvalue Problems

In this chapter, we extend the one-group FMC method derived in Chapter 2 to multigroup k-eigenvalue problems. We follow the same basic procedure in developing the multigroup FMC method as was used for monoenergetic problems, but now there is additional complexity because of the occurrence of between-group scattering processes. As in the monoenergetic case, the resulting multigroup FMC estimates of eigenvalues and eigenfunctions have only statistical errors. The FMC method has no spatial, angular, or energy truncation errors, beyond the errors associated with the multigroup approximation.

4.1 Analytical Formulation of the Functional Monte Carlo Method for the Multigroup k-eigenvalue Problem

To derive the multigroup approximation to the continuous-energy transport equation, the energy variable E is discretized into G energy groups.

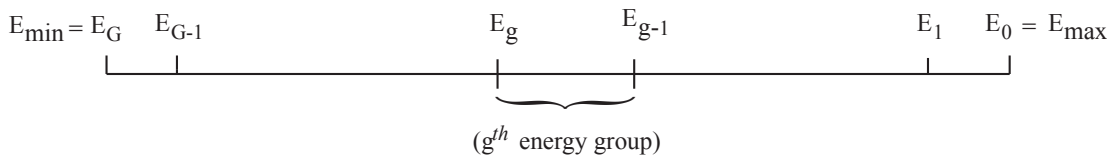

The general planar-geometry, multigroup, anisotropically-scattering transport equation

for a k-eigenvalue problem is:

$$\mu\frac{\partial\psi_g}{\partial x}(x,\mu)+\Sigma_{tg}(x)\psi_g(x,\mu)=\sum_{g'=1}^{G}\int_{-1}^{1}\Sigma_{s,g'\to g}(x,\mu',\mu)\psi_{g'}(x,\mu')d\mu'$$

$$+\frac{\chi_g(x)}{2k}\sum_{g'=1}^{G}\int_{-1}^{1}\nu\Sigma_{fg'}(x)\psi_{g'}(x,\mu')d\mu' \ , \ 0<x<X \ , \ 1\le g\le G \ , \tag{4.1a}$$

$$\psi_g(0,\mu)=0 \ , \ 0<\mu\le 1 \ , \ 1\le g\le G \ , \tag{4.1b}$$

$$\psi_g(X,\mu)=0 \ , \ -1\le\mu<0 \ , \ 1\le g\le G \ . \tag{4.1c}$$

For each energy group g , we have defined the following parameters:

$$\psi_g(x,\mu)=\int_{E_g}^{E_{g+1}}\psi(x,\mu,E)dE \tag{4.2a}$$

$$=\text{angular flux for the } g^{th} \text{ energy group} \ ,$$

$$\chi_g(x)=\int_{E_g}^{E_{g+1}}\chi(x,E)dE \tag{4.2b}$$

$$=\text{multigroup fission spectrum} \ .$$

The g^{th} multigroup cross sections in Eq. (4.1a) are defined as neutron-spectrum-weighted average cross sections over the g^{th} energy range:

$$\Sigma_{tg}(x)=\frac{\int_{E_g}^{E_{g+1}}\Sigma_t(x)\Psi(x,E)dE}{\int_{E_g}^{E_{g+1}}\Psi(x,E)dE} \ , \tag{4.2c}$$

$$\Sigma_{fg}(x)=\frac{\int_{E_g}^{E_{g+1}}\Sigma_f(x)\Psi(x,E)dE}{\int_{E_g}^{E_{g+1}}\Psi(x,E)dE} \ , \tag{4.2d}$$

where $\Psi(x,E)$ is the specified neutron spectrum. In this chapter, we assume that the multigroup cross sections have been assigned and are fixed, and we develop an FMC method that solves Eqs. (4.1) with only statistical errors. (Thus, errors due to the multigroup approximation will be present in the FMC solution.)

The differential scattering cross section in Eq. (4.1a) can be expanded as a summation of Legendre polynomials:

$$\Sigma_{s,g'\to g}(x,\mu',\mu) = \sum_{n=0}^{\infty} \frac{2n+1}{2} \Sigma_{sn,g'\to g}(x) P_n(\mu') P_n(\mu) \,. \tag{4.3}$$

The FMC equations are obtained by calculating certain space-angle moments of Eqs. (4.1). To begin, we operate on Eq. (4.1a) by $\int_{-1}^{1} \mu^n(\cdot)\, d\mu$ for $n = 0$ and 1. Defining $\phi_{gn}(x) = \int_{-1}^{1} \mu^n \psi_g(x,\mu)\, d\mu$, we obtain:

$$\frac{d\phi_{g1}}{dx}(x) + \Sigma_{tg}(x)\phi_{g0}(x) = \sum_{g'=1}^{G} \Sigma_{s0,g'\to g}(x)\phi_{g'0}(x) + \frac{\chi_g}{k} \sum_{g'=1}^{G} \nu\Sigma_{fg'}(x)\phi_{g'0}(x) \,, \tag{4.4a}$$

$$\frac{d\phi_{g2}}{dx}(x) + \Sigma_{tg}(x)\phi_{g1}(x) = \sum_{g'=1}^{G} \Sigma_{s1,g'\to g}(x)\phi_{g'1}(x) \,. \tag{4.4b}$$

Also, we operate on the left boundary condition [Eq. (4.1b)] by $\int_0^1 \mu(\cdot)\, d\mu$:

$$0 = \int_0^1 \mu\, \psi_g(0,\mu)\, d\mu = \phi_{g1}(0) + \int_{-1}^{1} |\mu| \psi_g(0,\mu)\, d\mu \,, \tag{4.4c}$$

and on the right boundary condition [Eq. (4.1c)] by $\int_{-1}^0 \mu(\cdot)\, d\mu$:

$$0 = \int_{-1}^0 \mu\, \psi_g(X,\mu)\, d\mu = \phi_{g1}(X) - \int_{-1}^{1} |\mu| \psi_g(X,\mu)\, d\mu \,. \tag{4.4d}$$

Eq. (4.4b) can be written explicitly as:

$$\begin{pmatrix} \frac{d\phi_{12}}{dx} \\ \frac{d\phi_{22}}{dx} \\ \vdots \\ \frac{d\phi_{G2}}{dx} \end{pmatrix} + \begin{pmatrix} \Sigma_{t1} & 0 & \cdots & 0 \\ 0 & \Sigma_{t2} & \cdots & 0 \\ \vdots & \vdots & \ddots & \\ 0 & 0 & 0 & \Sigma_{tG} \end{pmatrix} \begin{pmatrix} \phi_{11} \\ \phi_{21} \\ \vdots \\ \phi_{G1} \end{pmatrix} = \begin{pmatrix} \Sigma_{s1,1\to 1} & \Sigma_{s1,2\to 1} & \cdots & \Sigma_{s1,G\to 1} \\ \Sigma_{s1,1\to 2} & \Sigma_{s1,2\to 2} & \cdots & \Sigma_{s1,G\to 2} \\ \vdots & \vdots & \ddots & \vdots \\ \Sigma_{s1,1\to G} & \Sigma_{s1,2\to G} & \cdots & \Sigma_{s1,G\to G} \end{pmatrix} \begin{pmatrix} \phi_{11} \\ \phi_{21} \\ \vdots \\ \phi_{G1} \end{pmatrix} . \tag{4.5}$$

By rearranging Eq. (4.5), we obtain

$$\begin{pmatrix} \frac{d\phi_{12}}{dx} \\ \frac{d\phi_{22}}{dx} \\ \vdots \\ \frac{d\phi_{G2}}{dx} \end{pmatrix} = - \begin{pmatrix} \Sigma_{t1} - \Sigma_{s1,1\to1} & -\Sigma_{s1,2\to1} & \cdots & -\Sigma_{s1,G\to1} \\ -\Sigma_{s1,1\to2} & \Sigma_{t2} - \Sigma_{s1,2\to2} & \cdots & -\Sigma_{s1,G\to2} \\ \vdots & \vdots & \ddots & \vdots \\ -\Sigma_{s1,1\to G} & -\Sigma_{s1,2\to G} & \cdots & \Sigma_{tG} - \Sigma_{s1,G\to G} \end{pmatrix} \begin{pmatrix} \phi_{11} \\ \phi_{21} \\ \vdots \\ \phi_{G1} \end{pmatrix} . \quad (4.6)$$

Solving the set of G simultaneous equations Eq. (4.6) for multigroup first moments in terms of the second moments, we have

$$\begin{pmatrix} \phi_{11} \\ \phi_{21} \\ \vdots \\ \phi_{G1} \end{pmatrix} = - \begin{pmatrix} \Sigma_{t1} - \Sigma_{s1,1\to1} & -\Sigma_{s1,2\to1} & \cdots & -\Sigma_{s1,G\to1} \\ -\Sigma_{s1,1\to2} & \Sigma_{t2} - \Sigma_{s1,2\to2} & \cdots & -\Sigma_{s1,G\to2} \\ \vdots & \vdots & \ddots & \vdots \\ -\Sigma_{s1,1\to G} & -\Sigma_{s1,2\to G} & \cdots & \Sigma_{tG} - \Sigma_{s1,G\to G} \end{pmatrix}^{-1} \begin{pmatrix} \frac{d\phi_{12}}{dx} \\ \frac{d\phi_{22}}{dx} \\ \vdots \\ \frac{d\phi_{G2}}{dx} \end{pmatrix} . \quad (4.7)$$

If we define the $G \times G$ matrix

$$\begin{pmatrix} D_{11} & D_{21} & \cdots & D_{G1} \\ D_{12} & D_{22} & \cdots & D_{G2} \\ \vdots & \vdots & \ddots & \vdots \\ D_{1G} & D_{2G} & \cdots & D_{GG} \end{pmatrix} = \begin{pmatrix} \Sigma_{t1} - \Sigma_{s1,1\to1} & -\Sigma_{s1,2\to1} & \cdots & -\Sigma_{s1,G\to1} \\ -\Sigma_{s1,1\to2} & \Sigma_{t2} - \Sigma_{s1,2\to2} & \cdots & -\Sigma_{s1,G\to2} \\ \vdots & \vdots & \ddots & \vdots \\ -\Sigma_{s1,1\to G} & -\Sigma_{s1,2\to G} & \cdots & \Sigma_{tG} - \Sigma_{s1,G\to G} \end{pmatrix}^{-1} \quad (4.8)$$

then for each energy group g, the first order moment $\phi_{g1}(x)$ can be written as:

$$\phi_{g1}(x) = -\sum_{g'=1}^{G} D_{g'g}(x) \frac{d\phi_{g'2}(x)}{dx} . \quad (4.9)$$

Using this result to eliminate ϕ_{g1} from Eqs. (4.4a), (4.4c), and (4.4d), we obtain:

$$-\frac{d}{dx}\left[\sum_{g'=1}^{G} D_{g'g}(x) \frac{d\phi_{g'2}(x)}{dx}\right] + \Sigma_{tg}\phi_{g0} = \sum_{g'=1}^{G} \Sigma_{s0,g'\to g}(x)\phi_{g'0}(x) + \frac{\chi_g}{k} \sum_{g'=1}^{G} \nu\Sigma_{fg'}(x)\phi_{g'0}(x) , \quad (4.10a)$$

$$\sum_{g'=1}^{G} D_{g'g}(0)\frac{d\phi_{g'2}(0)}{dx} = \int_{-1}^{1} |\mu|\psi_g(0,\mu)\,d\mu\ , \tag{4.10b}$$

$$\sum_{g'=1}^{G} D_{g'g}(X)\frac{d\phi_{g'2}(X)}{dx} = -\int_{-1}^{1} |\mu|\psi_g(X,\mu)\,d\mu\ . \tag{4.10c}$$

These angularly-integrated equations are exactly satisfied by the solution to Eqs. (4.1).

To perform the spatial integrations, we define a spatial grid $0 = x_{1/2} < x_{3/2} < \cdots < x_{J+1/2} = X$, and for each grid point $x_{j+1/2}$ we define the tent functions $f(x) = f_{j+1/2}(x)$ as in Chapter 2.

For each j, we now perform the operation $\int_0^X f_{j+1/2}(x)(\cdot)dx$ on Eq. (4.10a). For the interior j's, i.e. for $1 \le j \le J-1$, we get:

$$\begin{aligned}
&-\int_0^X f(x)\frac{d}{dx}\left[\sum_{g'=1}^{G} D_{g'g}(x)\frac{d\phi_{g'2}(x)}{dx}\right]dx + \int_0^X f(x)\Sigma_{tg}(x)\phi_{g0}(x)dx \\
&\quad = \int_0^X f(x)\sum_{g'=1}^{G}\Sigma_{s0,g'\to g}(x)\phi_{g'0}(x)dx + \int_0^X f(x)\frac{\chi_g}{k}\sum_{g'=1}^{G}\nu\Sigma_{fg'}(x)\phi_{g'0}(x)dx\ .
\end{aligned} \tag{4.11}$$

Integrating the leakage (first) term by parts, we get:

$$\begin{aligned}
&-\int_0^X f(x)\frac{d}{dx}\left[\sum_{g'=1}^{G} D_{g'g}(x)\frac{d\phi_{g'2}(x)}{dx}\right]dx \\
&= -\int_{x_{j-1/2}}^{x_{j+3/2}} f_{j+1/2}(x)\frac{d}{dx}\left[\sum_{g'=1}^{G} D_{g'g}(x)\frac{d\phi_{g'2}(x)}{dx}\right]dx \\
&= -\left[f_{j+1/2}(x)\sum_{g'=1}^{G} D_{g'g}(x)\frac{d\phi_{g'2}(x)}{dx}\Big|_{x_{j-1/2}}^{x_{j+3/2}} - \int_{x_{j-1/2}}^{x_{j+3/2}}\frac{df_{j+1/2}(x)}{dx}\sum_{g'=1}^{G} D_{g'g}(x)\frac{d\phi_{g'2}(x)}{dx}dx\right] \\
&= \int_{x_{j-1/2}}^{x_{j+1/2}}\frac{1}{h_j}\sum_{g'=1}^{G} D_{g'g}(x)\frac{d\phi_{g'2}(x)}{dx}dx + \int_{x_{j+1/2}}^{x_{j+3/2}}(-\frac{1}{h_{j+1}})\sum_{g'=1}^{G} D_{g'g}(x)\frac{d\phi_{g'2}(x)}{dx}dx \\
&= \sum_{g'=1}^{G}\frac{D_{g'g,j}}{h_j}[\phi_{g'2}(x_{j+1/2}) - \phi_{g'2}(x_{j-1/2})] - \sum_{g'=1}^{G}\frac{D_{g'g,j+1}}{h_{j+1}}[\phi_{g'2}(x_{j+3/2}) - \phi_{g'2}(x_{j+1/2})]\ .
\end{aligned} \tag{4.12}$$

Thus, Eq. (4.10a) yields the following result:

$$\sum_{g'=1}^{G} \frac{D_{g'g,j}}{h_j}[\phi_{g'2}(x_{j+1/2}) - \phi_{g'2}(x_{j-1/2})] - \sum_{g'=1}^{G} \frac{D_{g'g,j+1}}{h_{j+1}}[\phi_{g'2}(x_{j+3/2}) - \phi_{g'2}(x_{j+1/2})]$$
$$+ \Sigma_{tg,j} \int_{x_{j-1/2}}^{x_{j+1/2}} f^{-}_{j+1/2}(x)\phi_{g0}(x)dx + \Sigma_{tg,j+1} \int_{x_{j+1/2}}^{x_{j+3/2}} f^{+}_{j+1/2}(x)\phi_{g0}(x)dx$$
$$= \sum_{g'=1}^{G} \left[\Sigma_{s0,g'g,j} \int_{x_{j-1/2}}^{x_{j+1/2}} f^{-}_{j+1/2}(x)\phi_{g'0}(x)dx + \Sigma_{s0,g'g,j+1} \int_{x_{j+1/2}}^{x_{j+3/2}} f^{+}_{j+1/2}(x)\phi_{g'0}(x)dx \right]$$
$$+ \frac{\chi_g}{k} \sum_{g'=1}^{G} \left[\nu\Sigma_{fg',j} \int_{x_{j-1/2}}^{x_{j+1/2}} f^{-}_{j+1/2}(x)\phi_{g'0}(x)dx + \nu\Sigma_{fg',j+1} \int_{x_{j+1/2}}^{x_{j+3/2}} f^{+}_{j+1/2}(x)\phi_{g'0}(x)dx \right]. \tag{4.13}$$

To define the FMC flux unknowns, we define functions $g_{j+1/2}(x)$ for $0 \le j \le J$. As before, we consider two sets of such functions; the first set is:

$$g_{j+1/2}(x) = \delta(x - x_{j+1/2}) \,, \;\; 0 \le j \le J \,. \tag{4.14}$$

The second set is defined by taking $x_j = (x_{j+1/2} + x_{j-1/2})/2$ = midpoint of the j^{th} cell and setting, for $j = 0$,

$$g_{1/2}(x) = \begin{cases} \frac{2}{h_1} & , \quad x_{1/2} \le x \le x_1 \\ 0 & , \quad \text{otherwise} \;\; , \end{cases} \tag{4.15a}$$

for $1 \le j \le J-1$,

$$g_{j+1/2}(x) = \begin{cases} \frac{2}{h_j + h_{j+1}} & , \quad x_j \le x \le x_{j+1} \\ 0 & , \quad \text{otherwise} \;\; , \end{cases} \tag{4.15b}$$

and for $j = J$,

$$g_{J+1/2}(x) = \begin{cases} \frac{2}{h_J} & , \quad x_J \le x \le x_{J+1/2} \\ 0 & , \quad \text{otherwise} \;\; . \end{cases} \tag{4.15c}$$

We now use either definition of $g_{j+1/2}(x)$ to define flux quantities:

$$\Phi_{g0}(x_{j+1/2}) = \int_0^X g_{j+1/2}(x)\phi_{g0}(x)\,dx\,. \tag{4.16}$$

With Eq. (4.14), $\Phi_{g0}(x_{j+1/2})$ is a cell-edge flux at $x_{j+1/2}$. With Eqs. (4.15), $\Phi_{g0}(x_{j+1/2})$ is a cell-averaged flux between the midpoints of the j^{th} and $(j+1)^{st}$ cells. With either definition, $\Phi_{g0}(x_{j+1/2})$ can be used to define the nonlinear functionals:

$$E_g(x_{j+1/2}) = \frac{\int_{-1}^{1}\mu^2\psi_g(x_{j+1/2},\mu)d\mu}{\Phi_{g0}(x_{j+1/2})} \qquad 0 \le j \le J\ ,\ 1 \le g \le G\,, \tag{4.17a}$$

$$F_g^-(x_{j+1/2}) = \frac{\int_{x_{j-1/2}}^{x_{j+1/2}} f^-_{j+1/2}(x)\phi_{g0}(x)dx}{\Phi_{g0}(x_{j+1/2})} \quad 1 \le j \le J\ ,\ 1 \le g \le G\,, \tag{4.17b}$$

$$F_g^+(x_{j+1/2}) = \frac{\int_{x_{j+1/2}}^{x_{j+3/2}} f^+_{j+1/2}(x)\phi_{g0}(x)dx}{\Phi_{g0}(x_{j+1/2})} \quad 0 \le j \le J-1\ ,\ 1 \le g \le G\,. \tag{4.17c}$$

We use these functionals to rewrite the interior Eq. (4.13) as:

$$\begin{aligned}
&-\sum_{g'=1}^{G}\frac{D_{g'g,j}}{h_j}E_{g'}(x_{j-1/2})\Phi_{g'0}(x_{j-1/2}) + \sum_{g'=1}^{G}\left[\frac{D_{g'g,j}}{h_j}+\frac{D_{g'g,j+1}}{h_{j+1}}\right]E_{g'}(x_{j+1/2})\Phi_{g'0}(x_{j+1/2})\\
&-\sum_{g'=1}^{G}\frac{D_{g'g,j+1}}{h_{j+1}}E_{g'}(x_{j+3/2})\Phi_{g'0}(x_{j+3/2}) + \left[\Sigma_{tg,j}F_g^-(x_{j+1/2})+\Sigma_{tg,j+1}F_g^+(x_{j+1/2})\right]\Phi_{g0}(x_{j+1/2})\\
&=\sum_{g'=1}^{G}\left[\Sigma_{s0,g'g,j}F_{g'}^-(x_{j+1/2})+\Sigma_{s0,g'g,j+1}F_{g'}^+(x_{j+1/2})\right]\Phi_{g'0}(x_{j+1/2})\\
&+\frac{\chi_g}{k}\sum_{g'=1}^{G}\left[\nu\Sigma_{fg',j}F_{g'}^-(x_{j+1/2})+\nu\Sigma_{fg',j+1}F_{g'}^+(x_{j+1/2})\right]\Phi_{g'0}(x_{j+1/2})\,.
\end{aligned} \tag{4.18}$$

It remains to develop similar equations at the boundaries. Similarly, we define the boundary Eddington factors:

$$E_g^b(x_{1/2}) = \frac{\int_{-1}^{1}|\mu|\psi_g(x_{1/2},\mu)d\mu}{\Phi_{g0}(x_{1/2})} \qquad ,\ 1 \le g \le G \tag{4.19a}$$

$$E_g^b(x_{J+1/2}) = \frac{\int_{-1}^{1} |\mu| \psi_g(x_{J+1/2}, \mu) d\mu}{\Phi_{g0}(x_{J+1/2})} \quad , \ 1 \le g \le G \, . \tag{4.19b}$$

We may rewrite Eqs. (4.10b) and (4.10c) as:

$$\sum_{g'=1}^{G} D_{g'g}(0) \frac{d\phi_{g'2}(0)}{dx} = E_g^b(0) \Phi_{g0}(0) \, , \tag{4.20a}$$

$$\sum_{g'=1}^{G} D_{g'g}(X) \frac{d\phi_{g'2}(X)}{dx} = E_g^b(X) \Phi_{g0}(X) \, . \tag{4.20b}$$

For the left boundary ($j = 0$), we introduce $f_{1/2}(x) = f_{1/2}^{+}(x)$ (Eq. (2.22)) into Eq. (4.10a). Using Eq. (4.17a) and Eq. (4.20a), the leakage term becomes:

$$\begin{aligned}
&- \int_0^X f(x) \frac{d}{dx} \left[\sum_{g'=1}^{G} D_{g'g}(x) \frac{d\phi_{g'2}(x)}{dx} \right] dx \\
&= - \int_{x_{1/2}}^{x_{3/2}} f_{1/2}^{+}(x) \frac{d}{dx} \left[\sum_{g'=1}^{G} D_{g'g}(x) \frac{d\phi_{g'2}(x)}{dx} \right] dx \\
&= - \left[f_{1/2}^{+}(x) \sum_{g'=1}^{G} D_{g'g}(x) \frac{d\phi_{g'2}(x)}{dx} \Big|_{x_{1/2}}^{x_{3/2}} - \int_{x_{1/2}}^{x_{3/2}} \frac{df_{1/2}^{+}(x)}{dx} \sum_{g'=1}^{G} D_{g'g}(x) \frac{d\phi_{g'2}(x)}{dx} dx \right] \\
&= \sum_{g'=1}^{G} D_{g'g}(x_{1/2}) \frac{d\phi_{g'2}(x_{1/2})}{dx} + \int_{x_{1/2}}^{x_{3/2}} (-\frac{1}{h_1}) \sum_{g'=1}^{G} D_{g'g}(x) \frac{d\phi_{g'2}(x)}{dx} dx \\
&= E_g^b(x_{1/2}) \Phi_{g0}(x_{1/2}) - \sum_{g'=1}^{G} \frac{D_{g'g,1}}{h_1} [\phi_{g'2}(x_{3/2}) - \phi_{g'2}(x_{1/2})] \\
&= E_g^b(x_{1/2}) \Phi_{g0}(x_{1/2}) - \sum_{g'=1}^{G} \frac{D_{g'g,1}}{h_1} [E_{g'}(x_{3/2}) \Phi_{g'0}(x_{3/2}) - E_{g'}(x_{1/2}) \Phi_{g'0}(x_{1/2})] \, .
\end{aligned} \tag{4.21}$$

Then Eq. (4.10a) yields the following result:

$$\begin{aligned}
&E_g^b(x_{1/2}) \Phi_{g0}(x_{1/2}) - \sum_{g'=1}^{G} \frac{D_{g'g,1}}{h_1} [E_{g'}(x_{3/2}) \Phi_{g'0}(x_{3/2}) - E_{g'}(x_{1/2}) \Phi_{g'0}(x_{1/2})] \\
&+ \Sigma_{tg,1} F_g^{+}(x_{1/2}) \Phi_{g0}(x_{1/2}) \\
&= \sum_{g'=1}^{G} \Sigma_{s0,g'g,1} F_{g'}^{+}(x_{1/2}) \Phi_{g'0}(x_{1/2}) + \frac{\chi_g}{k} \sum_{g'=1}^{G} \nu \Sigma_{fg',1} F_{g'}^{+}(x_{1/2}) \Phi_{g'0}(x_{1/2}) \, .
\end{aligned} \tag{4.22}$$

For the right boundary $j = J$, we introduce $f_{J+1/2}(x) = f^-_{J+1/2}(x)$ into Eq. (4.10a). Using Eq. (4.17b) and Eq. (4.20b), the leakage term becomes:

$$
\begin{aligned}
&-\int_0^X f(x)\frac{d}{dx}\left[\sum_{g'=1}^{G} D_{g'g}(x)\frac{d\phi_{g'2}(x)}{dx}\right]dx \\
&= -\int_{x_{J-1/2}}^{x_{J+1/2}} f^-_{J+1/2}(x)\frac{d}{dx}\left[\sum_{g'=1}^{G} D_{g'g}(x)\frac{d\phi_{g'2}(x)}{dx}\right]dx \\
&= -\left[f^-_{J+1/2}(x)\sum_{g'=1}^{G} D_{g'g}(x)\frac{d\phi_{g'2}(x)}{dx}\Big|_{x_{J-1/2}}^{x_{J+1/2}} - \int_{x_{J-1/2}}^{x_{J+1/2}} \frac{df^-_{J+1/2}(x)}{dx}\sum_{g'=1}^{G} D_{g'g}(x)\frac{d\phi_{g'2}(x)}{dx}dx\right] \\
&= \sum_{g'=1}^{G} D_{g'g}(x_{J+1/2})\frac{d\phi_{g'2}(x_{J+1/2})}{dx} + \int_{x_{J-1/2}}^{x_{J+1/2}} \frac{1}{h_J}\sum_{g'=1}^{G} D_{g'g}(x)\frac{d\phi_{g'2}(x)}{dx}dx \\
&= E^b_g(x_{J+1/2})\Phi_{g0}(x_{J+1/2}) + \sum_{g'=1}^{G}\frac{D_{g'g,J}}{h_J}[\phi_{g'2}(x_{J+1/2}) - \phi_{g'2}(x_{J-1/2})] \\
&= E^b_g(x_{J+1/2})\Phi_{g0}(x_{J+1/2}) + \sum_{g'=1}^{G}\frac{D_{g'g,J}}{h_J}[E_{g'}(x_{J+1/2})\Phi_{g'0}(x_{J+1/2}) - E_{g'}(x_{J-1/2})\Phi_{g'0}(x_{J-1/2})]\,.
\end{aligned}
\tag{4.23}
$$

Then Eq. (4.10a) yields the following result:

$$
\begin{aligned}
&E^b_g(x_{J+1/2})\Phi_{g0}(x_{J+1/2}) + \sum_{g'=1}^{G}\frac{D_{g'g,J}}{h_J}[E_{g'}(x_{J+1/2})\Phi_{g'0}(x_{J+1/2}) - E_{g'}(x_{J-1/2})\Phi_{g'0}(x_{J-1/2})] \\
&+\Sigma_{tg,J}F^-_g(x_{J+1/2})\Phi_{g0}(x_{J+1/2}) \\
&= \sum_{g'=1}^{G}\Sigma_{s0,g'g,J}F^-_{g'}(x_{J+1/2})\Phi_{g'0}(x_{J+1/2}) + \frac{\chi_g}{k}\sum_{g'=1}^{G}\nu\Sigma_{fg',J}F^-_{g'}(x_{J+1/2})\Phi_{g'0}(x_{J+1/2})\,.
\end{aligned}
\tag{4.24}
$$

Eqs. (4.18), (4.22) and (4.24) are exactly satisfied by the solution to the original k-eigenvalue problem. No approximations have been introduced, even though the introduction and use of a spatial grid may suggest otherwise.

In the FMC method, we use the foregoing equations in the following way:

1. We run a standard Monte Carlo simulation of Eqs. (4.1). The standard Monte Carlo

estimate of k is obtained by averaging the k for each cycle over all active cycles. We also tally standard Monte Carlo estimates of the eigenfunctions ϕ_{g0} for each energy group.

2. During this standard Monte Carlo run, we also estimate the integrals used in Eqs. (4.17) and Eqs. (4.19) for each cycle. At the end of each active cycle, the estimated values of the integrals so obtained are used to estimate the functionals $E_g(x_{j+1/2})$, $F_g^-(x_{j+1/2})$, $F_g^+(x_{j+1/2})$, $E_g^b(x_{1/2})$, and $E_g^b(x_{J+1/2})$. These values are introduced into Eqs. (4.18), (4.22) and (4.24), which are then solved to obtain estimates of k and the space-angle moments of the eigenfunctions $\Phi_{g0}(x_{j+1/2})$. [We note that if the values of the nonlinear functionals are free of statistical errors, the resulting values of k and $\Phi_{g0}(x_{j+1/2})$ will be exact.] The FMC estimate of k is obtained by averaging the k values from Eqs. (4.18), (4.22) and (4.24) for each cycle over all active cycles.

We note that the basic procedure employed in this chapter is a straightforward generalization of the procedure developed previously in Chapter 2 for one-group problems.

4.2 Numerical Results

We consider a homogeneous slab of thickness $X = 100$ cm surrounded by 5.0-cm reflectors. We specified four energy groups. The probability that a fission neutron will be born in energy groups 1 to 4 is taken to be $0.5, 0.2, 0.2, 0.1$, respectively. We assume P_3 anisotropic scattering, with both up scattering and down scattering. The differential scattering cross sections are defined as follows: for each $1 \leq g, g' \leq 4$: $\Sigma_{s0,g'\to g} = 0.21$, $\Sigma_{s1,g'\to g} = \Sigma_{s2,g'\to g} = \Sigma_{s3,g'\to g} = 0.03$. Other data are listed in Table 4.1.

The Monte Carlo simulation starts with a flat fission source. This problem was run for 410 cycles, using 100,000 histories/cycle. The FMC calculations employed a grid with $h = 0.5$ cm. The estimated values of k, with their estimated standard deviations over 5 different ranges of 10 cycles, are given in Table 4.2 for the standard Monte Carlo and the

Table 4.1 Data for Multi-Group Problem.

Region	Location	Σ_{t1}	Σ_{t2}	Σ_{t3}	Σ_{t4}	Σ_{fg}
1	$0 < x < 5$	1.05	1.25	1.50	1.75	0
2	$5 < x < 105$	1.05	1.25	1.50	1.75	0.187
3	$105 < x < 110$	1.05	1.25	1.50	1.75	0

FMC methods. The fine-mesh ($h = 0.05$ cm) S_N eigenvalue estimate is $k = 0.996713$.

Also, the eigenfunction estimates for each energy group, averaged over cycles 11-20, 101-110, 201-210,301-310, and 401-410, for the standard Monte Carlo and FMC methods are shown in Figures 4.1-4.5. For comparison, the S_N results are plotted as well.

Table 4.2 Estimates of k and its Relative Standard Deviation for Multi-Group Problem.

Cycles	Standard MC	FMC Edge	FMC Average
11 to 20	0.995486 (0.0008962)	0.996711 (0.0000009)	0.996710 (0.0000003)
101 to 110	0.996010 (0.0009095)	0.996709 (0.0000006)	0.996712 (0.0000006)
201 to 210	0.996137 (0.0012731)	0.996709 (0.0000009)	0.996711 (0.0000006)
301 to 310	0.996661 (0.0011447)	0.996711 (0.0000006)	0.996710 (0.0000003)
401 to 410	0.996562 (0.0012978)	0.996710 (0.0000006)	0.996710 (0.0000006)

Figures 4.1-4.5 show that the standard Monte Carlo estimates of ϕ_g, averaged over cycles 11-20, 101-110, 201-210,301-310, and 401-410, are noisier and less accurate than the corresponding FMC estimates. Overall, the standard Monte Carlo method shows a very slow "convergence" of the fission source. In fact, the FMC eigenfunction is essentially converged after only 10 cycles, while the standard Monte Carlo estimate of the eigenfunction shows evidence of not being converged even after 400 cycles. Moreover, the standard Monte Carlo flux estimates never fully converge to the exact smooth nearly cosine-shape; these estimates always "wobble" in a noisy way around this estimate.

The reason for the more rapid and less noisy convergence of the FMC solution is that the

nonlinear functionals depend only weakly on the estimated eigenfunctions. (However, the Monte Carlo-estimated surface fluxes exhibit more fluctuation than the cell averaged fluxes, so the estimates of ϕ_g using the FMC "edge" method are slightly noisier than estimates using the FMC "average" method.)

Table 4.2 shows that the errors in k obtained with the FMC methods are much smaller than the errors in the standard Monte Carlo estimate of k. The standard Monte Carlo estimates are only accurate to the first two digits, while both FMC edge and FMC average results are accurate to five digits.

We did not pursue the development and testing of the FMC method for multigroup problems, for following reasons.

1. Although the resulting FMC solutions have no spatial or angular truncation errors, they have energy-truncation errors resulting from the multigroup approximation. (These solutions also of course have statistical errors.) It seemed inappropriate to invest effort into developing a method free of spatial and angular truncation errors, but not free of energy truncation errors.
2. As can be seen from the results described in this chapter, the FMC method adapted to multigroup problems is a reasonably straightforward extension of the monoenergetic FMC method.

For these reasons, we decided instead to generalize the FMC method to continuous-energy problems in such a way that the resulting solution would have either no or exceedingly small energy truncation errors. This work is described next.

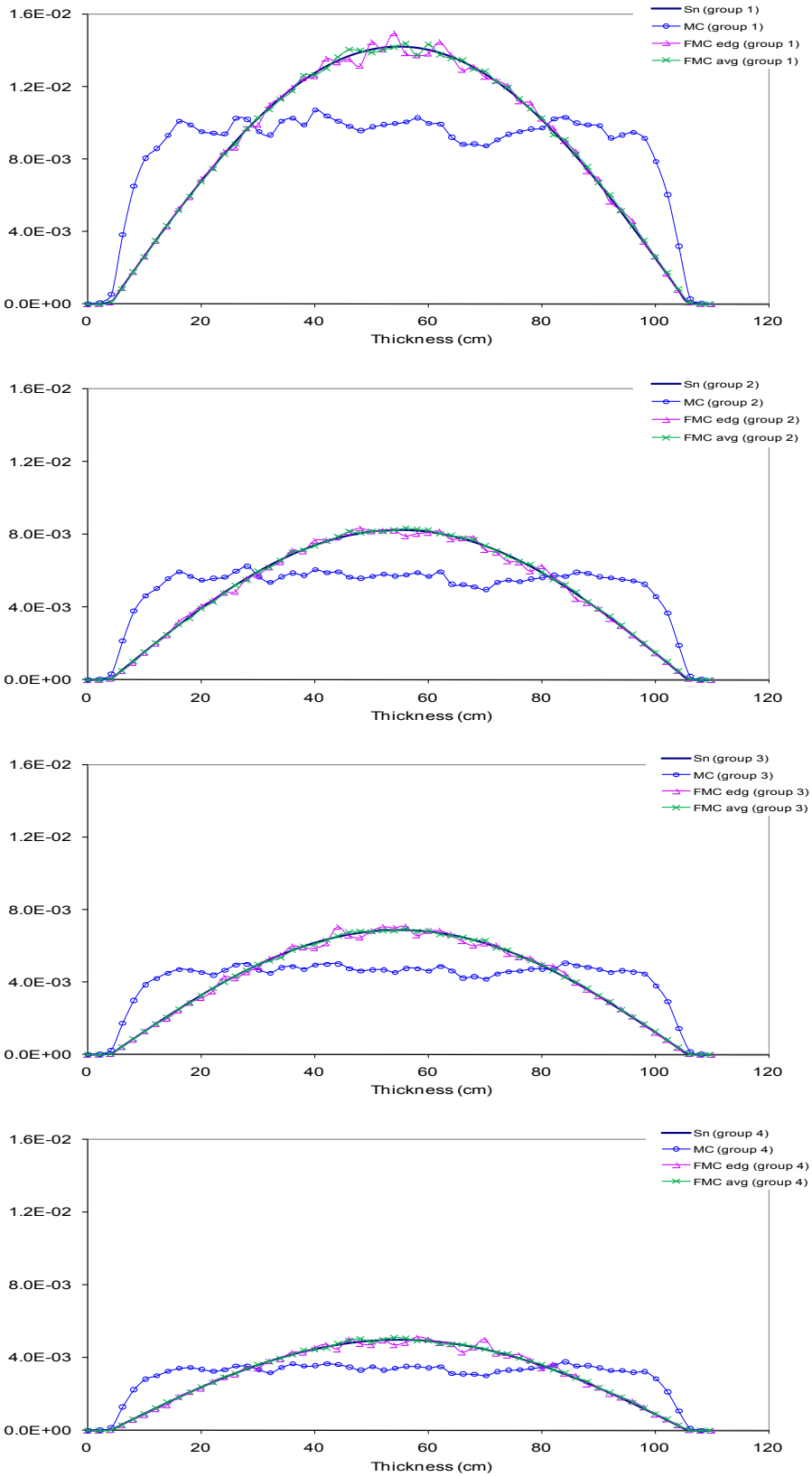

Figure 4.1 Estimates of the *k*-eigenfunction for cycles 11-20.

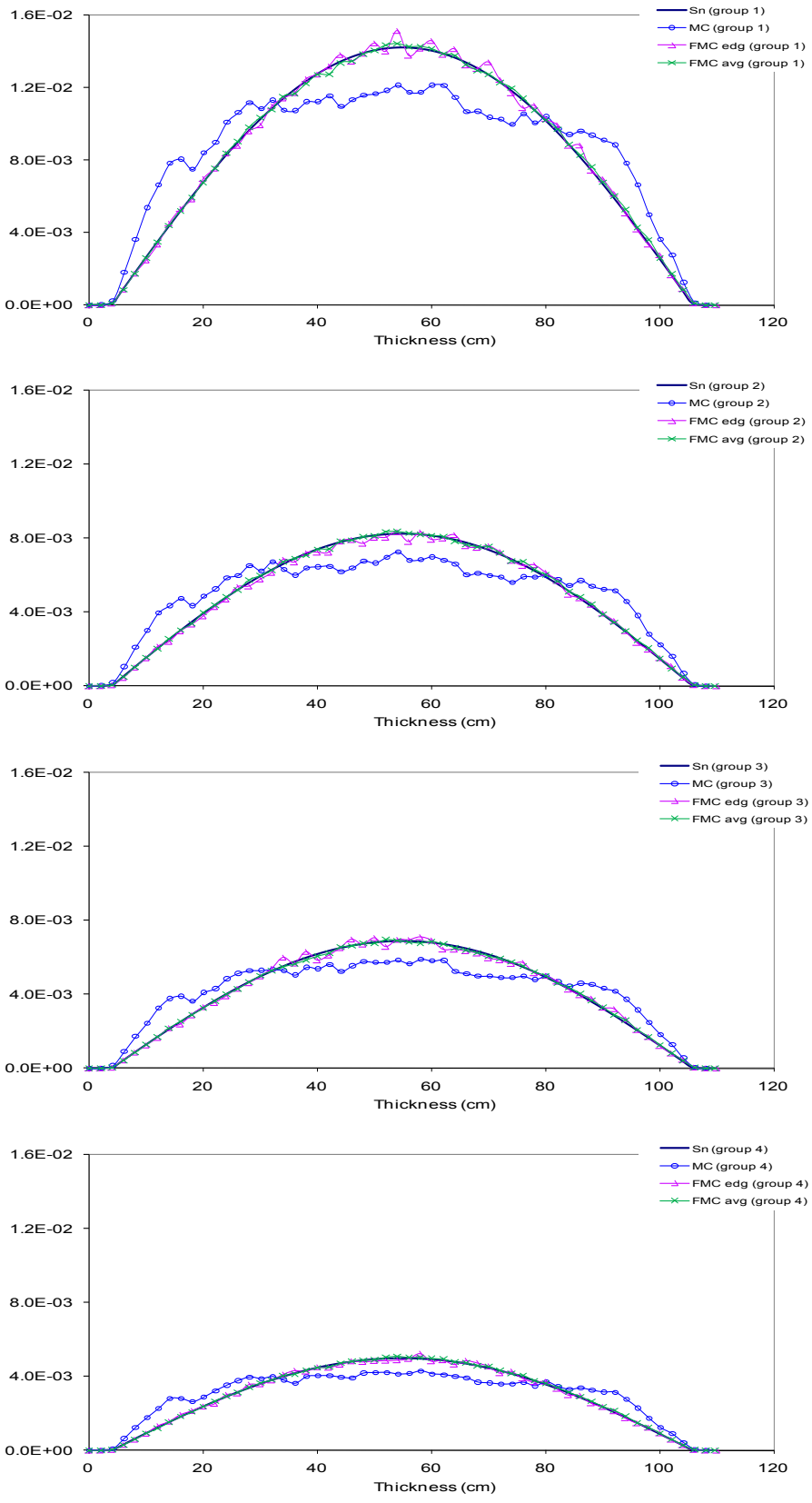

Figure 4.2 Estimates of the *k*-eigenfunction for cycles 101-110.

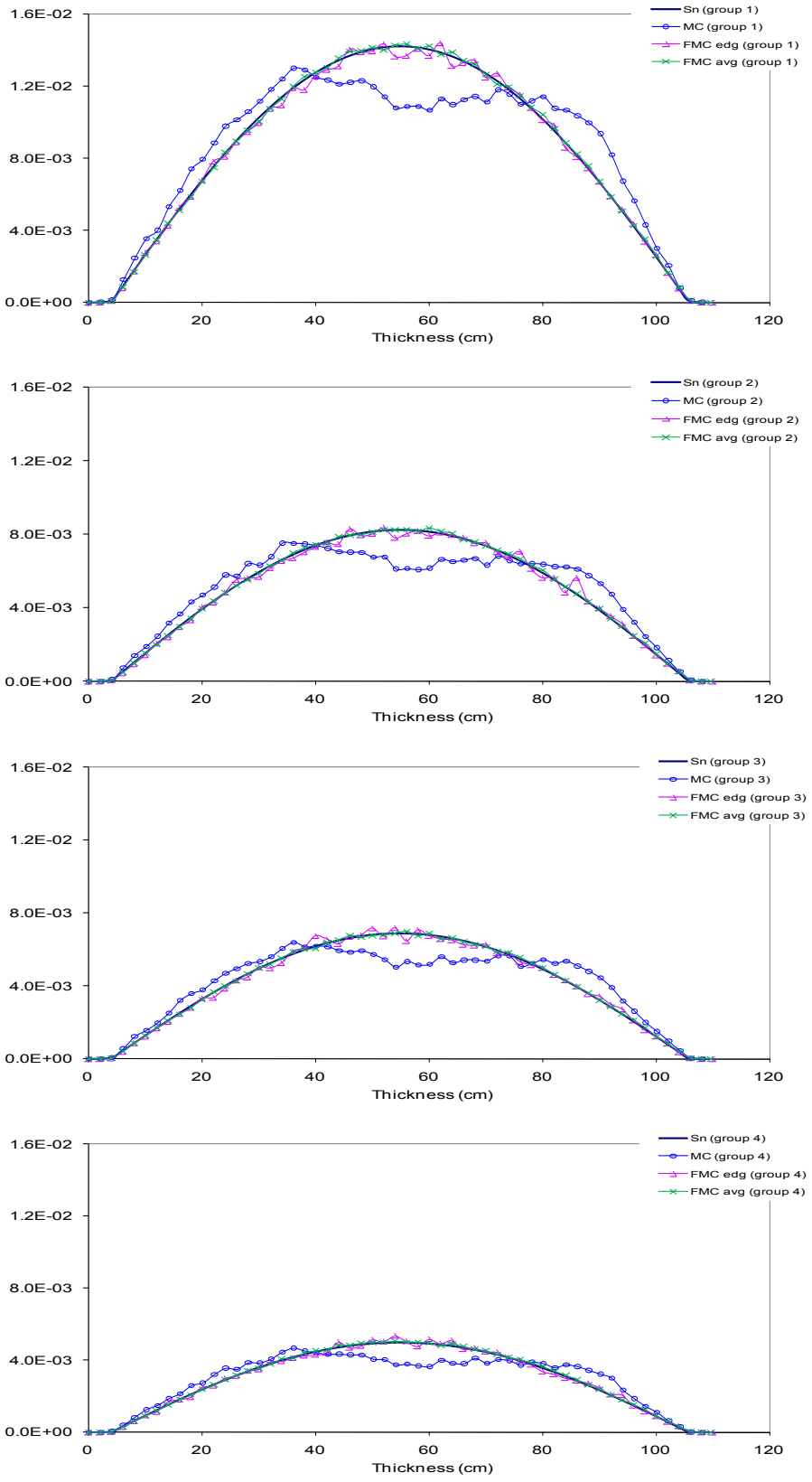

Figure 4.3 Estimates of the *k*-eigenfunction for cycles 201-210.

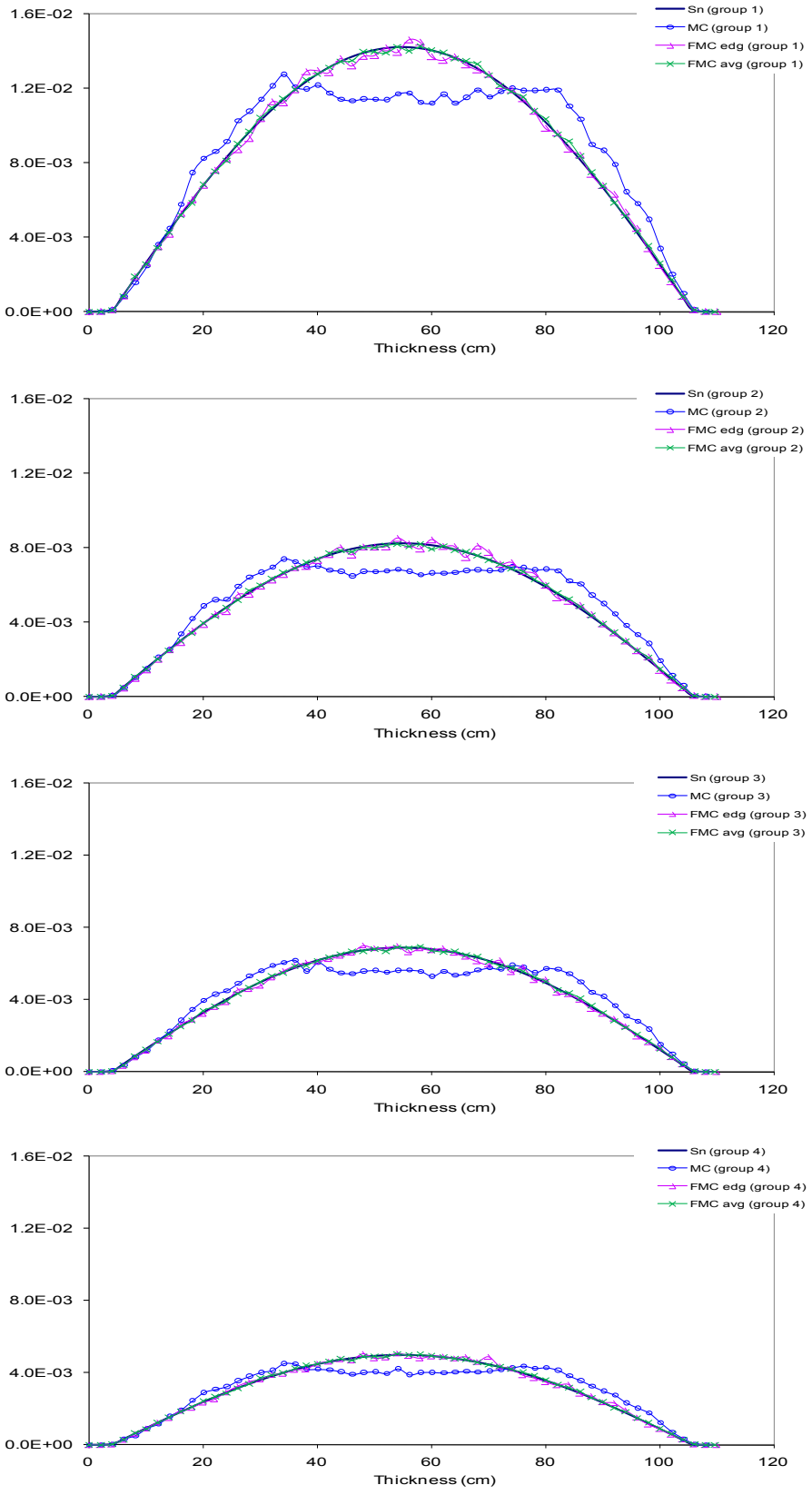

Figure 4.4 Estimates of the *k*-eigenfunction for cycles 301-310.

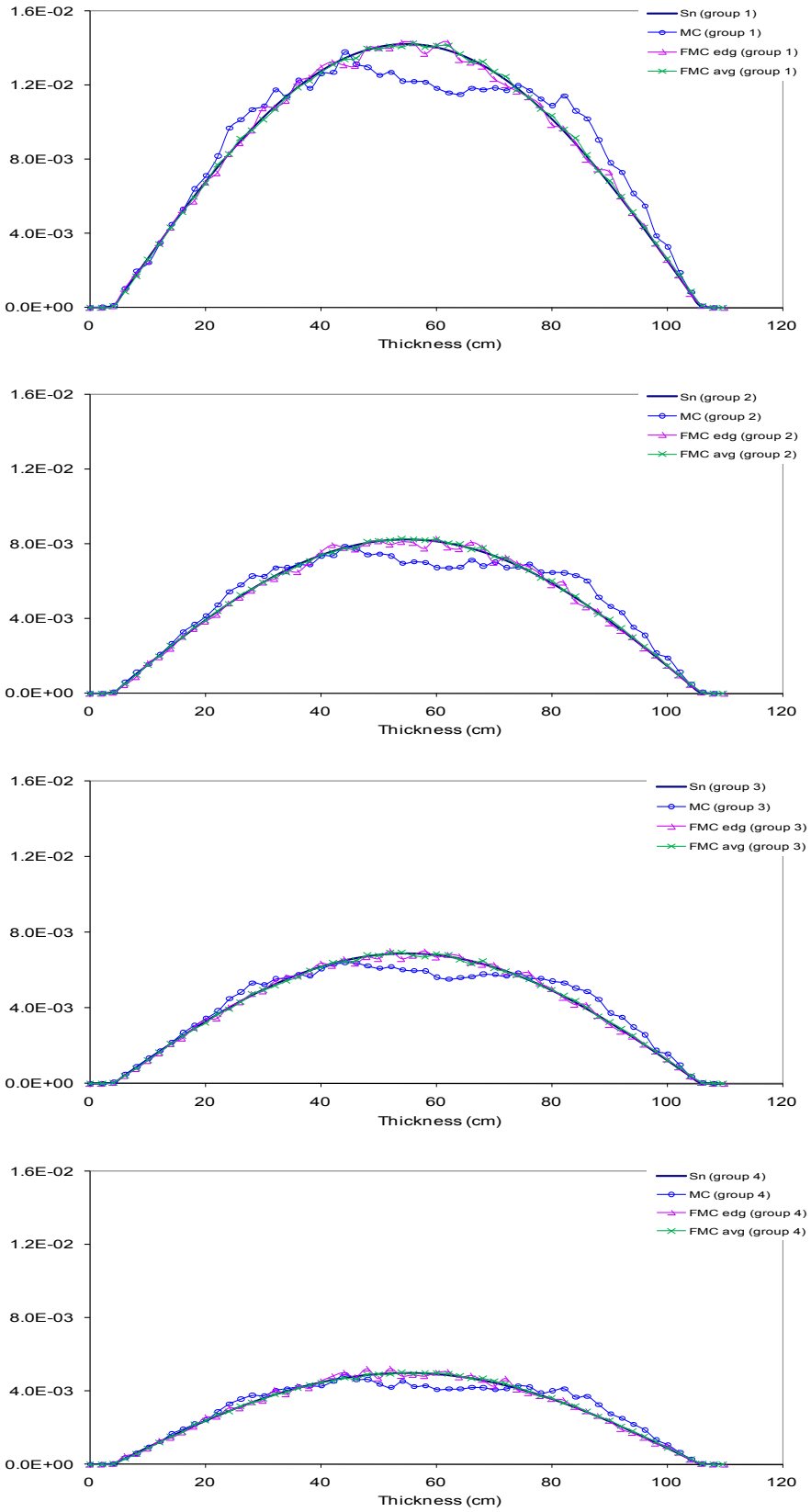

Figure 4.5 Estimates of the *k*-eigenfunction for cycles 401-410.

Chapter 5

The FMC method for 1-D Continuous Energy k-Eigenvalue Problems

In this chapter, we extend the FMC method to continuous-energy k-eigenvalue problems. This is an important step, because energy-varying cross-sections are much more realistic for practical applications. The continuous-energy approach has several noticeable differences compared with the monoenergetic and multigroup approaches. The low-order equations that we derive here are in two forms: (1) the low-order equations are energy-independent, and the eigenfunction is an energy-integrated scalar flux; (2) the low-order equations are multigroup in form with two or more groups. Specifically, (a) energy group nonlinear functionals are estimated using standard Monte Carlo with continuous-energy cross-sections; (b) these functionals are then used in low-order multigroup equations to estimate the eigenvalue and the multigroup fluxes. As in the previously-discussed monoenergetic and multigroup cases, the resulting FMC estimates of the eigenvalue and energy-integrated or multigroup fluxes have (i) no spatial or angular truncation errors, and (ii) very small energy truncation errors and statistical errors.

We begin by deriving the low-order energy-integrated equations and discussing a procedure to evaluate the $U(x,E)$ function. We then formulate the low-order multigroup equations, and accordingly we discuss a procedure to evaluate the multigroup $U_g(x,E)$ function introduced in our method of solution. Finally, a procedure to generate low-order equations with any number of material discontinuities of cross sections within a spatial cell is presented.

5.1 Procedure to Generate Low-Order Energy-Integrated Equations

We consider a general planar-geometry, continuous energy k-eigenvalue problem with vacuum boundaries

$$\mu\frac{\partial\psi}{\partial x}(x,\mu,E)+\Sigma_t(x,E)\psi(x,\mu,E)=\int\int\Sigma_s(x,\mu,\mu',E'\to E)\psi(x,\mu',E')d\mu'dE'$$
$$+\frac{\chi(x,E)}{2k}\int\int\nu\Sigma_f(x,E')\psi(x,\mu',E')d\mu'dE',\quad 0<x<X\ , \tag{5.1a}$$

$$\psi(0,\mu,E)=0\quad,\quad 0<\mu\leq 1\ , \tag{5.1b}$$

$$\psi(X,\mu,E)=0\quad,\quad -1\leq\mu<0\ , \tag{5.1c}$$

and with elastic neutron scattering:

$$\Sigma_s(x,\mu,\mu',E'\to E)=\sum_{n=0}^{\infty}\frac{2n+1}{2}\Sigma_{sn}(x,E'\to E)P_n(\mu)P_n(\mu')\ , \tag{5.1d}$$

$$\Sigma_t(x,E)=\Sigma_\gamma(x,E)+\Sigma_f(x,E)+\Sigma_s(x,E)\ , \tag{5.1e}$$

$$\Sigma_s(x,E)=\int_0^\infty\Sigma_{s0}(x,E\to E')dE'\ , \tag{5.1f}$$

$$\int_0^\infty\chi(x,E)dE=1\ , \tag{5.1g}$$

where

$$\Sigma_{sn}(x,E'\to E)=2\pi\int_{-1}^{1}P_n(\mu_0)\Sigma_s(x,\mu_0,E'\to E)d\mu_0$$
$$=2\pi\int_{-1}^{1}P_n(\mu_0)\Sigma_s(x,E')P(E'\to E)\frac{\delta(\mu_0-\hat{\mu}_0)}{2\pi}d\mu_0$$
$$=\Sigma_s(x,E')P(E'\to E)P_n(\hat{\mu}_0)\ ,$$

$$\hat{\mu}_0(E'\to E)=\left(\frac{A+1}{2}\right)\sqrt{\frac{E}{E'}}-\left(\frac{A-1}{2}\right)\sqrt{\frac{E'}{E}}\ ,$$

$$P(E'\to E)=\begin{cases}\frac{1}{(1-\alpha)E'} & \alpha E'<E<E'\\ 0 & \text{otherwise}\ .\end{cases}$$

Our procedure to solve Eqs. (5.1) consists of two principal parts. The first part follows closely the three-step procedure used earlier to determine and solve the monoenergetic low-order FMC equations in Section 2.2. However, we now must introduce a function $U(x,E)$ into these equations to accommodate the continuous-energy feature. The second part is to show how the function $U(x,E)$ is determined with very small energy truncation errors. These two parts are presented in Sections 5.1.1 and 5.1.2, respectively.

5.1.1 Low-Order Energy-Integrated Equations (Part 1)

For continuous energy problems, the FMC equations are obtained by calculating certain space-angle-energy moments of Eqs. (5.1). Following the first step used in the monoenergetic case, we begin by operating on Eq. (5.1a) with $\int_{-1}^{1} \mu^n(\cdot)\, d\mu$ for $n = 0$ and 1. We define

$$\Phi_n(x,E) = \int_{-1}^{1} \mu^n \psi(x,\mu,E) d\mu \quad , \qquad n = 0,1,2\,. \tag{5.2}$$

For $n = 0$, we obtain

$$\frac{\partial}{\partial x}\Phi_1(x,E) + \Sigma_t(x,E)\Phi_0(x,E) = \int_0^\infty \Sigma_{s0}(x,E' \to E)\Phi_0(x,E')dE' + \frac{\chi(x,E)}{k}\int_0^\infty \nu\Sigma_f(x,E')\Phi_0(x,E')dE'\,; \tag{5.3}$$

and for $n = 1$, we obtain

$$\frac{\partial}{\partial x}\Phi_2(x,E) + \Sigma_t(x,E)\Phi_1(x,E) = \int_0^\infty \Sigma_{s1}(x,E' \to E)\Phi_1(x,E')dE'\,. \tag{5.4}$$

Eqs. (5.3) and (5.4) are two exact equations satisfied by the angular flux moments $\Phi_0(x,E)$, $\Phi_1(x,E)$, and $\Phi_2(x,E)$. To derive the most efficient low-order equations for the FMC method, we found it beneficial to eliminate $\Phi_1(x,E)$ from these equations. Eliminating Φ_1 can be done by introducing a new function $U(x,E)$, which satisfies an infinite-medium adjoint transport equation, and which can be determined to arbitrary accuracy at the beginning

of an FMC calculation. Next, we derive the equation defining $U(x,E)$.

We subtract a term $u(x,E)\Phi_1(x,E)$ from both side of Eq. (5.4). [The definition of $u(x,E)$ will be stated below.]

$$\frac{\partial}{\partial x}\Phi_2(x,E)+[\Sigma_t(x,E)-u(x,E)]\Phi_1(x,E)=\int_0^\infty \Sigma_{s1}(x,E'\to E)\Phi_1(x,E')dE'-u(x,E)\Phi_1(x,E)\,.$$

From the preceding equation, we obtain

$$\begin{aligned}\Phi_1(x,E) = &-\frac{1}{\Sigma_t(x,E)-u(x,E)}\frac{\partial}{\partial x}\Phi_2(x,E)\\ &+\frac{1}{\Sigma_t(x,E)-u(x,E)}\left[\int_0^\infty \Sigma_{s1}(x,E'\to E)\Phi_1(x,E')dE'-u(x,E)\Phi_1(x,E)\right].\end{aligned} \tag{5.5}$$

Now we define the energy integrals

$$\phi_n(x)=\int_0^\infty \Phi_n(x,E)dE\,,\qquad n=0,1\,.$$

Then, operating on Eq. (5.3) by $\int_0^\infty(\cdot)dE$, we get:

$$\begin{aligned}\frac{d}{dx}\phi_1(x)+\int_0^\infty \Sigma_t(x,E)\Phi_0(x,E)dE = &\int_0^\infty \Sigma_s(x,E')\Phi_0(x,E')dE'\\ &+\frac{1}{k}\int_0^\infty \nu\Sigma_f(x,E')\Phi_0(x,E')dE'\,.\end{aligned} \tag{5.6}$$

However,

$$\begin{aligned}\Sigma_t(x,E) &= \Sigma_s(x,E)+\Sigma_\gamma(x,E)+\Sigma_f(x,E)\\ &= \Sigma_s(x,E)+\Sigma_a(x,E)\,,\end{aligned} \tag{5.7}$$

so Eq. (5.6) simplifies to

$$\frac{d}{dx}\phi_1(x) + \int_0^\infty \Sigma_a(x,E)\Phi_0(x,E)dE = \frac{1}{k}\int_0^\infty \nu\Sigma_f(x,E)\Phi_0(x,E)dE\ . \tag{5.8}$$

Also, operating on Eq. (5.5) by $\int_0^\infty(\cdot)dE$, we get

$$\begin{aligned}\phi_1(x) = &-\int_0^\infty \frac{1}{\Sigma_t(x,E)-u(x,E)}\frac{\partial}{\partial x}\Phi_2(x,E)dE \\ &+\int_0^\infty \frac{1}{\Sigma_t(x,E)-u(x,E)}\left[\int_0^\infty \Sigma_{s1}(x,E'\to E)\Phi_1(x,E')dE' - u(x,E)\Phi_1(x,E)\right]dE\ .\end{aligned}$$

Interchanging the dummy variables E and E', we find

$$\begin{aligned}\phi_1(x) = &-\int_0^\infty \frac{1}{\Sigma_t(x,E)-u(x,E)}\frac{\partial}{\partial x}\Phi_2(x,E)dE \\ &+\int_0^\infty \left[\int_0^\infty \frac{\Sigma_{s1}(x,E\to E')}{\Sigma_t(x,E')-u(x,E')}dE'\right]\Phi_1(x,E)dE \\ &-\int_0^\infty \frac{u(x,E)}{\Sigma_t(x,E)-u(x,E)}\Phi_1(x,E)dE \\ =&-\int_0^\infty \frac{1}{\Sigma_t(x,E)-u(x,E)}\frac{\partial}{\partial x}\Phi_2(x,E)dE \\ &+\int_0^\infty \underbrace{\left[\int_0^\infty \frac{\Sigma_{s1}(x,E\to E')}{\Sigma_t(x,E')-u(x,E')}dE' - \frac{u(x,E)}{\Sigma_t(x,E)-u(x,E)}\right]}_{\text{Set this term = 0.}}\Phi_1(x,E)dE\ .\end{aligned} \tag{5.9}$$

Now we specify that $u(x,E)$ be chosen to eliminate the $\Phi_1(x,E)$ term, yielding

$$\int_0^\infty \frac{\Sigma_{s1}(x,E\to E')}{\Sigma_t(x,E')-u(x,E')}dE' - \frac{u(x,E)}{\Sigma_t(x,E)-u(x,E)} = 0\ ;$$

or

$$\frac{\Sigma_t(x,E)}{\Sigma_t(x,E)-u(x,E)} - 1 = \int_0^\infty \frac{\Sigma_{s1}(x,E\to E')}{\Sigma_t(x,E')-u(x,E')}dE'. \tag{5.10}$$

Defining

$$U(x,E) = \frac{1}{\Sigma_t(x,E)-u(x,E)}\ ,$$

then Eq. (5.10) can be rewritten as the linear equation

$$\Sigma_t(x,E)U(x,E) - 1 = \int_0^\infty \Sigma_{s1}(x,E \to E')U(x,E')dE' \,, \tag{5.11}$$

where $U(x,E)$ satisfies $U(x,E) > 0$.

In Section 5.1.2, the function $U(x,E)$ is determined so as to satisfy Eq. (5.11). [Note that if scattering is isotropic, then $U(x,E) = \Sigma_t^{-1}(x,E)$.] Then Eq. (5.9) for $\phi_1(x)$ becomes

$$\phi_1(x) = -\int_0^\infty U(x,E)\frac{\partial}{\partial x}\Phi_2(x,E)dE \,. \tag{5.12}$$

Substituting Eq. (5.12) for $\phi_1(x)$ into Eq. (5.8) then gives:

$$-\frac{\partial}{\partial x}\int_0^\infty U(x,E)\frac{\partial}{\partial x}\Phi_2(x,E)dE + \int_0^\infty \Sigma_a(x,E)\Phi_0(x,E)dE = \frac{1}{k}\int_0^\infty \nu\Sigma_f(x,E)\Phi_0(x,E)dE \,. \tag{5.13}$$

Eq. (5.13) for $\Phi_0(x,E)$ and $\Phi_2(x,E)$ has been derived from Eqs. (5.3) and (5.4) using the function $U(x,E)$, which satisfies the infinite-medium adjoint Eq. (5.11). The important features of Eq. (5.13) are:

1. This equation contains $\Phi_0(x,E)$ and $\Phi_2(x,E)$ but not $\Phi_1(x,E)$. (We have found that eliminating Φ_1 is an important aspect of reducing the statistical errors in FMC simulations.)
2. The function $U(x,E)$ can be calculated for each material region at the beginning of a simulation, by applying a very fine energy grid to Eq. (5.11). This calculation only needs to be done once, and it can be made as accurate as desired by refining the energy grid.

Eq. (5.13) completes the first step in the method to solve Eq. (5.1).

In step 2, we perform the spatial integrations Eq. (5.13) using the same *tent functions* $f(x)$ as were used for monoenergetic problems. Thus, for each j, we perform the operation

$\int_0^X f_{j+1/2}(x)(\cdot)dx$ on Eq. (5.13). For $j=0$ we obtain

$$-\int_{x_{1/2}}^{x_{3/2}} f_{1/2}(x)\frac{\partial}{\partial x}\int_0^\infty U(x,E)\frac{\partial}{\partial x}\Phi_2(x,E)dEdx+\int_{x_{1/2}}^{x_{3/2}} f_{1/2}(x)\int_0^\infty \Sigma_a(x,E)\Phi_0(x,E)dEdx$$
$$=\frac{1}{k}\int_{x_{1/2}}^{x_{3/2}} f_{1/2}(x)\int_0^\infty \nu\Sigma_f(x,E)\Phi_0(x,E)dEdx\,. \tag{5.14}$$

Integrating the first term by parts gives

$$\begin{aligned}
&-\int_{x_{1/2}}^{x_{3/2}} f_{1/2}(x)\frac{\partial}{\partial x}\int_0^\infty U(x,E)\frac{\partial}{\partial x}\Phi_2(x,E)dE\,dx\\
&=-f_{1/2}(x)\int_0^\infty U(x,E)\frac{\partial}{\partial x}\Phi_2(x,E)dE\Big|_{x_{1/2}}^{x_{3/2}}-\frac{1}{h_1}\int_{x_{1/2}}^{x_{3/2}}\int_0^\infty U(x,E)\frac{\partial}{\partial x}\Phi_2(x,E)dE\\
&=\int_0^\infty U(x_{1/2},E)\frac{\partial}{\partial x}\Phi_2(x_{1/2},E)dE-\frac{1}{h_1}\int_{x_{1/2}}^{x_{3/2}}\int_0^\infty U(x,E)\frac{\partial}{\partial x}\Phi_2(x,E)dE\\
&=-\phi_1(x_{1/2})-\frac{1}{h_1}\int_0^\infty U_1(E)[\Phi_2(x_{3/2},E)-\Phi_2(x_{1/2},E)]dE\,.
\end{aligned}\tag{5.15}$$

In Eq. (5.15), we assumed that each spatial cell $[x_{j-1/2},x_{j+1/2}]$ consists of a single material. Therefore in the j^{th} cell, $U(x,E)=U_j(E)$ independent of x.

From the vacuum boundary condition, we have

$$\begin{aligned}
\phi_1(x_{1/2})&=\int_0^\infty\int_{-1}^1 \mu\psi(0,\mu,E)d\mu dE\\
&=\int_0^\infty\left[\int_0^1 \mu\psi(0,\mu,E)d\mu+\int_{-1}^0 \mu\psi(0,\mu,E)d\mu\right]dE\\
&=\int_0^\infty\int_{-1}^0 \mu\psi(0,\mu,E)d\mu dE\\
&=-\int_0^\infty\int_{-1}^0 |\mu|\psi(0,\mu,E)d\mu dE\,.
\end{aligned}\tag{5.16}$$

Substituting Eq. (5.16) into Eq. (5.15), the first term in Eq. (5.14) can be written

$$\begin{aligned}
&-\int_{x_{1/2}}^{x_{3/2}} f_{1/2}(x)\frac{\partial}{\partial x}\int_0^\infty U(x,E)\frac{\partial}{\partial x}\Phi_2(x,E)dE\,dx\\
&=\int_0^\infty\int_{-1}^0 |\mu|\psi(0,\mu,E)d\mu dE-\frac{1}{h_1}\int_0^\infty U_1(E)[\Phi_2(x_{3/2},E)-\Phi_2(x_{1/2},E)]dE\,.
\end{aligned}\tag{5.17}$$

Thus, for $j = 0$, Eq. (5.14) becomes

$$\int_0^\infty \int_{-1}^0 |\mu| \psi(0,\mu,E) d\mu dE - \frac{1}{h_1} \int_0^\infty U_1(E)[\Phi_2(x_{3/2},E) - \Phi_2(x_{1/2},E)]dE$$
$$+ \int_{x_{1/2}}^{x_{3/2}} f_{1/2}(x) \int_0^\infty \Sigma_a(x,E)\Phi_0(x,E) dE dx$$
$$= \frac{1}{k} \int_{x_{1/2}}^{x_{3/2}} f_{1/2}(x) \int_0^\infty \nu\Sigma_f(x,E)\Phi_0(x,E) dE dx \,. \tag{5.18}$$

We emphasize that this equation is exact; no approximations were introduced to derive it.

For the interior j's, i.e. for $1 \le j \le J-1$, we find

$$-\int_{x_{j-1/2}}^{x_{j+3/2}} f_{j+1/2}(x) \frac{\partial}{\partial x} \int_0^\infty U(x,E) \frac{\partial}{\partial x} \Phi_2(x,E) dE dx$$
$$+ \int_{x_{j-1/2}}^{x_{j+3/2}} f_{j+1/2}(x) \int_0^\infty \Sigma_a(x,E)\Phi_0(x,E) dE dx$$
$$= \frac{1}{k} \int_{x_{j-1/2}}^{x_{j+3/2}} f_{j+1/2}(x) \int_0^\infty \nu\Sigma_f(x,E)\Phi_0(x,E) dE dx \,. \tag{5.19}$$

Integrating the first term of Eq. (5.19) by parts, we get

$$-\int_{x_{j-1/2}}^{x_{j+3/2}} f_{j+1/2}(x) \left[\frac{\partial}{\partial x} \int_0^\infty U(x,E) \frac{\partial}{\partial x} \Phi_2(x,E) dE \right] dx$$
$$= \int_{x_{j-1/2}}^{x_{j+3/2}} \frac{d}{dx} f_{j+1/2}(x) \left[\int_0^\infty U(x,E) \frac{\partial}{\partial x} \Phi_2(x,E) dE \right] dx$$
$$= \int_{x_{j-1/2}}^{x_{j+1/2}} \frac{1}{h_j} \left[\int_0^\infty U(x,E) \frac{\partial}{\partial x} \Phi_2(x,E) dE \right] dx$$
$$- \int_{x_{j+1/2}}^{x_{j+3/2}} \frac{1}{h_{j+1}} \left[\int_0^\infty U(x,E) \frac{\partial}{\partial x} \Phi_2(x,E) dE \right] dx$$
$$= \frac{1}{h_j} \int_0^\infty U_j(E) \left[\Phi_2(x_{j+1/2},E) - \Phi_2(x_{j-1/2},E) \right] dE$$
$$- \frac{1}{h_{j+1}} \int_0^\infty U_{j+1}(E) \left[\Phi_2(x_{j+3/2},E) - \Phi_2(x_{j+1/2},E) \right] dE \,. \tag{5.20}$$

Substituting Eq. (5.20) into Eq. (5.19) then leads to

$$\begin{aligned}
&\frac{1}{h_j}\int_0^\infty U_j(E)\left[\Phi_2(x_{j+1/2},E)-\Phi_2(x_{j-1/2},E)\right]dE \\
&-\frac{1}{h_{j+1}}\int_0^\infty U_{j+1}(E)\left[\Phi_2(x_{j+3/2},E)-\Phi_2(x_{j+1/2},E)\right]dE \\
&+\int_{x_{j-1/2}}^{x_{j+3/2}} f_{j+1/2}(x)\int_0^\infty \Sigma_a(x,E)\Phi_0(x,E)dEdx \\
&=\frac{1}{k}\int_{x_{j-1/2}}^{x_{j+3/2}} f_{j+1/2}(x)\int_0^\infty \nu\Sigma_f(x,E)\Phi_0(x,E)dEdx\,. \qquad (5.21)
\end{aligned}$$

These equations also are exact.

For $j=J$, following similar steps as for $j=0$, we obtain another exact equation:

$$\begin{aligned}
&\int_0^\infty\int_0^1 \mu\psi(x_{J+1/2},\mu,E)d\mu dE \\
&+\frac{1}{h_J}\int_0^\infty U_J(E)[\Phi_2(x_{J+1/2},E)-\Phi_2(x_{J-1/2},E)]dE \\
&+\int_{x_{J-1/2}}^{x_{J+1/2}} f_{J+1/2}(x)\int_0^\infty \Sigma_a(x,E)\Phi_0(x,E)dEdx \\
&=\frac{1}{k}\int_{x_{J-1/2}}^{x_{J+1/2}} f_{J+1/2}(x)\int_0^\infty \nu\Sigma_f(x,E)\Phi_0(x,E)dEdx\,. \qquad (5.22)
\end{aligned}$$

We have now obtained a system of $J+1$ discrete equations, Eqs. (5.18), (5.21) and (5.22), which are exactly satisfied by the solution $\psi(x,\mu,E)$ and k of Eqs. (5.1). This completes the second step in the method to solve Eqs. (5.1).

In the third step, we use Eqs. (5.18), (5.21) and (5.22) to define energy-integrated nonlinear functionals. [These functionals are then used in energy-independent low-order equations derived from Eqs. (5.18), (5.21) and (5.22) to estimate the eigenvalue and the energy-integrated flux.]

We first define volume-averaged fluxes as in the monoenergetic case [15]

$$\bar{\phi}(x_{j+1/2})=\int_{x_{j-1/2}}^{x_{j+3/2}} g_{j+1/2}(x)\phi_0(x)\,dx\,. \qquad (5.23)$$

Next, we multiply and divide each term in Eqs. (5.18), (5.21), and (5.22) by a suitable volume-averaged flux defined by Eq. (5.23). This gives the following equivalent set of $J+1$ equations:

$$\left[\left(\frac{\int_0^\infty\int_{-1}^0|\mu|\psi(0,\mu,E)d\mu dE}{\int_0^\infty\int_{x_{1/2}}^{x_{3/2}}g_{1/2}(x)\Phi_0(x,E)dxdE}\right)+\left(\frac{\int_{x_{1/2}}^{x_{3/2}}f_{1/2}(x)\int_0^\infty\Sigma_a(x,E)\Phi_0(x,E)dEdx}{\int_0^\infty\int_{x_{1/2}}^{x_{3/2}}g_{1/2}(x)\Phi_0(x,E)dxdE}\right)\right.$$
$$\left.+\frac{1}{h_1}\left(\frac{\int_0^\infty U_1(E)\Phi_2(x_{1/2},E)dE}{\int_0^\infty\int_{x_{1/2}}^{x_{3/2}}g_{1/2}(x)\Phi_0(x,E)dxdE}\right)\right]\bar{\phi}(x_{1/2})-\frac{1}{h_1}\left(\frac{\int_0^\infty U_1(E)\Phi_2(x_{3/2},E)dE}{\int_0^\infty\int_{x_{1/2}}^{x_{5/2}}g_{3/2}(x)\Phi_0(x,E)dxdE}\right)\bar{\phi}(x_{3/2})$$
$$=\frac{1}{k}\left(\frac{\int_{x_{1/2}}^{x_{3/2}}f_{1/2}(x)\int_0^\infty\nu\Sigma_f(x,E)\Phi_0(x,E)dEdx}{\int_0^\infty\int_{x_{1/2}}^{x_{3/2}}g_{1/2}(x)\Phi_0(x,E)dxdE}\right)\bar{\phi}(x_{1/2})\,, \tag{5.24a}$$

$$-\frac{1}{h_j}\left(\frac{\int_0^\infty U_j(E)\Phi_2(x_{j-1/2},E)dE}{\int_0^\infty\int_{x_{j-3/2}}^{x_{j+1/2}}g_{j-1/2}(x)\Phi_0(x,E)dx\,dE}\right)\bar{\phi}(x_{j-1/2})$$
$$+\left[\frac{1}{h_j}\left(\frac{\int_0^\infty U_j(E)\Phi_2(x_{j+1/2},E)dE}{\int_0^\infty\int_{x_{j-1/2}}^{x_{j+3/2}}g_{j+1/2}(x)\Phi_0(x,E)dx\,dE}\right)+\frac{1}{h_{j+1}}\left(\frac{\int_0^\infty U_{j+1}(E)\Phi_2(x_{j+1/2},E)dE}{\int_0^\infty\int_{x_{j-1/2}}^{x_{j+3/2}}g_{j+1/2}\Phi_0(x,E)dx\,dE}\right)\right.$$
$$\left.+\left(\frac{\int_{x_{j-1/2}}^{x_{j+3/2}}f_{j+1/2}(x)\int_0^\infty\Sigma_a(x,E)\Phi_0(x,E)dx\,dE}{\int_0^\infty\int_{x_{j-1/2}}^{x_{j+3/2}}g_{j+1/2}(x)\Phi_0(x,E)dx\,dE}\right)\right]\bar{\phi}(x_{j+1/2})$$
$$-\frac{1}{h_{j+1}}\left(\frac{\int_0^\infty U_{j+1}(E)\Phi_2(x_{j+3/2},E)dE}{\int_0^\infty\int_{x_{j+1/2}}^{x_{j+5/2}}g_{j+3/2}\Phi_0(x,E)dx\,dE}\right)\bar{\phi}(x_{j+3/2})$$
$$=\frac{1}{k}\left(\frac{\int_{x_{j-1/2}}^{x_{j+3/2}}f_{j+1/2}(x)\int_0^\infty\nu\Sigma_f(x,E)\Phi_0(x,E)dx\,dE}{\int_0^\infty\int_{x_{j-1/2}}^{x_{j+3/2}}g_{j+1/2}(x)\Phi_0(x,E)dx\,dE}\right)\bar{\phi}(x_{j+1/2}),\quad 1\le j\le J-1\,, \tag{5.24b}$$

$$
\begin{aligned}
&-\frac{1}{h_J}\left(\frac{\int_0^\infty U_J(E)\Phi_2(x_{J-1/2},E)dE}{\int_0^\infty\int_{x_{J-3/2}}^{x_{J+1/2}} g_{J-1/2}(x)\Phi_0(x,E)dxdE}\right)\bar{\phi}(x_{J-1/2})\\
&\left[\left(\frac{\int_0^\infty\int_0^1 \mu\psi(x_{J+1/2},\mu,E)d\mu dE}{\int_0^\infty\int_{x_{J-1/2}}^{x_{J+1/2}} g_{J+1/2}(x)\Phi_0(x,E)dxdE}\right)+\left(\frac{\int_{x_{J-1/2}}^{x_{J+1/2}} f_{J+1/2}(x)\int_0^\infty \Sigma_a(x,E)\Phi_0(x,E)dEdx}{\int_0^\infty\int_{x_{J-1/2}}^{x_{J+1/2}} g_{J+1/2}(x)\Phi_0(x,E)dxdE}\right)\right.\\
&\left.+\frac{1}{h_J}\left(\frac{\int_0^\infty U_J(E)\Phi_2(x_{J+1/2},E)dE}{\int_0^\infty\int_{x_{J-1/2}}^{x_{J+1/2}} g_{J+1/2}(x)\Phi_0(x,E)dxdE}\right)\right]\bar{\phi}_(x_{J+1/2})\\
&=\frac{1}{k}\left(\frac{\int_{x_{J-1/2}}^{x_{J+1/2}} f_{J+1/2}(x)\int_0^\infty \nu\Sigma_f(x,E)\Phi_0(x,E)dEdx}{\int_0^\infty\int_{x_{J-1/2}}^{x_{J+1/2}} g_{J+1/2}(x)\Phi_0(x,E)dxdE}\right)\bar{\phi}_(x_{J+1/2})\,. \qquad (5.24c)
\end{aligned}
$$

We simplify the foregoing equations by defining the following energy-integrated nonlinear functionals:

$$B_{1/2}=\frac{\int_0^\infty\int_{-1}^0|\mu|\psi(0,\mu,E)d\mu dE}{\int_0^\infty\int_{x_{1/2}}^{x_{3/2}} g_{1/2}(x)\Phi_0(x,E)dxdE}\,, \qquad (5.25a)$$

$$B_{J+1/2}=\frac{\int_0^\infty\int_0^1 \mu\psi(x_{J+1/2},\mu,E)d\mu dE}{\int_0^\infty\int_{x_{J-1/2}}^{x_{J+1/2}} g_{J+1/2}(x)\Phi_0(x,E)dxdE}\,, \qquad (5.25b)$$

$$F_{j+1/2}=\frac{\int_{x_{j-1/2}}^{x_{j+3/2}} f_{j+1/2}(x)\int_0^\infty \nu\Sigma_f(x,E)\Phi_0(x,E)dE\,dx}{\int_0^\infty\int_{x_{j-1/2}}^{x_{j+3/2}} g_{j+1/2}(x)\Phi_0(x,E)dx\,dE}\,, \qquad (5.25c)$$

$$A_{j+1/2}=\frac{\int_{x_{j-1/2}}^{x_{j+3/2}} f_{j+1/2}(x)\int_0^\infty \Sigma_a(x,E)\Phi_0(x,E)dx\,dE}{\int_0^\infty\int_{x_{j-1/2}}^{x_{j+3/2}} g_{j+1/2}(x)\Phi_0(x,E)dE\,dx}\,, \qquad (5.25d)$$

$$U^L_{j+1/2}=\frac{\int_0^\infty U_{j+1}(E)\Phi_2(x_{j+1/2},E)dE}{\int_0^\infty\int_{x_{j-1/2}}^{x_{j+3/2}} g_{j+1/2}(x)\Phi_0(x,E)dx\,dE}\,, \qquad (5.25e)$$

$$U^R_{j+1/2}=\frac{\int_0^\infty U_j(E)\Phi_2(x_{j+1/2},E)dE}{\int_0^\infty\int_{x_{j-1/2}}^{x_{j+3/2}} g_{j+1/2}(x)\Phi_0(x,E)dx\,dE}\,. \qquad (5.25f)$$

Then, in terms of the functionals in Eq. (5.25), Eqs. (5.24) may be written:

$$\left[B_{1/2}+A_{1/2}+\frac{1}{h_1}U^L_{1/2}\right]\bar{\phi}(x_{1/2})-\frac{1}{h_1}U^R_{3/2}\bar{\phi}(x_{3/2})=\frac{1}{k}F_{1/2}\bar{\phi}(x_{1/2})\,, \qquad (5.26a)$$

$$-\frac{1}{h_j}U^L_{j-1/2}\bar{\phi}(x_{j-1/2})+\left[\frac{1}{h_j}U^R_{j+1/2}+\frac{1}{h_{j+1}}U^L_{j+1/2}+A_{j+1/2}\right]\bar{\phi}(x_{j+1/2})$$
$$-\frac{1}{h_{j+1}}U^R_{j+3/2}\bar{\phi}(x_{j+3/2})=\frac{1}{k}F_{j+1/2}\bar{\phi}(x_{j+1/2}),\quad 1\le j\le J-1\ , \tag{5.26b}$$

$$-\frac{1}{h_J}U^L_{J-1/2}\bar{\phi}(x_{J-1/2})+\left[B_{J+1/2}+A_{J+1/2}+\frac{1}{h_J}U^R_{J+1/2}\right]\bar{\phi}(x_{J+1/2})=\frac{1}{k}F_{J+1/2}\bar{\phi}(x_{J+1/2})\ . \tag{5.26c}$$

The functionals in these equations can be evaluated using the standard Monte Carlo method. Once they are obtained, Eqs. (5.24) then become energy-independent, low-order equations which can be used to estimate the k-eigenvalue and the energy-integrated volume-averaged scalar fluxes $\bar{\phi}_{j+1/2}$. This concludes the step 3 of Part 1 of our method to solve Eqs. (5.1).

Remark: At this point, we wish to point out that other approaches are possible in deriving low-order FMC equations from Eqs. (5.3) and (5.4). For example, one can write Eq. (5.4) as

$$\frac{\partial}{\partial x}\Phi_2(x,E)+\Sigma_{tr}(x,E)\Phi_1(x,E)=\int_0^\infty\Sigma_{s1}(x,E'\to E)\Phi_1(x,E')dE'-\Sigma_{s1}(x,E)\Phi_1(x,E)$$
$$\equiv L\Phi_1(x,E)\ .$$

This gives:

$$\Phi_1(x,E)=-\frac{1}{\Sigma_{tr}(x,E)}\left[\frac{\partial}{\partial x}\Phi_2(x,E)-L\Phi_1(x,E)\right]\ .$$

Introducing this result into Eq. (5.3), we obtain

$$-\frac{\partial}{\partial x}\frac{1}{\Sigma_{tr}(x,E)}\frac{\partial}{\partial x}\Phi_2(x,E)+\Sigma_t(x,E)\Phi_0(x,E)=\int_0^\infty\Sigma_{s0}(x,E'\to E)\Phi_0(x,E')dE'$$
$$+\frac{\chi(x,E)}{k}\int_0^\infty\nu\Sigma_f(x,E')\Phi_0(x,E')dE'-\frac{\partial}{\partial x}\frac{1}{\Sigma_{tr}(x,E)}L\Phi_1(x,E)\ . \tag{5.27}$$

We attempted to develop an FMC method for Eq. (5.27), by using the same techniques described above for Eq. (5.13). Unfortunately, numerical tests showed that this approach

was not as efficient as the approach described in detail in Eqs. (5.14)- (5.26). Our experience has indicated that eliminating $\Phi_1(x,E)$ by using the U-function is an important step in developing an efficient FMC method.

It remains to determine $U(x,E)$ [Part 2 of our procedure to solve Eqs. (5.1)]. A numerical procedure to accomplish this is described next.

5.1.2 Procedure for Evaluating $U(x,E)$ (Part 2)

We recall from Section 5.1.1, Eq. (5.11), that $U(x,E)$ satisfies the following adjoint equation:

$$\Sigma_t(x,E)U(x,E) - \int_0^\infty \Sigma_{s1}(x,E \to E')U(x,E')dE' = 1 \; . \tag{5.28}$$

We introduce the scattering ratio

$$C(x,E) = \frac{\Sigma_s(x,E)}{\Sigma_t(x,E)} \; ,$$

and note that

$$\Sigma_{s1}(x,E \to E') = \Sigma_s(x,E)P(E \to E')\hat{\mu}(E \to E') \; .$$

Thus, Eq. (5.28) can be rewritten as

$$U(x,E) - C(x,E)\int_0^\infty P(E \to E')\hat{\mu}(E \to E')U(x,E')dE' = \frac{1}{\Sigma_t(x,E)} \; . \tag{5.29}$$

Eq. (5.29) cannot be solved analytically, so we proceed to solve it numerically. To do this, we take account of down-scattering only. Energy grids $1 \leq l \leq L$ can be specified at arbitrary intervals as shown in Figure 5.1. For simplicity, we assume that the edges of the energy grid satisfy the condition $E_{l+m+1} = \alpha E_l$, which means that a neutron with energy E_l can scatter into its own energy group and the following m neighboring energy groups.

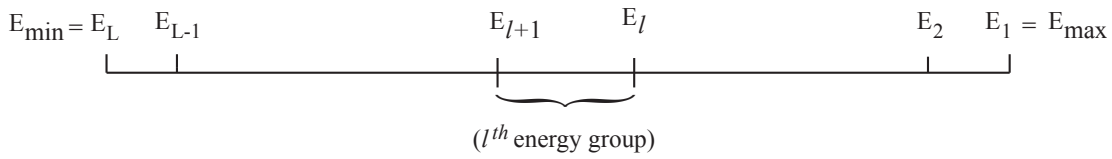

Figure 5.1 The energy grid.

For each energy E_l, Eq. (5.29) can be written as

$$U(x,E_l) - C(x,E_l)\int_{\alpha E_l}^{E_l} P(E_l \to E')\hat{\mu}(E_l \to E')U(x,E')dE' = \frac{1}{\Sigma_t(x,E_l)} \,. \tag{5.30}$$

Substituting the following expression for $\hat{\mu_0}(E_l \to E')$ and $P(E_l \to E')$:

$$\hat{\mu_0}(E_l \to E') = \left(\frac{A+1}{2}\right)\sqrt{\frac{E'}{E_l}} - \left(\frac{A-1}{2}\right)\sqrt{\frac{E_l}{E'}} \,,$$

$$P(E_l \to E') = \begin{cases} \frac{1}{(1-\alpha)E_l} & \alpha E_l < E < E_l \\ 0 & \text{otherwise} \,, \end{cases}$$

Eq. (5.30) becomes

$$U(x,E_l) - C(x,E_l)\int_{\alpha E_l}^{E_l} \frac{1}{(1-\alpha)E_l}\left[\frac{A+1}{2}\sqrt{\frac{E'}{E_l}} - \frac{A-1}{2}\sqrt{\frac{E_l}{E'}}\right]U(x,E')dE' = \frac{1}{\Sigma_t(x,E_l)} \,,$$

or

$$U(x,E_l) - \frac{C(x,E_l)}{(1-\alpha)E_l}\left[\frac{A+1}{2\sqrt{E_l}}\int_{\alpha E_l}^{E_l}\sqrt{E'}U(x,E')dE' - \frac{(A-1)\sqrt{E_l}}{2}\int_{\alpha E_l}^{E_l}\frac{1}{\sqrt{E'}}U(x,E')dE'\right] = \frac{1}{\Sigma_t(x,E_l)} \,. \tag{5.31}$$

Here we make an approximation. We assume that for $E_{l+1} \le E \le E_l$, $U(x,E)$ is a linear

interpolation of $U(x,E_l)$ and $U(x,E_{l+1})$, i.e.

$$\begin{aligned} U(E) \cong & \frac{U_l - U_{l+1}}{E_l - E_{l+1}} E + \frac{U_{l+1}E_l - U_l E_{l+1}}{E_l - E_{l+1}} \\ = & \frac{U_l - U_{l+1}}{\Delta E_l} E + \frac{U_{l+1}E_l - U_l E_{l+1}}{\Delta E_l} \ , \end{aligned} \tag{5.32}$$

where for simplicity, we denote $U(x,E_l) = U_l$. This linear interpolation will generate a small truncation error in $U(x,E)$. Using Eq. (5.32), we evaluate the two energy integrals in Eq. (5.31) as:

$$\begin{aligned} \int_{\alpha E_l}^{E_l} \sqrt{E'} U(x,E') dE' &= \int_{E_{l+m+1}}^{E_l} \sqrt{E'} U(x,E') dE' \\ &= \sum_{l'=l}^{l+m} \int_{E_{l'+1}}^{E_{l'}} \sqrt{E'} \left[\frac{U_{l'} - U_{l'+1}}{\Delta E_{l'}} E' + \frac{U_{l'+1}E_{l'} - U_{l'}E_{l'+1}}{\Delta E_{l'}} \right] dE' \\ &= \sum_{l'=l}^{l+m} \left\{ \left[\frac{2}{5\Delta E_{l'}} (E_{l'}^{\frac{5}{2}} - E_{l'+1}^{\frac{5}{2}}) - \frac{2E_{l'+1}}{3\Delta E_{l'}} (E_{l'}^{\frac{3}{2}} - E_{l'+1}^{\frac{3}{2}}) \right] U_{l'} \right. \\ &+ \left. \left[-\frac{2}{5\Delta E_{l'}} (E_{l'}^{\frac{5}{2}} - E_{l'+1}^{\frac{5}{2}}) + \frac{2E_{l'}}{3\Delta E_{l'}} (E_{l'}^{\frac{3}{2}} - E_{l'+1}^{\frac{3}{2}}) \right] U_{l'+1} \right\} \\ &= \sum_{l'=l}^{l+m+1} R_{l'} U_{l'} \ , \end{aligned} \tag{5.33}$$

where

$$\begin{aligned} R_l &= \frac{2}{5\Delta E_l} (E_l^{\frac{5}{2}} - E_{l+1}^{\frac{5}{2}}) - \frac{2E_{l+1}}{3\Delta E_l} (E_l^{\frac{3}{2}} - E_{l+1}^{\frac{3}{2}}) \ , \\ R_{l+i} &= -\frac{2}{5\Delta E_{l+i-1}} (E_{l+i-1}^{\frac{5}{2}} - E_{l+i}^{\frac{5}{2}}) + \frac{2E_{l+i-1}}{3\Delta E_{l+i-1}} (E_{l+i-1}^{\frac{3}{2}} - E_{l+i}^{\frac{3}{2}}) \\ &\quad + \frac{2}{5\Delta E_{l+i}} (E_{l+i}^{\frac{5}{2}} - E_{l+i+1}^{\frac{5}{2}}) - \frac{2E_{l+i+1}}{3\Delta E_{l+i}} (E_{l+i}^{\frac{3}{2}} - E_{l+i+1}^{\frac{3}{2}}) \ , \qquad 1 \le i \le m \\ R_{l+m+1} &= -\frac{2}{5\Delta E_{l+m}} (E_{l+m}^{\frac{5}{2}} - E_{l+m+1}^{\frac{5}{2}}) + \frac{2E_{l+m}}{3\Delta E_{l+m}} (E_{l+m}^{\frac{3}{2}} - E_{l+m+1}^{\frac{3}{2}}) \ , \end{aligned}$$

and

$$\begin{aligned}
\int_{\alpha E_l}^{E_l} \frac{1}{\sqrt{E'}} U(x,E')dE' &= \int_{E_{l+m+1}}^{E_l} \frac{1}{\sqrt{E'}} U(x,E')dE' \\
&= \sum_{l'=l}^{l+m} \int_{E_{l'+1}}^{E_{l'}} \frac{1}{\sqrt{E'}} \left[\frac{U_{l'} - U_{l'+1}}{\Delta E_{l'}} E' + \frac{U_{l'+1}E_{l'} - U_{l'}E_{l'+1}}{\Delta E_{l'}} \right] dE' \\
&= \sum_{l'=l}^{l+m} \left\{ \left[\frac{2}{3\Delta E_{l'}} (E_{l'}^{\frac{3}{2}} - E_{l'+1}^{\frac{3}{2}}) - \frac{2E_{l'+1}}{\Delta E_{l'}} (E_{l'}^{\frac{1}{2}} - E_{l'+1}^{\frac{1}{2}}) \right] U_{l'} \right. \\
&+ \left. \left[-\frac{2}{3\Delta E_{l'}} (E_{l'}^{\frac{3}{2}} - E_{l'+1}^{\frac{3}{2}}) + \frac{2E_{l'}}{\Delta E_{l'}} (E_{l'}^{\frac{1}{2}} - E_{l'+1}^{\frac{1}{2}}) \right] U_{l'+1} \right\} \\
&= \sum_{l'=l}^{l+m+1} S_{l'} U_{l'} \,, \qquad (5.34)
\end{aligned}$$

where

$$\begin{aligned}
S_l &= \frac{2}{3\Delta E_l} (E_l^{\frac{3}{2}} - E_{l+1}^{\frac{3}{2}}) - \frac{2E_{l+1}}{\Delta E_l} (E_l^{\frac{1}{2}} - E_{l+1}^{\frac{1}{2}}) \,, \\
S_{l+i} &= -\frac{2}{3\Delta E_{l+i-1}} (E_{l+i-1}^{\frac{3}{2}} - E_{l+i}^{\frac{3}{2}}) + \frac{2E_{l+i-1}}{\Delta E_{l+i-1}} (E_{l+i-1}^{\frac{1}{2}} - E_{l+i}^{\frac{1}{2}}) \\
&\quad + \frac{2}{3\Delta E_{l+i}} (E_{l+i}^{\frac{3}{2}} - E_{l+i+1}^{\frac{3}{2}}) - \frac{2E_{l+i+1}}{\Delta E_{l+i}} (E_{l+i}^{\frac{1}{2}} - E_{l+i+1}^{\frac{1}{2}}) \,, \qquad 1 \le i \le m \\
S_{l+m+1} &= -\frac{2}{3\Delta E_{l+m}} (E_{l+m}^{\frac{3}{2}} - E_{l+m+1}^{\frac{3}{2}}) + \frac{2E_{l+m}}{\Delta E_{l+m}} (E_{l+m}^{\frac{1}{2}} - E_{l+m+1}^{\frac{1}{2}}) \,.
\end{aligned}$$

Next,we rewrite Eq. (5.31) as

$$\begin{aligned}
&U_l - \underbrace{\frac{C_l(A+1)}{2(1-\alpha)E_l^{\frac{3}{2}}}}_{H_l} \int_{\alpha E_l}^{E_l} \sqrt{E'} U(x,E')dE' + \underbrace{\frac{C_l(A-1)}{2(1-\alpha)\sqrt{E_l}}}_{I_l} \int_{\alpha E_l}^{E_l} \frac{1}{\sqrt{E'}} U(x,E')dE' \\
&= \frac{1}{\Sigma_t(x,E_l)} \,.
\end{aligned}$$

Using the indicated definitions of H_l and I_l, and substituting the integral expressions Eqs.

(5.33) and (5.34), we find

$$U_l - H_l\Big[\sum_{l'=l}^{l+m+1} R_{l'}U_{l'}\Big] + I_l\Big[\sum_{l'=l}^{l+m+1} S_{l'}U_{l'}\Big] = \frac{1}{\Sigma_t(x,E_l)}\,,$$

or

$$[1 - H_lR_l + I_lS_l]U_l + \sum_{l'=l}^{l+m}[-H'_lR_{l'+1} + I'_lS_{l'+1}]U_{l'+1} = \frac{1}{\Sigma_t(x,E_l)}, \tag{5.35}$$

where:

$$H_l = \frac{C_l(A+1)}{2(1-\alpha)E_l^{\frac{3}{2}}} = \frac{(A+1)}{2(1-\alpha)E_l^{\frac{3}{2}}}\frac{\Sigma_s(x,E_l)}{\Sigma_t(x,E_l)}\,,$$

$$I_l = \frac{C_l(A-1)}{2(1-\alpha)E_l^{\frac{1}{2}}} = \frac{(A-1)}{2(1-\alpha)E_l^{\frac{1}{2}}}\frac{\Sigma_s(x,E_l)}{\Sigma_t(x,E_l)}\,.$$

Using the expressions stated for the coefficients, we now solve the set of linear Eqs. (5.35) for values of $U(x,E_l)$ over the entire energy grid. For this purpose, we assume the first $m+1$ values $U(x,E_L)$, $U(x,E_{L-1}),\cdots,U(x,E_{L-m})$ to be equal to one another. The value of $U(x,E_l)$ so obtained can then be used to generate, by linear interpolation, all values of $U(x,E)$ required to solve Eq. (5.26).

The calculation of $U(x,E)$ only needs to be done once, in each material region, at the start of calculation. Also, $U(x,E)$ can be calculated as accurately as desired by taking the energy grid sufficiently fine. We assume that $U(x,E)$ has been calculated to an accuracy comparable to the accuracy of $\Sigma_s(\Omega'\cdot\Omega, E'\rightarrow E)$.

5.2 Procedure to Generate Low-Order Multigroup Equations

For many problems encountered in practical nuclear reactor design, the energy-integrated scalar flux is not adequate; multigroup fluxes are more desirable. In this section, we extend the FMC method in the following ways: (a) Energy group nonlinear functionals

are estimated using standard Monte Carlo with continuous-energy cross-sections; (b) These functionals are then used in low-order multigroup equations to estimate the eigenvalue and the multigroup fluxes. As in the case of energy-integrated flux, the resulting FMC estimates of eigenvalue and multigroup fluxes have very small energy truncation errors and statistical errors. Furthermore, the FMC method has no spatial or angular truncation errors.

5.2.1 Low-Order Multigroup Equations

The procedure to obtain the low-order multigroup equations from Eq. (5.1) follows closely the three-step procedure used earlier to solve the energy-integrated low-order FMC equations in Section 5.1.1. These three steps are presented as follows.

In the first step, we take the zeroth and first angular moments of Eq. (5.1) by operating on Eq. (5.1a) with $\int_{-1}^{1} \mu^n(\cdot)\, d\mu$ for $n = 0$ and 1. We define

$$\Phi_n(x,E) = \int_{-1}^{1} \mu^n \psi(x,\mu,E) d\mu \quad , \qquad n = 0,1,2 \; .$$

For $n = 0$, we obtain

$$\frac{\partial}{\partial x}\Phi_1(x,E) + \Sigma_t(x,E)\Phi_0(x,E) = \int_0^\infty \Sigma_{s0}(x,E' \rightarrow E)\Phi_0(x,E')dE' + \frac{\chi(x,E)}{k}\int_0^\infty \nu\Sigma_f(x,E')\Phi_0(x,E')dE' \; ; \quad (5.36)$$

and for $n = 1$, we have

$$\frac{\partial}{\partial x}\Phi_2(x,E) + \Sigma_t(x,E)\Phi_1(x,E) = \int_0^\infty \Sigma_{s1}(x,E' \rightarrow E)\Phi_1(x,E')dE' \; . \quad (5.37)$$

To obtain the multigroup fluxes, we first define an energy group structure as shown in Figure 5.2:

[Note that this energy grid is not necessarily related to the energy grid described previously for calculating $U(x,E)$; see Figure 5.1.]

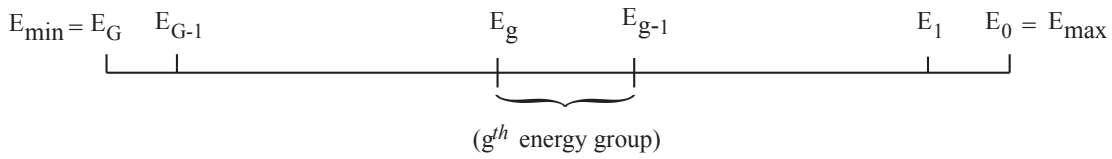

Figure 5.2 The energy group structure.

Next, we define the "characteristic" functions $\hat{\chi}_g(E)$ for each g^{th} energy group as:

$$\hat{\chi}_g(E) = \begin{cases} 1 & E_g < E < E_{g-1} \\ 0 & \text{otherwise} , \end{cases} \tag{5.38}$$

and we define multigroup functions $U_g(x,E)$ that satisfy the following adjoint equations:

$$\boxed{\Sigma_t(x,E)U_g(x,E) - \int_0^\infty \Sigma_{s1}(x,E \to E')U_g(x,E')dE' = \hat{\chi}_g(E),\ 0 < E < \infty .} \tag{5.39}$$

The multigroup functions $U_g(x,E)$ are used to eliminate the first-order moment $\Phi_1(x,E)$ in Eqs.(5.36) and (5.37). Eq.(5.39) for $U_g(x,E)$ cannot be solved analytically. A small energy truncation error in $U_g(x,E)$ will be generated when we solve it numerically in the following Section 5.2.2.

To proceed, we operate on Eq.(5.36) by

$$\int_0^\infty \hat{\chi}_g(E)(\cdot)dE = \int_{E_g}^{E_{g-1}} (\cdot)dE ,$$

and get

$$\frac{\partial}{\partial x}\int_{E_g}^{E_{g-1}}\phi_1(x,E)dE+\int_{E_g}^{E_{g-1}}\Sigma_t(x,E)\phi_0(x,E)dE=$$
$$\int_0^\infty\left[\int_{E_g}^{E_{g-1}}\Sigma_{s0}(x,E'\rightarrow E)dE\right]\phi_0(x,E')dE'$$
$$+\frac{\chi_g(x)}{k}\int_0^\infty\nu\Sigma_f(x,E')\phi_0(x,E')dE'\,, \tag{5.40}$$

where $\chi_g(x)=\int_{E_g}^{E_{g-1}}\chi(x,E)dE$. Next, we operate on Eq.(5.37) by $\int_0^\infty U_g(x,E)(\cdot)dE$, and get

$$\int_0^\infty U_g(x,E)\frac{\partial}{\partial x}\phi_2(x,E)dE$$
$$=\int_0^\infty U_g(x,E)\left[\int_0^\infty\Sigma_{s1}(x,E'\rightarrow E)\phi_1(x,E')dE'-\Sigma_t(x,E)\phi_1(x,E)\right]dE$$
$$=\int_0^\infty\left[\int_0^\infty\Sigma_{s1}(x,E\rightarrow E')U_g(x,E')dE'\right]\phi_1(x,E)dE-\int_0^\infty U_g(x,E)\Sigma_t(x,E)\phi_1(x,E)dE$$
$$=\int_0^\infty\left[\int_0^\infty\Sigma_{s1}(x,E\rightarrow E')U_g(x,E')dE'-\Sigma_t(x,E)U_g(x,E)\right]\phi_1(x,E)dE$$
$$=-\int_0^\infty\hat{\chi}_g(E)\phi_1(x,E)dE=-\int_{E_g}^{E_{g-1}}\phi_1(x,E)dE\,. \tag{5.41}$$

Substituting Eq.(5.41) into Eq.(5.40) then gives the following identities, which are exactly satisfied by the solution of Eq.(5.1):

$$-\frac{\partial}{\partial x}\int_0^\infty U_g(x,E)\frac{\partial}{\partial x}\phi_2(x,E)dE+\int_{E_g}^{E_{g-1}}\Sigma_t(x,E)\phi_0(x,E)dE$$
$$=\sum_{g'=1}^{G}\int_{E_{g'}}^{E_{g'-1}}\left[\int_{E_g}^{E_{g-1}}\Sigma_{s0}(x,E'\rightarrow E)dE\right]\phi_0(x,E')dE'$$
$$+\frac{\chi_g(x)}{k}\sum_{g'=1}^{G}\int_{E_{g'}}^{E_{g'-1}}\nu\Sigma_f(x,E')\phi_0(x,E')dE'\,,\ \ 1\le g\le G\,. \tag{5.42}$$

To proceed, we consider elastic down-scattering only. Thus, the integral in square brackets in Eq.(5.42) may be evaluated explicitly as shown below.

For elastic scattering, we have $\Sigma_{s0}(x,E' \to E) = \Sigma_{s0}(x,E')p(E' \to E)$, where

$$p(E' \to E) = \begin{cases} \frac{1}{(1-\alpha)E'} & \alpha E' < E < E' \\ 0 & \text{otherwise .} \end{cases} \tag{5.43}$$

Then we define for each energy group:

$$\begin{aligned} \Sigma_{s0,g}(x,E') &= \int_{E_g}^{E_{g-1}} \Sigma_{s0}(x,E' \to E)dE \\ &= \int_{E_g}^{E_{g-1}} \Sigma_{s0}(x,E')p(E' \to E)dE \\ &= \Sigma_{s0}(x,E') \int_{E_g}^{E_{g-1}} p(E' \to E)dE \ , \end{aligned}$$

which leads to

$$\boxed{\Sigma_{s0,g}(x,E') = \frac{\Sigma_s(x,E')}{(1-\alpha)E'} Q_g(E'),} \tag{5.44}$$

where

$$Q_g(E') = \begin{cases} 0 & E_{g-1} < \alpha E' & \text{(Case A)} \\ E_{g-1} - \alpha E' & E_g < \alpha E' < E_{g-1} < E' & \text{(Case B)} \\ E_{g-1} - E_g & \alpha E' < E_g < E_{g-1} < E' & \text{(Case C)} \\ E' - \alpha E' & E_g < \alpha E' < E' < E_{g-1} & \text{(Case D)} \\ E' - E_g & \alpha E' < E_g < E' < E_{g-1} & \text{(Case E)} \\ 0 & E' < E_g & \text{(Case F) .} \end{cases}$$

Eq.(5.44) then gives for these cases:

$$\text{For Case} = \begin{cases} (A), & \Sigma_{s0,g}(x,E') = 0 \\ (B), & \Sigma_{s0,g}(x,E') = \frac{\Sigma_s(E')}{(1-\alpha)E'}(E_{g-1} - \alpha E') \\ (C), & \Sigma_{s0,g}(x,E') = \frac{\Sigma_s(E')}{(1-\alpha)E'}(E_{g-1} - E_g) \\ (D), & \Sigma_{s0,g}(x,E') = \frac{\Sigma_s(E')}{(1-\alpha)E'}(E' - \alpha E') = \Sigma_s(E') \\ (E), & \Sigma_{s0,g}(x,E') = \frac{\Sigma_s(E')}{(1-\alpha)E'}(E' - E_g) \\ (F), & \Sigma_{s0,g}(x,E') = 0 \end{cases}$$

Substituting Eq.(5.44) into Eq.(5.42), we get:

$$\begin{aligned} &-\frac{\partial}{\partial x}\int_0^\infty U_g(x,E)\frac{\partial}{\partial x}\phi_2(x,E)dE + \int_{E_g}^{E_{g-1}} \Sigma_t(x,E)\phi_0(x,E)dE \\ &= \sum_{g'=1}^{G}\int_{E_{g'}}^{E_{g'-1}} \frac{\Sigma_s(x,E')}{(1-\alpha)E'} Q_g(E')\phi_0(x,E')dE' \\ &+ \frac{\chi_g(x)}{k}\left(\sum_{g'=1}^{G}\int_{E_{g'}}^{E_{g'-1}} \nu\Sigma_f(x,E')\phi_0(x,E')dE'\right), 1 \le g \le G \ . \end{aligned} \tag{5.45}$$

If $U_g(x,E)$ is exact, then Eq.(5.45) is satisfied exactly by the solution $\psi(x,\mu,E)$ of the continuous-energy transport equation (5.1a). Eq.(5.45) completes the first step.

Steps 2 and 3 follow closely the derivation in Section 5.1.1. In the following, we only give highlights from these steps.

We define a spatial grid $0 = x_{1/2} < x_{3/2} \ldots < x_{J+1/2} = X$. For each grid point $x_{j+1/2}$, we define the same tent functions $f_{j+1/2}(x)$ as were used in the energy-integrated flux case.

For each j we now perform the operation $\int_0^X f_{j+1/2}(x)(\cdot)dx$ on Eq. (5.45).

For $j = 0$ we obtain:

$$
\begin{aligned}
&-\int_{x_{1/2}}^{x_{3/2}} f_{1/2}(x)\frac{\partial}{\partial x}\int_0^{\infty} U_g(x,E)\frac{\partial}{\partial x}\phi_2(x,E)dEdx \\
&+\int_{x_{1/2}}^{x_{3/2}} f_{1/2}(x)\int_{E_g}^{E_{g-1}} \Sigma_t(x,E)\phi_0(x,E)dEdx \\
&=\sum_{g'=1}^{G}\int_{E_{g'}}^{E_{g'-1}}\int_{x_{1/2}}^{x_{3/2}} f_{1/2}(x)\frac{\Sigma_s(x,E')}{(1-\alpha)E'}Q_g(E')\phi_0(x,E')dxdE' \\
&+\frac{1}{k}\int_{x_{1/2}}^{x_{3/2}} f_{1/2}(x)\chi_g(x)\left(\sum_{g'=1}^{G}\int_{E_{g'}}^{E_{g'-1}} \nu\Sigma_f(x,E')\phi_0(x,E')dE'\right)dx\,. \qquad (5.46)
\end{aligned}
$$

Following the exact same steps as in the energy-integrated flux case, Eq.(5.46) becomes

$$
\begin{aligned}
&\int_{E_g}^{E_{g-1}}\int_{-1}^{0}|\mu|\psi(0,\mu,E)\,d\mu\,dE+\frac{1}{h_1}\int_0^{\infty}U_g(x_1,E)\phi_2(x_{1/2},E)dE \\
&-\frac{1}{h_1}\int_0^{\infty}U_g(x_1,E)\phi_2(x_{3/2},E)dE+\int_{x_{1/2}}^{x_{3/2}} f_{1/2}(x)\int_{E_g}^{E_{g-1}}\Sigma_t(x,E)\phi_0(x,E)\,dE\,dx \\
&=\sum_{g'=1}^{G}\int_{E_{g'}}^{E_{g'-1}}\int_{x_{1/2}}^{x_{3/2}} f_{1/2}(x)\frac{\Sigma_s(x,E')}{(1-\alpha)E'}Q_g(E')\phi_0(x,E')\,dx\,dE' \\
&+\frac{1}{k}\int_{x_{1/2}}^{x_{3/2}} f_{1/2}(x)\chi_g(x)\left(\sum_{g'=1}^{G}\int_{E_{g'}}^{E_{g'-1}}\nu\Sigma_f(x,E')\phi_0(x,E')\,dE'\right)dx\,. \qquad (5.47)
\end{aligned}
$$

Next, we define cell-averaged fluxes as in the monoenergetic case:

$$
\bar{\phi}_g(x_{j+1/2})=\int_{E_g}^{E_{g-1}}\int_{x_{j-1/2}}^{x_{j+3/2}} g_{j+1/2}(x)\phi_0(x,E)\,dx\,dE\,.
$$

We multiply and divide each term in Eq.(5.47) by a suitable cell-averaged flux. The $j = 0$ case may be written

$$
\begin{aligned}
& \left[\left(\frac{\int_{E_g}^{E_{g-1}} \int_{-1}^{0} |\mu| \psi(0,\mu,E)\, d\mu\, dE}{\int_{E_g}^{E_{g-1}} \int_{x_{1/2}}^{x_{3/2}} g_{1/2}(x) \phi_0(x,E)\, dx\, dE} \right) + \frac{1}{h_1} \left(\frac{\int_0^{\infty} U_g(x_1,E) \phi_2(x_{1/2},E) dE}{\int_{E_g}^{E_{g-1}} \int_{x_{1/2}}^{x_{3/2}} g_{1/2}(x) \phi_0(x,E)\, dx\, dE} \right) \right. \\
+ & \left. \left(\frac{\int_{x_{1/2}}^{x_{3/2}} f_{1/2}(x) \int_{E_g}^{E_{g-1}} \Sigma_t(x,E) \phi_0(x,E)\, dE\, dx}{\int_{E_g}^{E_{g-1}} \int_{x_{1/2}}^{x_{3/2}} g_{1/2}(x) \phi_0(x,E)\, dx\, dE} \right) \right] \bar{\phi}_g(x_{1/2}) \\
- & \frac{1}{h_1} \left(\frac{\int_0^{\infty} U_g(x_1,E) \phi_2(x_{3/2},E) dE}{\int_{E_g}^{E_{g-1}} \int_{x_{1/2}}^{x_{3/2}} g_{1/2}(x) \phi_0(x,E)\, dx\, dE} \right) \bar{\phi}_g(x_{3/2}) \\
= & \sum_{g'=1}^{G} \left[\left(\frac{\int_{E_{g'}}^{E_{g'-1}} \int_{x_{1/2}}^{x_{3/2}} f_{1/2}(x) \frac{\Sigma_s(x,E')}{(1-\alpha)E'} Q_g(E') \phi_0(x,E')\, dx\, dE'}{\int_{E_{g'}}^{E_{g'-1}} \int_{x_{1/2}}^{x_{3/2}} g_{1/2}(x) \phi_0(x,E')\, dx\, dE'} \right) \bar{\phi}_{g'}(x_{1/2}) \right] \\
+ & \frac{1}{k} \sum_{g'=1}^{G} \left[\left(\frac{\int_{E_{g'}}^{E_{g'-1}} \int_{x_{1/2}}^{x_{3/2}} f_{1/2}(x) \chi_g(x) \nu \Sigma_f(x,E') \phi_0(x,E')\, dx\, dE'}{\int_{E_{g'}}^{E_{g'-1}} \int_{x_{1/2}}^{x_{3/2}} g_{1/2}(x) \phi_0(x,E')\, dx\, dE'} \right) \bar{\phi}_{g'}(x_{1/2}) \right] . \quad (5.48)
\end{aligned}
$$

Similarly, for $1 \leq j \leq J-1$, we get Eq.(5.49), and for the right boundary $j = J$, we get Eq.(5.50).

$$
\begin{aligned}
- \quad & \frac{1}{h_j}\left(\frac{\int_0^\infty U_{g,j}(E)\phi_2(x_{j-1/2},E)dE}{\int_{E_g}^{E_{g-1}}\int_{x_{j-3/2}}^{x_{j-1/2}} g_{j-1/2}(x)\phi_0(x,E)\,dx\,dE}\right)\bar{\phi}_g(x_{j-1/2}) \\
+ \quad & \left[\frac{1}{h_j}\left(\frac{\int_0^\infty U_{g,j}(E)\phi_2(x_{j+1/2},E)\,dE}{\int_{E_g}^{E_{g-1}}\int_{x_{j-1/2}}^{x_{j+3/2}} g_{j+1/2}(x)\phi_0(x,E)\,dx\,dE}\right)\right. \\
+ \quad & \frac{1}{h_{j+1}}\left(\frac{\int_0^\infty U_{g,j+1}(E)\phi_2(x_{j+1/2},E)dE}{\int_{E_g}^{E_{g-1}}\int_{x_{j-1/2}}^{x_{j+3/2}} g_{j+1/2}(x)\phi_0(x,E)\,dx\,dE}\right) \\
+ \quad & \left.\left(\frac{\int_{x_{j-1/2}}^{x_{j+3/2}} f_{j+1/2}(x)\int_{E_g}^{E_{g-1}}\Sigma_t(x,E)\phi_0(x,E)\,dE\,dx}{\int_{E_g}^{E_{g-1}}\int_{x_{j-1/2}}^{x_{j+3/2}} g_{j+1/2}(x)\phi_0(x,E)\,dx\,dE}\right)\right]\bar{\phi}_g(x_{j+1/2}) \\
- \quad & \frac{1}{h_{j+1}}\left(\frac{\int_0^\infty U_{g,j+1}(E)\phi_2(x_{j+3/2},E)dE}{\int_{E_g}^{E_{g-1}}\int_{x_{j+1/2}}^{x_{j+5/2}} g_{j+3/2}(x)\phi_0(x,E)\,dx\,dE}\right)\bar{\phi}_g(x_{j+3/2}) \\
= \quad & \sum_{g'=1}^{G}\left(\frac{\int_{E_{g'}}^{E_{g'-1}}\int_{x_{j-1/2}}^{x_{j+3/2}} f_{j+1/2}(x)\frac{\Sigma_s(x,E')}{(1-\alpha)E'}Q_g(E')\phi_0(x,E')\,dx\,dE'}{\int_{E_{g'}}^{E_{g'-1}}\int_{x_{j-1/2}}^{x_{j+3/2}} g_{j+1/2}(x)\phi_0(x,E')\,dx\,dE'}\right)\bar{\phi}_{g'}(x_{j+1/2}) \qquad (5.49) \\
+ \quad & \frac{1}{k}\sum_{g'=1}^{G}\left(\frac{\int_{E_{g'}}^{E_{g'-1}}\int_{x_{j-1/2}}^{x_{j+3/2}} f_{j+1/2}(x)\chi_g(x)\nu\Sigma_f(x,E')\phi_0(x,E')\,dx\,dE'}{\int_{E_{g'}}^{E_{g'-1}}\int_{x_{j-1/2}}^{x_{j+3/2}} g_{j+1/2}(x)\phi_0(x,E')\,dx\,dE'}\right)\bar{\phi}_{g'}(x_{j+1/2})\,.
\end{aligned}
$$

$$
\begin{aligned}
- \quad & \frac{1}{h_J}\left(\frac{\int_0^\infty U_{g,J}(E)\phi_2(x_{J-1/2},E)dE}{\int_{E_g}^{E_{g-1}}\int_{x_{J-3/2}}^{x_{J+1/2}} g_{J-1/2}(x)\phi_0(x,E)\,dx\,dE}\right)\bar{\phi}_g(x_{J-1/2}) \\
+ \quad & \left[\left(\frac{\int_{E_g}^{E_{g-1}}\int_0^1 \mu\,\psi(x_{J+1/2},\mu,E)\,d\mu\,dE}{\int_{E_g}^{E_{g-1}}\int_{x_{J-1/2}}^{x_{J+1/2}} g_{J+1/2}(x)\phi_0(x,E)\,dx\,dE}\right)\right. \\
+ \quad & \frac{1}{h_J}\left(\frac{\int_0^\infty U_{g,J}(E)\phi_2(x_{J+1/2},E)dE}{\int_{E_g}^{E_{g-1}}\int_{x_{J-1/2}}^{x_{J+1/2}} g_{J+1/2}(x)\phi_0(x,E)\,dx\,dE}\right) \\
+ \quad & \left.\left(\frac{\int_{x_{J-1/2}}^{x_{J+1/2}} f_{J+1/2}(x)\int_{E_g}^{E_{g-1}}\Sigma_t(x,E)\phi_0(x,E)\,dE\,dx}{\int_{E_g}^{E_{g-1}}\int_{x_{J-1/2}}^{x_{J+1/2}} g_{J+1/2}(x)\phi_0(x,E)\,dx\,dE}\right)\right]\bar{\phi}_g(x_{J+1/2}) \\
= \quad & \sum_{g'=1}^{G}\left(\frac{\int_{E_{g'}}^{E_{g'-1}}\int_{x_{J-1/2}}^{x_{J+1/2}} f_{J+1/2}(x)\frac{\Sigma_s(x,E')}{(1-\alpha)E'}Q_g(E')\phi_0(x,E')\,dx\,dE'}{\int_{E_{g'}}^{E_{g'-1}}\int_{x_{J-1/2}}^{x_{J+1/2}} g_{J+1/2}(x)\phi_0(x,E')\,dx\,dE'}\right)\bar{\phi}_{g'}(x_{J+1/2}) \quad (5.50) \\
+ \quad & \frac{1}{k}\sum_{g'=1}^{G}\left(\frac{\int_{E_{g'}}^{E_{g'-1}}\int_{x_{J-1/2}}^{x_{J+1/2}} f_{J+1/2}(x)\chi_J(x)\nu\Sigma_f(x,E')\phi_0(x,E')\,dx\,dE'}{\int_{E_{g'}}^{E_{g'-1}}\int_{x_{J-1/2}}^{x_{J+1/2}} g_{J+1/2}(x)\phi_0(x,E')\,dx\,dE'}\right)\bar{\phi}_{g'}(x_{J+1/2})\,.
\end{aligned}
$$

To simply the notation, we define the following energy group nonlinear functionals:

$$
\begin{aligned}
B_{g,1/2} &= \frac{\int_{E_g}^{E_{g-1}} \int_{-1}^{0} |\mu| \psi(0,\mu,E)\, d\mu\, dE}{\int_{E_g}^{E_{g-1}} \int_{x_{1/2}}^{x_{3/2}} g_{1/2}(x) \phi_0(x,E)\, dx dE} \\
B_{g,J+1/2} &= \frac{\int_{E_g}^{E_{g-1}} \int_{0}^{1} \mu \psi(x_{J+1/2},\mu,E)\, d\mu\, dE}{\int_{E_g}^{E_{g-1}} \int_{x_{J-1/2}}^{x_{J+1/2}} g_{J+1/2}(x) \phi_0(x,E)\, dx dE} \\
F_{g,g',j+1/2} &= \frac{\int_{E_g}^{E_{g-1}} \int_{x_{j-1/2}}^{x_{j+3/2}} f_{j+1/2}(x) \chi_{g'}(x) \nu\Sigma_f(x,E) \phi_0(x,E)\, dx dE}{\int_{E_g}^{E_{g-1}} \int_{x_{j-1/2}}^{x_{j+3/2}} g_{j+1/2}(x) \phi_0(x,E)\, dx dE} \\
U^R_{g,j+1/2} &= \frac{h_{j+1} \int_0^{\infty} U_{g,j+1}(E) \phi_2(x_{j+1/2},E)\, dE}{\int_{E_g}^{E_{g-1}} \int_{x_{j-1/2}}^{x_{j+3/2}} g_{j+1/2}(x) \phi_0(x,E)\, dx dE} \\
U^L_{g,j+1/2} &= \frac{h_{j} \int_0^{\infty} U_{g,j}(E) \phi_2(x_{j+1/2},E)\, dE}{\int_{E_g}^{E_{g-1}} \int_{x_{j-1/2}}^{x_{j+3/2}} g_{j+1/2}(x) \phi_0(x,E)\, dx dE} \\
\tilde{\Sigma}_{s,g\to g',j+1/2} &= \frac{\int_{E_g}^{E_{g-1}} \int_{x_{j-1/2}}^{x_{j+3/2}} f_{j+1/2}(x) \frac{\Sigma_s(x,E)}{(1-\alpha)E} Q_{g'}(E) \phi_0(x,E)\, dx dE}{\int_{E_g}^{E_{g-1}} \int_{x_{j-1/2}}^{x_{j+3/2}} g_{j+1/2}(x) \phi_0(x,E)\, dx dE} \\
\tilde{\Sigma}_{t,g,j+1/2} &= \frac{\int_{x_{j-1/2}}^{x_{j+3/2}} f_{j+1/2}(x) \int_{E_g}^{E_{g-1}} \Sigma_t(x,E) \phi_0(x,E)\, dE\, dx}{\int_{E_g}^{E_{g-1}} \int_{x_{j-1/2}}^{x_{j+3/2}} g_{j+1/2}(x) \phi_0(x,E)\, dx dE} \,. \qquad (5.51)
\end{aligned}
$$

Then in terms of these functionals in Eq.(5.51), Eqs.(5.48), (5.49), and (5.50) can be written more concisely as:

$$
\begin{aligned}
&\left[B_{g,1/2} + \frac{1}{h_1^2} U^R_{g,1/2} + \tilde{\Sigma}_{t,g,1/2} \right] \bar{\phi}_g(x_{1/2}) - \frac{1}{h_1^2} U^L_{g,3/2} \bar{\phi}_g(x_{3/2}) \\
&= \sum_{g'=1}^{G} \tilde{\Sigma}_{s,g'\to g,1/2} \bar{\phi}_{g'}(x_{1/2}) + \frac{1}{k} \sum_{g'=1}^{G} F_{g',g,1/2} \bar{\phi}_{g'}(x_{1/2}) \,, \qquad (5.52a)
\end{aligned}
$$

$$
\begin{aligned}
&-\frac{1}{h_j^2} U^R_{g,j-1/2} \bar{\phi}_g(x_{j-1/2}) + \left[\frac{1}{h_j^2} U^L_{g,j+1/2} + \frac{1}{h_{j+1}^2} U^R_{g,j+1/2} + \tilde{\Sigma}_{t,g,j+1/2} \right] \bar{\phi}_g(x_{j+1/2}) \\
&-\frac{1}{h_{j+1}^2} U^L_{g,j+3/2} \bar{\phi}_g(x_{j+3/2}) = \sum_{g'=1}^{G} \tilde{\Sigma}_{s,g'\to g,j+1/2} \bar{\phi}_{g'}(x_{j+1/2}) + \frac{1}{k} \sum_{g'=1}^{G} F_{g',g,j+1/2} \bar{\phi}_{g'}(x_{j+1/2}), \\
&\qquad\qquad 1 \le j \le J-1 \,, \qquad (5.52b)
\end{aligned}
$$

$$-\frac{1}{h_J^2}U^R_{g,J-1/2}\,\bar{\phi}_g(x_{J-1/2})+\left[B_{g,J+1/2}+\frac{1}{h_J^2}U^L_{g,J+1/2}+\tilde{\Sigma}_{t,g,J+1/2}\right]\bar{\phi}_g(x_{J+1/2})$$
$$=\sum_{g'=1}^{G}\tilde{\Sigma}_{s,g'\to g,J+1/2}\,\bar{\phi}_{g'}(x_{J+1/2})+\frac{1}{k}\sum_{g'=1}^{G}F_{g',g,J+1/2}\,\bar{\phi}_{g'}(x_{J+1/2})\,. \tag{5.52c}$$

The energy group nonlinear functionals in Eq.(5.51) can be evaluated using the standard Monte Carlo method. Once these functionals are obtained, Eqs.(5.52) then become low-order multigroup equations, which can be solved to estimate the k-eigenvalue and the multigroup fluxes $\bar{\phi}_g(x_{j+1/2})$.

In this section, the multigroup flux $\bar{\phi}_g(x_{j+1/2})$ is defined on a "staggered" grid rather then on the original spatial grid of the problem as shown in Figure 5.3.

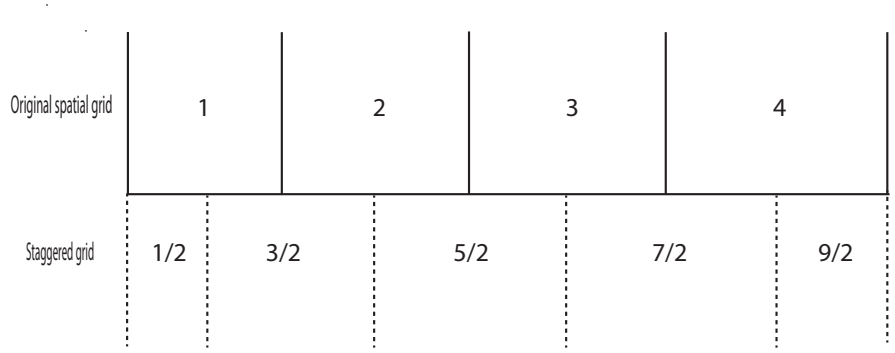

Figure 5.3 Original spatial grid and the staggered grid.

In Section 5.3, we are going to generalize the method to: (1) obtain fluxes on the original spatial gird; and (2) accommodate "a fine grid" with many material discontinuities inside each coarse cell.

5.2.2 Procedure for Evaluating $U_g(x,E)$

We recall from Section 5.2.1, Eq. (5.39), that $U_g(x,E)$ satisfies the following adjoint equation:

$$\Sigma_t(x,E)U_g(x,E) - \int_0^\infty \Sigma_{s1}(x,E\to E')U_g(x,E')dE' = \hat{\chi}_g(E),\ 0<E<\infty\,, \tag{5.53}$$

where for each g^{th} energy group, the characteristic functions $\hat{\chi}_g(E)$ are defined as:

$$\hat{\chi}_g(E) = \begin{cases} 1 & E_g < E < E_{g-1}\,, \\ 0 & \text{otherwise}\,. \end{cases}$$

Eq. (5.53) for the multigroup functions $U_g(x,E)$ cannot be solved analytically. To solve it numerically, we discretize Eq. (5.53) following the same procedure for the one-group functions $U(x,E)$ as described in Section 5.1.2, which yields:

$$[1 - H_l R_l + I_l S_l]U_{g,l} + \sum_{l'=l}^{l+m}[-H_{l'}R_{l'+1} + I_{l'}S_{l'+1}]U_{g,l'+1} = \frac{\hat{\chi}_g(E_l)}{\Sigma_t(x,E_l)}\,, \tag{5.54}$$

where:

$$H_l = \frac{C_l(A+1)}{2(1-\alpha)E_l^{\frac{3}{2}}} = \frac{(A+1)}{2(1-\alpha)E_l^{\frac{3}{2}}}\frac{\Sigma_s(x,E_l)}{\Sigma_t(x,E_l)}\,,$$

$$I_l = \frac{C_l(A-1)}{2(1-\alpha)E_l^{\frac{1}{2}}} = \frac{(A-1)}{2(1-\alpha)E_l^{\frac{1}{2}}}\frac{\Sigma_s(x,E_l)}{\Sigma_t(x,E_l)}\,,$$

$$R_l = \frac{2}{5\Delta E_l}(E_l^{\frac{5}{2}} - E_{l+1}^{\frac{5}{2}}) - \frac{2E_{l+1}}{3\Delta E_l}(E_l^{\frac{3}{2}} - E_{l+1}^{\frac{3}{2}})\,,$$

$$\begin{aligned} R_{l+i} = &-\frac{2}{5\Delta E_{l+i-1}}(E_{l+i-1}^{\frac{5}{2}} - E_{l+i}^{\frac{5}{2}}) + \frac{2E_{l+i-1}}{3\Delta E_{l+i-1}}(E_{l+i-1}^{\frac{3}{2}} - E_{l+i}^{\frac{3}{2}}) \\ &+ \frac{2}{5\Delta E_{l+i}}(E_{l+i}^{\frac{5}{2}} - E_{l+i+1}^{\frac{5}{2}}) - \frac{2E_{l+i+1}}{3\Delta E_{l+i}}(E_{l+i}^{\frac{3}{2}} - E_{l+i+1}^{\frac{3}{2}})\,, \qquad 1 \le i \le m \end{aligned}$$

$$R_{l+m+1} = -\frac{2}{5\Delta E_{l+m}}(E_{l+m}^{\frac{5}{2}} - E_{l+m+1}^{\frac{5}{2}}) + \frac{2E_{l+m}}{3\Delta E_{l+m}}(E_{l+m}^{\frac{3}{2}} - E_{l+m+1}^{\frac{3}{2}})\,,$$

$$S_l = \frac{2}{3\Delta E_l}(E_l^{\frac{3}{2}} - E_{l+1}^{\frac{3}{2}}) - \frac{2E_{l+1}}{\Delta E_l}(E_l^{\frac{1}{2}} - E_{l+1}^{\frac{1}{2}})\,,$$

$$\begin{aligned} S_{l+i} = &-\frac{2}{3\Delta E_{l+i-1}}(E_{l+i-1}^{\frac{3}{2}} - E_{l+i}^{\frac{3}{2}}) + \frac{2E_{l+i-1}}{\Delta E_{l+i-1}}(E_{l+i-1}^{\frac{1}{2}} - E_{l+i}^{\frac{1}{2}}) \\ &+ \frac{2}{3\Delta E_{l+i}}(E_{l+i}^{\frac{3}{2}} - E_{l+i+1}^{\frac{3}{2}}) - \frac{2E_{l+i+1}}{\Delta E_{l+i}}(E_{l+i}^{\frac{1}{2}} - E_{l+i+1}^{\frac{1}{2}})\,, \qquad 1 \le i \le m \end{aligned}$$

$$S_{l+m+1} = -\frac{2}{3\Delta E_{l+m}}(E_{l+m}^{\frac{3}{2}} - E_{l+m+1}^{\frac{3}{2}}) + \frac{2E_{l+m}}{\Delta E_{l+m}}(E_{l+m}^{\frac{1}{2}} - E_{l+m+1}^{\frac{1}{2}})\,.$$

For clarification, the integer g represents the energy group used in generating the low-order multigroup FMC equations. $U_{g,l} = U_g(x,E_l)$ represents the value of the multigroup function $U_g(x,E)$ evaluated at the energy grid point l. The integer l is an energy grid point index used in discretizing Eq. (5.53), where $1 \le l \le L$. Figure 5.4 shows the multigroup structure and the energy grid adopted for evaluating $U_g(x,E)$.

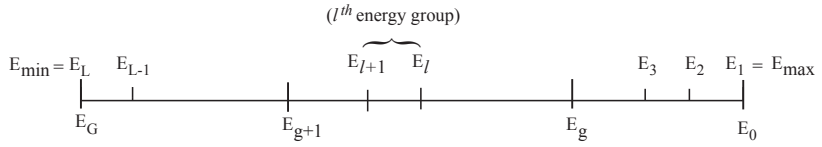

Figure 5.4 Multigroup structure and the energy grid adopted for evaluating $U_g(x,E)$

Eq. (5.54) is a discretized multigroup adjoint equation. For each energy group g, we solve the set of linear Eq. (5.54) for the value of $U_g(x,E_l)$ over the entire energy gird point l. Again, we start with the assumption that the first $m+1$ values $U_g(x,E_L)$, $U_g(x,E_{L-1})$, $\cdots$, $U_g(x,E_{L-m})$ are equal to one another. Because $\hat{\chi}_g(E)$ is nonzero only within the energy group $[E_g \;\; E_{g-1}]$, the numerical values for $U_g(x,E)$ will change dramatically at the energy group boundaries. However, operating on Eq. (5.54) by $\sum_{g=1}^{G}(\cdot)$, we get

$$[1-H_lR_l+I_lS_l]\sum_{g=1}^{G}U_{g,l}+\sum_{l'=l}^{l+m}[-H_{l'}R_{l'+1}+I_{l'}S_{l'+1}]\sum_{g=1}^{G}U_{g,l'+1}=\frac{\sum_{g=1}^{G}\hat{\chi}_g(E_l)}{\Sigma_t(x,E_l)}\,,$$

or

$$[1-H_lR_l+I_lS_l]\sum_{g=1}^{G}U_{g,l}+\sum_{l'=l}^{l+m}[-H_{l'}R_{l'+1}+I_{l'}S_{l'+1}]\sum_{g=1}^{G}U_{g,l'+1}=\frac{1}{\Sigma_t(x,E_l)}\,. \qquad (5.55)$$

Comparing Eq. (5.55) with Eq. (5.35), we have

$$U_l=\sum_{g=1}^{G}U_{g,l}\,. \qquad (5.56)$$

In the numerical results presented in Chapter 6, we assume that the edges of the energy grid for evaluating $U_g(x,E)$ function satisfy the condition $E_{l+21}=\alpha E_l$, which means that a neutron with energy E_l can scatter into its own fine energy group and the following 20 fine energy groups indicated in Figure 5.4.

We have also tested the one group U(x,E) function and the two group $U_g(x,E)$ function

with a finer energy gird, where the edges of the energy grid satisfy the condition $E_{l+41} = \alpha E_l$. This means that a neutron with energy E_l can scatter into its own fine energy group and the following 40 fine energy groups.

For the one group U(x,E) function, the results show that the eigenvalues obtained from the low order energy-integrated FMC equations are essentially the same for the 20 fine group and 40 fine group cases. This is because the one group U(x,E) function is smooth with respect to energy E.

For the two group $U_g(x,E)$ function, the results show that the eigenvalue obtained from the low order multigroup FMC equations with 40 fine groups is slightly more accurate than the eigenvalue with the 20 fine groups. This is because the two group $U_g(x,E)$ function has a discontinuity at the energy group boundary. Thus, a finer energy grid for evaluating $U_g(x,E)$ function is recommended for the multigroup case.

5.3 Procedure to Generate Multigroup Low-Order Equations with Material Discontinuities within a Coarse Cell

In Section 5.1 and Section 5.2, we assumed that a cell only contains one kind of cross section. This assumption will limit the application of the FMC method to more realistic multi-dimensional problems. Realistic reactor core structures contain many fuel assemblies, and each assembly contains a number of different pin cells. Thus, for practical use, it is necessary to introduce the assumption that a cell can contain any number of fine mesh cells with different cross sections. The goal of this section is to apply the FMC method to generate mutligroup low-order equations with any number of material discontinuities within a cell (coarse cell). In doing this, we shall also obtain the flux average over a spatial coarse cell.

We prescribe a spatial coarse grid, consisting of $J+1$ points $x_{j+1/2}$ satisfying $0 = x_{1/2} < x_{3/2} < \cdots < x_{j-1/2} < x_{j+1/2} < \cdots < x_{J-1/2} < x_{J+1/2} = X$. The j^{th} spatial cell consists of

the interval $x_{j-1/2} < x < x_{j+1/2}$; the width of this cell is $h_j = x_{j+1/2} - x_{j-1/2}$.

For the interval $x_{j-1/2} < x < x_{j+1/2}$, the "fine grid" and "coarse grid" are related in the following Figure 5.5:

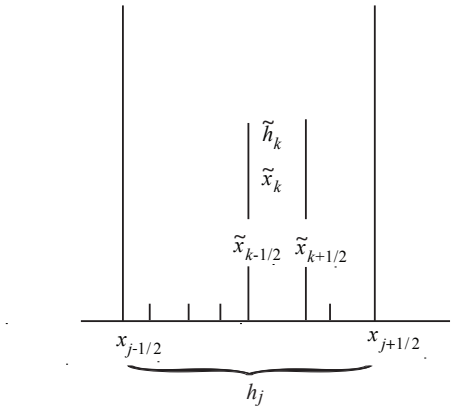

Figure 5.5 Detailed structure of the fine grid within a coarse grid.

To obtain the multigroup flux average over a spatial cell:

$$\begin{aligned}\Phi_{g,j} &= \frac{1}{x_{j+1/2} - x_{j-1/2}} \int_{x_{j-1/2}}^{x_{j+1/2}} \int_{E_g}^{E_{g-1}} \phi(x,E) dE dx \\ &= \frac{1}{h_j} \int_{x_{j-1/2}}^{x_{j+1/2}} \int_{E_g}^{E_{g-1}} \phi(x,E) dE dx \qquad 1 \le j \le J \ , \end{aligned} \tag{5.57}$$

we introduce a *staggered grid point* x_j such that $x_{j-1/2} < x_j < x_{j+1/2}$ for $2 \le j \le J-1$. x_j is chosen near to the center of the j^{th} coarse cell, and x_j is the edge of a fine mesh cell. Let $h_j^L = x_j - x_{j-1/2}$, and $h_j^R = x_{j+1/2} - x_j$. Clearly the width of the j^{th} cell $h_j = h_j^L + h_j^R$.

We also make use of the notation:

$$\sum_{k \in j+1/2} f_k = \text{Sum over all fine cells } k \text{ that lie between } x_j \text{ and } x_{j+1} \ .$$

For $1 \le j \le J$, we define tent functions $f_j(x)$ on the staggered grid.

For $j = 1$:

$$f_1(x) = \begin{cases} \frac{1}{h_1 + h_2^L}(x_2 - x) & , \ 0 = x_1 < x < x_2 \\ 0 & , \ \text{otherwise} \ . \end{cases} \tag{5.58a}$$

For $2 \leq j \leq J-1$:

$$f_j(x) = \begin{cases} \frac{1}{h_{j-1}^R + h_j^L}(x - x_{j-1}) & , \ x_{j-1} < x < x_j \\ \frac{1}{h_j^R + h_{j+1}^L}(x_{j+1} - x) & , \ x_j < x < x_{j+1} \\ 0 & , \ \text{otherwise} \ . \end{cases} \tag{5.58b}$$

And for $j = J$:

$$f_J(x) = \begin{cases} \frac{1}{h_{J-1}^R + h_J}(x - x_{J-1}) & , \ x_{J-1} < x < x_J = X \\ 0 & , \ \text{otherwise} \ . \end{cases} \tag{5.58c}$$

The tent functions defined on a staggered grid are displayed in Figure 5.6, while the detailed structure surrounding a staggered grid point x_j is shown in Figure 5.7. We note that the number of tent functions is equal to the number of coarse cells.

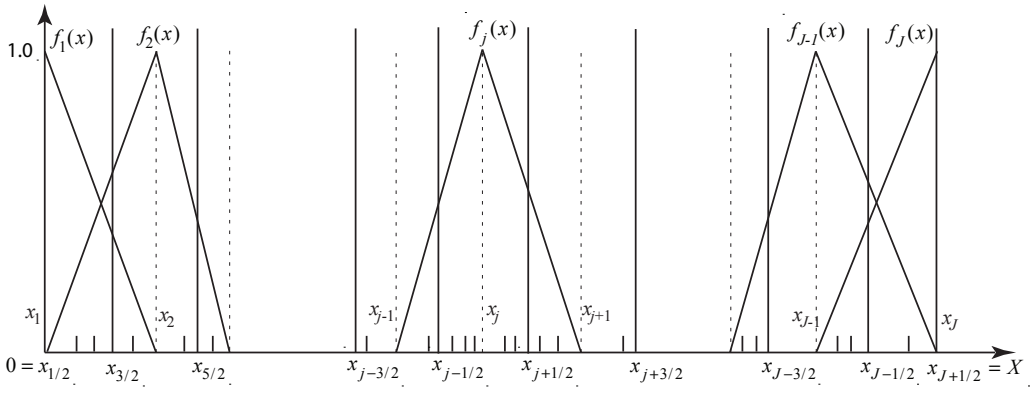

Figure 5.6 The tent functions defined on a coarse staggered grid.

We begin by deriving the multigroup low-order FMC equations. We multiply Eq. (5.45) by

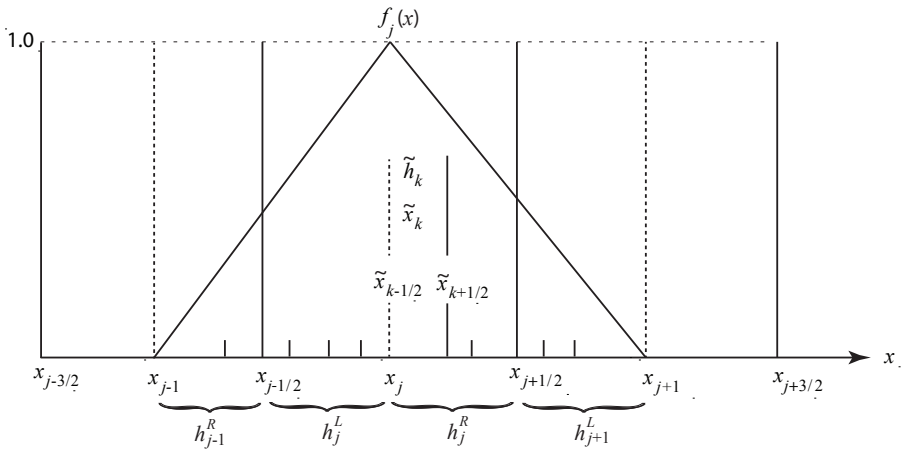

Figure 5.7 Detailed structure surrounding a staggered grid point x_j.

$f_j(x)$ and integrate over $0 \le x \le X$. For $2 \le j \le J-1$, we obtain:

$$
\begin{aligned}
&-\int_{x_{j-1}}^{x_{j+1}} f_j(x)\frac{\partial}{\partial x}\int_0^\infty U_g(x,E)\frac{\partial}{\partial x}\phi_2(x,E)dEdx \\
&+\int_{x_{j-1}}^{x_{j+1}} f_j(x)\int_{E_g}^{E_{g-1}} \Sigma_t(x,E)\phi_0(x,E)dEdx \\
&=\sum_{g'=1}^{G}\int_{E_{g'}}^{E_{g'-1}}\int_{x_{j-1}}^{x_{j+1}} f_j(x)\frac{\Sigma_s(x,E')}{(1-\alpha)E'}Q_g(E')\phi_0(x,E')dxdE' \\
&+\frac{1}{k}\int_{x_{j-1}}^{x_{j+1}} f_j(x)\chi_g(x)\left(\sum_{g'=1}^{G}\int_{E_{g'}}^{E_{g'-1}}\nu\Sigma_f(x,E')\phi_0(x,E')dE'\right)dx\,. \qquad (5.59)
\end{aligned}
$$

We expand the first term of Eq. (5.59) using integration by parts, which yields:

$$
\begin{aligned}
&-\int_{x_{j-1}}^{x_{j+1}} f_j(x)\frac{\partial}{\partial x}\int_0^\infty U_g(x,E)\frac{\partial}{\partial x}\phi_2(x,E)dEdx \\
&=\int_{x_{j-1}}^{x_{j+1}} \frac{df_j}{dx}(x)\int_0^\infty U_g(x,E)\frac{\partial}{\partial x}\phi_2(x,E)dEdx \\
&=\frac{1}{h^R_{j-1}+h^L_j}\int_{x_{j-1}}^{x_j}\int_0^\infty U_g(x,E)\frac{\partial}{\partial x}\phi_2(x,E)dEdx \\
&\quad-\frac{1}{h^R_j+h^L_{j+1}}\int_{x_j}^{x_{j+1}}\int_0^\infty U_g(x,E)\frac{\partial}{\partial x}\phi_2(x,E)dEdx\,. \qquad (5.60)
\end{aligned}
$$

The two terms on the right hand side of Eq. (5.60) are similar. We evaluate the last term by

introducing the coarse grid $U_{g,j+1/2}(E)$ function as follows:

$$
\begin{aligned}
&-\frac{1}{h_j^R+h_{j+1}^L}\int_{x_j}^{x_{j+1}}\int_0^\infty U_g(x,E)\frac{\partial}{\partial x}\phi_2(x,E)dEdx \\
&=-\frac{1}{h_j^R+h_{j+1}^L}\sum_{k\in j+1/2}\int_{\tilde{x}_{k-1/2}}^{\tilde{x}_{k+1/2}}\int_0^\infty \tilde{U}_{g,k}(E)\frac{\partial}{\partial x}\phi_2(x,E)dEdx \\
&=-\frac{1}{h_j^R+h_{j+1}^L}\sum_{k\in j+1/2}\int_0^\infty \tilde{U}_{g,k}(E)\left[\phi_2(\tilde{x}_{k+1/2},E)-\phi_2(\tilde{x}_{k-1/2},E)\right]dE \\
&=-\frac{1}{h_j^R+h_{j+1}^L}\int_0^\infty U_{g,j+1/2}(E)\left[\phi_2(x_{j+1},E)-\phi_2(x_j,E)\right]dE \\
&\quad-\frac{1}{h_j^R+h_{j+1}^L}\left\{\sum_{k\in j+1/2}\int_0^\infty \tilde{U}_{g,k}(E)\left[\phi_2(\tilde{x}_{k+1/2},E)-\phi_2(\tilde{x}_{k-1/2},E)\right]dE\right. \\
&\quad\left.-\int_0^\infty U_{g,j+1/2}(E)\left[\phi_2(x_{j+1},E)-\phi_2(x_j,E)\right]dE\right\}. \qquad (5.61)
\end{aligned}
$$

We now specify that the coarse grid $U_{g,j+1/2}(E)$ be chosen so that the expression in curly brackets $\{\ \}$ in Eq. (5.61) vanishes under the condition that $\phi_2(x,E)=f(E)+xg(E)$ is a linear function of x. This requirement leads to

$$
\begin{aligned}
0&=\sum_{k\in j+1/2}\int_0^\infty \tilde{U}_{g,k}(E)\overbrace{(\tilde{x}_{k+1/2}-\tilde{x}_{k-1/2})}^{\tilde{h_k}}g(E)dE-\int_0^\infty U_{g,j+1/2}(E)(x_{j+1}-x_j)g(E)dE \\
&=\int_0^\infty\left[\sum_{k\in j+1/2}\tilde{U}_{g,k}(E)\tilde{h_k}-U_{g,j+1/2}(E)(x_{j+1}-x_j)\right]g(E)\,dE\,.
\end{aligned}
$$

The above quantity in square brackets is then set equal to zero, yielding the following definition for the coarse grid $U_{g,j+1/2}(E)$ function:

$$
U_{g,j+1/2}(E)=\frac{\sum_{k\in j+1/2}\tilde{U}_{g,k}(E)\tilde{h_k}}{\sum_{k\in j+1/2}\tilde{h_k}}\,. \qquad (5.62)
$$

The coarse grid $U_{g,j+1/2}(E)$ function is seen to be a weighted sum of fine grid $\tilde{U}_{g,k}(E)$ functions. The fine grid $\tilde{U}_{g,k}(E)$ functions satisfy the adjoint equation which was shown earlier.

In addition, let us define a correction term

$$W_{g,j+1/2} = -\frac{1}{h_j^R + h_{j+1}^L}\left\{ \sum_{k\in j+1/2} \int_0^\infty \tilde{U}_{g,k}(E)\left[\phi_2(\tilde{x}_{k+1/2},E) - \phi_2(\tilde{x}_{k-1/2},E)\right] dE \right.$$
$$\left. - \int_0^\infty U_{g,j+1/2}(E)\left[\phi_2(x_{j+1},E) - \phi_2(x_j,E)\right] dE \right\}; \tag{5.63}$$

then Eq. (5.61) can be written as

$$-\frac{1}{h_j^R + h_{j+1}^L}\int_{x_j}^{x_{j+1}}\int_0^\infty U_g(x,E)\frac{\partial}{\partial x}\phi_2(x,E)dEdx$$
$$= -\frac{1}{h_j^R + h_{j+1}^L}\int_0^\infty U_{g,j+1/2}(E)\left[\phi_2(x_{j+1},E) - \phi_2(x_j,E)\right] dE + W_{g,j+1/2}\,. \tag{5.64}$$

Using Eq. (5.64), the first term in Eq. (5.59) becomes:

$$-\int_{x_{j-1}}^{x_{j+1}} f_j(x)\frac{\partial}{\partial x}\int_0^\infty U_g(x,E)\frac{\partial}{\partial x}\phi_2(x,E)dEdx$$
$$= \frac{1}{h_{j-1}^R + h_j^L}\int_{x_{j-1}}^{x_j}\int_0^\infty U_g(x,E)\frac{\partial}{\partial x}\phi_2(x,E)dEdx$$
$$-\frac{1}{h_j^R + h_{j+1}^L}\int_{x_j}^{x_{j+1}}\int_0^\infty U_g(x,E)\frac{\partial}{\partial x}\phi_2(x,E)dEdx$$
$$= \frac{1}{h_{j-1}^R + h_j^L}\int_0^\infty U_{g,j-1/2}(E)\left[\phi_2(x_j,E) - \phi_2(x_{j-1},E)\right] dE - W_{g,j-1/2}$$
$$-\frac{1}{h_j^R + h_{j+1}^L}\int_0^\infty U_{g,j+1/2}(E)\left[\phi_2(x_{j+1},E) - \phi_2(x_j,E)\right] dE + W_{g,j+1/2}\,. \tag{5.65}$$

Incorporating the result in Eq. (5.65) into Eq. (5.59), for $2 \leq j \leq J-1$, we have:

$$\begin{aligned}
&\frac{1}{h_{j-1}^R + h_j^L} \int_0^\infty U_{g,j-1/2}(E) \left[\phi_2(x_j,E) - \phi_2(x_{j-1},E)\right] dE - W_{g,j-1/2} \\
&- \frac{1}{h_j^R + h_{j+1}^L} \int_0^\infty U_{g,j+1/2}(E) \left[\phi_2(x_{j+1},E) - \phi_2(x_j,E)\right] dE + W_{g,j+1/2} \\
&+ \int_{x_{j-1}}^{x_{j+1}} f_j(x) \int_{E_g}^{E_{g-1}} \Sigma_t(x,E)\phi_0(x,E) dE dx \\
&= \sum_{g'=1}^{G} \int_{E_{g'}}^{E_{g'-1}} \int_{x_{j-1}}^{x_{j+1}} f_j(x) \frac{\Sigma_s(x,E')}{(1-\alpha)E'} Q_g(E') \phi_0(x,E') dx dE' \\
&+ \frac{1}{k} \int_{x_{j-1}}^{x_{j+1}} f_j(x) \chi_g(x) \left(\sum_{g'=1}^{G} \int_{E_{g'}}^{E_{g'-1}} \nu\Sigma_f(x,E')\phi_0(x,E') dE' \right) dx \,. \qquad (5.66)
\end{aligned}$$

Similarly, we multiply Eq. (5.45) by $f_1(x)$ and integrate, for $j = 1$ (Figure 5.8), we have

$$\begin{aligned}
&- \int_{x_1}^{x_2} f_1(x) \frac{\partial}{\partial x} \int_0^\infty U_g(x,E) \frac{\partial}{\partial x} \phi_2(x,E) dE dx \\
&+ \int_{x_1}^{x_2} f_1(x) \int_{E_g}^{E_{g-1}} \Sigma_t(x,E)\phi_0(x,E) dE dx \\
&= \sum_{g'=1}^{G} \int_{E_{g'}}^{E_{g'-1}} \int_{x_1}^{x_2} f_1(x) \frac{\Sigma_s(x,E')}{(1-\alpha)E'} Q_g(E') \phi_0(x,E') dx dE' \\
&+ \frac{1}{k} \int_{x_1}^{x_2} f_1(x) \chi_g(x) \left(\sum_{g'=1}^{G} \int_{E_{g'}}^{E_{g'-1}} \nu\Sigma_f(x,E')\phi_0(x,E') dE' \right) dx \,. \qquad (5.67)
\end{aligned}$$

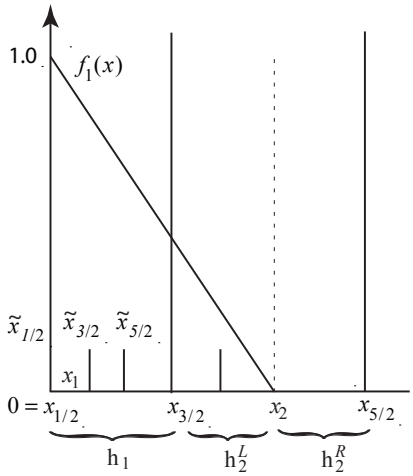

Figure 5.8 Detailed structure at the left boundary for a coarse grid.

Integrating the first term of Eq. (5.67) by parts, we get:

$$
\begin{aligned}
&-\int_{x_1}^{x_2} f_1(x)\frac{\partial}{\partial x}\int_0^{\infty} U_g(x,E)\frac{\partial}{\partial x}\phi_2(x,E)dEdx \\
&=\int_{E_g}^{E_{g-1}}\int_{-1}^{0}|\mu|\psi(0,\mu,E)\,d\mu\,dE-\frac{1}{h_1+h_2^L}\int_{x_1}^{x_2}\int_0^{\infty} U_g(x,E)\frac{\partial}{\partial x}\phi_2(x,E)dEdx \\
&=\int_{E_g}^{E_{g-1}}\int_{-1}^{0}|\mu|\psi(0,\mu,E)\,d\mu\,dE \\
&\quad-\frac{1}{h_1+h_2^L}\int_0^{\infty} U_{g,3/2}(E)\left[\phi_2(x_2,E)-\phi_2(x_1,E)\right]dE+W_{g,3/2}\,. \qquad (5.68)
\end{aligned}
$$

Thus, substituting Eq. (5.68) into Eq. (5.67), for $j=1$ yields:

$$
\begin{aligned}
&\int_{E_g}^{E_{g-1}}\int_{-1}^{0}|\mu|\psi(0,\mu,E)\,d\mu\,dE-\frac{1}{h_1+h_2^L}\int_0^{\infty} U_{g,3/2}(E)\left[\phi_2(x_2,E)-\phi_2(x_1,E)\right]dE+W_{g,3/2} \\
&+\int_{x_1}^{x_2} f_1(x)\int_{E_g}^{E_{g-1}}\Sigma_t(x,E)\phi_0(x,E)dEdx \\
&=\sum_{g'=1}^{G}\int_{E_{g'}}^{E_{g'-1}}\int_{x_1}^{x_2} f_1(x)\frac{\Sigma_s(x,E')}{(1-\alpha)E'}Q_g(E')\phi_0(x,E')dxdE' \\
&+\frac{1}{k}\int_{x_1}^{x_2} f_1(x)\chi_g(x)\left(\sum_{g'=1}^{G}\int_{E_{g'}}^{E_{g'-1}}\nu\Sigma_f(x,E')\phi_0(x,E')dE'\right)dx\,. \qquad (5.69)
\end{aligned}
$$

For $j=J$ (Figure 5.9), we follow similar steps as for $j=1$, multiplying Eq. (5.45) with $f_J(x)$ and integrating. This yields

$$
\begin{aligned}
&-\int_{x_{J-1}}^{x_J} f_J(x)\frac{\partial}{\partial x}\int_0^{\infty} U_g(x,E)\frac{\partial}{\partial x}\phi_2(x,E)dEdx \\
&+\int_{x_{J-1}}^{x_J} f_J(x)\int_{E_g}^{E_{g-1}}\Sigma_t(x,E)\phi_0(x,E)dEdx \\
&=\sum_{g'=1}^{G}\int_{E_{g'}}^{E_{g'-1}}\int_{x_{J-1}}^{x_J} f_J(x)\frac{\Sigma_s(x,E')}{(1-\alpha)E'}Q_g(E')\phi_0(x,E')dxdE' \\
&+\frac{1}{k}\int_{x_{J-1}}^{x_J} f_J(x)\chi_g(x)\left(\sum_{g'=1}^{G}\int_{E_{g'}}^{E_{g'-1}}\nu\Sigma_f(x,E')\phi_0(x,E')dE'\right)dx\,. \qquad (5.70)
\end{aligned}
$$

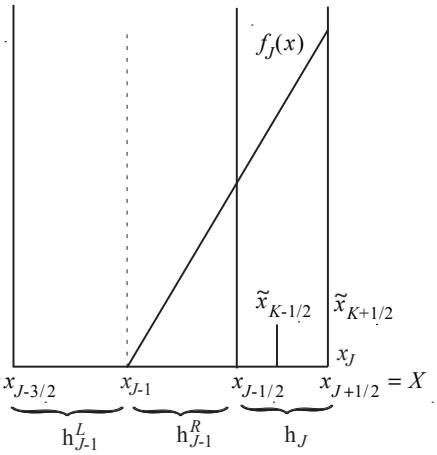

Figure 5.9 Detailed structure at the right boundary for a coarse grid.

Integrating the first term of Eq. (5.70) by parts, we get:

$$
\begin{aligned}
&-\int_{x_{J-1}}^{x_J} f_J(x)\frac{\partial}{\partial x}\int_0^\infty U_g(x,E)\frac{\partial}{\partial x}\phi_2(x,E)dEdx \\
&=\int_{E_g}^{E_{g-1}}\int_{-1}^{1}|\mu|\psi(X,\mu,E)\,d\mu\,dE \\
&+\frac{1}{h^R_{J-1}+h_J}\int_0^\infty U_{g,J-1/2}(E)\left[\phi_2(x_J,E)-\phi_2(x_{J-1},E)\right]dE - W_{g,J-1/2}\,. \qquad (5.71)
\end{aligned}
$$

Thus, substituting Eq. (5.71) into Eq. (5.70), for $j = J$ yields:

$$
\begin{aligned}
&\int_{E_g}^{E_{g-1}}\int_{-1}^{1}|\mu|\psi(X,\mu,E)\,d\mu\,dE \\
&+\frac{1}{h^R_{J-1}+h_J}\int_0^\infty U_{g,J-1/2}(E)\left[\phi_2(x_J,E)-\phi_2(x_{J-1},E)\right]dE - W_{g,J-1/2} \\
&+\int_{x_{J-1}}^{x_J} f_J(x)\int_{E_g}^{E_{g-1}}\Sigma_t(x,E)\phi_0(x,E)dEdx \\
&=\sum_{g'=1}^{G}\int_{E_{g'}}^{E_{g'-1}}\int_{x_{J-1}}^{x_J} f_J(x)\frac{\Sigma_s(x,E')}{(1-\alpha)E'}Q_g(E')\phi_0(x,E')dxdE' \\
&+\frac{1}{k}\int_{x_{J-1}}^{x_J} f_J(x)\chi_g(x)\left(\sum_{g'=1}^{G}\int_{E_{g'}}^{E_{g'-1}}\nu\Sigma_f(x,E')\phi_0(x,E')dE'\right)dx\,. \qquad (5.72)
\end{aligned}
$$

Next, for $1 \leq j \leq J$, we introduce functions $g_j(x)$ that satisfy:

$$g_j(x) = \begin{cases} \frac{1}{h_j} & x_{j-1/2} < x < x_{j+1/2} \\ 0 \quad , \quad \text{otherwise} \ . \end{cases}$$

For $1 \leq j \leq J$, we define:

$$\Phi_{g,j} = \int_{x_{j-1}}^{x_{j+1}} \int_{E_g}^{E_{g-1}} g_j(x)\phi(x,E)dEdx \ , \tag{5.73}$$

where $x_0 = x_{1/2} = x_1 = 0$, and $x_{J+1} = x_{J+1/2} = x_J = X$. The quantities $\Phi_{g,j}$ are the multi-group flux average over spatial coarse cells, which are also unknowns for the low-order FMC equations as indicated in Figure 5.10. We note that Eq. (5.73) is equivalent to the Eq. (5.57).

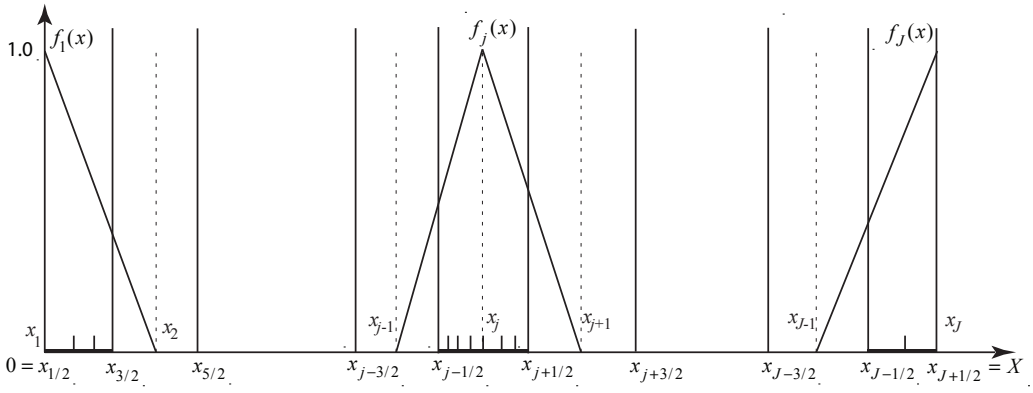

Figure 5.10 The heavy line (spatial coarse cell) intervals indicate the regions where $\Phi_{g,j}$ are averaged using tent functions defined on a staggered grid.

We multiply and divide each term in Eq. (5.69) by a suitable $\Phi_{g,j}$ and rearrange the terms.

The $j=1$ case may be written

$$\left[\left(\frac{\int_{E_g}^{E_{g-1}}\int_{-1}^{0}|\mu|\psi(0,\mu,E)\,d\mu\,dE}{\int_{x_1}^{x_2}\int_{E_g}^{E_{g-1}}g_1(x)\phi(x,E)dEdx}\right)+\frac{1}{h_1+h_2^L}\left(\frac{\int_0^\infty U_{g,3/2}(E)\phi_2(x_1,E)dE}{\int_{x_1}^{x_2}\int_{E_g}^{E_{g-1}}g_1(x)\phi(x,E)dEdx}\right)\right.$$
$$+\left(\frac{W_{g,3/2}}{\int_{x_1}^{x_2}\int_{E_g}^{E_{g-1}}g_1(x)\phi(x,E)dEdx+\int_{x_1}^{x_3}\int_{E_g}^{E_{g-1}}g_2(x)\phi(x,E)dEdx}\right)$$
$$\left.+\left(\frac{\int_{x_1}^{x_2}f_1(x)\int_{E_g}^{E_{g-1}}\Sigma_t(x,E)\phi_0(x,E)dEdx}{\int_{x_1}^{x_2}\int_{E_g}^{E_{g-1}}g_1(x)\phi(x,E)dEdx}\right)\right]\Phi_{g,1}$$
$$-\left[\frac{1}{h_1+h_2^L}\left(\frac{\int_0^\infty U_{g,3/2}(E)\phi_2(x_2,E)dE}{\int_{x_1}^{x_3}\int_{E_g}^{E_{g-1}}g_2(x)\phi(x,E)dEdx}\right)\right.$$
$$\left.-\left(\frac{W_{g,3/2}}{\int_{x_1}^{x_2}\int_{E_g}^{E_{g-1}}g_1(x)\phi(x,E)dEdx+\int_{x_1}^{x_3}\int_{E_g}^{E_{g-1}}g_2(x)\phi(x,E)dEdx}\right)\right]\Phi_{g,2}$$
$$=\sum_{g'=1}^{G}\left[\left(\frac{\int_{E_{g'}}^{E_{g'-1}}\int_{x_1}^{x_2}f_1(x)\frac{\Sigma_s(x,E')}{(1-\alpha)E'}Q_g(E')\phi_0(x,E')dxdE'}{\int_{x_1}^{x_2}\int_{E_{g'}}^{E_{g'-1}}g_1(x)\phi(x,E')dE'dx}\right)\Phi_{g',1}\right]$$
$$+\frac{1}{k}\sum_{g'=1}^{G}\left[\left(\frac{\int_{E_{g'}}^{E_{g'-1}}\int_{x_1}^{x_2}f_1(x)\chi_g(x)\nu\Sigma_f(x,E')\phi_0(x,E')dxdE'}{\int_{x_1}^{x_2}\int_{E_{g'}}^{E_{g'-1}}g_1(x)\phi(x,E')dE'dx}\right)\Phi_{g',1}\right]. \tag{5.74}$$

Similarly, for $2\leq j\leq J-1$ we get Eq. (5.75) and for $j=J$ we get Eq. (5.76).

$$
\begin{aligned}
&- \left[\frac{1}{h_{j-1}^R + h_j^L} \left(\frac{\int_0^\infty U_{g,j-1/2}(E)\phi_2(x_{j-1},E)dE}{\int_{x_{j-2}}^{x_j}\int_{E_g}^{E_{g-1}} g_{j-1}(x)\phi(x,E)dEdx} \right) \right. \\
&\left. + \left(\frac{W_{g,j-1/2}}{\int_{x_{j-2}}^{x_j}\int_{E_g}^{E_{g-1}} g_{j-1}(x)\phi(x,E)dEdx + \int_{x_{j-1}}^{x_{j+1}}\int_{E_g}^{E_{g-1}} g_j(x)\phi(x,E)dEdx} \right) \right] \Phi_{g,j-1} \\
&+ \left[\frac{1}{h_{j-1}^R + h_j^L} \left(\frac{\int_0^\infty U_{g,j-1/2}(E)\phi_2(x_j,E)dE}{\int_{x_{j-1}}^{x_{j+1}}\int_{E_g}^{E_{g-1}} g_j(x)\phi(x,E)dEdx} \right) \right. \\
&+ \frac{1}{h_j^R + h_{j+1}^L} \left(\frac{\int_0^\infty U_{g,j+1/2}(E)\phi_2(x_j,E)dE}{\int_{x_{j-1}}^{x_{j+1}}\int_{E_g}^{E_{g-1}} g_j(x)\phi(x,E)dEdx} \right) \\
&- \left(\frac{W_{g,j-1/2}}{\int_{x_{j-2}}^{x_j}\int_{E_g}^{E_{g-1}} g_{j-1}(x)\phi(x,E)dEdx + \int_{x_{j-1}}^{x_{j+1}}\int_{E_g}^{E_{g-1}} g_j(x)\phi(x,E)dEdx} \right) \\
&\left. + \left(\frac{W_{g,j+1/2}}{\int_{x_{j-1}}^{x_{j+1}}\int_{E_g}^{E_{g-1}} g_j(x)\phi(x,E)dEdx + \int_{x_j}^{x_{j+2}}\int_{E_g}^{E_{g-1}} g_{j+1}(x)\phi(x,E)dEdx} \right) \right. \\
&\left. + \left(\frac{\int_{x_{j-1}}^{x_{j+1}} f_j(x)\int_{E_g}^{E_{g-1}} \Sigma_t(x,E)\phi_0(x,E)dEdx}{\int_{x_{j-1}}^{x_{j+1}}\int_{E_g}^{E_{g-1}} g_j(x)\phi(x,E)dEdx} \right) \right] \Phi_{g,j} \\
&- \left[\frac{1}{h_j^R + h_{j+1}^L} \left(\frac{\int_0^\infty U_{g,j+1/2}(E)\phi_2(x_{j+1},E)E}{\int_{x_j}^{x_{j+2}}\int_{E_g}^{E_{g-1}} g_{j+1}(x)\phi(x,E)dEdx} \right) \right. \\
&\left. - \left(\frac{W_{g,j+1/2}}{\int_{x_{j-1}}^{x_{j+1}}\int_{E_g}^{E_{g-1}} g_j(x)\phi(x,E)dEdx + \int_{x_j}^{x_{j+2}}\int_{E_g}^{E_{g-1}} g_{j+1}(x)\phi(x,E)dEdx} \right) \right] \Phi_{g,j+1} \\
&= \sum_{g'=1}^{G} \left[\left(\frac{\int_{E_{g'}}^{E_{g'-1}}\int_{x_{j-1}}^{x_{j+1}} f_j(x)\frac{\Sigma_s(x,E')}{(1-\alpha)E'}Q_g(E')\phi_0(x,E')dxdE'}{\int_{x_{j-1}}^{x_{j+1}}\int_{E_{g'}}^{E_{g'-1}} g_j(x)\phi(x,E')dE'dx} \right) \Phi_{g',j} \right] \\
&+ \frac{1}{k}\sum_{g'=1}^{G} \left[\left(\frac{\int_{E_{g'}}^{E_{g'-1}}\int_{x_{j-1}}^{x_{j+1}} f_j(x)\chi_g(x)\nu\Sigma_f(x,E')\phi_0(x,E')dxdE'}{\int_{x_{j-1}}^{x_{j+1}}\int_{E_{g'}}^{E_{g'-1}} g_j(x)\phi(x,E')dE'dx} \right) \Phi_{g',j} \right] . \qquad (5.75)
\end{aligned}
$$

$$
\begin{aligned}
&- \left[\frac{1}{h^R_{J-1}+h_J} \left(\frac{\int_0^\infty U_{g,J-1/2}(E)\phi_2(x_{J-1},E)dE}{\int_{x_{J-2}}^{x_J}\int_{E_g}^{E_{g-1}} g_{J-1}(x)\phi(x,E)dEdx} \right) \right. \\
&\left. + \left(\frac{W_{g,J-1/2}}{\int_{x_{J-2}}^{x_J}\int_{E_g}^{E_{g-1}} g_{J-1}(x)\phi(x,E)dEdx + \int_{x_{J-1}}^{x_J}\int_{E_g}^{E_{g-1}} g_J(x)\phi(x,E)dEdx} \right) \right] \Phi_{g,J-1} \\
&+ \left[\left(\frac{\int_{E_g}^{E_{g-1}}\int_{-1}^{1} |\mu|\psi(X,\mu,E)\,d\mu\,dE}{\int_{x_{J-1}}^{x_J}\int_{E_g}^{E_{g-1}} g_J(x)\phi(x,E)dEdx} \right) + \frac{1}{h^R_{J-1}+h_J} \left(\frac{\int_0^\infty U_{g,J-1/2}(E)\phi_2(x_J,E)dE}{\int_{x_{J-1}}^{x_J}\int_{E_g}^{E_{g-1}} g_J(x)\phi(x,E)dEdx} \right) \right. \\
&- \left(\frac{W_{g,J-1/2}}{\int_{x_{J-2}}^{x_J}\int_{E_g}^{E_{g-1}} g_{J-1}(x)\phi(x,E)dEdx + \int_{x_{J-1}}^{x_J}\int_{E_g}^{E_{g-1}} g_J(x)\phi(x,E)dEdx} \right) \\
&\left. + \left(\frac{\int_{x_{J-1}}^{x_J} f_J(x)\int_{E_g}^{E_{g-1}} \Sigma_t(x,E)\phi_0(x,E)dEdx}{\int_{x_{J-1}}^{x_J}\int_{E_g}^{E_{g-1}} g_J(x)\phi(x,E)dEdx} \right) \right] \Phi_{g,J} \\
&= \sum_{g'=1}^{G} \left[\left(\frac{\int_{E_{g'}}^{E_{g'-1}}\int_{x_{J-1}}^{x_J} f_J(x)\frac{\Sigma_s(x,E')}{(1-\alpha)E'}Q_g(E')\phi_0(x,E')dxdE'}{\int_{x_{J-1}}^{x_J}\int_{E_{g'}}^{E_{g'-1}} g_J(x)\phi(x,E')dE'dx} \right) \Phi_{g',J} \right] \\
&+ \frac{1}{k}\sum_{g'=1}^{G} \left[\left(\frac{\int_{E_{g'}}^{E_{g'-1}}\int_{x_{J-1}}^{x_J} f_J(x)\chi_g(x)\nu\Sigma_f(x,E')\phi_0(x,E')dxdE'}{\int_{x_{J-1}}^{x_J}\int_{E_{g'}}^{E_{g'-1}} g_J(x)\phi(x,E')dE'dx} \right) \Phi_{g',J} \right] . \qquad (5.76)
\end{aligned}
$$

We define the nonlinear functionals as follows:

$$
\begin{aligned}
B_{g,1} &= \frac{\int_{E_g}^{E_{g-1}} \int_{-1}^{0} |\mu| \psi(0,\mu,E)\, d\mu\, dE}{\int_{E_g}^{E_{g-1}} \int_{x_1}^{x_2} g_1(x)\phi(x,E)\, dx dE} \\
B_{g,J} &= \frac{\int_{E_g}^{E_{g-1}} \int_{-1}^{1} |\mu| \psi(x_J,\mu,E)\, d\mu\, dE}{\int_{E_g}^{E_{g-1}} \int_{x_{J-1}}^{x_J} g_J(x)\phi(x,E)\, dx dE} \\
F_{g,g',j} &= \frac{\int_{E_g}^{E_{g-1}} \int_{x_{j-1}}^{x_{j+1}} f_j(x)\chi_{g'}(x)\nu\Sigma_f(x,E)\phi_0(x,E)\, dx dE}{\int_{E_g}^{E_{g-1}} \int_{x_{j-1}}^{x_{j+1}} g_j(x)\phi(x,E)\, dx dE} \\
U^R_{g,j+1/2} &= \frac{\int_0^{\infty} U_{g,j+1/2}(E)\phi_2(x_{j+1},E)\, dE}{\int_{E_g}^{E_{g-1}} \int_{x_j}^{x_{j+2}} g_{j+1}(x)\phi(x,E)\, dx dE} \\
U^L_{g,j+1/2} &= \frac{\int_0^{\infty} U_{g,j+1/2}(E)\phi_2(x_j,E)\, dE}{\int_{E_g}^{E_{g-1}} \int_{x_{j-1}}^{x_{j+1}} g_j(x)\phi(x,E)\, dx dE} \\
\tilde{\Sigma}_{s,g\to g',j} &= \frac{\int_{E_g}^{E_{g-1}} \int_{x_{j-1}}^{x_{j+1}} f_j(x)\frac{\Sigma_s(x,E)}{(1-\alpha)E} Q_{g'}(E)\phi(x,E)\, dx dE}{\int_{E_g}^{E_{g-1}} \int_{x_{j-1}}^{x_{j+1}} g_j(x)\phi(x,E)\, dx dE} \\
\tilde{\Sigma}_{t,g,j} &= \frac{\int_{x_{j-1}}^{x_{j+1}} f_j(x) \int_{E_g}^{E_{g-1}} \Sigma_t(x,E)\phi(x,E)\, dE\, dx}{\int_{E_g}^{E_{g-1}} \int_{x_{j-1}}^{x_{j+1}} g_j(x)\phi(x,E)\, dx dE} \\
\tilde{W}_{g,j-1/2} &= \frac{W_{g,j-1/2}}{\int_{x_{j-2}}^{x_j} \int_{E_g}^{E_{g-1}} g_{j-1}(x)\phi(x,E) dE dx + \int_{x_{j-1}}^{x_{j+1}} \int_{E_g}^{E_{g-1}} g_j(x)\phi(x,E) dE dx} \,. \qquad (5.77)
\end{aligned}
$$

In terms of the nonlinear functionals, Eqs. (5.74), (5.75), and (5.76) can be written as:

$$
\begin{aligned}
&\left[B_{g,1} + \frac{1}{h_1+h_2^L} U^L_{g,3/2} + \tilde{W}_{g,3/2} + \tilde{\Sigma}_{t,g,1}\right] \Phi_{g,1} - \left[\frac{1}{h_1+h_2^L} U^R_{g,3/2} - \tilde{W}_{g,3/2}\right] \Phi_{g,2} \\
&= \sum_{g'=1}^{G} \tilde{\Sigma}_{s,g'\to g,1}\, \Phi_{g',1} + \frac{1}{k} \sum_{g'=1}^{G} F_{g',g,1}\, \Phi_{g',1} \,, \qquad (5.78a)
\end{aligned}
$$

$$
\begin{aligned}
&-\left[\frac{1}{h_{j-1}^R+h_j^L}U_{g,j-1/2}^L+\tilde{W}_{g,j-1/2}\right]\Phi_{g,j-1}+\left[\frac{1}{h_{j-1}^R+h_j^L}U_{g,j-1/2}^R+\frac{1}{h_j^R+h_{j+1}^L}U_{g,j+1/2}^L\right.\\
&\left.-\tilde{W}_{g,j-1/2}+\tilde{W}_{g,j+1/2}+\tilde{\Sigma}_{t,g,j}\right]\Phi_{g,j}-\left[\frac{1}{h_j^R+h_{j+1}^L}U_{g,j+1/2}^R-\tilde{W}_{g,j+1/2}\right]\Phi_{g,j+1}\\
&=\sum_{g'=1}^{G}\tilde{\Sigma}_{s,g'\to g,j}\Phi_{g',j}+\frac{1}{k}\sum_{g'=1}^{G}F_{g',g,j}\Phi_{g',j}, \qquad 2\le j\le J-1\,, \qquad (5.78b)
\end{aligned}
$$

$$
\begin{aligned}
&-\left[\frac{1}{h_{J-1}^R+h_J}U_{g,J-1/2}^L+\tilde{W}_{g,J-1/2}\right]\Phi_{g,J-1}\\
&\qquad+\left[B_{g,J}+\frac{1}{h_{J-1}^R+h_J}U_{g,J-1/2}^R-\tilde{W}_{g,J-1/2}+\tilde{\Sigma}_{t,g,J}\right]\Phi_{g,J}\\
&\qquad=\sum_{g'=1}^{G}\tilde{\Sigma}_{s,g'\to g,J}\Phi_{g',J}+\frac{1}{k}\sum_{g'=1}^{G}F_{g',g,J+1/2}\Phi_{g',J}\,. \qquad (5.78c)
\end{aligned}
$$

Eqs. (5.78) are the FMC multigroup low-order equations on a coarse grid. In Section 5.2, we also derived the FMC multigroup low-order equations Eqs. (5.52). The differences are that Eqs. (5.52) are limited to one kind of material in each cell, and the FMC tent functions are defined on a spatial grid. The FMC eigenfunctions are obtained on a staggered grid. On the other hand, Eqs. (5.78) can contain any number of material discontinuities within a coarse cell. The tent functions here are defined on a staggered grid, and the FMC eigenfunctions are averaged over spatial coarse cells. These FMC eigenfunctions averaged over spatial coarse cells can then be used in the FMC feedback calculation.

Chapter 6

Continuous Energy k-Eigenvalue Problems: Numerical Results

In this Chapter, we present two different types of problem for the FMC method as applied to the continuous energy method that we derived in Chapter 5.

6.1 Continuous Energy Problem 1: Large Homogeneous Fissile Slab Problem

In this section, we apply both the one-group and the two-group FMC method to a homogeneous fissile slab problem with continuous energy.

We consider a homogeneous fissile region of thickness $X = 300$ cm surrounded by two 5.0 cm non-fissile regions. The two energy groups are used in the low-order FMC equations as shown:

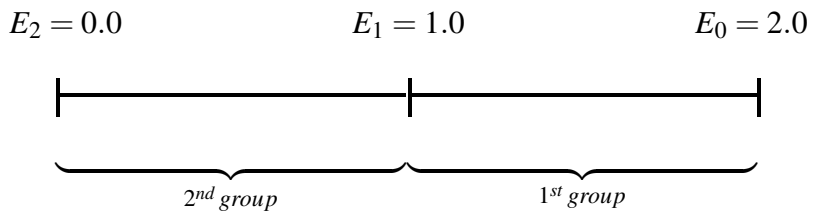

Fission neutrons are born uniformly within the energy range 1.0 MeV - 2.0 MeV. The

model fission spectrum is :

$$\chi(E) = \begin{cases} 1.0 \text{ Mev}^{-1} & , \quad 1 \text{ Mev} < E < 2 \text{ Mev} , \\ 0 & , \qquad \text{otherwise} . \end{cases} \tag{6.1}$$

The Monte Carlo simulation starts with a spatially flat fission source. The fissile material consists of atomic mass number 56, while the non-fissile material consists of atomic mass number 27. The relevant model cross sections are taken to be inversely proportional to the square root of energy, given by

$$\Sigma_s(x,E) = \Sigma_s^0(x) + \Sigma_s^1(x)\sqrt{\frac{E_0}{E}} , \tag{6.2a}$$

$$\Sigma_\gamma(x,E) = \Sigma_\gamma(x)\sqrt{\frac{E_0}{E}} , \tag{6.2b}$$

$$\Sigma_f(x,E) = \Sigma_f(x)\sqrt{\frac{E_0}{E}} . \tag{6.2c}$$

The various cross section coefficients in Eqs. (6.2) are presented in Table 6.1, where x has units of cm and Σ has units of cm^{-1}.

Table 6.1 Cross Section Coefficients for a Homogeneous Fissile Slab Problem 1.

Region	Location	$\Sigma_s^0(x)$	$\Sigma_s^1(x)$	$\Sigma_\gamma(x)$	$\Sigma_f(x)$
1	$0 < x < 5$	0.856	0.01	0.01	0
2	$5 < x < 305$	0.856	0.01	0.01	0.0071
3	$305 < x < 310$	0.856	0.01	0.01	0

6.1.1 The One-Group $U(x,E)$ and Two-Group $U_g(x,E)$ Calculations

The procedure for evaluating the one-group $U(x,E)$ function is given in Section 5.12, while the procedure for evaluating the two-group $U_g(x,E)$ function is given in Section 5.22. We assume that the edges of the energy grid satisfy the condition $E_{l+20} = \alpha E_l$, which means that a neutron with energy E_l can scatter into its own energy group and the following 19

neighboring energy groups. The calculation of the U function only needs to be done once, for each material, at the beginning of the calculation.

Figure 6.1 shows the one-group $U(x,E)$ and two-group $U_g(x,E)$ functions for the material consisting of mass number 56. Figure 6.2 shows the one-group $U(x,E)$ and two-group $U_g(x,E)$ functions for the material consisting of mass number 27. From Figures 6.1 and 6.2, we note that the numerical values for the two-group functions $U_1(x,E)$ and $U_2(x,E)$ fluctuate significantly near the energy group boundary $1MeV$. On the other hand, the one-group $U(x,E)$ is a very smooth function. Furthermore, we notice that $U(x,E) = U_1(x,E) + U_2(x,E)$.

6.1.2 FMC Coarse Mesh ($5cm$ Grid) without FMC Feedback

We now present the results of Problem 1 for a flat initial fission source guess, and without FMC feedback. This problem was run for 1000 cycles, using 100,000 histories/cycle. The FMC calculation employs a coarse grid with $h = 5.0$ cm and a fine grid 1.0 cm .

In Figures 6.3-6.5 we compare results for one-group fluxes and two-group fluxes, averaged over 100 cycle intervals (from a 1000-cycle sequence), i.e. cycles 101-200, 201-300, 301-400, 401-500, 501-600, 601-700,701-800,801-900, and 901-1000. Results are compared for (a) standard Monte Carlo simulations and (b) the hybrid FMC calculations. For both the one-group and two-group cases, the FMC results are seen to converge almost immediately and to remain stable in all 100-cycle averages of the run. The standard Monte Carlo results do not achieve equilibrium at any point during the 1000 cycle test run because of undersampling of the fission source.

Figure 6.6 shows the one-group estimates of the eigenfunction, averaged over the last 500 cycles (501-1000), and the estimated apparent relative standard deviations and true relative standard deviations in the Monte Carlo and FMC eigenfunctions over the cycles. Figure 6.7 shows the two-group estimates of the eigenfunction, averaged over the last 500 cycles, and the estimated apparent relative standard deviations and true relative standard

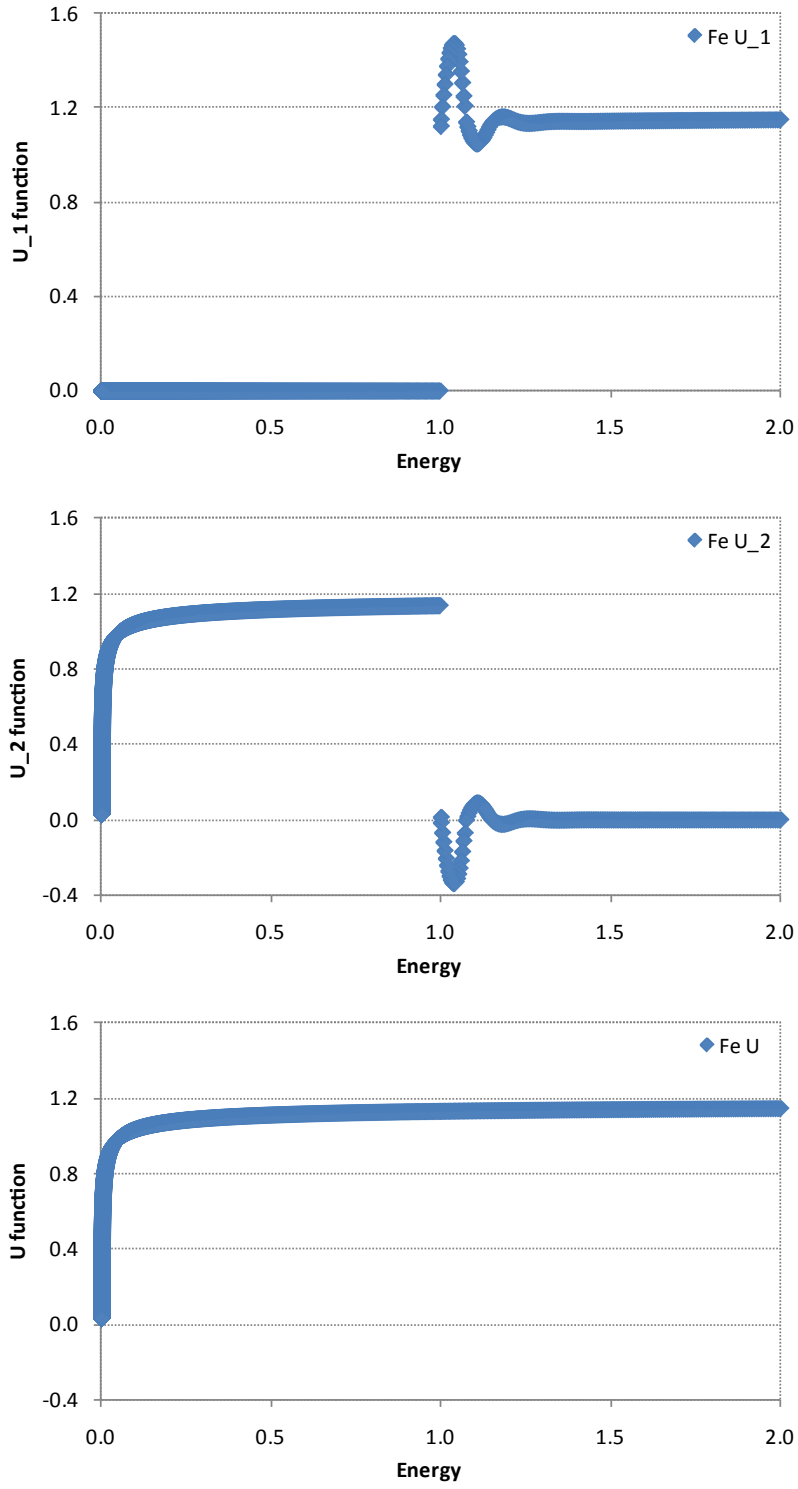

Figure 6.1 The one-group $U(x,E)$ and the two-group $U_g(x,E)$ functions for the material with mass number 56.

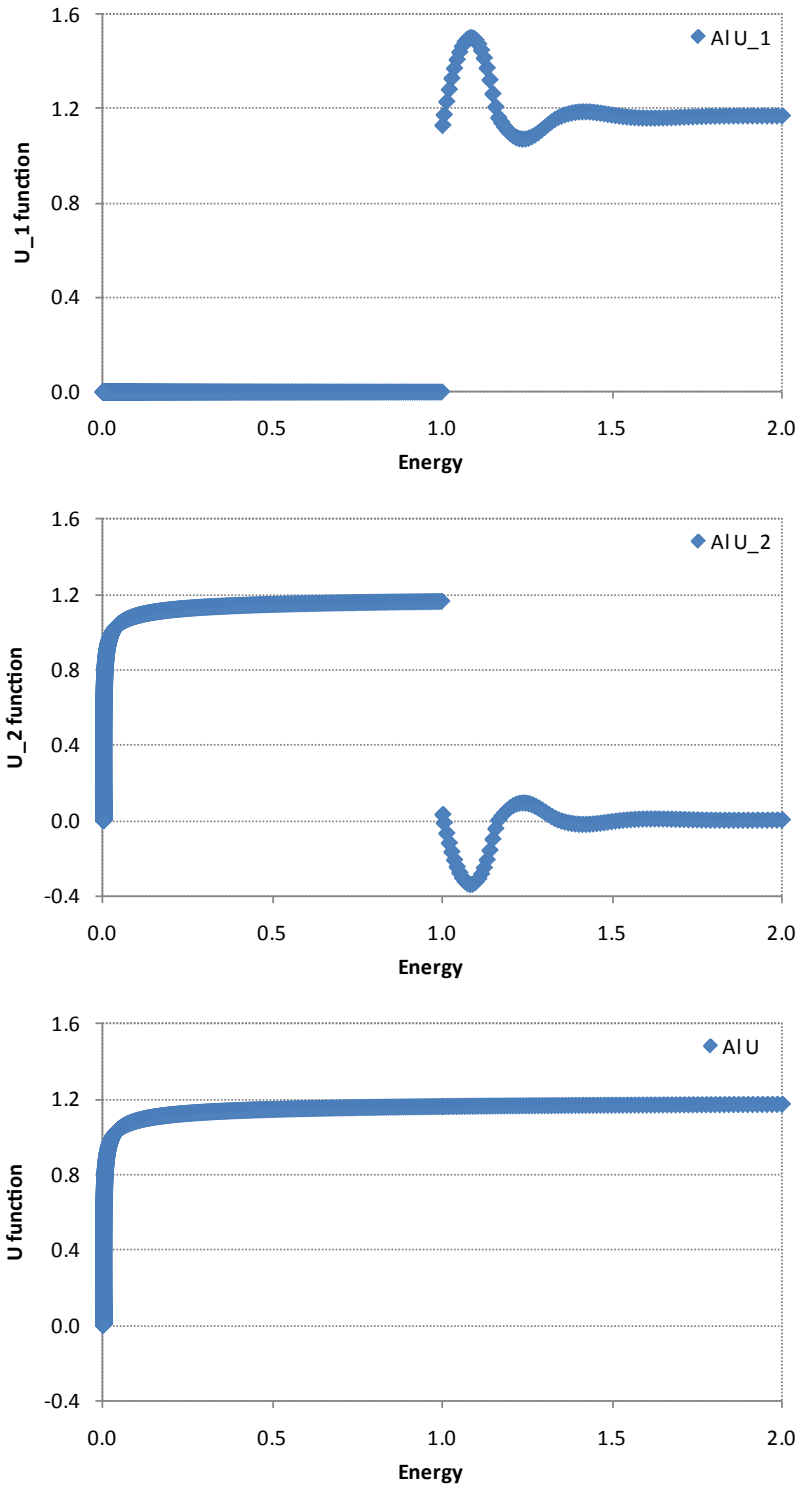

Figure 6.2 The one-group $U(x,E)$ and the two-group $U_g(x,E)$ functions for the material with mass number 27.

deviations. The apparent relative standard deviations are obtained from a single 1000-cycle (500 inactive cycles, and 500 active cycles) run, while the true relative standard deviations are obtained from 25 independent 1000-cycle runs.

Figures 6.6-6.7 show that, even though it is averaged over a large number of cycles, both the one-group and two-group MC estimates of the eigenfunction are inaccurate and "tilted." The estimated relative standard deviations (both apparent and true) in the FMC one-group and two-group eigenfunctions are smaller than those of the MC eigenfunctions, and the FMC eigenfunction estimates are clearly much more accurate. A detailed comparison between the apparent relative standard deviation and the true relative standard deviation in the MC, FMC eigenfunction estimates for the two-group energy case are given in Figure 6.8 and Figure 6.9. Figure 6.8 shows that the true relative standard deviations are more than a factor of 10 greater than the apparent relative standard deviations in the MC eigenfunction estimates. This is because of correlations in the fission source between one cycle and the next. Figure 6.9 shows that the true relative standard deviations in the FMC eigenfunction estimates are approximately the same as the apparent relative standard deviations.

The estimated values of k and their estimated relative standard deviations over 100 different ranges of 1000 cycles each are compared for the one-group eigenfunction case and the two-group eigenfunction case in Table 6.2.

Table 6.2 shows that the errors in k obtained with the FMC method are much smaller than the errors in the standard Monte Carlo estimates of k. In this homogenous problem, the estimates of k from the one-group FMC method and the two-group FMC method agree, as they should. (Apart from statistical differences, the FMC estimates of k should not be affected by the choice of spatial or energy grid.)

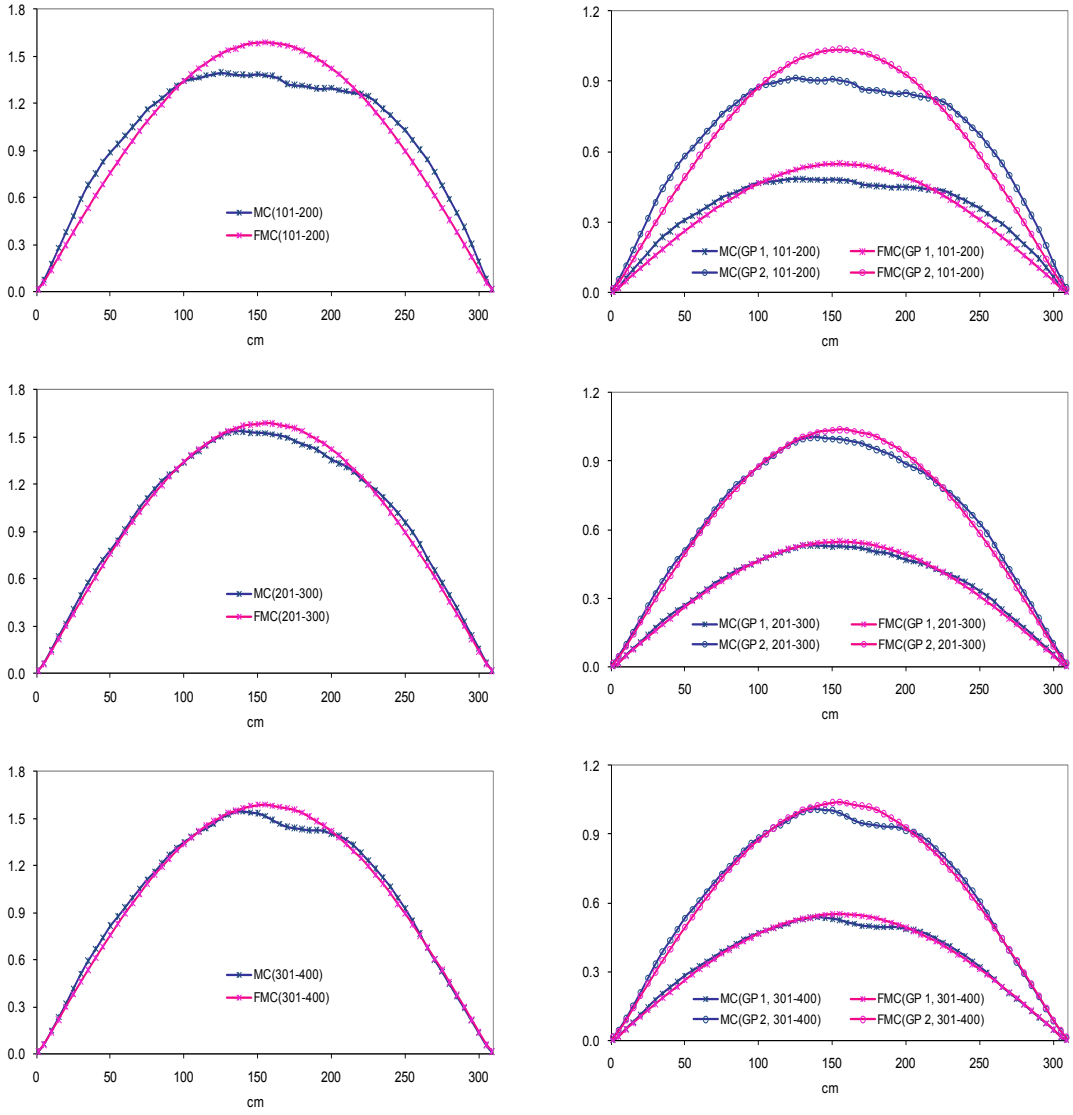

Figure 6.3 Continuous energy Problem 1 one-group and two-group eigenfunction estimates during cycles 101-400 without FMC feedback (5*cm* Grid).

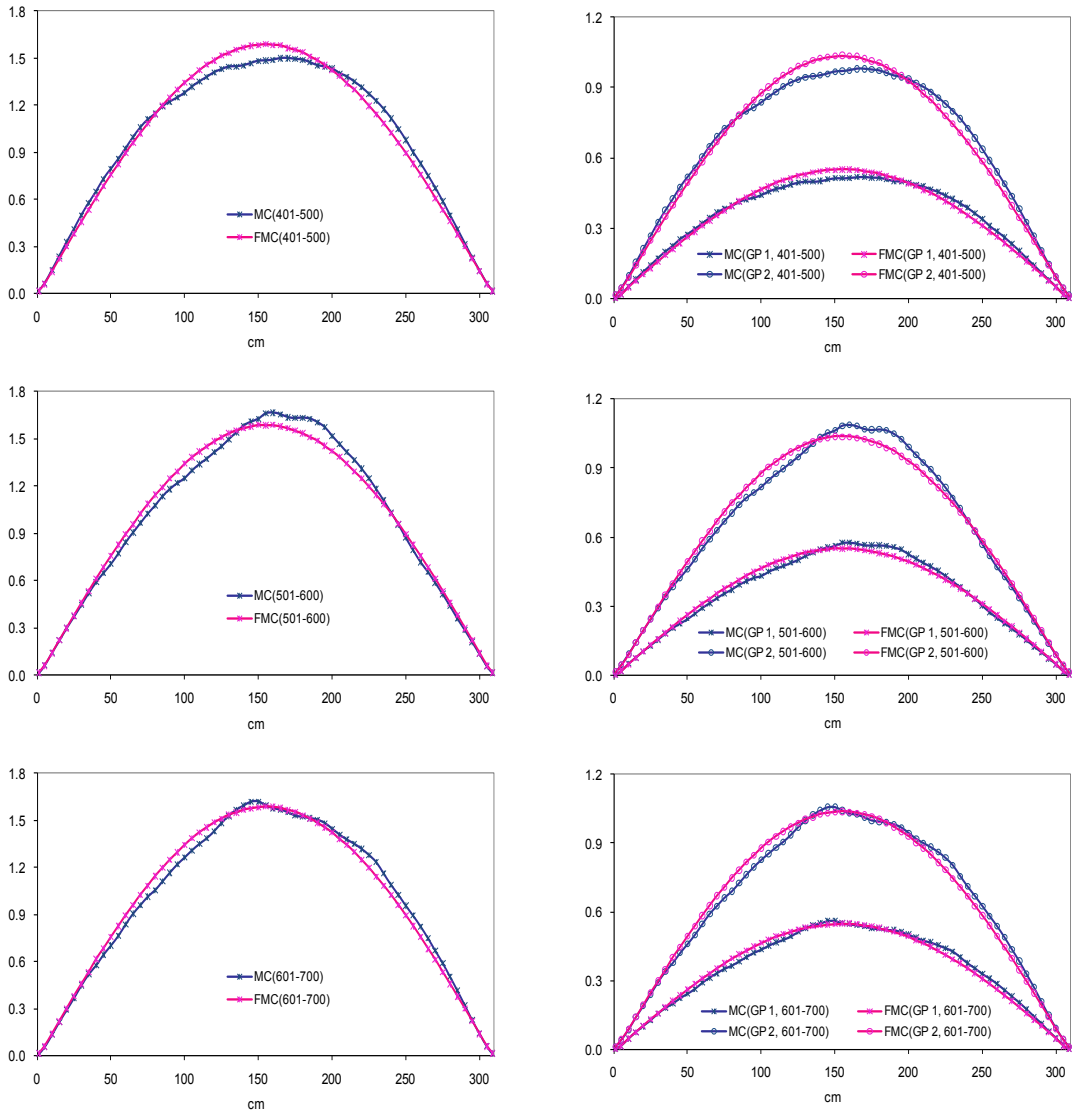

Figure 6.4 Continuous energy Problem 1 one-group and two-group eigenfunction estimates during cycles 401-700 without FMC feedback (5*cm* Grid).

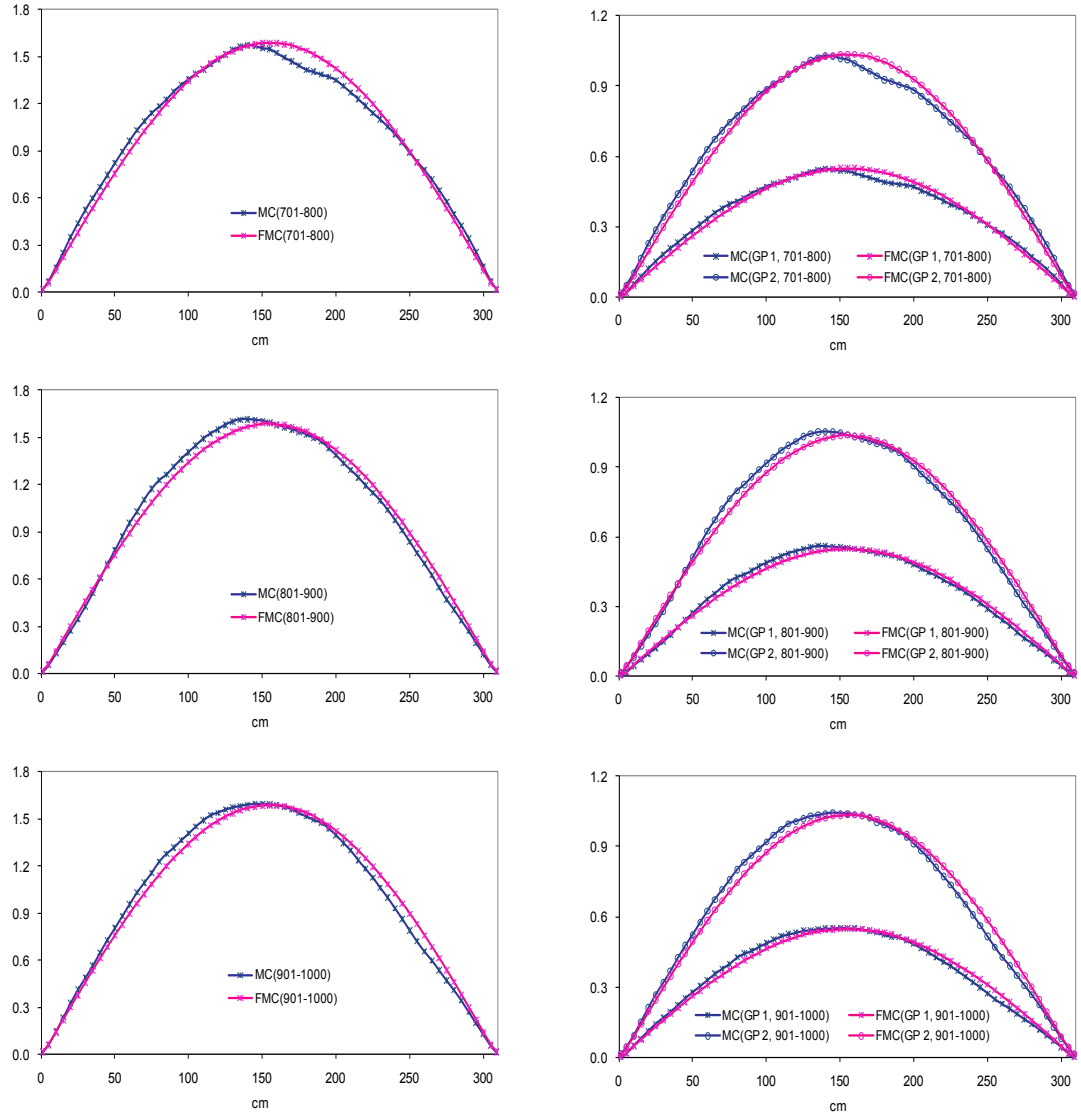

Figure 6.5 Continuous energy Problem 1 one-group and two-group eigenfunction estimates during cycles 701-1000 without FMC feedback (5*cm* Grid).

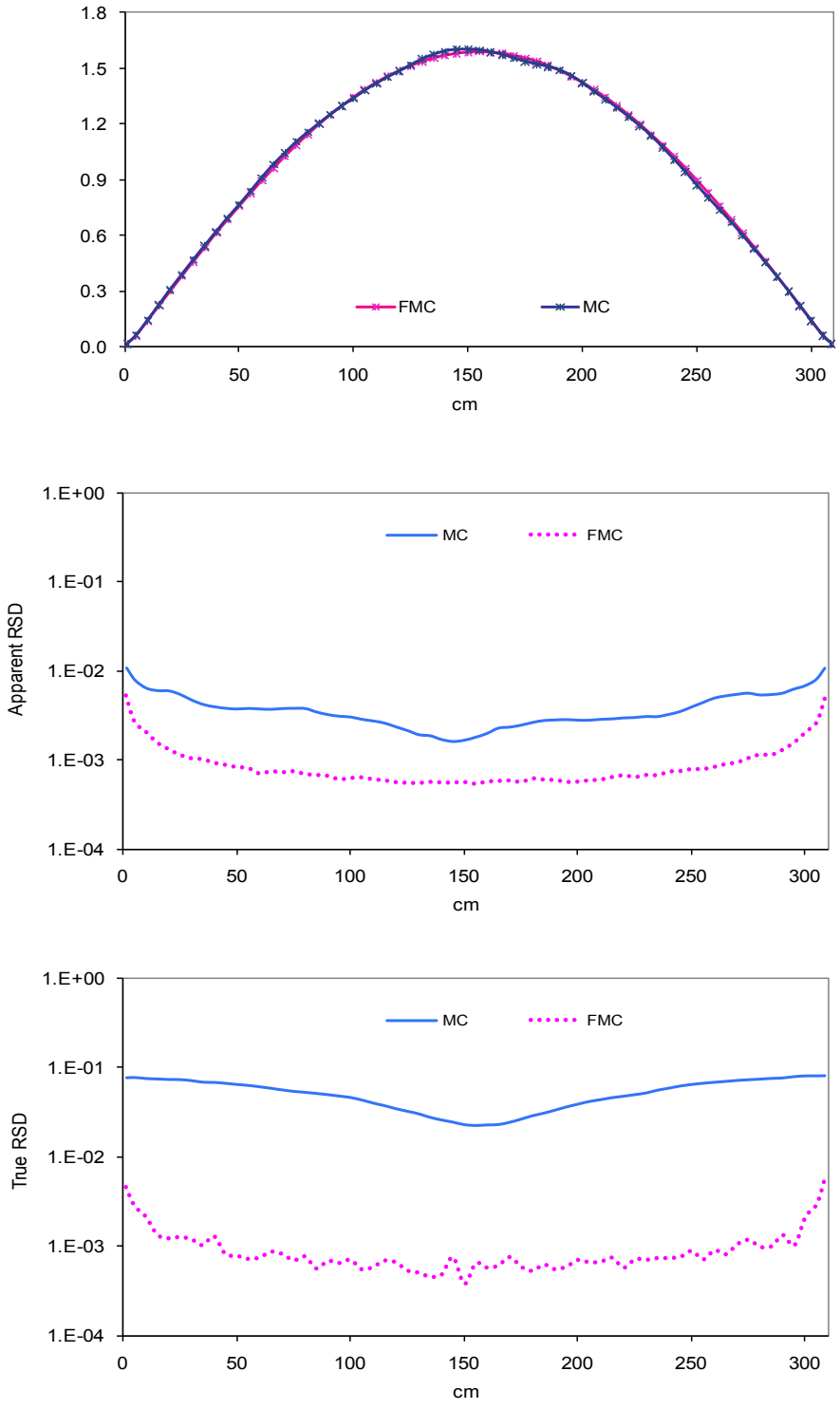

Figure 6.6 Continuous energy Problem 1 one-group averaged eigenfunctions and their RSDs over 501-1000 Cycles without feedback (5*cm* Grid).

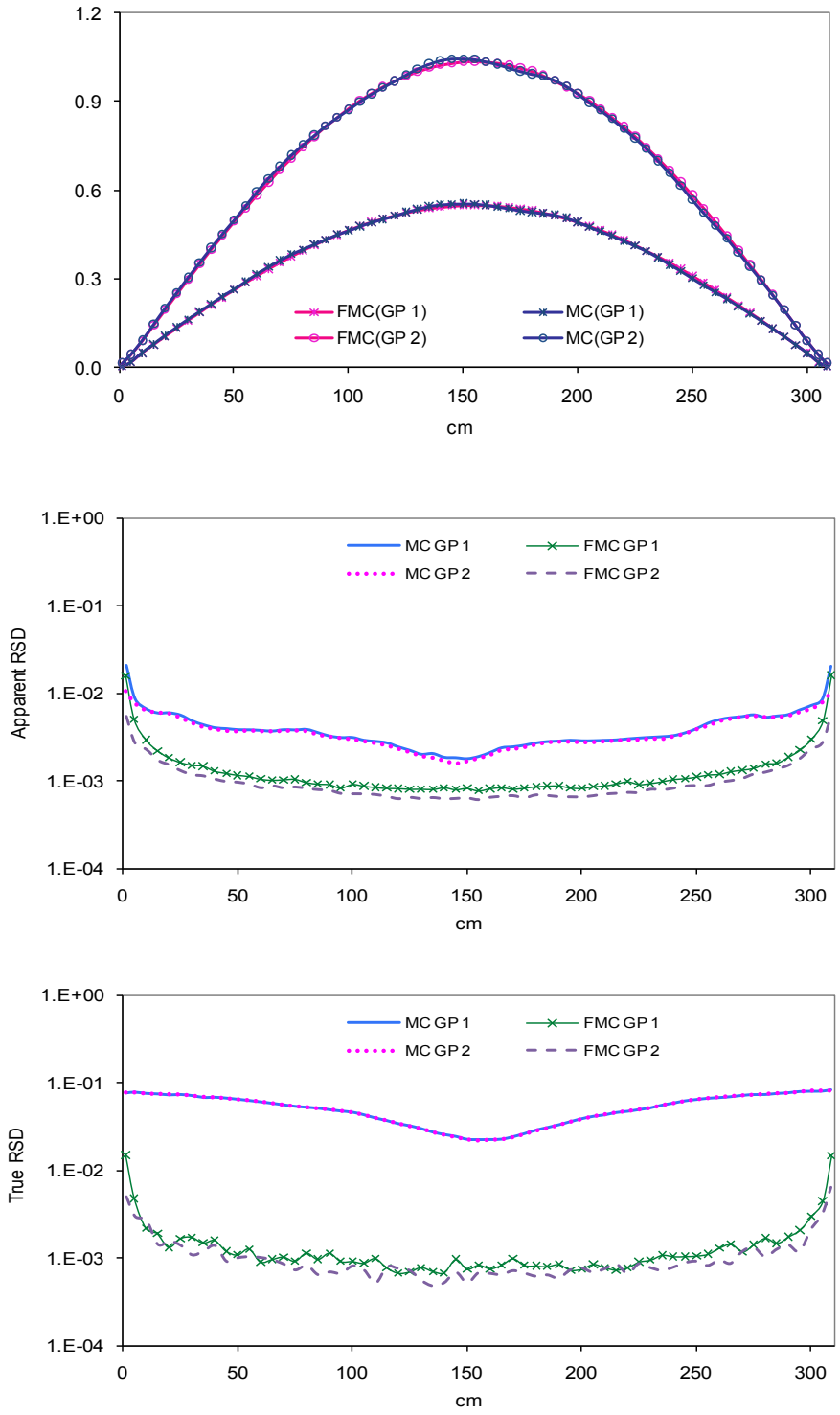

Figure 6.7 Continuous energy Problem 1 two-group averaged eigenfunctions and their RSDs over 501-1000 Cycles without feedback (5*cm* Grid).

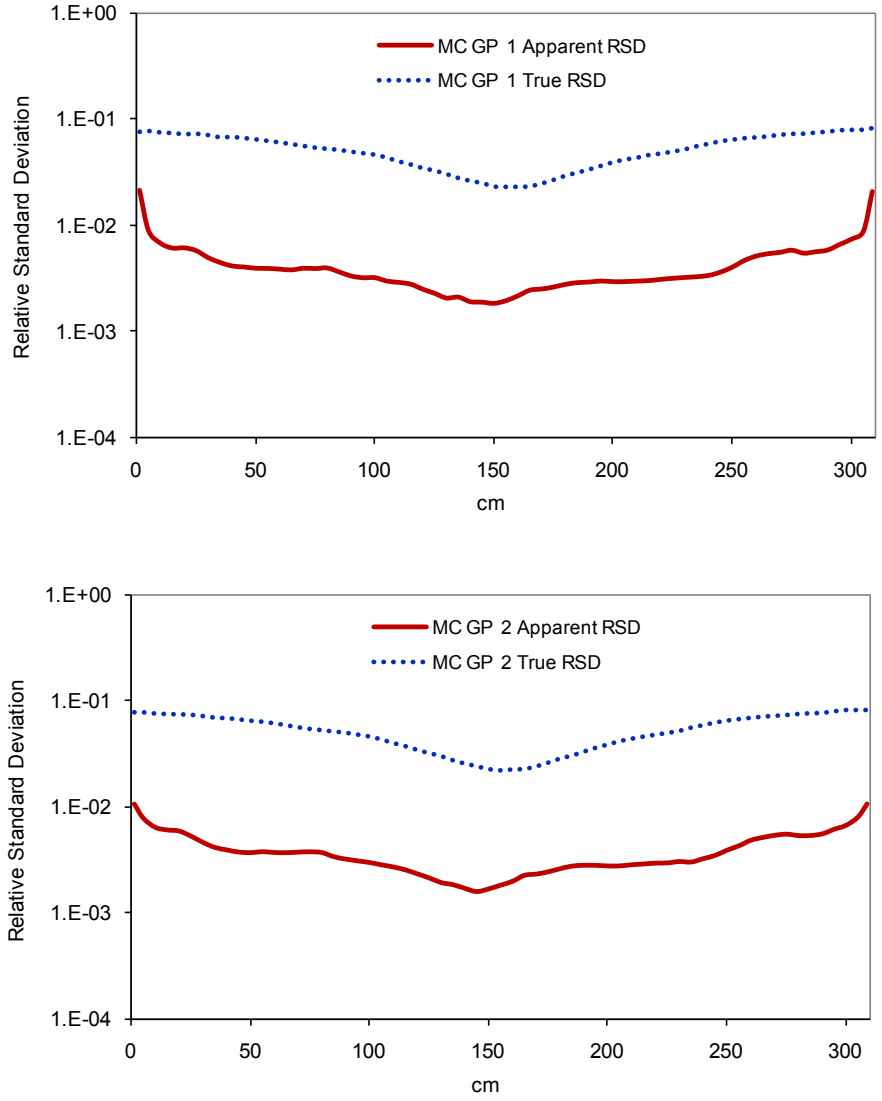

Figure 6.8 Comparison for continuous energy Problem 1 of apparent RSDs and true RSDs in two-group MC eigenfunction estimates (5*cm* Grid).

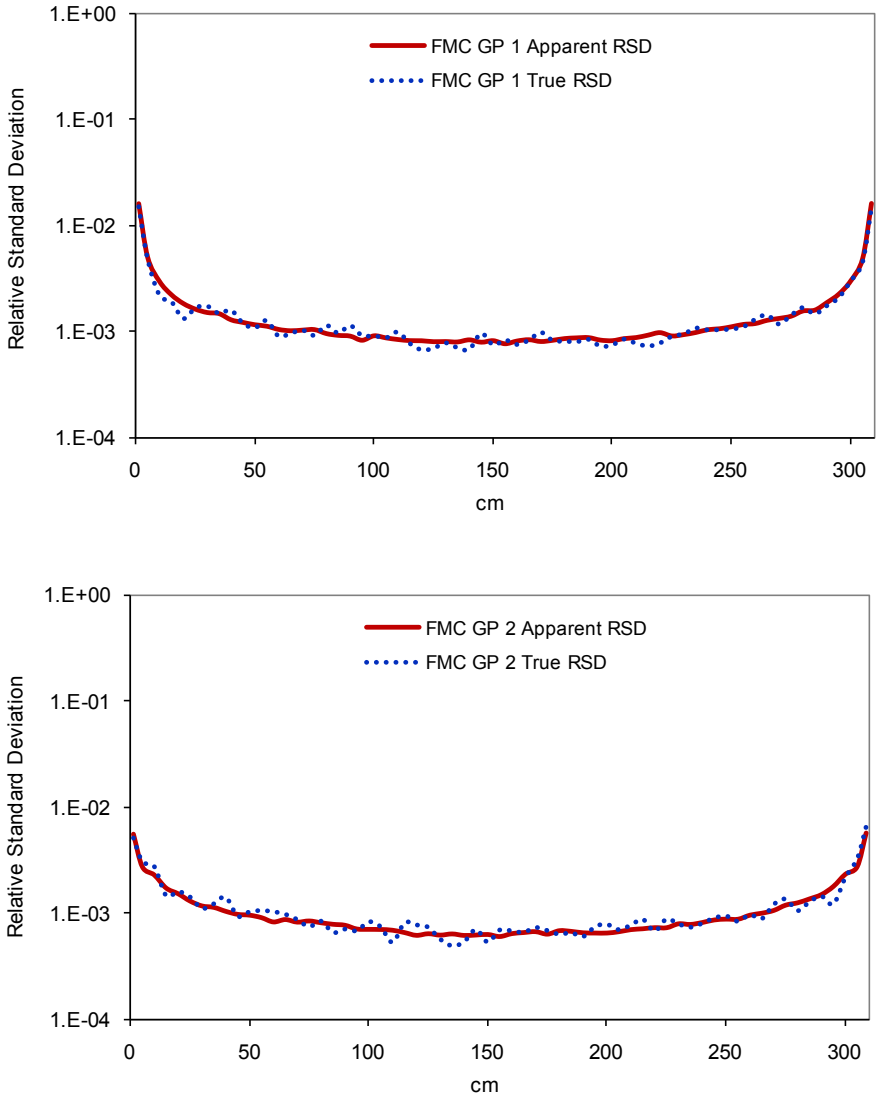

Figure 6.9 Comparison for continuous energy Problem 1 of apparent RSDs and true RSDs in two-group FMC eigenfunction estimates (5*cm* Grid).

Table 6.2 Estimates of k and its Relative Standard Deviation for Continuous Energy Problem 1 ($5cm$ Grid).

Cycles	Standard MC	FMC	
		One-Group eigenvalue	Two-Group eigenvalue
1 to 100	0.993626 (0.0005722)	0.995227 (0.0000004)	0.995227 (0.0000004)
101 to 200	0.994973 (0.0003738)	0.995227 (0.0000004)	0.995227 (0.0000004)
201 to 300	0.994574 (0.0003649)	0.995228 (0.0000004)	0.995228 (0.0000003)
301 to 400	0.995646 (0.0003614)	0.995228 (0.0000003)	0.995228 (0.0000003)
401 to 500	0.995841 (0.0004063)	0.995228 (0.0000003)	0.995228 (0.0000003)
501 to 600	0.995330 (0.0003679)	0.995228 (0.0000004)	0.995228 (0.0000004)
601 to 700	0.995400 (0.0004416)	0.995228 (0.0000004)	0.995228 (0.0000003)
701 to 800	0.995075 (0.0003765)	0.995228 (0.0000003)	0.995228 (0.0000003)
801 to 900	0.995485 (0.0003580)	0.995227 (0.0000003)	0.995227 (0.0000003)
901 to 1000	0.995647 (0.0003895)	0.995227 (0.0000003)	0.995227 (0.0000003)

6.1.3 FMC Coarse Mesh ($5cm$ Grid) with FMC Feedback

Figure 6.10 shows the one-group and two-group estimates of the eigenfunction with FMC feedback for the standard MC method and the FMC method. These figures are obtained by averaging the Monte Carlo estimates of the eigenfunction over 100-cycle spans, i.e. cycles 1-100, 101-200, and 201-300. Examining Figure 6.10 we see that the Monte Carlo estimates of the eigenfunction with FMC feedback converge within the first 100-cycle average.

Figure 6.11 shows the one-group estimates of the eigenfunction, averaged over the last 500 cycles (501-1000), and the estimated apparent relative standard deviations and true relative standard deviations in the Monte Carlo and FMC eigenfunctions over the cycles

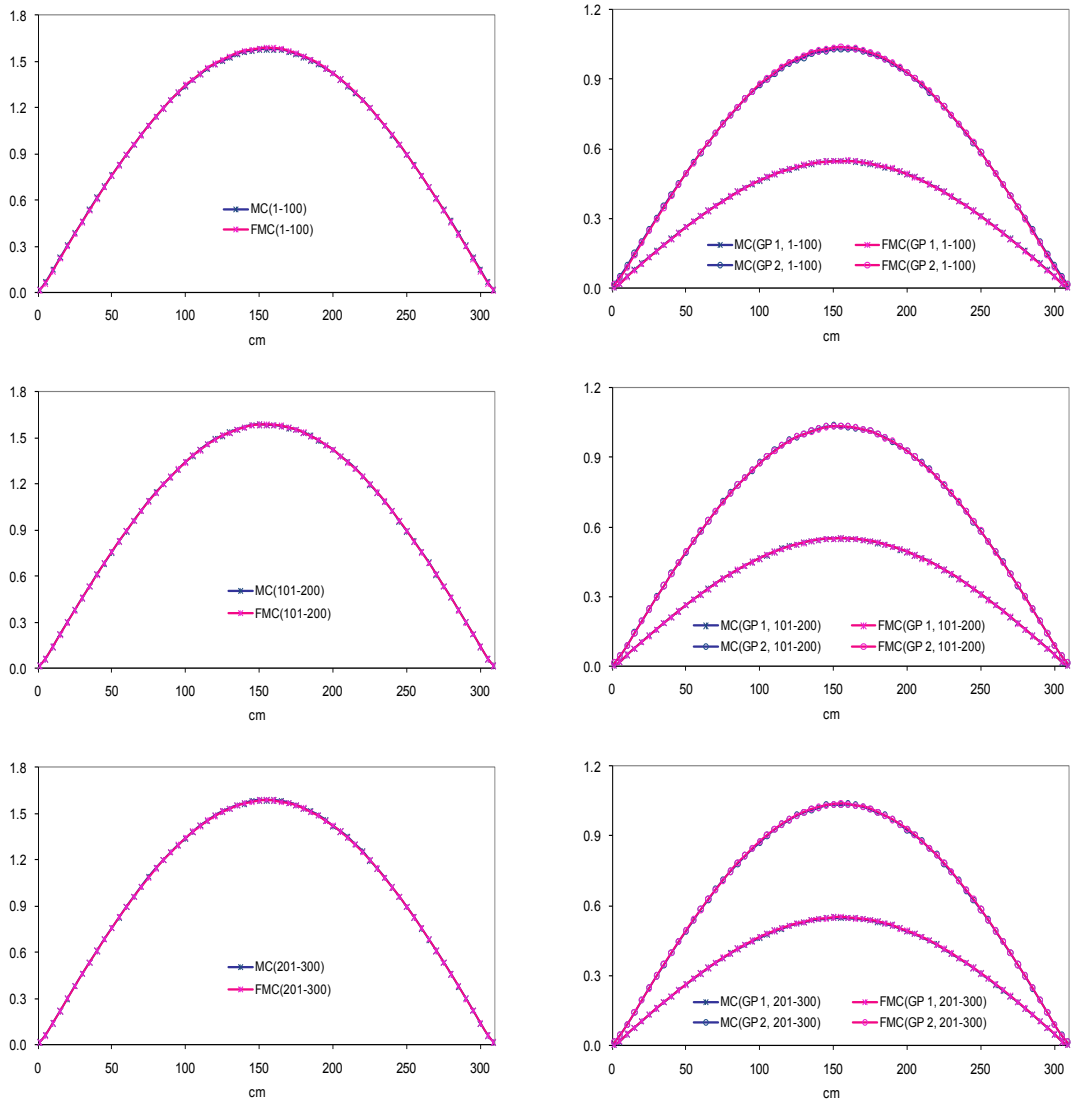

Figure 6.10 Continuous energy Problem 1 one-group and two-group eigenfunction estimates during cycles 1-300 with FMC feedback (5*cm* Grid).

with FMC feedback. Accordingly, Figure 6.12 shows the two-group estimates of the eigenfunction, averaged over the last 500 cycles, and the estimated apparent relative standard deviations and true relative standard deviations with FMC feedback. The apparent relative standard deviations are obtained from a single 1000-cycle (500 inactive cycles, and 500 active cycles) run with feedback, while the true relative standard deviations are obtained from 25 independent 1000-cycle runs with feedback.

Figures 6.11-6.12 show that the true relative standard deviation in MC with FMC feed-

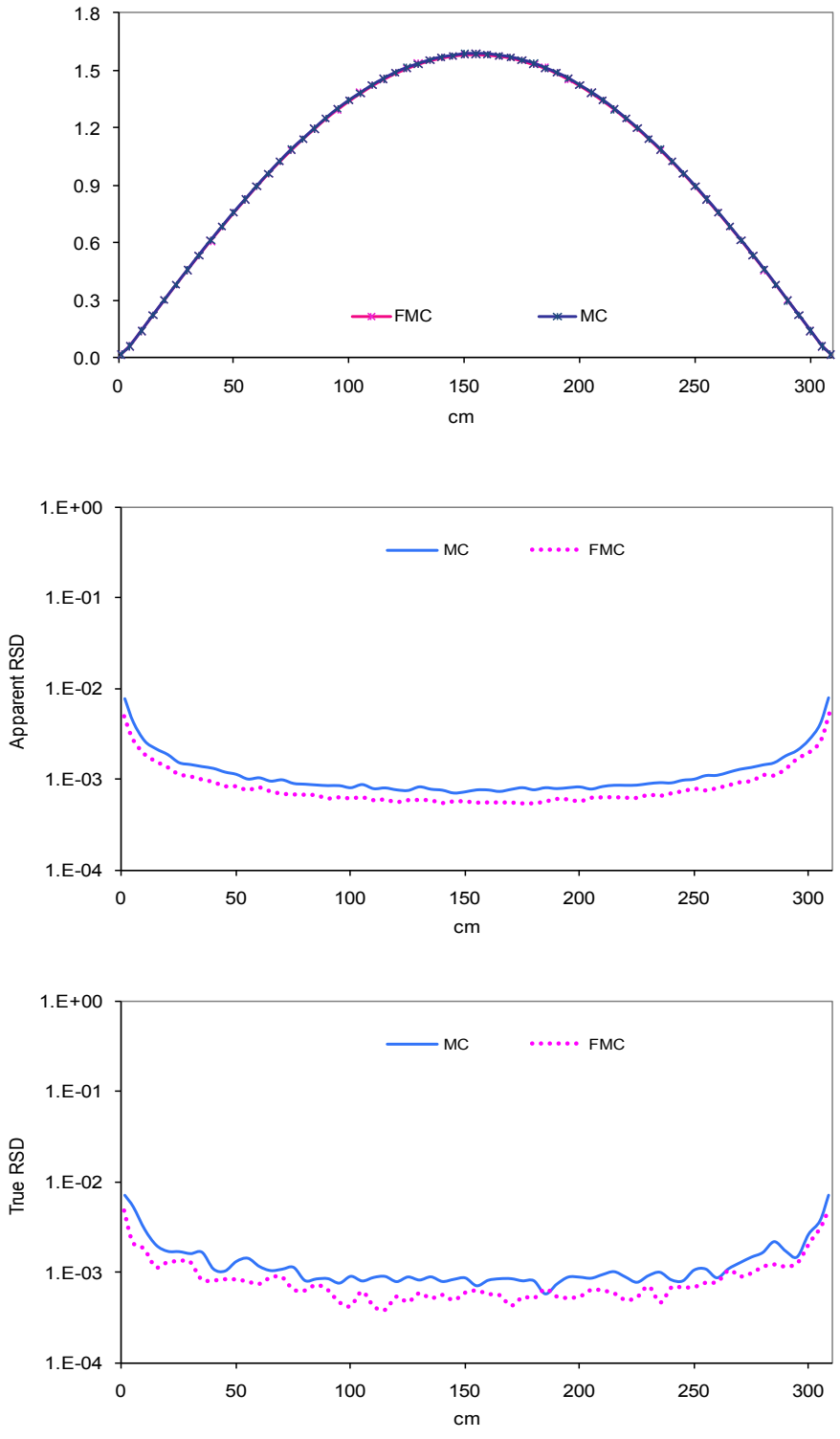

Figure 6.11 Continuous energy Problem 1 one-group averaged eigenfunctions and their RSDs over 501-1000 Cycles with FMC feedback (5*cm* Grid).

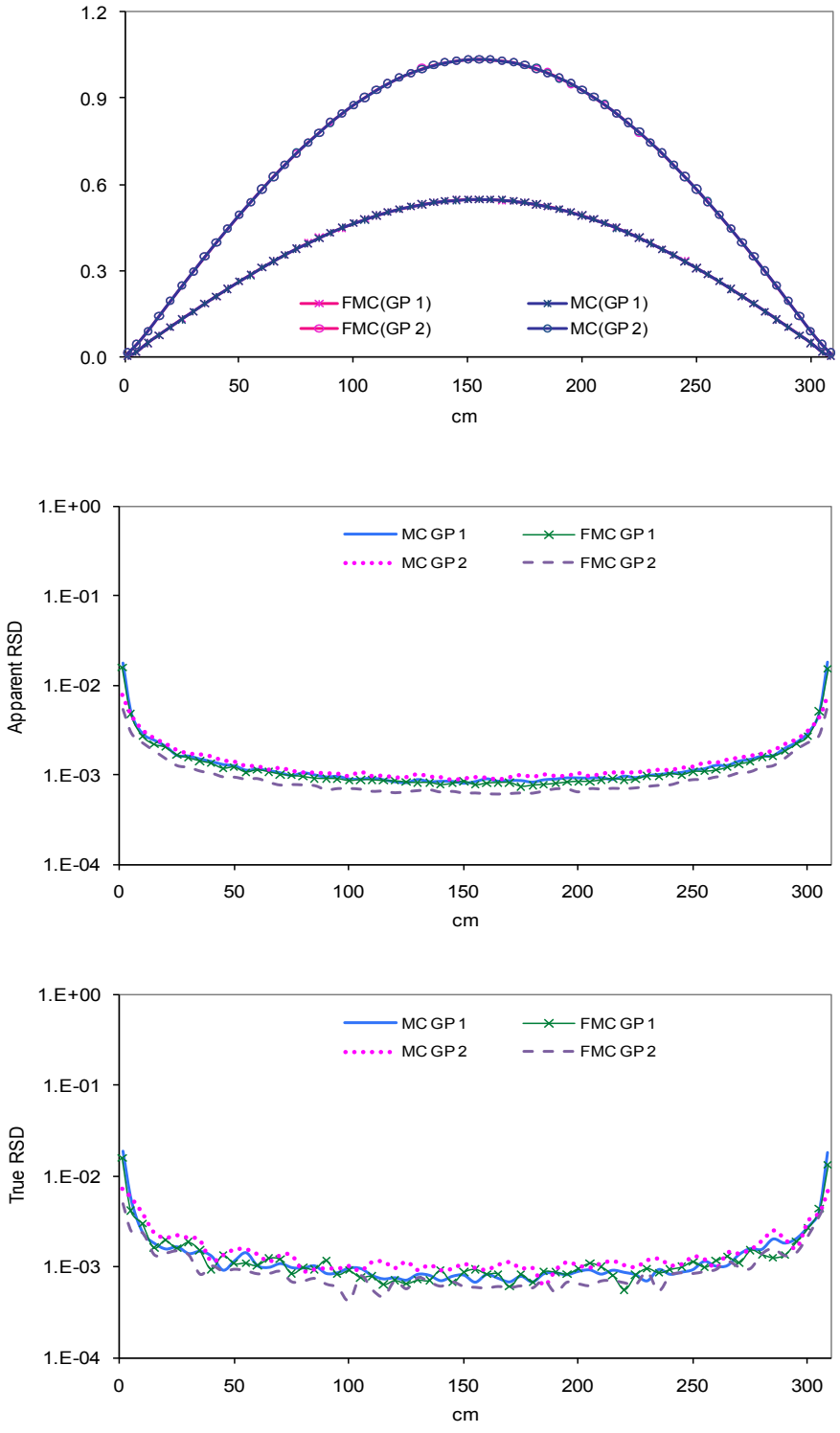

Figure 6.12 Continuous energy Problem 1 two-group averaged eigenfunctions and their RSDs over 501-1000 Cycles with FMC feedback (5*cm* Grid).

back is greatly reduced compared to the true relative standard deviation without FMC feedback. Meanwhile, the true relative standard deviation in MC with FMC feedback is still marginally bigger then the true relative standard deviation in FMC. The true relative standard deviations in FMC do not change with FMC feedback or without FMC feedback. A detailed comparison between the apparent relative standard deviation and the true relative standard deviation in the MC, FMC eigenfunction estimates with FMC feedback for the two-group energy case are given in Figure 6.13 and Figure 6.14. Figures 6.13-6.14 show that the true relative standard deviations in the MC and FMC eigenfunction estimates are approximately the same as the apparent relative standard deviations.

The Shannon entropy behavior of the fission source for Problem 1 without FMC feedback is shown in Figure 6.15, while the Shannon entropy behavior of the fission source for Problem 1 with FMC feedback is shown in Figure 6.16. As expected, Figure 6.16 shows that the Monte Carlo estimates of the eigenfunction with FMC feedback converge almost immediately.

With FMC feedback, the estimates of the Problem 1 eigenvalue with their estimated relative standard deviations over ten 100-cycle spans are given in Table 6.3 for the standard Monte Carlo and FMC one-group and two-group methods. We note that with FMC feedback (Table 6.3) or without FMC feedback (Table 6.2), the eigenvalue estimates agree to the 6^{th} digit for the FMC average, and the eigenvalue estimates agree within statistical errors for the standard Monte Carlo.

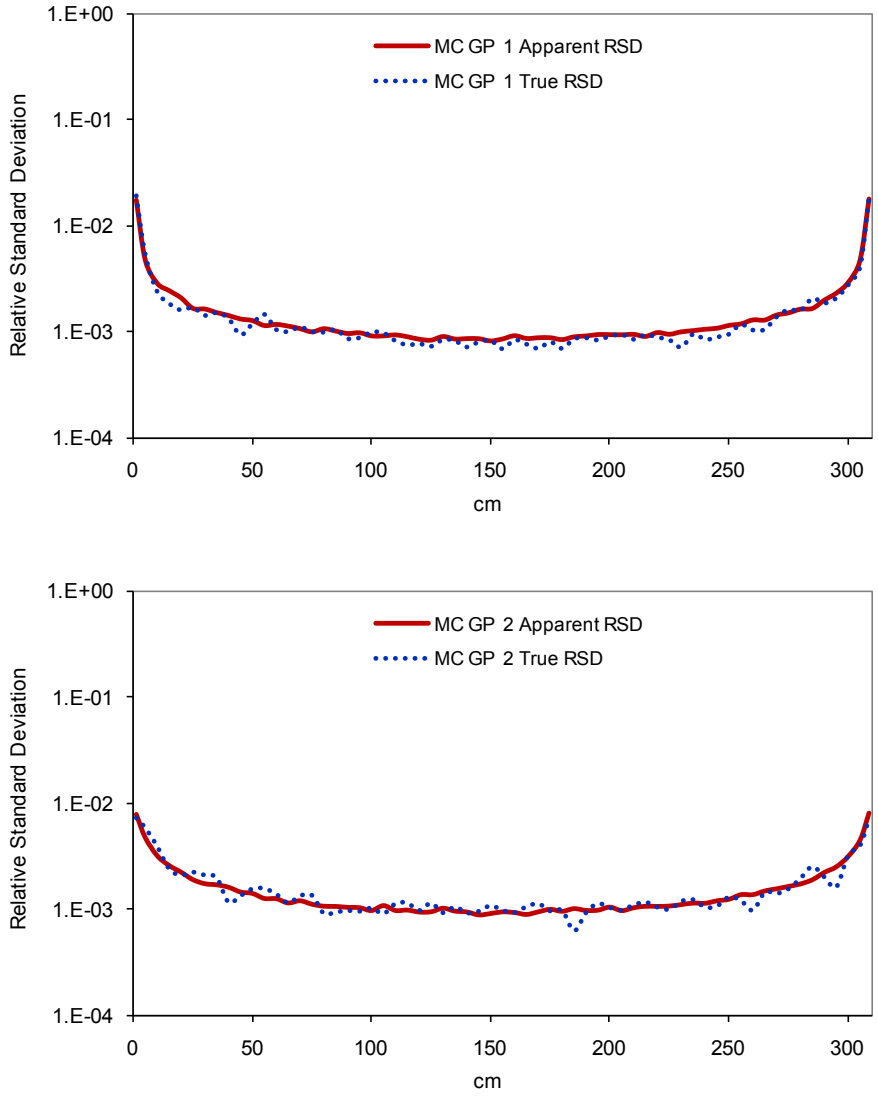

Figure 6.13 Comparison for continuous energy Problem 1 of apparent RSDs and true RSDs in two-group MC eigenfunction estimates with FMC feedback (5*cm* Grid).

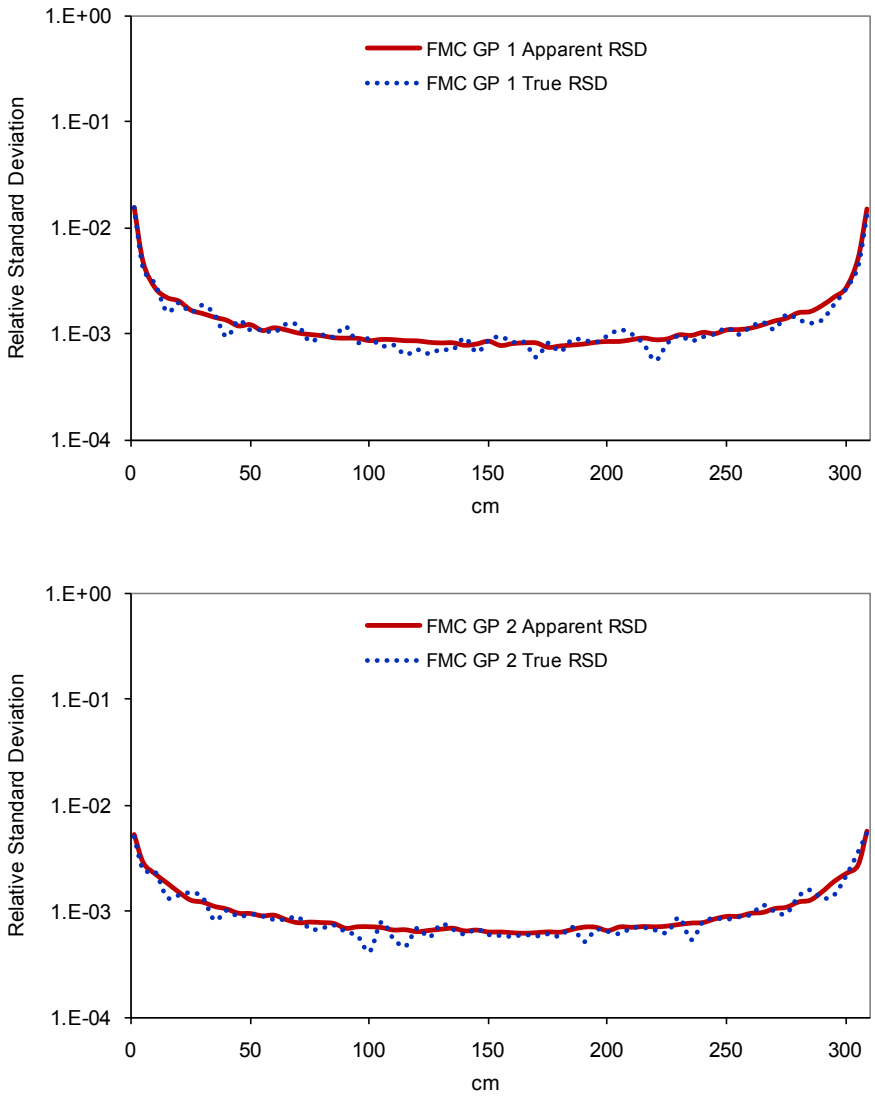

Figure 6.14 Comparison for continuous energy Problem 1 of apparent RSDs and true RSDs in two-group FMC eigenfunction estimates with FMC feedback (5*cm* Grid).

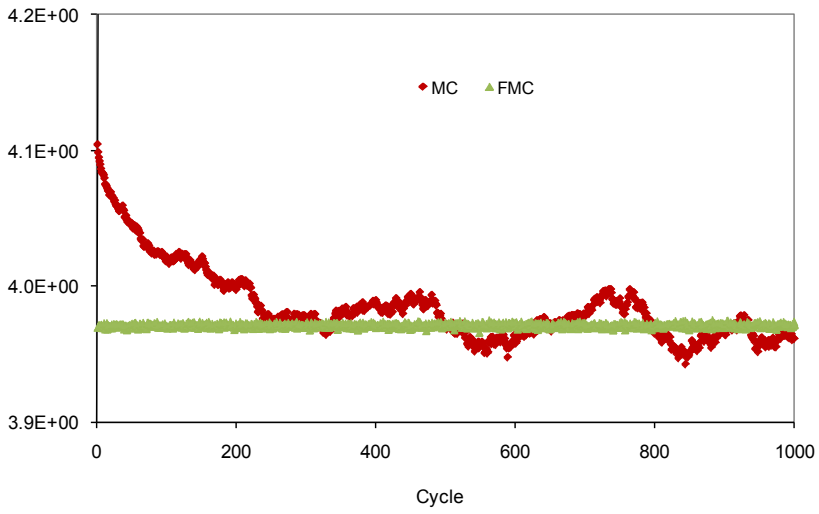

Figure 6.15 Shannon entropy behavior of the fission source for continuous energy Problem 1 without FMC feedback (5*cm* Grid).

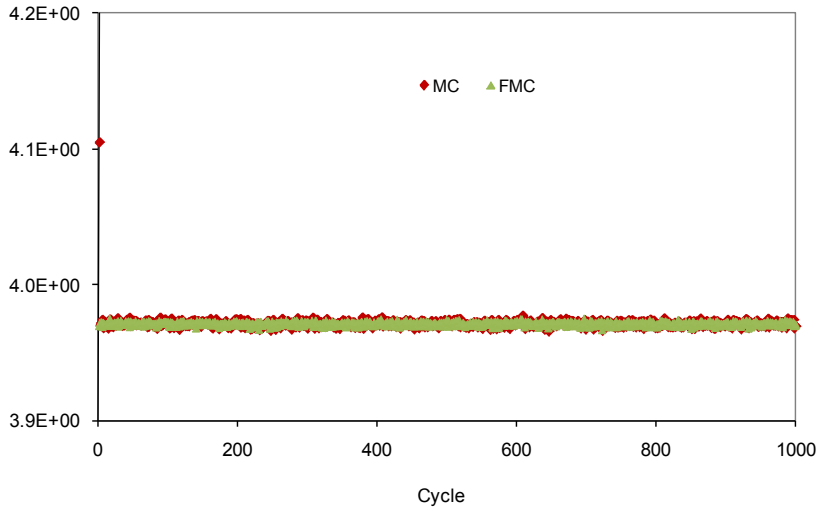

Figure 6.16 Shannon entropy behavior of the fission source for continuous energy Problem 1 with FMC feedback (5*cm* Grid).

Table 6.3 Estimates of k and its relative standard deviation for continuous energy Problem 1 with FMC feedback ($5cm$ Grid).

Cycles	Standard MC	FMC	
		One-Group eigenvalue	Two-Group eigenvalue
1 to 100	0.995210 (0.0005763)	0.995227 (0.0000004)	0.995227 (0.0000003)
101 to 200	0.995459 (0.0003445)	0.995227 (0.0000003)	0.995227 (0.0000003)
201 to 300	0.994690 (0.0003614)	0.995227 (0.0000003)	0.995227 (0.0000003)
301 to 400	0.995495 (0.0003390)	0.995228 (0.0000003)	0.995228 (0.0000003)
401 to 500	0.995938 (0.0003995)	0.995228 (0.0000003)	0.995228 (0.0000003)
501 to 600	0.995195 (0.0003910)	0.995228 (0.0000003)	0.995227 (0.0000003)
601 to 700	0.995547 (0.0004257)	0.995227 (0.0000003)	0.995228 (0.0000003)
701 to 800	0.995483 (0.0003572)	0.995227 (0.0000004)	0.995227 (0.0000003)
801 to 900	0.995079 (0.0003774)	0.995227 (0.0000003)	0.995228 (0.0000003)
901 to 1000	0.995628 (0.0003739)	0.995228 (0.0000003)	0.995228 (0.0000003)

6.1.4 FMC Coarse Mesh ($10cm$ Grid) with and without FMC Feedback

The one-group FMC method is insensitive to the choice of mesh grid. The choice of mesh grid has some impact on the two-group FMC method. To illustrate this point, we reran problem 1 with $h = 10.0$ cm grid, using the same 100,000 histories/cycle.

Figure 6.17 shows the one-group estimates of the eigenfunction, averaged over the last 500 cycles (501-1000), and the estimated apparent relative standard deviations in the Monte Carlo and FMC eigenfunctions for $h = 10.0$ cm grid case. Comparing Figure 6.17 (10 cm grid) and Figure 6.6 (5 cm grid), we see no obvious change in the apparent relative standard deviations in the Monte Carlo and FMC eigenfunctions.

Figure 6.18 shows the two-group estimates of the eigenfunction, averaged over the last 500 cycles, and the estimated apparent relative standard deviations for $h = 10.0$ cm grid case. Comparing Figure 6.18 (10 cm grid) and Figure 6.7 (5 cm grid), we see there are slight increases in the relative standard deviations in the FMC eigenfunction at both edges of the system. This is due to the fact that the low-order equations are two-group equations. The two-group nonlinear functionals require more MC particles to obtain comparable accuracy to the one-group nonlinear functionals.

Figures 6.19-6.20 show the results for one-group and two-group fluxes and the estimated apparent relative standard deviations with FMC feedback. Comparing Figure 6.19 (10 cm grid) to Figure 6.11 (5 cm grid) for the one-group case, we see only slight changes in the apparent relative standard deviations. Comparing Figure 6.20 (10 cm grid) to Figure 6.12 (5 cm grid) for the two-group case, we see small increases in the apparent relative standard deviations for FMC at the edge of the system.

Table 6.4 shows the estimated k and its relative standard deviations for continuous energy Problem 1 with coarse mesh $10cm$ grid without FMC feedback. Table 6.5 shows the estimated k and its relative standard deviations for continuous energy Problem 1 with coarse mesh $10cm$ grid with FMC feedback. Comparing Table 6.4 (10 cm grid) with Table 6.2 (5 cm grid), and comparing Table 6.5 (10 cm grid) with Table 6.3 (5 cm grid), we see basically no change in k and its relative standard deviation for the one-group case for both with FMC feedback and without FMC feedback. Therefore, in general when applying the FMC method to a system, we may be able to use a relatively coarse grid but still maintain the accuracy.

Figures 6.21-6.23 show the results for one-group and two-group fluxes, averaged over 100 cycle intervals without FMC feedback. Figure 6.24 shows the results for one-group and two-group fluxes, averaged over the first three 100 cycle intervals with feedback, i.e. cycles 1-100, 101-200, and 201-300. As in the coarse mesh $5cm$ grid case, for both the one-group and two-group cases without FMC feedback, the FMC results are seen to converge almost immediately and to remain stable in all 100-cycle averages of the run. The standard Monte

Carlo results do not achieve equilibrium at any point during the 1000 cycle test run. However, with FMC feedback, the Monte Carlo estimates of the eigenfunction converge within the first 100-cycle average.

The Shannon entropy behavior of the fission source for Problem 1 for the coarse mesh $10cm$ grid case without FMC feedback is shown in Figure 6.25, while the Shannon entropy behavior of the fission source for Problem 1 with FMC feedback is shown in Figure 6.26. The Shannon entropy of Problem 1 for the coarse mesh $10cm$ grid case has the same behavior as for the coarse mesh $5cm$ grid case. The only difference is the magnitude of the Shannon entropy. This is caused by the difference in the total number of coarse mesh grid points for the $10cm$ case and $5cm$ case. Again, as expected, Figure 6.26 shows that the Monte Carlo estimates of the eigenfunction with FMC feedback converge almost immediately.

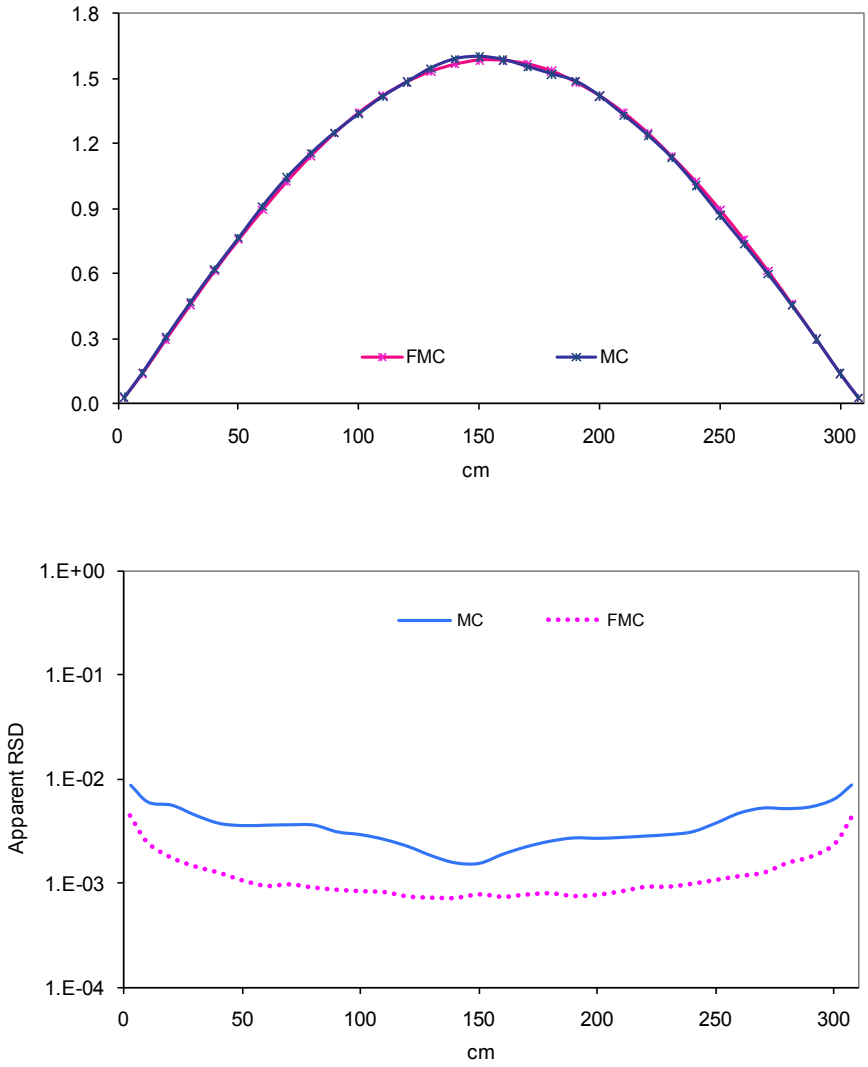

Figure 6.17 Continuous energy Problem 1 one-group averaged eigenfunctions and their RSDs over 501-1000 Cycles without feedback (10*cm* Grid).

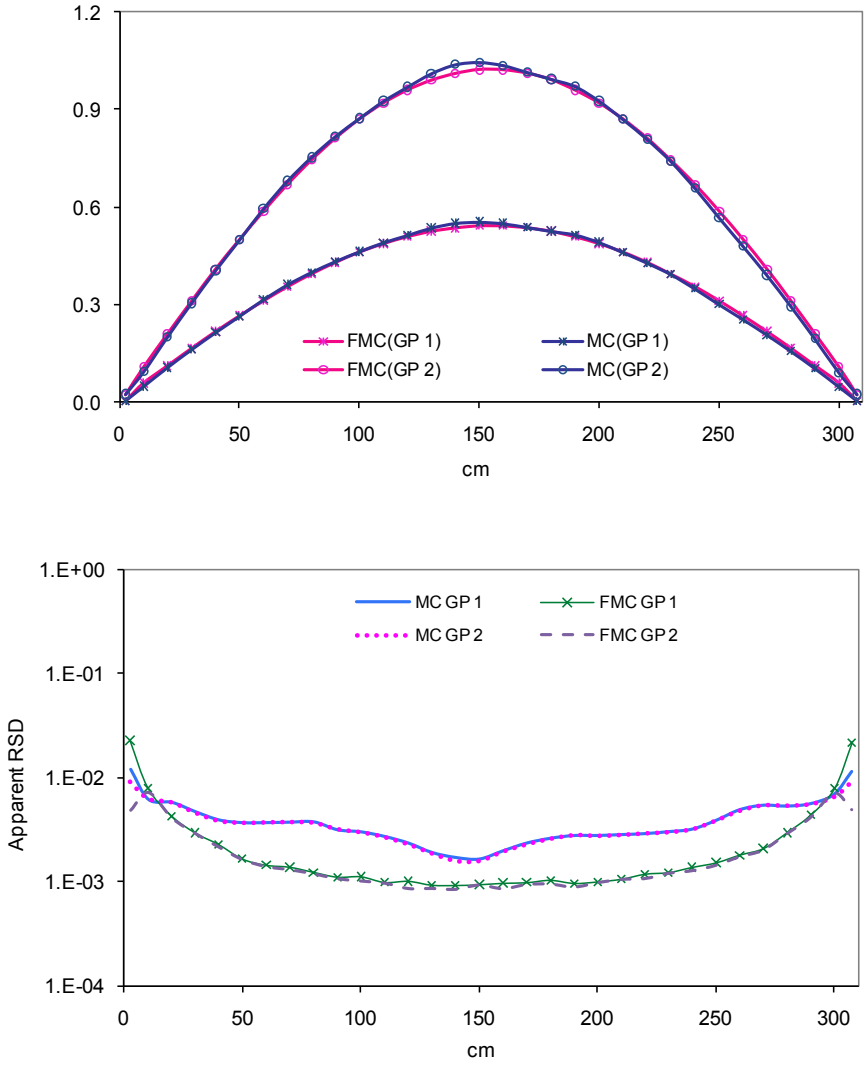

Figure 6.18 Continuous energy Problem 1 two-group averaged eigenfunctions and their RSDs over 501-1000 Cycles without feedback (10*cm* Grid).

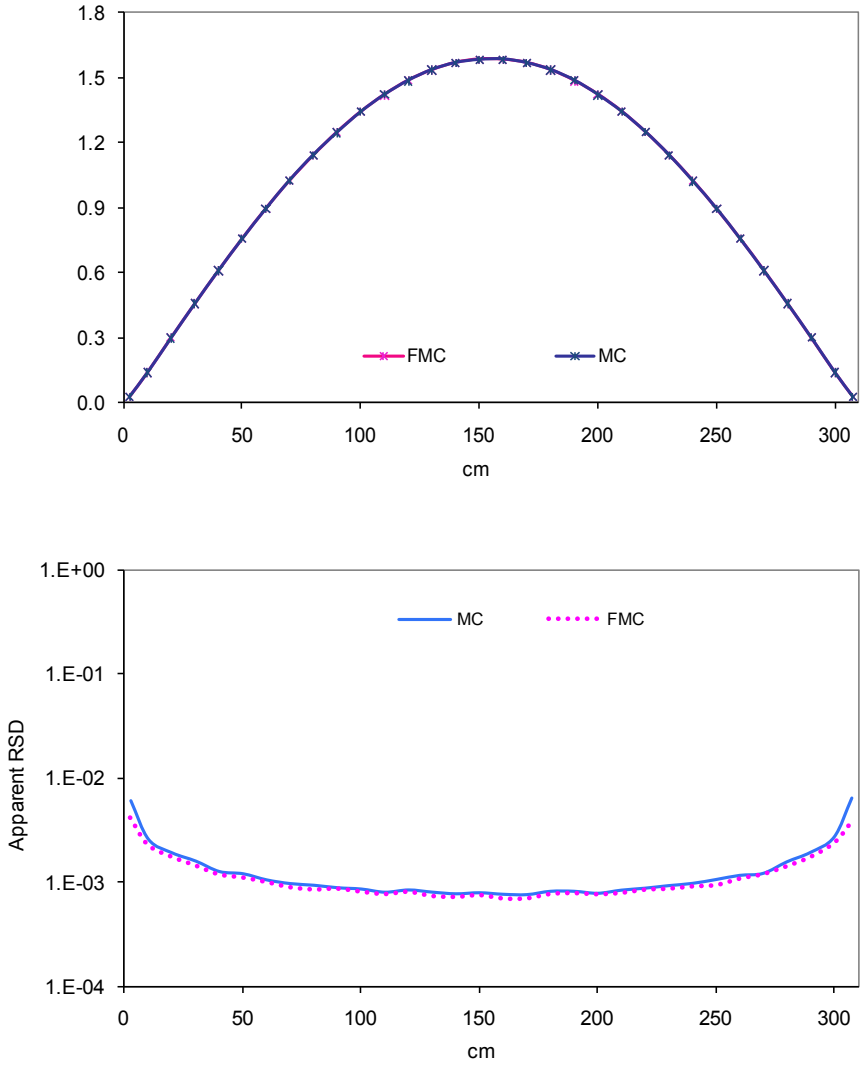

Figure 6.19 Continuous energy Problem 1 one-group averaged eigenfunctions and their RSDs over 501-1000 Cycles with FMC feedback (10*cm* Grid).

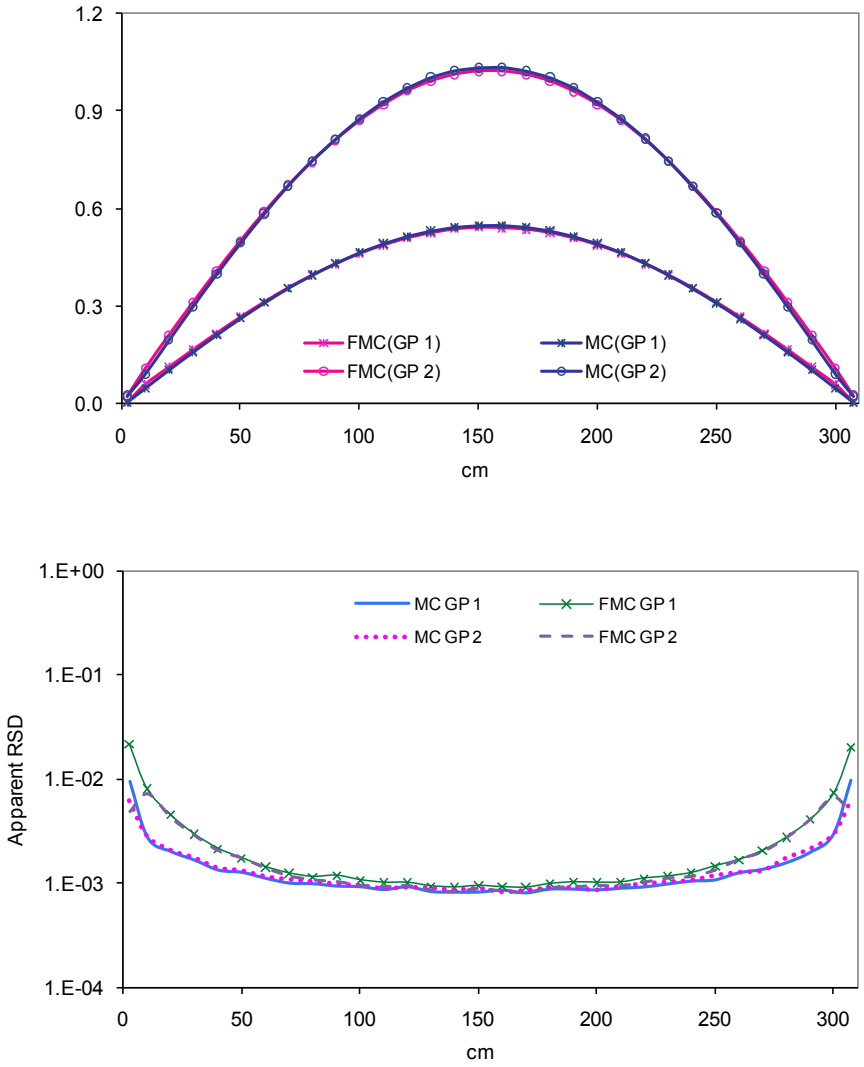

Figure 6.20 Continuous energy Problem 1 two-group averaged eigenfunctions and their RSDs over 501-1000 Cycles with FMC feedback (10*cm* Grid).

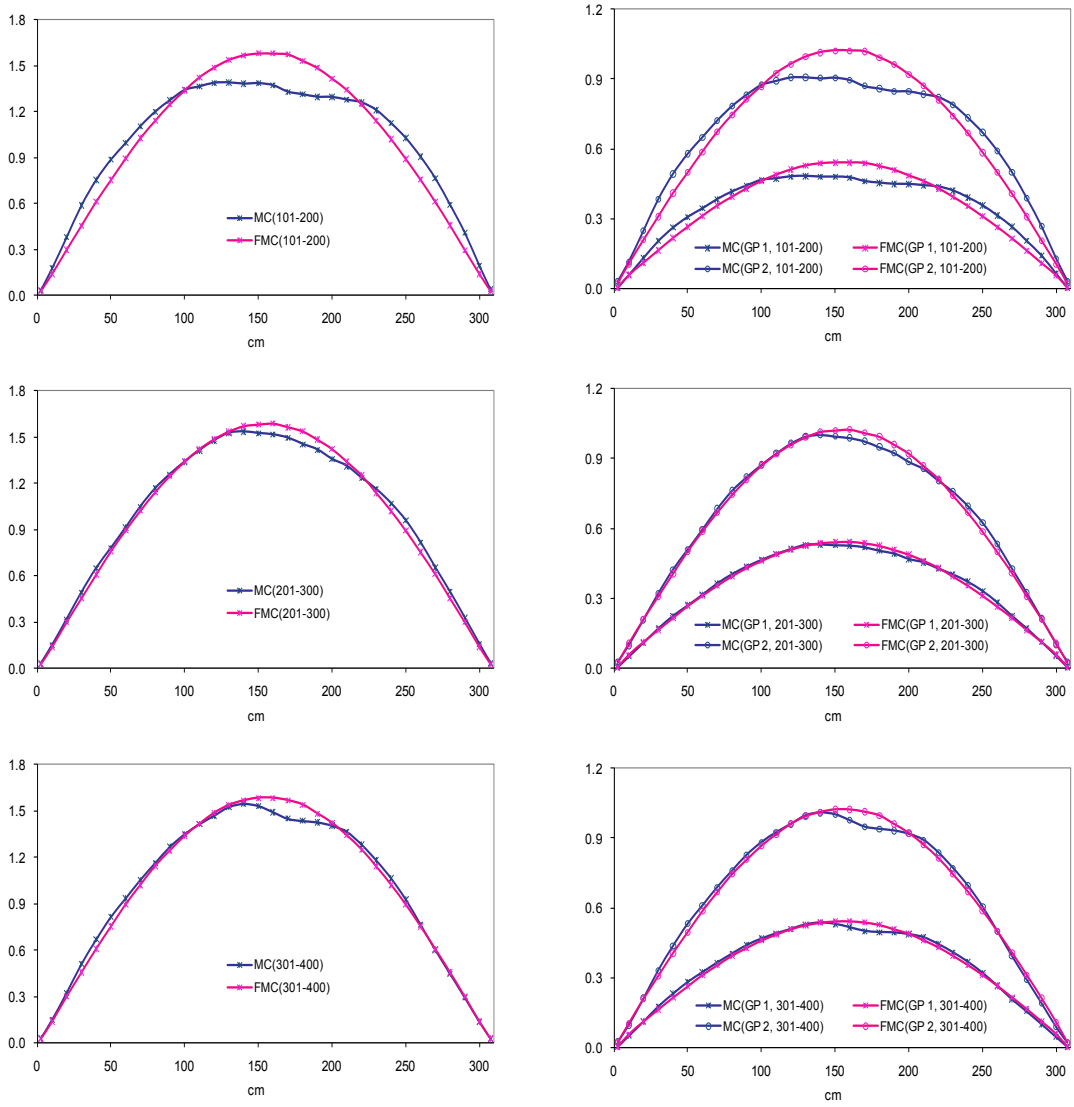

Figure 6.21 Continuous energy Problem 1 one-group and two-group eigenfunction estimates during cycles 101-400 without FMC feedback (10*cm* Grid).

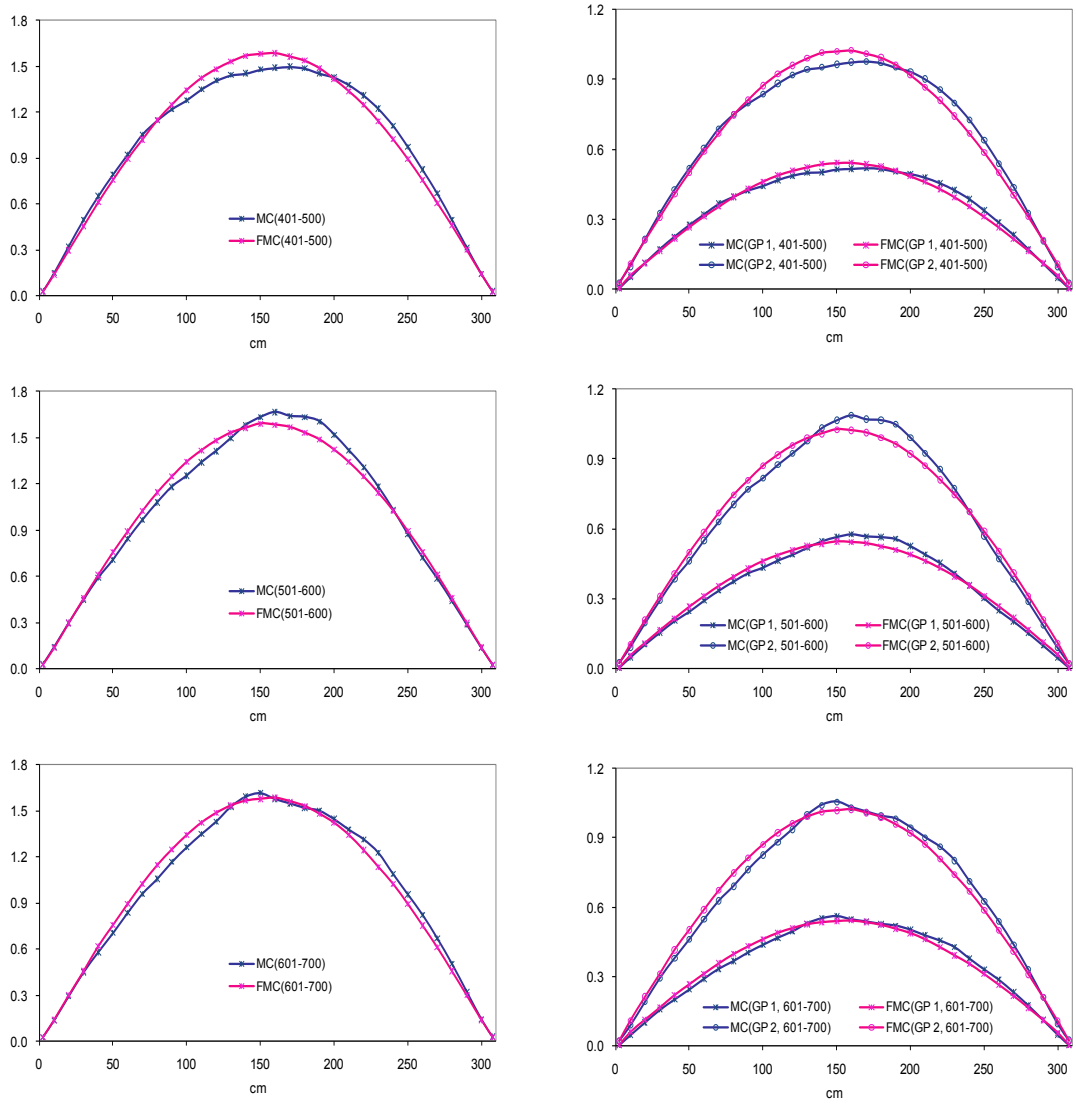

Figure 6.22 Continuous energy Problem 1 one-group and two-group eigenfunction estimates during cycles 401-700 without FMC feedback (10*cm* Grid).

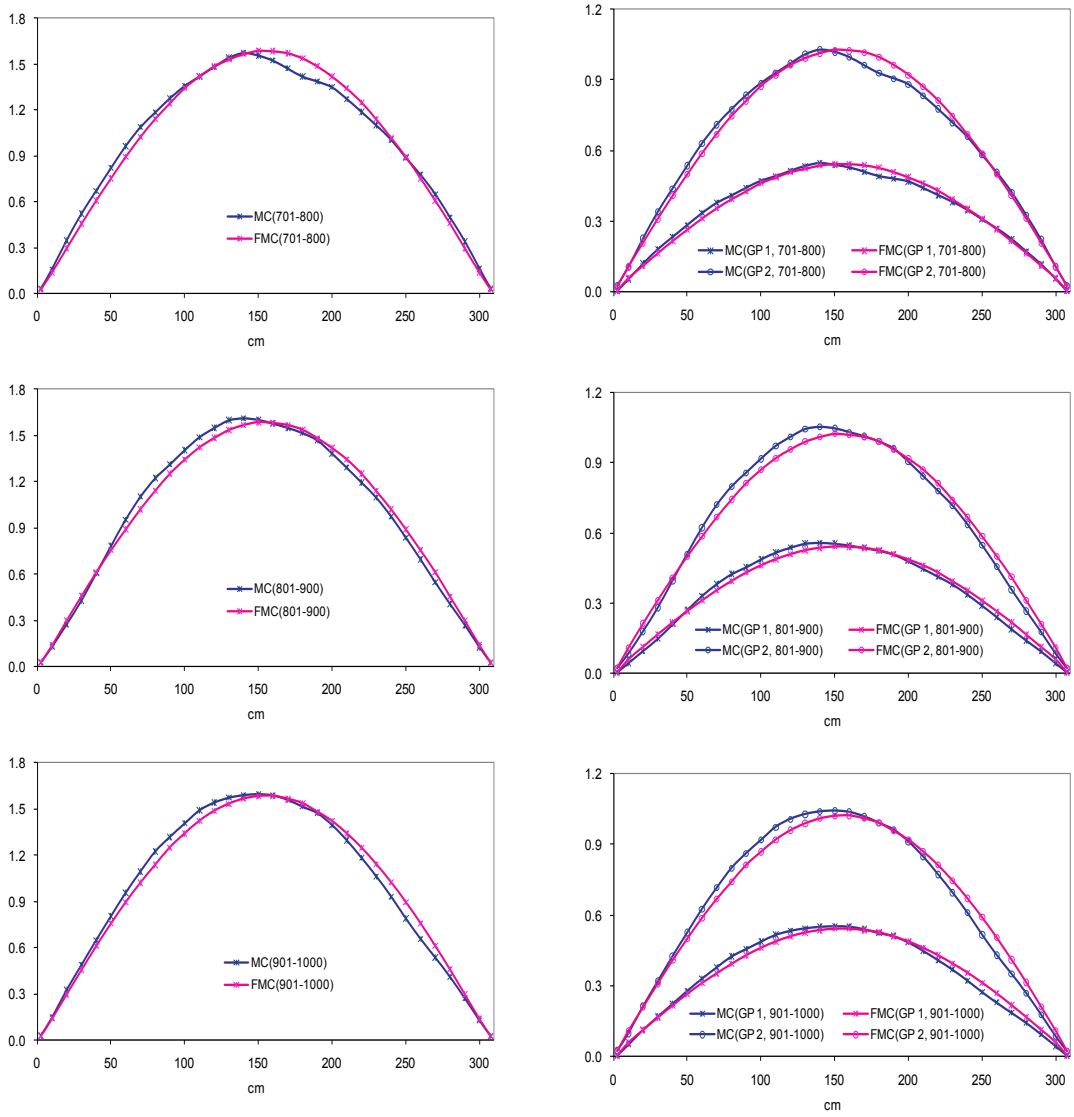

Figure 6.23 Continuous energy Problem 1 one-group and two-group eigenfunction estimates during cycles 701-1000 without FMC feedback (10*cm* Grid).

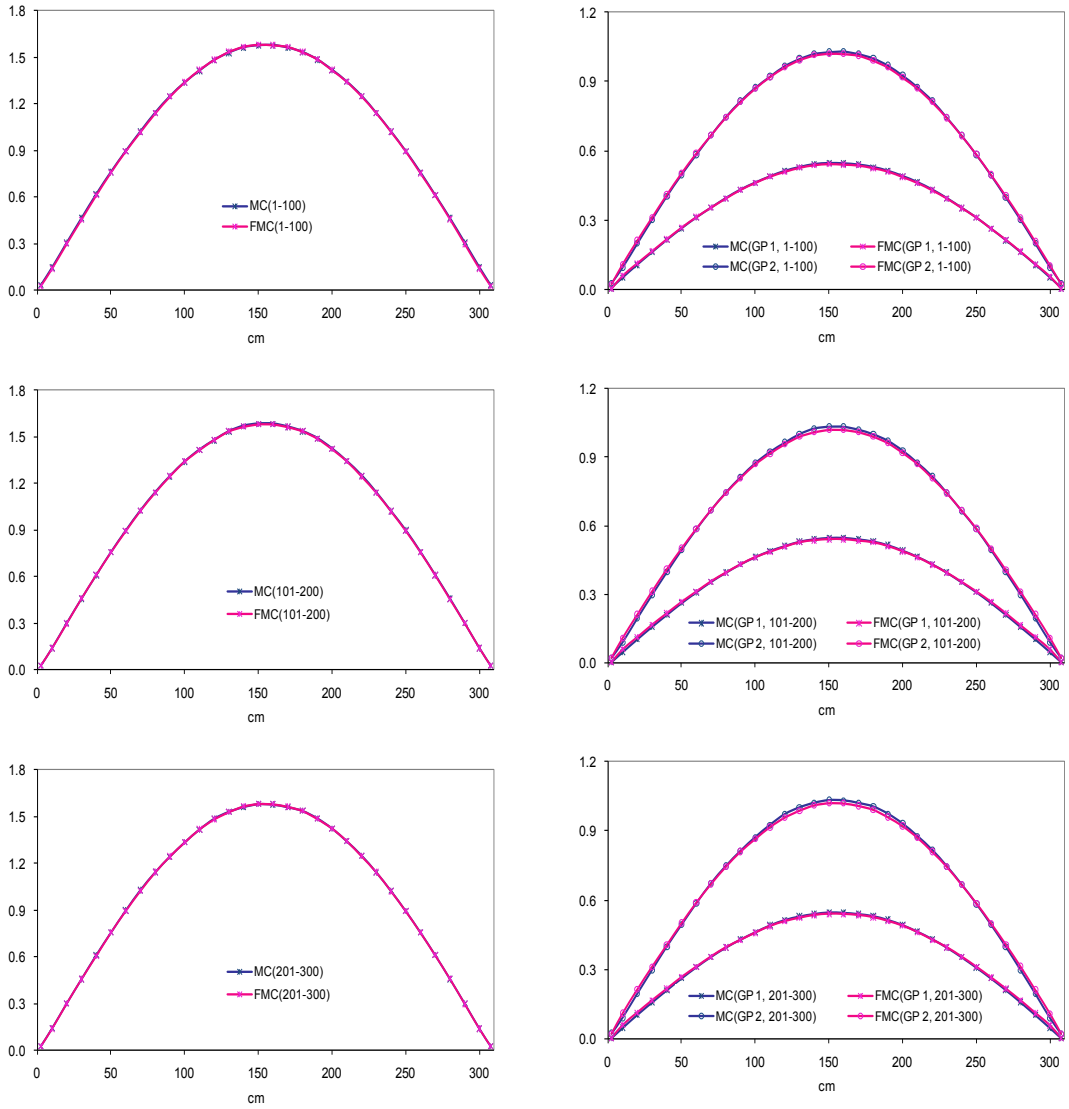

Figure 6.24 Continuous energy Problem 1 one-group and two-group eigenfunction estimates during cycles 1-300 with FMC feedback (10*cm* Grid).

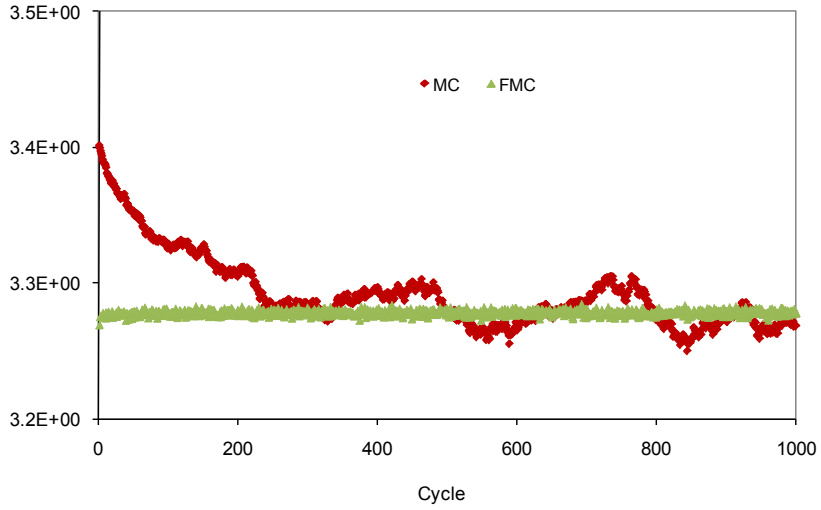

Figure 6.25 Shannon entropy behavior of the fission source for continuous energy Problem 1 without FMC feedback (10*cm* Grid).

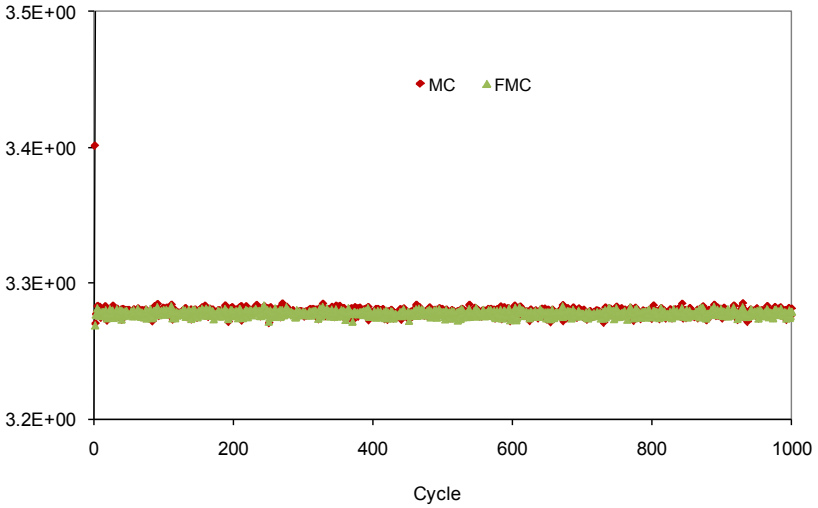

Figure 6.26 Shannon entropy behavior of the fission source for continuous energy Problem 1 with FMC feedback (10*cm* Grid).

Table 6.4 Estimates of k and its Relative Standard Deviation for Continuous Energy Problem 1 without FMC feedback (10cm Grid).

Cycles	Standard MC	FMC	
		One-Group eigenvalue	Two-Group eigenvalue
1 to 100	0.993626 (0.0005722)	0.995228 (0.0000007)	0.995254 (0.0000019)
101 to 200	0.994973 (0.0003738)	0.995228 (0.0000006)	0.995257 (0.0000019)
201 to 300	0.994574 (0.0003649)	0.995228 (0.0000006)	0.995259 (0.0000019)
301 to 400	0.995646 (0.0003614)	0.995228 (0.0000006)	0.995260 (0.0000022)
401 to 500	0.995841 (0.0004063)	0.995228 (0.0000006)	0.995258 (0.0000020)
501 to 600	0.995330 (0.0003679)	0.995230 (0.0000006)	0.995262 (0.0000023)
601 to 700	0.995400 (0.0004416)	0.995229 (0.0000006)	0.995262 (0.0000022)
701 to 800	0.995075 (0.0003765)	0.995228 (0.0000005)	0.995258 (0.0000020)
801 to 900	0.995485 (0.0003580)	0.995227 (0.0000005)	0.995262 (0.0000023)
901 to 1000	0.995647 (0.0003895)	0.995228 (0.0000006)	0.995261 (0.0000028)

Table 6.5 Estimates of k and its Relative Standard Deviation for Continuous Energy Problem 1 with FMC feedback (10cm Grid).

Cycles	Standard MC	FMC	
		One-Group eigenvalue	Two-Group eigenvalue
1 to 100	0.995225 (0.0005648)	0.995227 (0.0000006)	0.995258 (0.0000025)
101 to 200	0.995396 (0.0003711)	0.995228 (0.0000007)	0.995263 (0.0000021)
201 to 300	0.994758 (0.0003123)	0.995228 (0.0000006)	0.995264 (0.0000020)
301 to 400	0.995545 (0.0003404)	0.995229 (0.0000006)	0.995263 (0.0000022)
401 to 500	0.995944 (0.0003934)	0.995228 (0.0000006)	0.995255 (0.0000020)
501 to 600	0.995214 (0.0003705)	0.995229 (0.0000006)	0.995262 (0.0000025)
601 to 700	0.995513 (0.0003984)	0.995227 (0.0000006)	0.995257 (0.0000025)
701 to 800	0.995398 (0.0003634)	0.995228 (0.0000006)	0.995259 (0.0000024)
801 to 900	0.995087 (0.0003513)	0.995227 (0.0000006)	0.995264 (0.0000024)
901 to 1000	0.995795 (0.0003800)	0.995227 (0.0000006)	0.995259 (0.0000021)

6.2 Continuous Energy Problem 2: Heterogeneous 1-D Slab Problem

In this section, we apply the FMC method to a heterogeneous 1-D slab problem with continuous energy. We consider nine identical fissile (F) regions, each of thickness 10.0 cm, enclosed by ten 11.0 cm non-fissile (NF) regions. The detailed configuration is shown in Figure 6.27.

Figure 6.27 Continuous energy problem 2 configuration.

As for Problem 1, the coarse-grid problem has two energy groups:

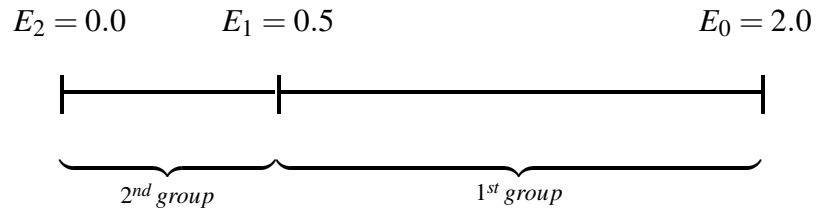

Fission neutrons are born uniformly within the energy range 0.5 MeV - 2.0 MeV. The model fission spectrum is :

$$\chi(E) = \begin{cases} \frac{2}{3}\ \text{Mev}^{-1} & , \quad 0.5\ \text{Mev} < E < 2\ \text{Mev}\ , \\ 0 & , \quad \text{otherwise}\ . \end{cases} \tag{6.3}$$

The Monte Carlo simulation starts with a spatially flat fission source. The fissile material consists of atomic mass number 238, while the non-fissile material has atomic mass number 27. The model continuous-energy capture cross section and fission cross section are taken to be inversely proportional to the square root of energy:

$$\Sigma_s(x,E) = \Sigma_s^0(x)\ , \tag{6.4a}$$

$$\Sigma_\gamma(x,E) = \Sigma_\gamma(x)\sqrt{\frac{E_0}{E}}\ , \tag{6.4b}$$

$$\Sigma_f(x,E) = \Sigma_f(x)\sqrt{\frac{E_0}{E}}\ . \tag{6.4c}$$

The various cross section coefficients from Eqs. (6.4) used for this case are presented in Table 6.6, where x has units of cm and Σ has units of cm^{-1}.

Table 6.6 Cross Section Coefficients for Problem 2: A Heterogeneous 1-D Slab Problem.

Material	Description	$\Sigma_s^0(x)$	$\Sigma_\gamma(x)$	$\Sigma_f(x)$
m1	*NF*	0.856	0.01	0
m2	*F*	0.856	0.01	0.01272

This problem was run for 200 cycles (generations), using 1,000,000 histories/cycle. The

FMC calculation employed a coarse grid with $h = 2.0$ cm. We compare results for the one-group fluxes, averaged over 20 cycle intervals (from the 200-cycle sequence). Results are compared for (a) standard Monte Carlo simulations, and (b) the hybrid FMC calculations, averaged over 20 cycle intervals (Figures 6.28-6.29). We also compare results for the two-group fluxes, averaged over 20 cycle intervals in Figures 6.30-6.32. For both the one-group and the two-group cases, the FMC results are seen to converge almost immediately and to remain stable in all 20-cycle averages of the run. The standard Monte Carlo results do not achieve equilibrium at any point during the 200 cycle test run.

Figures 6.33-6.34 show the one-group and the two-group estimates of the eigenfunction with FMC feedback for the standard MC method and the FMC method. These figures are obtained by skipping 1 inactive cycle and averaging the Monte Carlo estimates of the eigenfunction over 10-cycle spans. Examining Figures 6.33-6.34, we see that the Monte Carlo estimates of the eigenfunction with FMC feedback converge within the first 10 active cycle averages.

The Shannon entropy behavior of the fission source for Problem 2 without FMC feedback is shown in Figure 6.35. The Shannon entropy behavior of Problem 2 with FMC feedback is shown in Figure 6.36. With FMC feedback, the MC Shannon entropy has the same character as that of the FMC Shannon entropy.

Without FMC feedback, the estimated values of k and their estimated relative standard deviations over 10 different ranges of 200 cycles each are compared for the standard Monte Carlo, FMC one-group and two-group cases in Table 6.7. With FMC feedback, the estimated values of k and their estimated relative standard deviations are given in Table 6.8.

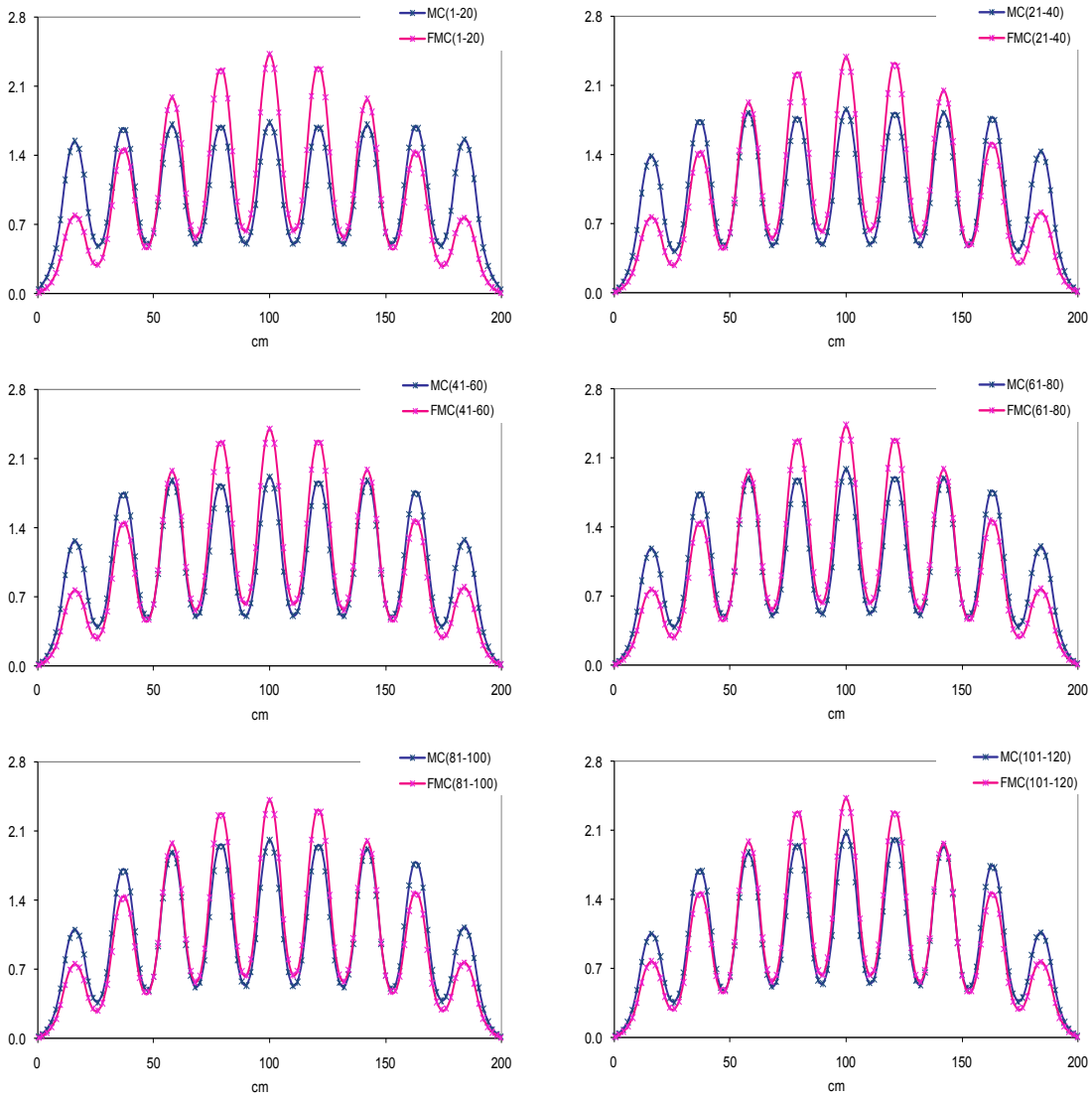

Figure 6.28 Continuous energy Problem 2 one-group eigenfunction estimates during cycles 1-120 without FMC feedback.

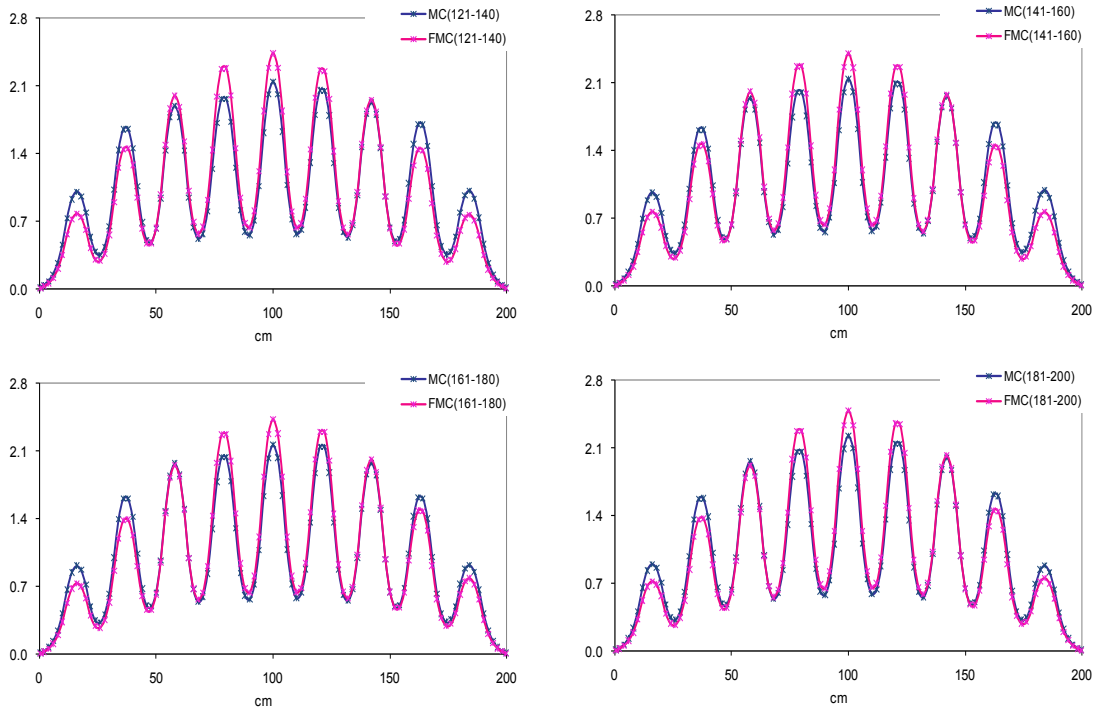

Figure 6.29 Continuous energy Problem 2 one-group eigenfunction estimates during cycles 121-200 without FMC feedback.

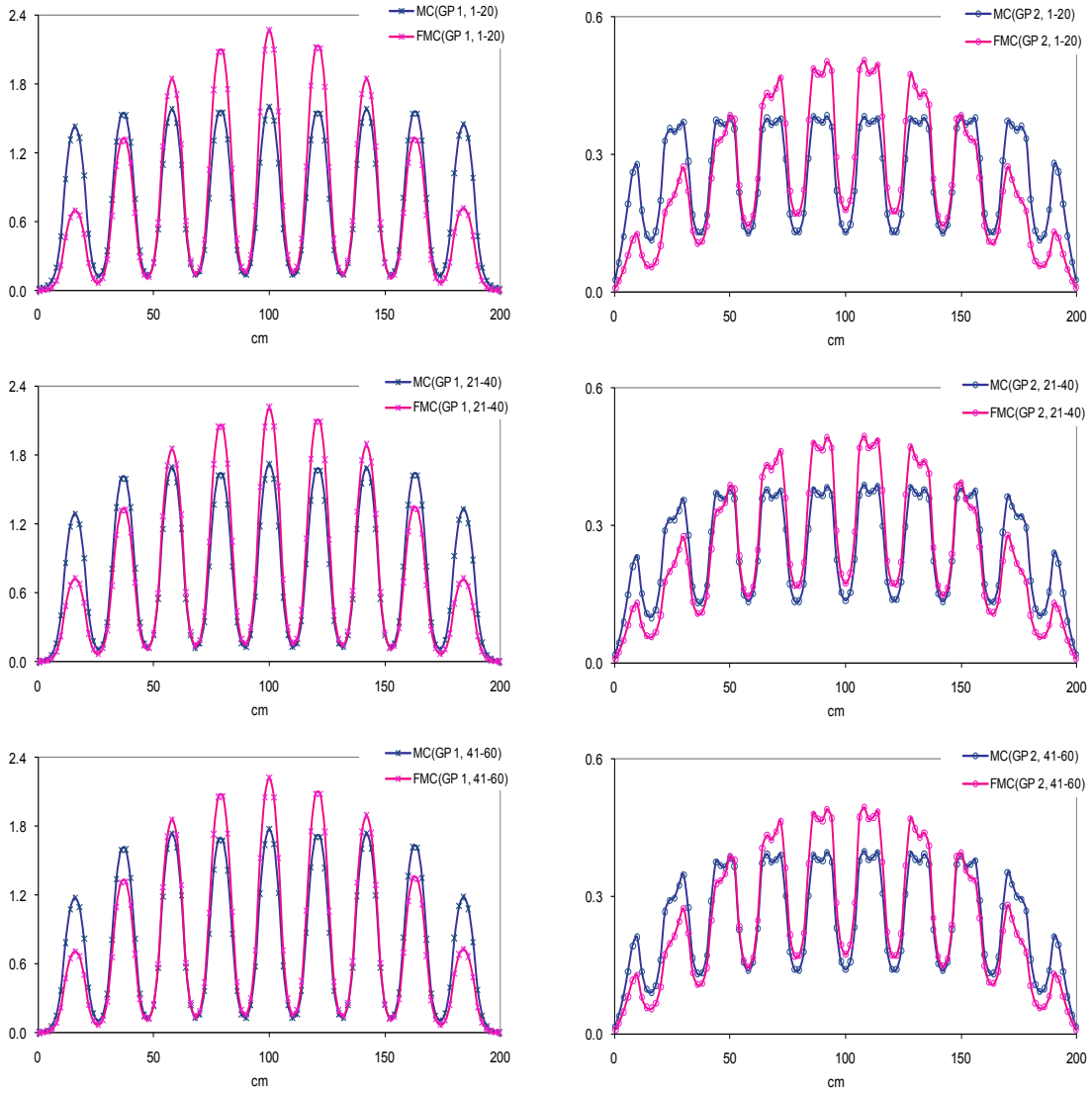

Figure 6.30 Continuous energy Problem 2 two-group eigenfunction estimates during cycles 1-60 without FMC feedback.

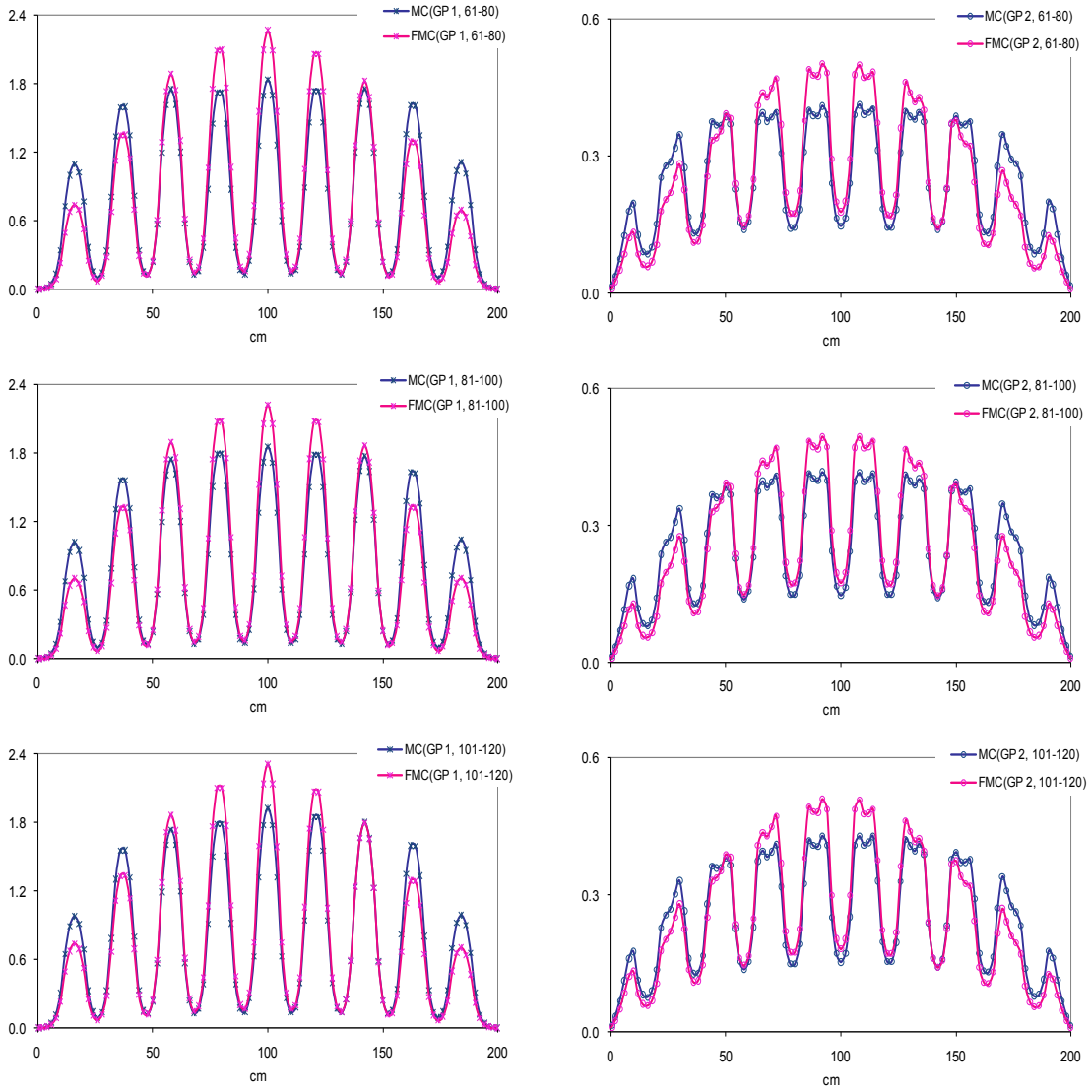

Figure 6.31 Continuous energy Problem 2 two-group eigenfunction estimates during cycles 61-120 without FMC feedback.

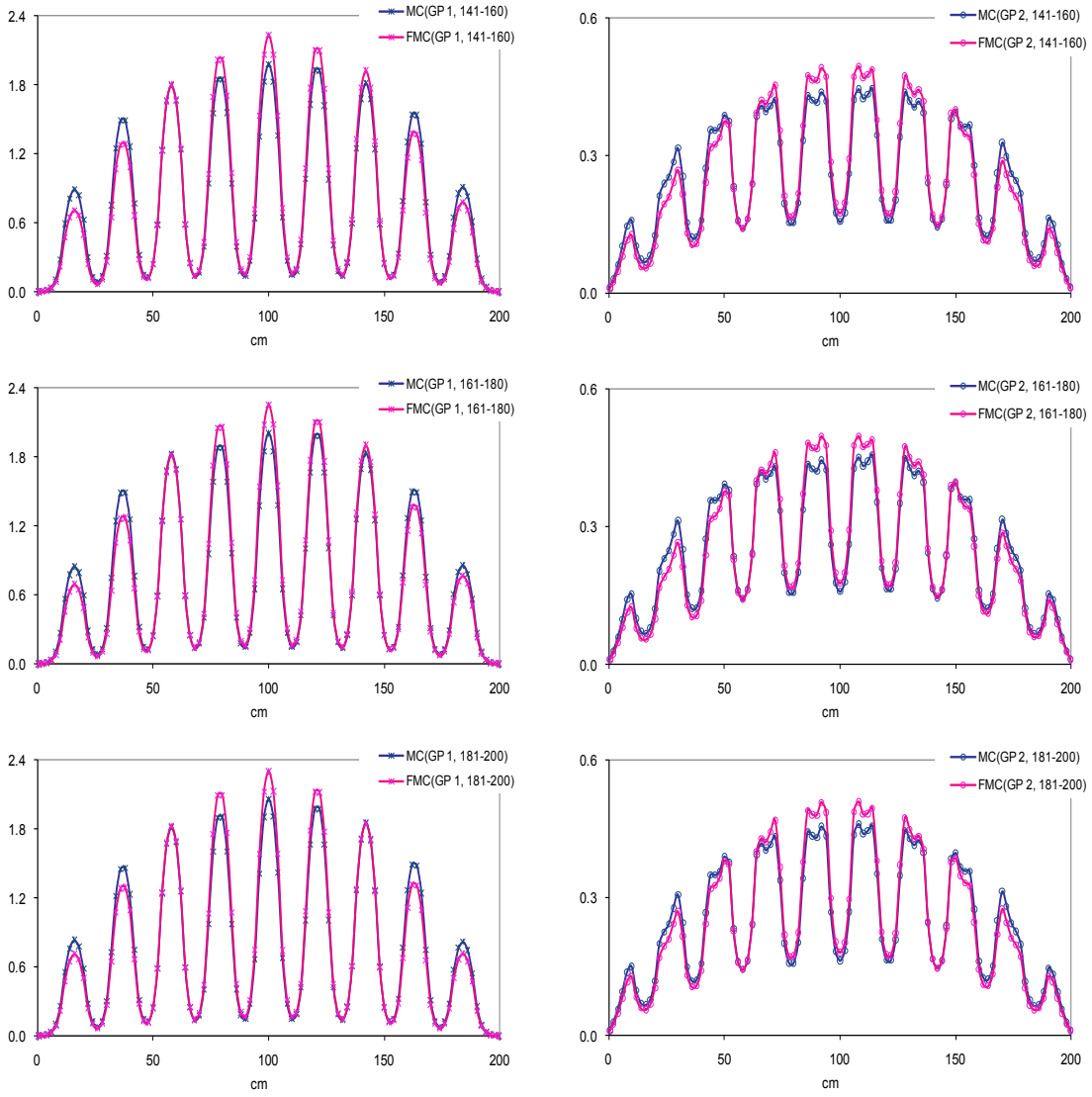

Figure 6.32 Continuous energy Problem 2 two-group eigenfunction estimates during cycles 141-200 without FMC feedback.

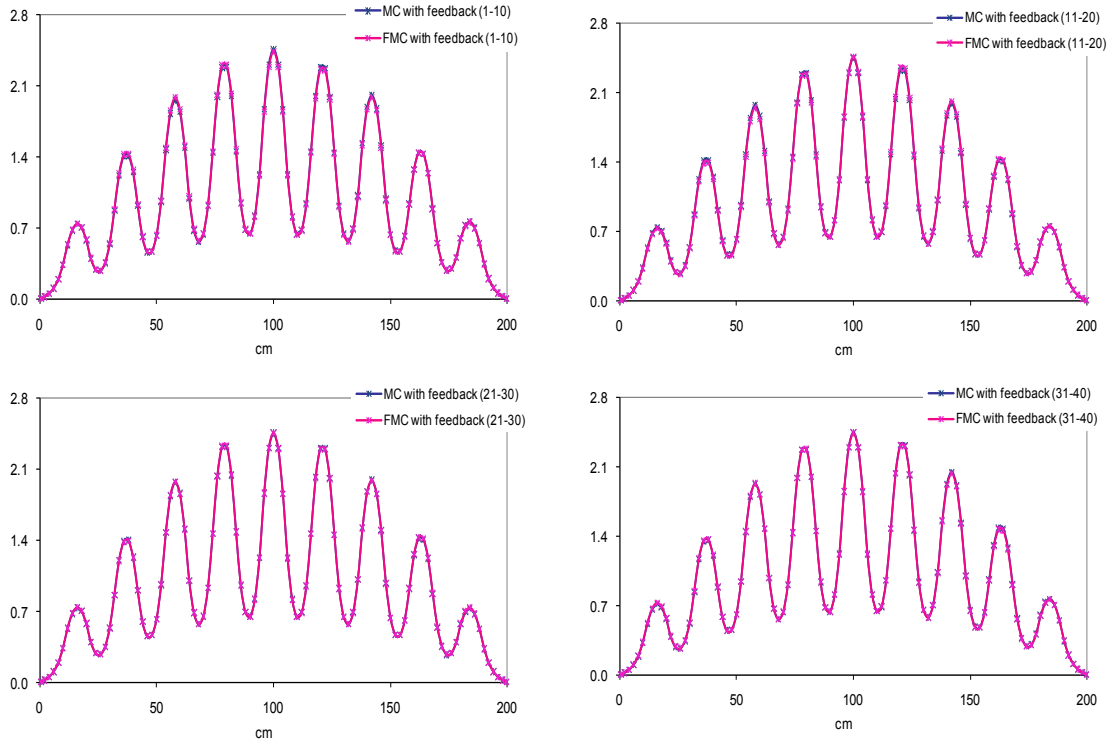

Figure 6.33 Continuous energy Problem 2 one-group eigenfunction estimates during active cycles 1-40 (1 inactive cycle) with FMC feedback.

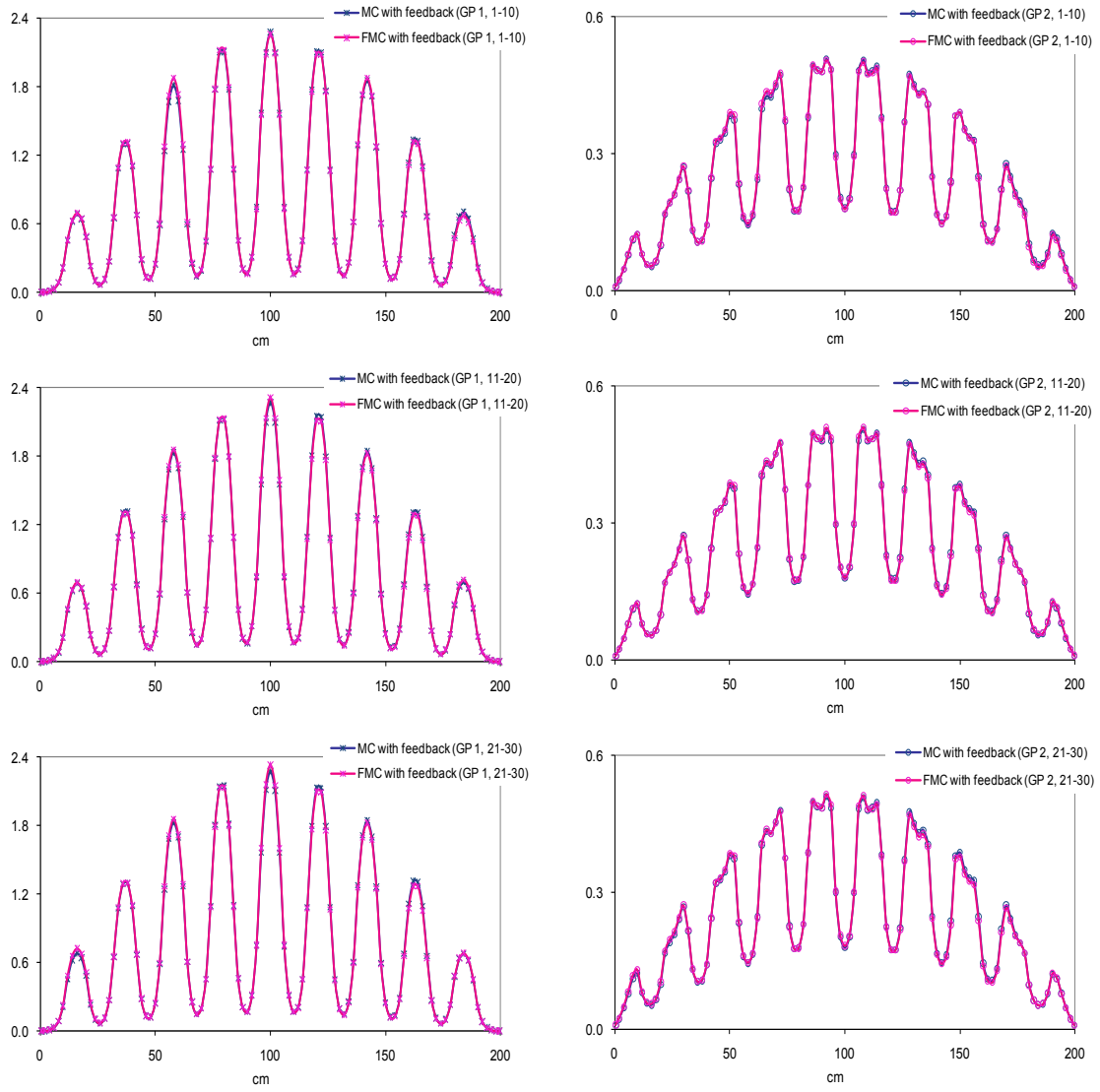

Figure 6.34 Continuous energy Problem 2 two-group eigenfunction estimates during active cycles 1-30 (1 inactive cycle) with FMC feedback.

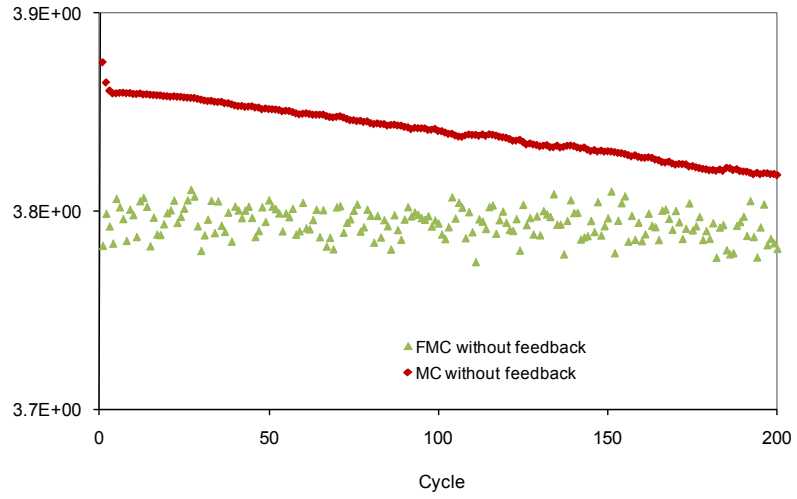

Figure 6.35 Coarse mesh Shannon entropy behavior of the fission source for continuous energy Problem 2 without FMC feedback.

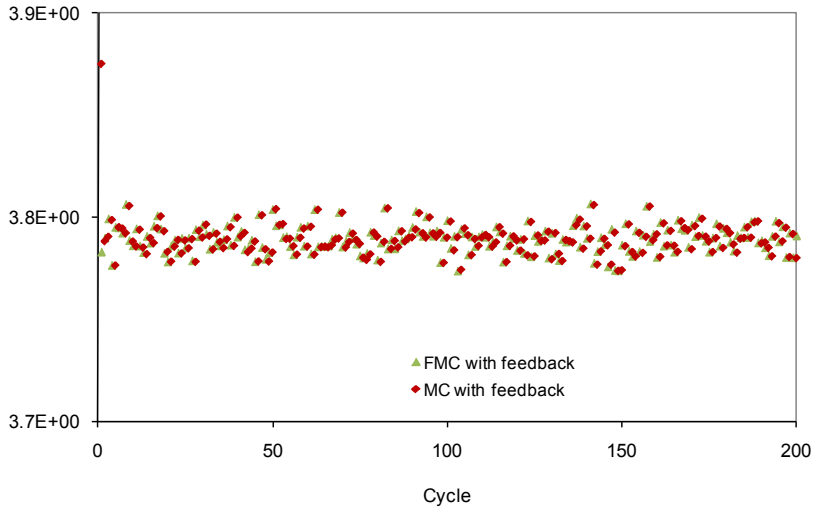

Figure 6.36 Coarse mesh Shannon entropy behavior of the fission source for continuous energy Problem 2 with FMC feedback.

Table 6.7 Estimates of k and its Relative Standard Deviation for Continuous Energy Problem 2 without FMC feedback.

Cycles	Standard MC	FMC	
		One-Group eigenvalue	Two-Group eigenvalue
1 to 20	0.975435 (0.0152102)	0.993884 (0.0006118)	0.993192 (0.0001252)
21 to 40	0.992383 (0.0002770)	0.993262 (0.0000452)	0.993519 (0.0000628)
41 to 60	0.992291 (0.0002587)	0.993260 (0.0000378)	0.993498 (0.0000778)
61 to 80	0.992935 (0.0002820)	0.993234 (0.0000311)	0.993561 (0.0000648)
81 to 100	0.993177 (0.0002791)	0.993201 (0.0000420)	0.993544 (0.0000765)
101 to 120	0.992901 (0.0002900)	0.993276 (0.0000326)	0.993545 (0.0000845)
121 to 140	0.993393 (0.0002665)	0.993265 (0.0000443)	0.993504 (0.0000758)
141 to 160	0.993081 (0.0002636)	0.993231 (0.0000436)	0.993589 (0.0000691)
161 to 180	0.992692 (0.0002876)	0.993252 (0.0000398)	0.993584 (0.0000595)
181 to 200	0.993328 (0.0002965)	0.993330 (0.0000407)	0.993570 (0.0000588)

Table 6.8 Estimates of k and its Relative Standard Deviation for Continuous Energy Problem 2 with FMC feedback.

Cycles	Standard MC	FMC	
		One-Group eigenvalue	Two-Group eigenvalue
1 to 20	0.977879 (0.0153202)	0.993904 (0.0006080)	0.993397 (0.0001442)
21 to 40	0.993050 (0.0002706)	0.993309 (0.0000322)	0.993651 (0.0000590)
41 to 60	0.992968 (0.0002958)	0.993275 (0.0000371)	0.993505 (0.0000660)
61 to 80	0.993078 (0.0001521)	0.993291 (0.0000293)	0.993673 (0.0000626)
81 to 100	0.993456 (0.0002952)	0.993285 (0.0000324)	0.993569 (0.0000633)
101 to 120	0.993003 (0.0002261)	0.993291 (0.0000411)	0.993453 (0.0000579)
121 to 140	0.993710 (0.0002482)	0.993293 (0.0000479)	0.993709 (0.0000997)
141 to 160	0.992803 (0.0002699)	0.993193 (0.0000371)	0.993538 (0.0000686)
161 to 180	0.993110 (0.0002026)	0.993319 (0.0000326)	0.993637 (0.0000809)
181 to 200	0.993362 (0.0002583)	0.993314 (0.0000418)	0.993655 (0.0000917)

6.3 Summary of the Continuous Energy Numerical Results

In this Chapter, we first solved the U-function for both the one-group case and the two-group case. We then tested the FMC method on two continuous energy problems in which the following questions were examined:

1. Accuracy in the estimates of eigenvalue and eigenfunction.
2. Source convergence with a flat initial source guess.
3. Sensitivity to the coarse mesh size.
4. Inter-cycle correlation before and after FMC feedback.

As in the monoenergetic case, estimates of the eigenvalue and eigenfunction with the FMC method were more accurate and more rapidly convergent. For the large, homogeneous fissile region problem, we increased the coarse mesh size from $5cm$ to $10cm$. The resulting FMC estimates of the eigenvalue and energy-integrated eigenfunction and their apparent relative standard deviations were about the same. There was only a slight increase in the apparent relative standard deviations in the two-group eigenfunction estimates. This is due to the fact that more MC particles are needed to get better estimates of the nonlinear functionals, which are associated with the two-group, low-order equations. In the homogeneous test problem, the apparent relative standard deviations are more than a factor of 10 less than the true relative standard deviations for the MC method without FMC feedback. With FMC feedback, the apparent relative standard deviations are about the same as the true relative standard deviations for the MC method. We then applied the FMC method to a heterogenous 1-D slab problem with nine identical fissile regions, enclosed by ten non-fissile regions. The one-group and two-group FMC fluxes are seen to converge almost immediately, while the standard Monte Carlo results did not converge after a 200 cycle run. With FMC feedback, the Monte Carlo estimates of the eigenfunction converge within the first 10-cycle average (1 inactive cycle). To summarize: the FMC feedback dramatically improves the performance of the Monte Carlo method in all the test problems we have run.

Chapter 7
Conclusions

In this thesis, we have developed and tested a new hybrid deterministic and Monte Carlo method, called the Functional Monte Carlo (FMC) method, to solve slowly converging k-eigenvalue problems. The FMC method is different from any previous hybrid method. It does not directly estimate the eigenfunction and eigenvalue via Monte Carlo particle simulation. Instead, it uses MC techniques to directly estimate certain *nonlinear functionals*. These estimated functionals are then used in the low-order FMC equations to calculate the k-eigenfunction and eigenvalue. The resulting estimates of the k-eigenfunction and eigenvalue have no spatial or angular truncation errors, and are generally more accurate and have less statistical noise than estimates obtained using conventional Monte Carlo methods.

The FMC method is based on two assumptions:

1. The functionals depend weakly on the angular flux and can be evaluated with Monte Carlo more accurately than direct Monte Carlo estimates of the angular flux or scalar flux.
2. If the low-order FMC equations are solved with small errors in the functionals, the resulting errors in the eigenfunction and eigenvalue will be small.

In this work, we have developed the FMC method for monoenergetic, multigroup, and continuous energy k-eigenvalue problems in 1-D planar geometry.

7.1 The FMC method for 1-D Monoenergetic k-Eigenvalue Problems

First, we considered a steady-state, planar-geometry k-eigenvalue problem with anisotropic scattering and vacuum boundaries. The "low-order" FMC equations were derived in the following three steps: (1) We first construct the zero-th and first angular moments of the Boltzmann transport equation. (2) Next, we define tent functions. Using these, we construct certain spatial moments of the angularly-integrated equations obtained in Step 1. (3) Introducing no approximations, we manipulate the spatially- and angularly-integrated equations to obtain a discrete system of "low-order" FMC equations. Because the low-order FMC equations are derived without approximation from the high-order Boltzmann equation, the FMC method has no angular, spatial, or energy truncation errors. The only error is the statistical error that is introduced from the Monte Carlo estimates of the nonlinear functionals.

Initially, the eigenfunctions obtained from the low order FMC equations were defined either "at" the cell edges or averaged on a "staggered" grid. We then developed a procedure to generate low-order equations with material discontinuities within a cell. This allowed us to accurately estimate the scalar flux over the spatial cells. The FMC results can then be used to improve the Monte Carlo fission source distribution.

We tested the FMC method on four problems (including a simplified 1-D full PWR reactor core) in which standard MC estimates of the eigenfunction "wobble." (These problems have high dominance ratios.) The results show that the FMC method has the following advantages compared to standard Monte Carlo.

1. The FMC estimates of the eigenvalue and eigenfunction are much more accurate than standard Monte Carlo estimates. For a large, homogeneous fissile region problem, the FMC estimates of k are three orders of magnitude more accurate than the MC estimates.
2. The fission source distribution converged much faster using the FMC approach than

the MC approach.

3. Inter-cycle correlation is very weak for the FMC method. The true relative errors are about the same as the apparent relative errors for the FMC method. The apparent relative errors are more than a factor of 10 less than the true relative errors for the MC method in these four test problems.
4. With FMC feedback, the MC estimates of the eigenfunction converged at the same speed as the FMC estimates.

7.2 The FMC method for 1-D Multigroup k-Eigenvalue Problems

The multigroup FMC method is a straightforward extension of the monoenergetic FMC method, although there is additional complexity because of the occurrence of between-group scattering. As in the monoenergetic case, the resulting multigroup FMC estimates of eigenvalues and eigenfunctions have only statistical errors. The FMC method has no spatial, angular, or energy truncation errors, beyond the errors associated with the multigroup approximation. This method was implemented and successfully tested.

7.3 The FMC method for 1-D Continuous Energy k-Eigenvalue Problems

We also extended the FMC method to continuous-energy k-eigenvalue problems. The continuous-energy approach has several noticeable differences compared with the monoenergetic and multigroup approaches. The low-order equations that we derived in this thesis are in two forms: (1) the low-order equations are energy-independent, and the eigenfunction is an energy-integrated scalar flux; (2) the low-order equations are multigroup in form. The resulting FMC estimates of the eigenvalue and energy-integrated or multigroup fluxes have (i) no spatial or angular truncation errors, and (ii) very small energy truncation errors and

statistical errors. We also developed a procedure to generate FMC multigroup low-order equations with any number of material discontinuities within a coarse cell. This makes it possible to improve the Monte Carlo fission source with FMC feedback.

We tested the FMC method on two continuous energy problems. Compared to the standard MC approach, the results show that the FMC approach in the continuous energy case has the same advantages as in the monoenergetic case. The results also showed that the FMC approach is not sensitive to the size of the coarse mesh. Here we emphasize that although the low-order FMC equations do not produce highly accurate fine-mesh solutions, the FMC estimates of the coarse-mesh averaged fluxes are consistently more accurate than the standard Monte Carlo estimates. With FMC feedback (using FMC coarse-mesh information and MC fine-mesh information), the performance of the Monte Carlo method was dramatically improved in all the test problems we ran.

Overall, in this thesis we have demonstrated that the FMC method offers significant advantages in solving slowly converging k-eigenvalue problems with high dominance ratios. We would like to emphasize that the FMC method can be understood as a "global" Monte Carlo approach in which estimates of the solution are obtained that span across the entire physical system. The FMC method yields "global" information about a physical problem through Monte Carlo techniques.

The "FMC Method" is not really a single method, but is a general approach – and there are many different ways to implement it. The FMC hybrid technique developed in this thesis is algebraically more complicated than the standard Monte Carlo method and most other hybrid techniques, such as CMFD. However, the FMC method has noticeable advantages. The nonlinear functionals defined in the FMC method are ratios of the even-order angular moments of the flux; thus, they are inherently more stable with less statistical noise than functionals containing the ratios of odd-order angular moments. Before we settled on the approach of eliminating the current J(x,E) from the equations, we tried other approaches that included the current term, but these did not work so well. The CMFD method and

its variations, studied by Professor Han Gyu Joo, Ming-Jae Lee, and Emily Wolters, is a type of FMC method in which the current term is not eliminated from the equations. Preliminary work by Lee showed that the FMC method is more efficient than CMFD, but these comparisons have been very limited. Also, CMFD is simpler to implement, and in his work, Lee has gone in the direction of 2-D multigroup rather than 1-D continuous energy, so comparisons between FMC and CMFD have really not been made except for simple 1-D, 1-group problems.

7.4 Future work

We should continue testing and improving the FMC method performance in the following ways:

1. A more extensive examination and comparison of the different FMC and CMFD methods in 1-D should be done, first for energy-independent problems, then for multigroup problems, and finally, for continuous-energy problems. In addition to comparing the results for very difficult problems with high dominance ratios, we should also compare the FMC and CMFD methods with standard Monte Carlo for simpler problems, with dominance ratios that are not close to unity to see if they are similar in accuracy. From the test problems we ran, the FMC method gives more accurate values of k even for simpler problems with low dominance ratios.
2. The continuous-energy FMC approach in this thesis has assumed for simplicity that the cross sections for each material are inversely proportional to the square root of energy, and each material region contains only one kind of element. These assumptions can be easily removed. In this thesis, the FMC approach considers the elastic scattering only. For other types of scattering, such as inelastic scattering with tabulated data structure, we may use the multigroup approach with a very find grid. For neutron thermal scattering in analog format, we may treat it in a similar manner as we treat

the elastic scattering in the thesis. In future work, the continuous-energy problems should be upgraded to include realistic cross sections.

3. The 1-D FMC method has shown significant improvement in solving the slow convergence of Monte Carlo k-eigenvalue problems. This method should be extended to 2-D and then to 3-D.
4. The algebraic complexity of the FMC method in this thesis is a concern. We are certain that the work done in 1-D can be extended to 2-D and 3-D, but it will not be simple. The treatment of problems in which each coarse cell contains spatial heterogeneities is not "simple". It would be beneficial to improve the current FMC approach by simplifying it in a way that does not impede performance.
5. The current FMC and CMFD methods have been implemented without the use of conventional variance-reduction techniques, such as weight windows. However, there is no doubt that the Monte Carlo part of the FMC or CMFD methods could be run, for example, with weight windows. Doing this would add computational cost. Would this extra cost be offset by a sufficient decrease in variance in the FMC solution? This would be an interesting topic for future research.
6. Currently, there exists little solid theory to guide researchers with the development of new FMC-like methods. For deterministic methods, a Fourier analysis has proved to be reliable and accurate. Unfortunately, no such "stability" theory exists at this time for Monte Carlo FMC or CMFD methods. It would be very beneficial if such a theory could be developed.

Appendix

List of Nomenclature

$\vec{r} = (x, y, z) =$ spatial variable

$\vec{\Omega} = (\Omega_x, \Omega_y, \Omega_z) =$ direction, or angular variable

$E =$ energy

$t =$ time

$\Sigma_s(\vec{r}, \vec{\Omega}' \cdot \vec{\Omega}, E' \rightarrow E) =$ differential macroscopic scattering cross section

$\Sigma_t(\vec{r}, E) =$ total macroscopic cross section

$\Sigma_\gamma(\vec{r}, E) =$ macroscopic capture cross section

$\Sigma_s(\vec{r}, E) =$ macroscopic scattering cross section

$\Sigma_f(\vec{r}, E) =$ macroscopic fission cross section

$Q(\vec{r}, \vec{\Omega}, E, t) =$ external source

$k =$ eigenvalue $=$ effective multiplication factor

$\psi(\vec{r}, \vec{\Omega}, E) =$ angular flux, fundamental mode eigenfunction

$P(E' \rightarrow E) =$ scattering probability distribution for elastic scattering

$\hat{\mu}_0(E' \rightarrow E) =$ scattering cosine from energy E' to E

$A =$ mass number of nucleus

DR = dominance ratio

RSD = relative standard deviation of the sample mean

apparent RSD = apparent relative standard deviation of the sample mean

true RSD = true relative standard deviation of the sample mean

$\psi(x,\mu,E)$ = 1-D angular flux, fundamental mode eigenfunction

$\Phi(x,E)$ = scalar flux, zeroth order moment of the angular flux

$\Phi_1(x,E)$ = first order moment of the angular flux

$\Phi_2(x,E)$ = second order moment of the angular flux

$\Phi_{g,j}$ = multigroup flux averaged over j^{th} spatial (coarse) cell

$f_{j+1/2}$ = tent function defined on the spatial grid

f_j = tent function defined on the staggered grid

$g_{j+1/2}$ = histogram function defined on the staggered grid

g_j = histogram function defined on the spatial grid

$U(x,E)$ = U function which satisfies an infinite medium adjoint equation

$U_g(x,E)$ = multigroup U function

$\hat{\chi}_g(E)$ = characteristic function which is used to define FMC multigroup adjoint equations

$B_{1/2}, B_{J+1/2}, E_{j+1/2}, A_{j+1/2}, F_{j+1/2}$

= monoenergetic nonlinear functionals defined on the staggered grid

B_1, B_J, E_j, A_j, F_j

= monoenergetic nonlinear functionals defined on the spatial grid

$B_{1/2}, B_{J+1/2}, A_{j+1/2}, F_{j+1/2}, U^L_{j+1/2}, U^R_{j+1/2}$

= one group continuous energy nonlinear functionals defined on the staggered grid

$B_{g,1/2}, B_{g,J+1/2}, F_{g,g',j+1/2}, U^R_{g,j+1/2}, U^L_{g,j+1/2}, \tilde{\Sigma}_{s,g\to g',j+1/2}, \tilde{\Sigma}_{t,g,j+1/2}$

= two group continuous energy nonlinear functionals defined on the staggered grid

$B_{g,1}, B_{g,J}, F_{g,g',j}, U^R_{g,j+1/2}, U^L_{g,j+1/2}, \tilde{\Sigma}_{s,g\to g',j}, \tilde{\Sigma}_{t,g,j}, \tilde{W}_{g,j-1/2}$

= two group continuous energy nonlinear functionals defined on the spatial grid

Bibliography

[1] M.L. Adams and E.W. Larsen. Fast Iterative Methods for Discrete-Ordinates Particle Transport Calculations. *Progress in Nuclear Energy*, 40:3, 2002.

[2] T.L. Becker and E.W. Larsen. The Application of Weight Windows to 'Global' Monte Carlo Problems. In *Proc. 2009 International Conference on Advances in Mathematics, Computational Methods, and Reactor Physics*, Saratoga Springs, New York, May 2009.

[3] T.L. Becker, A.B. Wollaber, and E.W. Larsen. A Hybrid Monte Carlo-Deterministic Method for Global Particle Transport Calcuations. *Nucl. Sci. Eng.*, 155:155–167, 2007.

[4] F.B. Brown. Fundamentals of Monte Carlo Particle Transport. LA-UR-05-4983, Los Alamos National Laboratory, 2005.

[5] J.Y. Cho, H.G. Joo, K.S. Kim, and S.Q. Zee. Cell Based CMFD Formulation for Acceleration of Whole-Core Method of Characteristics Calculations. *Journal Korean Nucl. Soc.*, 34:250, 2002.

[6] M.A. Cooper. *An Automated Variance Reduction Method for Global Monte Carlo Neutral Particle Transport Problems*. PhD thesis, University of Michigan, 1999.

[7] M.A. Cooper and E.W. Larsen. An Automated Variance Reduction Method for Global Monte Carlo Deep Penetration Neutron Transport Problems. In *Proc. Joint Int. Conf. Mathematical Methods and Supercomputing for Nuclear Applications*, volume 1, page 681, Saratoga Springs, New York, October 5-9 1997. American Nuclear Society.

[8] M.A. Cooper and E.W. Larsen. Automated Weight Windows for Global Monte Carlo Particle Transport Calculations. *Nucl. Sci. Eng.*, 137:1, 2001.

[9] J.D. Densmore and E.W. Larsen. Variational Variance Reduction for Particle Transport Eigenvalue Calculations Using Monte Carlo Adjoint Simulation. *Journal of Computational Physics*, 192:387–405, 2003.

[10] J.J. Duderstadt and L.J. Hamilton. *Nuclear Reactor Analysis*. John Wiley and Sons, Inc., New York, 1976.

[11] J.J. Duderstadt and W.M. Martin. *Transport Theory*. John Wiley and Sons, Inc., New York, 1979.

[12] V.Ya. Gol'din. A Quasi-Diffusion Method for Solving the Kinetic Equation. *Zh. Vych. Mat. Fiz.*, 4:1078, 1964 English translation published in USSR Comp. Math. and Math. Phys. 4,6,136 (1967).

[13] A. Haghighat and J.C. Wagner. Monte Carlo Variance Reduction with Deterministic Importance Functions. *Progress in Nuclear Energy*, 42(1):25–53, 2003.

[14] M.H. Kalos. Importance Sampling in Monte Carlo Shielding Calculations. *Nuclear Science and Engineering*, 16:227, 1963.

[15] M.H. Kalos and P.A. Whitlock. *Monte Carlo Methods. Volume I: Basics*. John Wiley and Sons, Inc., New York, 1986.

[16] E.W. Larsen and J. Yang. New Monte Carlo Functional Methods for Evaluating k-Eigenvalues and Eigenfunctions. *Trans. Am. Nucl. Soc.,*, 97:469, 2007.

[17] E.W. Larsen and J. Yang. A Functional Monte Carlo Method for k-Eigenvalue Problems. *Nucl. Sci. Eng.*, 159:107–126, 2008.

[18] D. Lee, T.J. Downar, and Y. Kim. Convergence Analysis of the Nonlinear Coarse-Mesh Finite Difference Method for One-Dimensional Fixed-Source Neutron Diffusion Problem. *Nucl. Sci. Eng.*, 147:127, 2004.

[19] M.J. Lee, H.G. Joo, D. Lee, and K.S. Smith. Investigation of CMFD Accelerated Monte Carlo Eigenvalue Calculation with Simplified Low Dimensional Multigroup Formulation. In *Proc. 2010 International Conference on the Physics of Reactors*, Pittsburgh, Pennsylvania, May 2010.

[20] M.J. Lee, H.G. Joo, D. Lee, and K.S. Smith. Multigroup Monte Carlo Reactor Calculation with Coarse Mesh Finite Difference Formulation for Real Variance Reduction. In *Proc. 2010 Joint International Conference on Supercomputing in Nuclear Applications and Monte Carlo*, Tokyo, Japan, October 2010.

[21] E.E. Lewis and Jr. W.F. Miller. *Computational Methods of Neutron Transport*. American Nuclear Society, Inc., LaGrange Park, IL, 1993.

[22] M.M. Miften. *The Quasi-Diffusion Method for Transport Problems in Multidimensional Geometries*. PhD thesis, University of Michigan, 1994.

[23] M.M. Miften and E.W. Larsen. The Quasi-Diffusion Method for Solving Transport Problems in Planar and Spherical Geometries. *Transport Theory Statist. Phys.*, 22:165, 1993.

[24] D.E. Peplow, E.D. Blakeman, and J.C. Wagner. Advanced Variance Reduction Stratgies for Optimizing Mesh Tallies in MAVRIC. *Trans. Am, Nucl. Soc.*, 97:595–597, 2007.

[25] K.S. Smith. Nodal Method Storage Reduction by Nonlinear Iteration. *Trans. Am Nucl. Soc.*, 44:265–266, 1983.

[26] K.S. Smith. Assembly Homogenization Techniques for Light Water Reactor Analysis. *Prog. Nucl. Energy*, 17:303, 1986.

[27] X-5 Monte Carlo Team. MCNP-A General N-Particle Transport Code, Version 5 - Volume 1: Overview and Theory. LA-UR-03-1987, Los Alamos National Laboratory, April 2003.

[28] T. Ueki. Intergenerational Correlation in Monte Carlo k-Eigenvalue Calculation. *Nucl. Sci. Eng.*, 141:101–110, 2002.

[29] T. Ueki. Information Theory and Undersampling Diagnostics for Monte Carlo Simulation of Nuclear Criticality. *Nucl. Sci. Eng.*, 151:283, 2005.

[30] T. Ueki, F.B. Brown, D.K. Parsons, and D.E. Kornreich. Autocorrelation and Dominance Ratio in Monte Carlo Criticality Calculations. *Nucl. Sci. Eng.*, 145:279–290, 2003.

[31] J.C. Wagner, E.D. Blakeman, and D.E. Peplow. Forward-Weighted CADIS Method for Global Variance Reduction. *Trans. Am. Nucl. Soc.*, 97:630–633, 2007.

[32] J.C. Wagner and A. Haghighat. Automated Variance Reduction of Monte Carlo Shielding Calculations Using the Discrete Ordinates Adjoint Function. *Nucl. Sci. Eng.*, 128:186, 1998.

[33] E.R. Wolters. *Hybrid Monte Carlo-Deterministic Neutron Transport Methods Using Nonlinear Functionals*. PhD thesis, University of Michigan, 2011.

[34] E.R. Wolters, E.W. Larsen, and W.R. Martin. A Hybrid Monte Carlo-S2 Method with No Spatial Truncation Error. *Trans. Am. Nucl. Soc.*, 101:714–716, 2009.

[35] A. Yamamoto. Generalized Coarse-Mesh Rebalance Method for Acceleration of Neutron Transport Calculations. *Nucl. Sci. Eng.*, 151:274, 2005.

[36] T. Yamamoto, T. Nakamura, and Y. Miyoshi. Fission Source Convergence of Monte Carlo Criticality Calculations in Weakly Coupled Fissile Arrays. *J. Nucl. Sci. Technology*, 37:41, 2000.

[37] J. Yang and E.W. Larsen. Application of the 'Functional Monte Carlo' Method to Estimate Continuous Energy Eigenvalues and Eigenfunctions. In *Proc. 2009 International Conference on Advances in Mathematics, Computational Methods, and Reactor Physics*, Saratoga Springs, New York, May 2009.

[38] J. Yang and E.W. Larsen. Calculation of k-Eigenvalues and Multigroup Eigenfunctions Using the Hybrid 'Functional Monte Carlo' Method. In *Proc. PHYSOR 2010 - Advances in Reactor Physics to Power the Nuclear Renaissance*, Pittsburgh, Pennsylvania, May 2010.